Distribution Agreement

Signature:

________________________________ ____________________________
Rong Ma Date

A toolbox based on DNA nanotechnology to investigate cell receptor mechanics

By

Rong Ma
Doctor of Philosophy

Chemistry

Khalid Salaita
Advisor

Laura Finzi
Committee Member

Jennifer Heemstra
Committee Member

Yonggang Ke
Committee Member

Accepted:

Lisa A. Tedesco, Ph.D. Dean of the James T. Laney School of Graduate Studies

Date

A toolbox based on DNA nanotechnology to investigate cell receptor mechanics

By

Rong Ma
M.Sc., City University of Hong Kong, 2013
B.Sc., Wuhan University, 2012

Advisor: Khalid Salaita, PhD

An abstract of
A dissertation submitted to the Faculty of the
James T. Laney School of Graduate Studies of Emory University
in partial fulfillment of the requirements for the degree of
Doctor of Philosophy
in Chemistry
2021

Abstract

A toolbox based on DNA nanotechnology to investigate cell receptor mechanics

By
Rong Ma

Mechanical forces exist widely at the interplay between a cell and extracellular matrix, or between cells, and are critical in mediating diverse biological functions, ranging from proliferation and differentiation, to cell activation and cancer development. To study these mechanical forces, innovative tools are needed. Thus, as one of the most intensively studied biopolymers, nucleic acids are becoming an important force-responsive material for the study of mechanobiology. Various platforms functionalized with DNA constructs have been designed to sense and manipulate receptor forces due to their well understood mechanical characteristics and highly modular composition. This dissertation introduces the current state of mechanobiology and mechano-immunology understanding, as well as the fundamental principles of DNA mechanics. Following an overview of the classic design and applications of DNA-based tools, this dissertation describes four unique DNA-based methods to investigate cell receptor mechanics from different perspectives and discusses the limitations of current techniques. Finally, future enrichment of the DNA mechanotechnology toolbox is envisioned.

A toolbox based on DNA nanotechnology to investigate cell receptor mechanics

By

Rong Ma
M.Sc., City University of Hong Kong, 2013
B.Sc., Wuhan University, 2012

Advisor: Khalid Salaita, PhD

A dissertation submitted to the Faculty of the
James T. Laney School of Graduate Studies of Emory University
in partial fulfillment of the requirements for the degree of
Doctor of Philosophy
in Chemistry
2021

Acknowledgement

First, I would like to express my gratitude to my advisor, Dr. Khalid Salaita, for his mentorship and guidance. I would not have made this progress without him. In the first 2 years of my PhD training, he nurtured me to grow with a lot of encouragement and patience, and as I became more independent later, he granted me a lot of freedom to follow my heart and go wherever my curiosity led me. I am very grateful to all other members on my committee. Dr. Laura Finzi, Dr. Jen Heemstra, and Dr Yonggang Ke have not only offered valuable feedback over the years on my projects, but also encouraged me and helped me build my confidence. I would also like to extend my gratitude to Dr. David Lynn. His support is always one of the “cures” for my frustrations in life.

Next, I shall extend my thanks to all my previous and current labmates (Kim, Jing, Yang, Yun, Yuan, Kornelia, Victor, Jessica, Roxy, Josh, Aaron, Han, Jiahui, Hiroaki, Alisina, Dale, Brendan, Yixiao, Anna, Allison, Rachel Bender, Yuxin, Aysha, Arventh, Radhika, Yuesong, Selma, Thea, and Steven), for the assistance they have given me and the experiences they have shared with me. The shared frustration of failed experiments and joy of research progress have relieved me from anxiety and doubled the fun.

My sincere appreciation also goes to our collaborating labs. Dr. Brain Evavold, Dr. Cheng Zhu, and Dr. Alexa Mattheyses have offered great help to me and insightful feedback to my projects. Dr. Kaitao Li, Dr. Wenchun Chen, Dr. Brian Petrich, and Dr. Tejeshwar Rao have also contributed a lot to project growth or to broadening my knowledge.

I would like to thank my friends for their support during the past few years, especially Zhigang, Anna, Selma, Dale, Thea, Roxy, Aysha, Han, Yuesong, and Alisina. They lent me the strength to power through difficulties in research and in life a number of times.

I would like to express my gratitude to my special collaborator, Brendan. He is a wonderful person and has made my life so much easier and happier! Without his support this work would not have been possible.

Finally, I would like to thank my parents. Without their love, support, and faith in me, I would never have been able to get here. They are truly incredible. I am who I am because of them, and this degree is not just granted to me, but also to them too.

Table of Contents

List of figures

List of tables

List of movies

Movie A2.1. Erasing the stored mechanical information with the unlocking strand.

Movie A2.2. Erasing of stored mechanical information was not due to photobleaching of Atto647N dye on the locking strand.

Movie A2.3. Control showing failed unlocking with scrambled unlocking strand 1.

Movie A2.4. Control showing failed unlocking with scrambled unlocking strand 2.

Movie A2.5. Real-time TCR-pMHC N4 tension during the migration of an OT-1 cell.

Movie A3.1. Locking kinetics of OT-1 TCR force with antiCD3ε.

Movie A3.2. Locking kinetics of OT-1 TCR force with pMHC N4.

Movie A3.3. Locking kinetics of OT-1 TCR force with pMHC Q4.

Movie A3.4. Locking kinetics of OT-1 TCR force with CD28-B7-1 engagement.

Movie A3.5. Locking kinetics of OT-1 TCR force with LFA-1-ICAM-1 engagement.

Movie A3.6. Locking kinetics of OT-1 TCR force with CK666 inhibition of Arp2/3.

Movie A3.7. Locking kinetics of OT-1 TCR force with Blebb inhibition of myosin II.

Movie A3.8. Locking kinetics of OT-1 TCR force with Jas arresting actin flow.

Movie A3.9. Locking kinetics of OT-1 TCR force with DMSO control.

List of abbreviations

A.U.	Arbitrary units
AFM	Atomic force microscopy
ANOVA	Analysis of variance
APC	Antigen presenting cell
APEX	Ascorbate peroxidase
APL	Altered peptide ligand
APTES	(3-Aminopropyl)triethoxysilane
AuNP	Gold nanoparticle
BCR	B cell receptor
BF	Brightfield
BFP	Biomembrane force probe
BHQ2	Blackhole Quencher-2
Blebb	Blebbistatin
BSA	Bovine serum albumin
CCS	Cosmic calf serum
CFN	Cellular force nanoscopy
CIM	Cell imaging media
cSMAC	Central supramolecular activation cluster
DMEM	Dulbecco’s Modified Eagle’s medium
DNA-PAINT	DNA-points accumulation for imaging in nanoscale topography

DPBS	Dulbecco's phosphate-buffered saline
dSMAC	Distal supramolecular activation cluster
ECM	Extracellular matrix
EDTA	Ethylenediaminetetraacetic acid
EMCCD	Electron multiplying charge coupled device
FA	Focal adhesion
FACS	Fluorescence-activated cell sorting
FBS	Fetal bovine serum
FLIM	Fluorescence lifetime imaging microscopy
FRET	Förster resonance energy transfer
GC	Guanine-Cytosine
HBSS	Hanks' balanced salt solution
HP	Hairpin
HPLC	High pressure liquid chromatography
HRP	Horseradish peroxidase
ICAM-1	Intercellular adhesion molecule 1
ITAM	Immunoreceptor tyrosine-based activation motifs
Jas	Jasplakinolide
LAT	Linker for activation of T cells
Lat B	Latrunculin B
LFA-1	Lymphocyte function-associated antigen 1
LIPID	Load-induced proximal insertion of DNA

MACS	Magnetic-activated cell sorting
MALDI-TOF-MS	Matrix-assisted laser desorption/ionization time-of-flight mass spectrometer
MFI	Median fluorescence intensity
MFM	Molecular force microscopy
MLCK	Myosin II light chain kinase
MTFM	Molecular tension-based fluorescence microscopy
NHS	N-Hydroxysuccinimide
NIH	National Institutes of Health
NTA-SAM	Nitrilotriacetate self-assembled monolayer
P/S	Penicillin/streptomycin
PBS	Phosphate-buffered saline
PD1	Programmed cell death receptor 1
PDL1	Programmed cell death ligand 1
PDL2	Programmed cell death ligand 2
PEG	Polyethylene glycol
pMHC	Peptide-major histocompatibility complex
PPI	Protein-protein interaction
pSMAC	Peripheral supramolecular activation cluster
RGD	Arginine-Glycine-Aspartic Acid
RICM	Reflection interference contrast microscopy
ROI	Region of interest

sCMOS	Scientific complementary metal–oxide–semiconductor
SD	Standard deviation
SDS-PAGE	Sodium dodecyl sulfate polyacrylamide gel electrophoresis
SEM	Standard error of the mean
SLB	Supported lipid bilayer
SMCC	Succinimidyl 4-(N-maleimidomethyl)cyclohexane-1-carboxylate
TCEP	Tris (2-carboxyethyl) phosphine
TCR	T cell receptor
TGT	Tension gauge tether
TIRF	Total internal reflection fluorescence
tPAINT	Tension points accumulation for imaging in nanoscale topography
Ttol	Tension tolerance
WLC	Worm-like chain
YAP	Yes-associated protein

Chapter 1. Mechanotransduction at the cell surface and methods to study receptor forces

1.1. Introduction

Mechanical forces play a critical role in modulating many cellular processes [1]. Once cells experience mechanical stimuli, including substrate rigidity, external forces, and endogenous forces, they dynamically transduce the mechanical input into biochemical signals. With these signals, cells adapt and respond to their microenvironments, as well as make decisions involving activation, migration, proliferation, differentiation, and apoptosis (**Figure 1.1**) [2]. These processes, known as mechanosensing and mechanotransduction, have been observed in various cells, including platelets, cancer cells, stem cells, and immune cells [3]. Receptors on the cell surface, including integrins, notch, T cell receptor (TCR), and B cell receptor (BCR), participate intensively in mechanically sensing the environment and guide the cell through decision-making processes [4-7]. This chapter will start with an introduction of cell receptor force transduction, specifically, force interplay between integrins and T cell receptor and their ligands, as well as its role in the cellular response. Then, this chapter will introduce tools that have been developed to study the receptor forces. Finally, this chapter will briefly introduce the aim and scope of this dissertation.

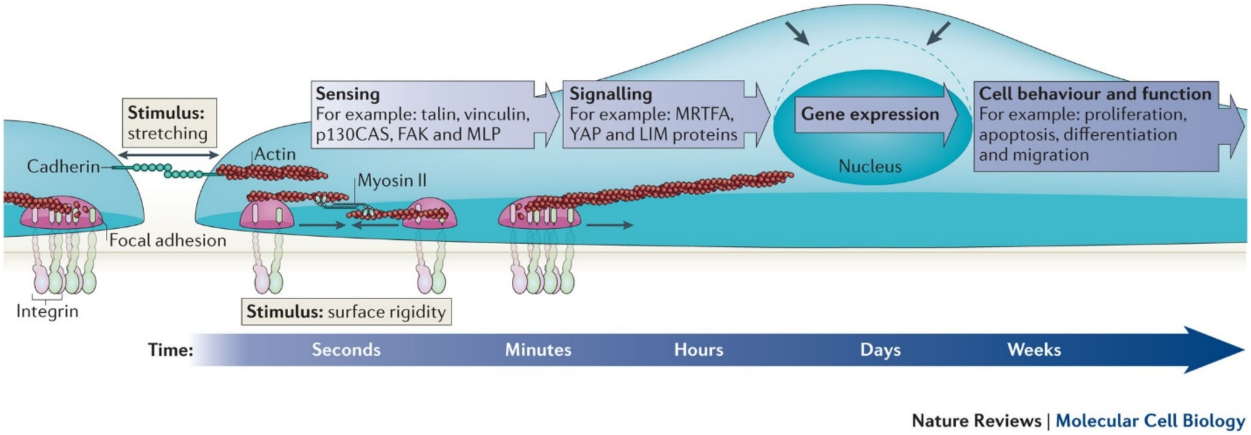

Figure 1.1. Mechanotransduction modulates various cellular processes. Reprinted from reference 2 with the permission of the publisher.

1.2. Mechanotransduction at the cell surface

1.2.1. Mechanotransduction through integrins

Integrins are adhesion proteins that bind to the extracellular matrix (ECM). An integrin molecule consists of an alpha and a beta subunit and forms a heterodimer. The integrin heterodimer has a large ectodomain, a transmembrane domain, and a short cytoplasmic tail. There are ~24 known integrin heterodimers mediating binding to diverse ECM molecules. One general ligand that these integrin ectodomains can recognize is a short amino-acid sequence, arginine-glycine-aspartic acid (RGD motif), which is abundant in ECM proteins such as fibronectin and fibrinogen [8]. Studies suggest that integrins exist in different conformations that exhibit different ligand affinities. The integrins in the inactive bent form have lower affinity for their ligand and the integrins in the active extended open form have high affinity (**Figure 1.2**). The integrin constantly and rapidly changes between the different conformations to bind a ligand. Integrin signaling can be initiated by either protein (talin and kindlin) binding on the cytoplasmic tail ("inside out") or ECM ligands binding to its ectodomain ("outside in"), and these two pathways can drive integrin activation cooperatively [9]. When activated and bound to its ligand, integrin molecules are fully extended, with the cytoplasmic tails separated. The activated integrins can cluster and recruit multiple proteins inside the cells, including talin, vinculin, and paxillin, to form focal adhesions (FA) [10]. FAs are coupled to the cytoskeleton and can transmit forces around tens of piconewtons (pN) to sense the environment [11-12]. As focal adhesions grow and mature, force transduction activates pathways such as Rho kinase-mediated phosphorylation of myosin II, which can then stabilize large focal adhesions. These stable focal adhesions aid in actin bundle assembly and stress fiber formation [13-16]. The actin stress fibers coupled to the FAs can transduce higher forces through actomyosin contractions and further facilitate mechanical signaling [17-18]. Consequently, through formation of FAs, integrins act as a main hub for mechanosensing and mechanotransduction in various cell types and facilitate activities like cell adhesion and migration.

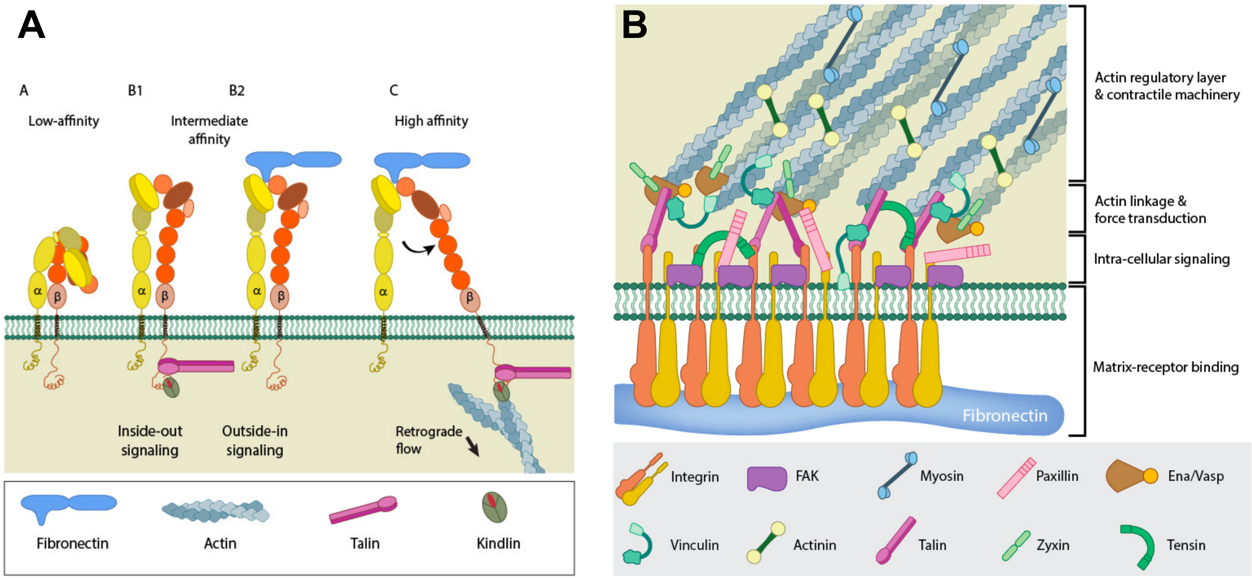

Figure 1.2. Integrin activation and focal adhesion assembly. (A) An integrin receptor in low affinity closed conformational A extending its extracellular domain to change into conformation B1. The cytoplasmic legs are further separated resulting in another structural change from the extend closed conformation B1/2 to extend opened conformation C, which has higher affinity to bind to its ligand and facilitate mechanosensing and transduction. (B) Upon matrix-receptor binding, multiple proteins are recruited to assemble focal adhesions, which bridge the ECM with the cytoskeleton. Adapted from MBinfo (https://www.mechanobio.info/) with permission.

1.2.2. Mechanotransduction through T cell receptor

1.2.2.1. General overview of T cell activation

T cells are critical in the adaptive immune system, as they constantly search for antigens and provide surveillance against viral infections and cancer. The T cell receptor (TCR) is a surface receptor that scans and test the antigens by binding to them. TCR has high specificity for antigenic peptides that are presented by a major histocompatibility complex (pMHCs) on the surface of the antigen presenting cell (**Figure 1.3A**), meaning it only recognizes antigenic peptides, exempting cells from autoimmune responses. TCR is a protein composed of a highly variable alpha chain and a beta chain, forming a heterodimer. TCR is usually expressed together with six invariant CD3 chain molecules that contain the signaling domains, forming a TCR-CD3 complex (**Figure 1.3**). When it encounters a potent pMHC, TCR binds to the pMHC, and initiates a discriminatory signaling cascade. The CD4 or CD8 co-receptors of TCR recruit Lck kinase, which can phosphorylate the signature tyrosine residues located at the signaling domain of the CD3 cytoplasmic tail, immunoreceptor tyrosine-based activation motifs (ITAMs). Phosphorylated ITAMs can bind to SH2 domain of the Zap70 kinase, and recruit Zap70 from the cytoplasm to the plasma membrane. Zap70 then phosphorylates linker for activation of T cells (LAT), which further recruits PLCγ1 and induces Ca^{2+} signaling. LAT also recruits adaptor proteins Grb2 and Gads, which bind to SOS and SLP-76 and lead to Ras, Rac, Rho GTPase activation [19]. This is an incredibly sensitive signaling cascade, which responds to an antigenic peptide within a few minutes after the first encounter with exceptional specificity.

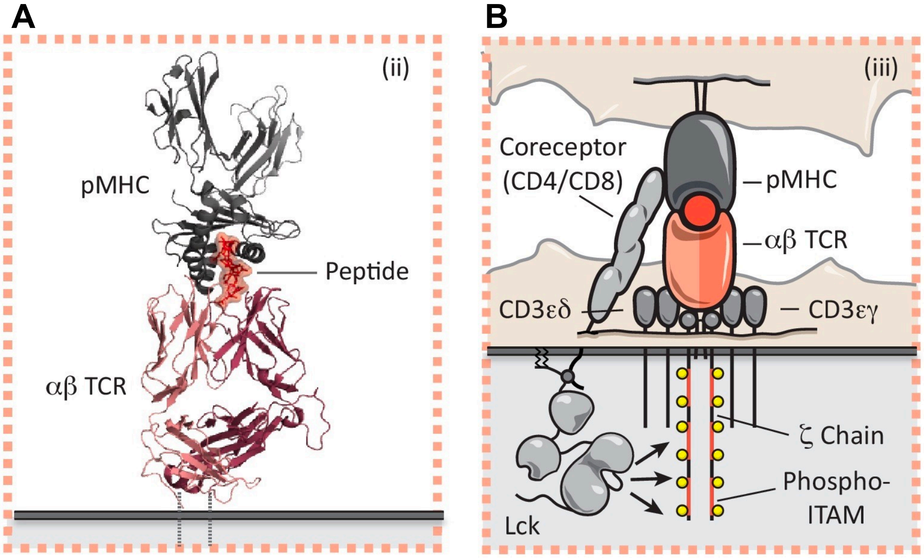

Figure 1.3. TCR-pMHC binding and the signaling pathway. (A) Structure of TCR binding to pMHC. (B) Signaling pathway after TCR triggering. Reprinted from reference 19 with permission.

Upon initial TCR triggering, the immune synapse is formed at the interface of the T cell and the antigen presenting cell (APC). The immune synapse is a highly organized dynamic structure, with a central region of the supra molecular activation complex (cSMAC), a peripheral region (pSMAC), and a distal ring (dSMAC). Together they form a "bull's eye" pattern, with distinct spatiotemporal distribution of surface receptors and signaling molecules. The TCR-CD3 complex, as well as the CD28 coreceptor are primarily located in the cSMAC upon activation. Adhesion ligands such as CD2 and LFA-1 (lymphocyte function-associated antigen 1) are relocated into the pSMAC, and the phosphatase CD45 is usually segregated to the dSMAC. Together, they facilitate T cells signaling and function, such as direct killing of the target cell [20].

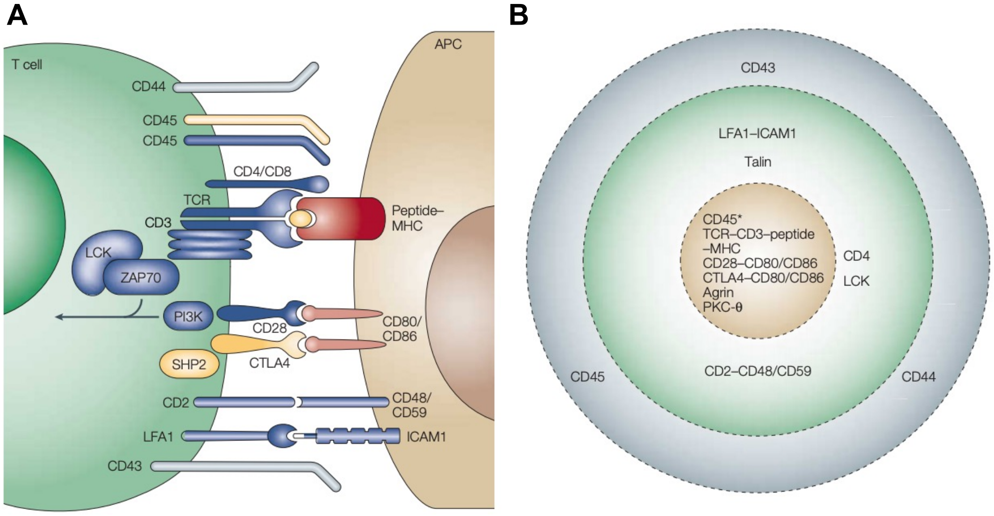

Figure 1.4. A mature immune synapse. (A) a side view showing the receptors and signaling proteins at the immune synapse formed between a T cell and an antigen presenting cell. (B) A top-down view showing the spatial organization of the proteins at the immune synapse. Reprinted from reference 20 with permission.

1.2.2.2. Proposed mechanism for initial TCR-pMHC recognition

TCR binds to antigens while patrolling, and upon antigen recognition, it can trigger a rapid whole cell response. This process can be initiated with as few as 1-2 cognate pMHC and within seconds to minutes. However, the affinity between TCRs and pMHCs in solution is usually between 1 μM to 10 μM, sometimes up to 100 μM, which does not provide much opportunity for antigen discrimination [19-22]. Therefore, a question that puzzles the field is how the TCR recognizes an antigen from the massive number of endogenous ligands that are displayed on antigen presenting cell surfaces with explicit specificity and sensitivity.

Several models have been proposed to explain the remarkable ability of T cells to recognize specific antigens, including (1) kinetic segregation, (2) kinetic proofreading, (3) serial triggering, and (4) conformational change triggering model [19, 23]. The kinetic segregation model proposed that the triggering is dependent on the segregation of large surface proteins like phosphatase CD45 from proteins that have small extracellular domains, such as TCR. The kinetic proofreading model suggests that the triggering is based on the differential binding durations, which provides the discrimination between strong and weak antigens. The serial engagement hypothesis suggested that successive rapid binding and unbinding events between clustered TCRs and a few pMHC is the mechanism of amplifying the discrimination signal that drives TCR triggering. The conformational change model argues that the binding to pMHC induces a structural change in the TCR ectodomain, which exposed the signaling ITAMs inside the cells.

1.2.2.3. Mechanical forces in TCR triggering

Originally, these models were proposed without the involvement of mechanical forces. However, over the past decade, growing evidence suggest that molecular mechanical forces play an important role in T cell activation. Single molecule force spectroscopy studies found that when a defined force is applied to immunoreceptors, the dissociation kinetics between the receptors and ligands is regulated by force (**Figure 1.5**).

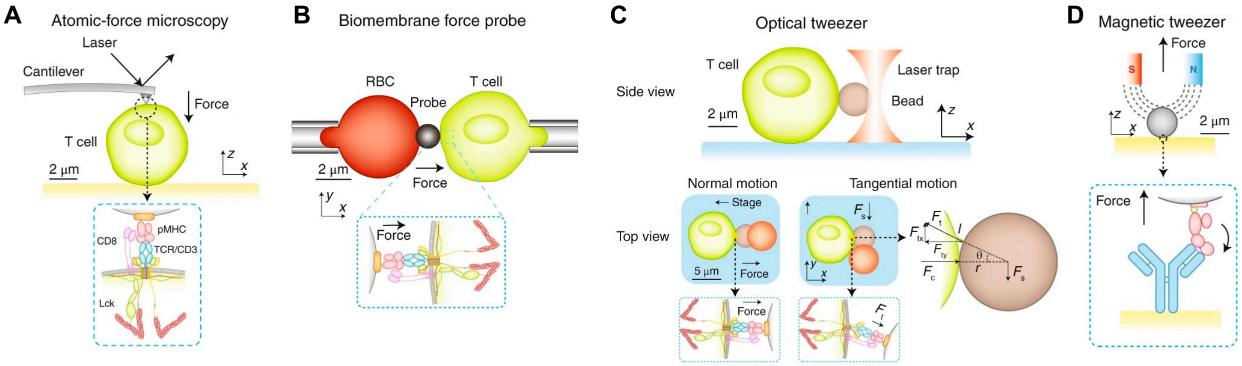

Figure 1.5. Single-molecule force spectroscopy methods to apply force to T cells. (A) Atomic force microscopy, (B) biomembrane force probe, (C) optical tweezer and (D) magnetic tweezer are all used to apply an external force and interrogate the force contribution in TCR-pMHC binding. Reprinted with permission from reference 24.

Moreover, the T cell triggering correlates with the duration of the receptor-ligand binding under a certain force (~10-20 pN). Specifically, the potent TCR-pMHC bindings exhibit a "catch-bond" behavior, i.e., the application of force prolongs the lifetime of the binding. Conversely, with weak agonist or antagonist peptides, the TCR exhibits a "slip-bond" behavior, i.e., the lifetime decreases upon force application (**Figure 1.6**). The catch-bond model can explain the differential potency of pMHCs when their affinities to TCR are similar.

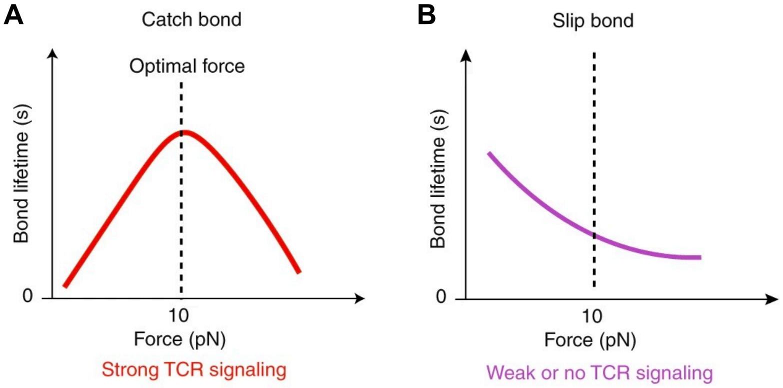

Figure 1.6. Illustration of catch-bond and slip-bond. Reprinted with permission from reference 24.

These findings suggest that immunoreceptors are mechanosensors. Evident from the forces revealed by traction force microscopy, micropillars, and molecular tension probes, the T cells generate traction forces and transmit defined pN forces through TCR to pMHC, and the force is correlated with functional output like cytotoxic cell killing [24-25]. These complementary methods have provided new insight into the TCR triggering mechanism, and further connected the role of cytoskeleton coordination in the T cell activation. Accordingly, the revised hypotheses of triggering mechanisms now including the role of force are discussed in the field and are shown in **Figure 1.7** [23]. Briefly, for the kinetic segregation model, the forces generated by cell cytoskeleton and transmitted through TCR can drive the segregation of CD45. And for the kinetic proofreading model, the catch-bond observation with single molecule methods can explain the amplified discrimination between potent and weak antigens in terms of its 2D binding kinetics. For the serial engagement model, the engagement of the cytoskeleton would drive the clustering, and potentially the successive bindings through the protrusive microvilli on the T cell surface [26]. For the conformational change model, a study using optical tweezers showed that the force can extend the FG loop on the TCR beta chain, prolong the lifetime, and initiate signaling [27], though whether force induces conformational change on the cytoplasmic tail of TCR-CD3 complex is still unclear. Taken together, mechanical force is a crucial parameter that regulates TCR triggering. However, as one of the most sensitive, specific, and efficient recognition-activation processes in biology, the TCR triggering is more likely to be explained by a collective effort rather than a single mechanism. For example, the initial fast bindings could extend FG loop, prolong the lifetime, press on the CD3ε and induce a TCR-CD3 conformational change, which could further release the ITAMs and allow phosphorylation in the cytoplasmic tail. As the phosphorylation rapidly signals through Ca^{2+} to the cytoskeleton, the actin network could engage and mediate the rearrangement of the receptors, including the segregation of phosphatases and the clustering of TCRs, strengthen the mechanical test on the TCR-pMHCs, and contribute to a significantly amplified discrimination by exposing more phosphorylation sites. (This delicately dictated process is absolutely the most beautiful and interesting thing I have ever seen.)

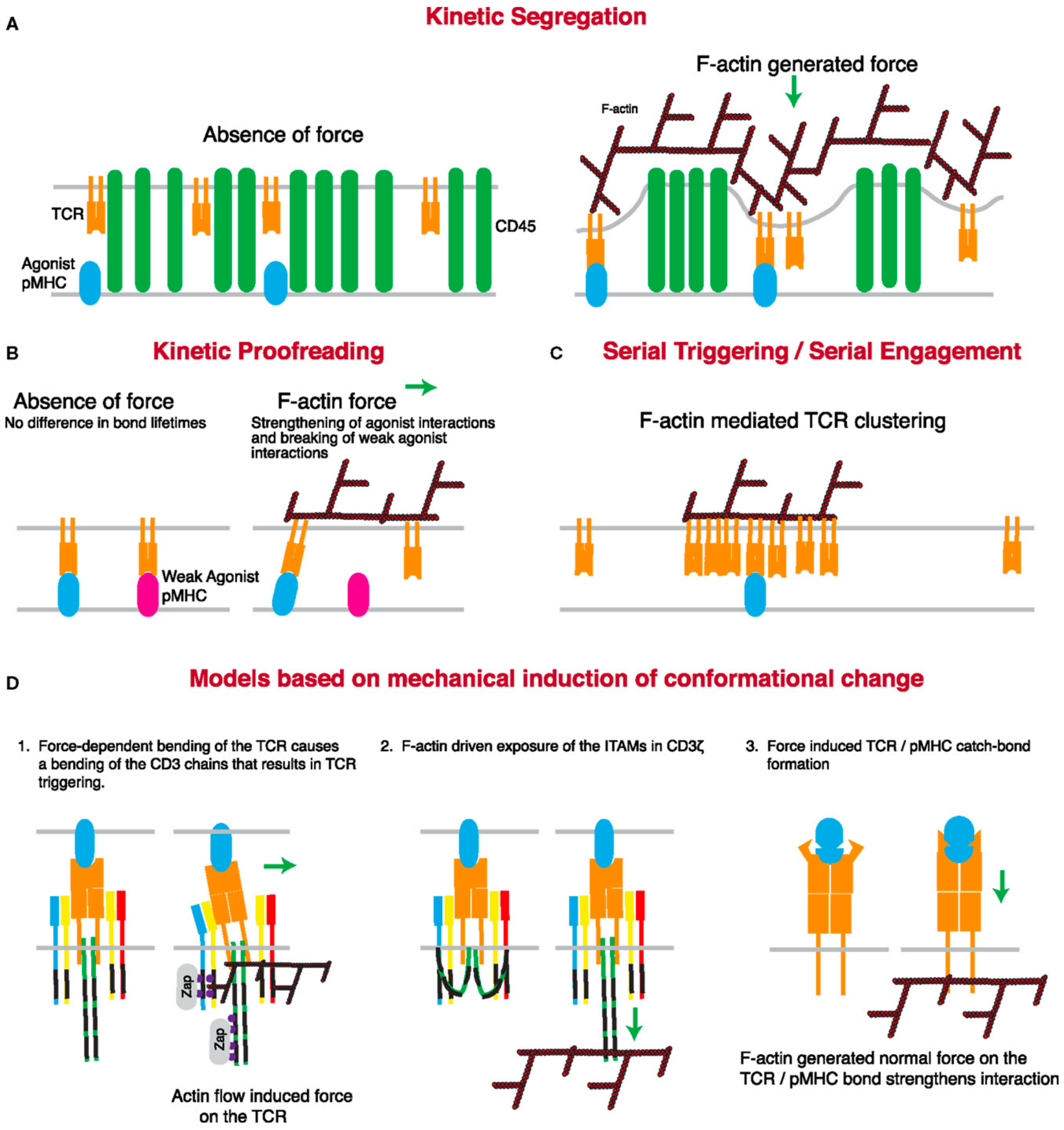

Figure 1.7. Revised models for TCR triggering with force and cytoskeleton engagement. Reprinted from reference 23 with permission.

1.3. Methods to study receptor forces

Methods like traction force microscopy and micropillar arrays have been widely used by the field of mechanobiology to reveal these mechanical events during biological processes [28-29]. However, their relatively poor spatiotemporal resolution as well as force sensitivity have long been the bottleneck of uncovering more details of cell receptor mechanics (**Figure 1.8**) [30]. The emergence of molecular tension probes in 2011 greatly enhanced the resolution of receptor force mapping. Our lab pioneered the use of entropic polyethylene glycol (PEG) as the force-sensing spring to report force in the range of 1-20 pN, but the "analog" force-responsive fluorescence signal (fluorescence intensity increases as force magnitude increases) could be confused with percentage of opened probes in force mapping [31-32]. Conveniently, using nucleic acids for force-sensing is advantageous, as it improves force mapping resolution and reports "digital" force-responsive fluorescence signal (fluorescence switches on as duplex mechanically melts), simplifying data processing and interpretation [33]. Moreover, DNA offers unrivaled flexibility in multiple ways. First, the probe assembly is simple yet still allows for a tunable force threshold. Second, different chemical modifications can be incorporated easily for conjugation with a ligand, fluorophore, quencher, or surface. Third, the simple rules of Watson-Crick base pairing also allow the probes to be highly modular and programmable with other additional features.

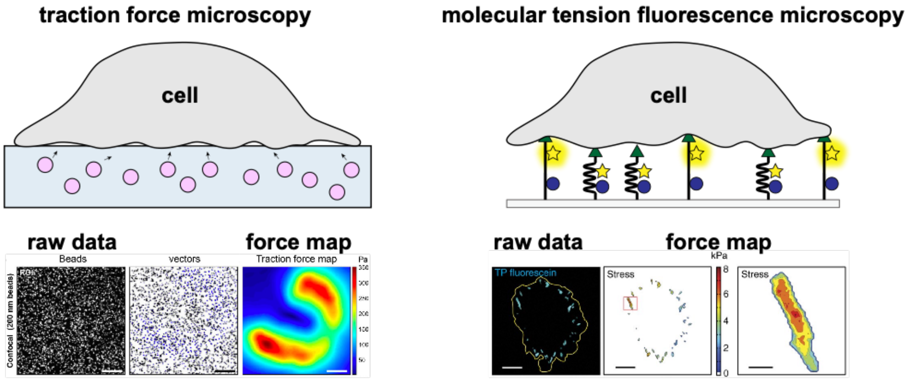

Figure 1.8. Traction force microscopy versus molecular tension fluorescence microscopy. Part of the figure reprinted with permission from reference 29 (https://pubs.acs.org/doi/10.1021/acs.nanolett.9b04083) and 34. Any reuse of the reprinted figure containing materials from reference 29 needs to request permission from the original publisher of the article.

1.3.1. DNA mechanics

Because DNA is extensively used a mechanical probe throughout this thesis, it is imperative to provide some background on the response of nucleic acids to external molecular forces. DNA is an elastic polymer, and its mechanical properties are often described using the worm-like chain model (WLC). The mechanical response of DNA under tensile force is usually characterized by single-molecule force spectroscopy methods, including optical tweezers, magnetic tweezers, and atomic force microscopy [35-36]. Various DNA structures have been examined under force, and among them, there are a few fundamental structural transitions that have been intensively used for tool development in the field of DNA nanotechnology for mechanobiology studies [37].

1.3.1.1. DNA hairpin unfolding under force

For a simple DNA hairpin, its energy landscape can be described as two wells for either the closed or open state, with a single energy barrier in between. The application of force tilts the energy landscape and changes the free energy for hairpins to transition from the closed state to open state. By observing the population of the two states under force, the force ($F_{1/2}$) that this structural transition happens can be measured (**Figure 1.9**). During the mechanical unfolding of the hairpin, the force must make up for the energy of base-pairing and stacking, as well as the stretching of the nucleotides [36]. Therefore, the $F_{1/2}$ can be defined as

$$F_{1/2} = (\Delta G_{unfold} + \Delta G_{stretch})/\Delta x \quad (1),$$

where ΔG_{unfold} is the free energy of hairpin unfolding at zero force, $\Delta G_{stretch}$ is the free energy of stretching the unfolded ssDNA at $F_{1/2}$, and Δx is the opening distance from folded to unfolded state. The $\Delta G_{stretch}$ can be calculated from a simple worm-like-chain (WLC) model,

$$\Delta G_{\mathrm{stretch}} = \left(\frac{k_b T}{L_p}\right)\left[\frac{L_0}{4(\frac{1-x}{L_0})}\right]\left[3\left(\frac{x}{L_0}\right)^2 - 2\left(\frac{x}{L_0}\right)^3\right] \qquad (2),$$

where k_b is Boltzmann constant, L_p is the persistent length of DNA, T is temperature, L_0 is ssDNA contour length, and x is the hairpin extension. The Δx can be estimated from the contour length following 0.44 ± 0.02 nm per nt (with a 2.0 nm width of duplex DNA correction). The $\Delta G_{\mathrm{unfold}}$ increases linearly with increasing stem GC% and stem length; however, increasing stem length also allows more energy to be stored, which affects $\Delta G_{\mathrm{stretch}}$, and collectively defines the range of $F_{1/2}$ to be within ~2-20 pN [28].

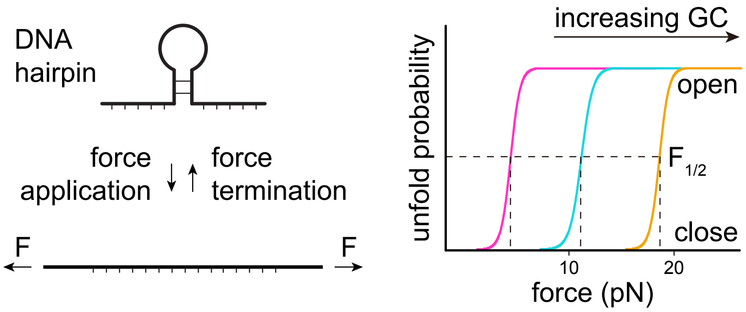

Figure 1.9. Mechanical unfolding of DNA hairpin.

1.3.1.2. DNA duplex rupture under force

Unlike DNA hairpins, DNA duplex melting is irreversible. The same DNA duplex can have identical chemical and thermal stability, but drastically different mechano-stability depending on the geometry of how force is applied (**Figure 1.10**). When a short DNA duplex is stretched in an antiparallel manner (shearing, 5'-5' or 3'-3' pulling), the critical force at which 50% of the duplexes rupture (in a fixed time 2 s) increases with duplex length and plateaus at a certain length [38]. It can be described by the de Gennes model, which treats a DNA duplex as an elastic ladder and takes into account the hydrogen bond between base pairs. As the force is not evenly distributed on the base pairs, the base pairs that are bearing the load is a finite number, which results in a finite length x^{-1} that can be described with the spring constant of the stretched DNA backbone Q, and the spring constant of the stretched hydrogen bonds between base pairs R, where

$$x^{-1} = \sqrt{Q/2R} \quad (3).$$

Therefore, in the de Gennes model, the rupture force for a DNA duplex in the shearing geometry can be described as

$$F = 2f_c\left[x^{-1}\tanh\left(x\frac{L}{2}\right) + 1\right] \quad (4),$$

where f_c is the critical force for separating a single base pair (~3.9 pN), x^{-1} = 6.8 bp by magnetic tweezer characterizations, and L is the number of DNA base pairs [7, 38].

Another geometry of short DNA duplex rupture, unzipping mode (5'-3' pulling perpendicular to the duplex), can be treated as a 1 bp shearing, while the remaining base pairs are only thermally stabilizing the duplex. According to Equation 4, the rupture force is ~12 pN, which is very close to what has been measured experimentally [39].

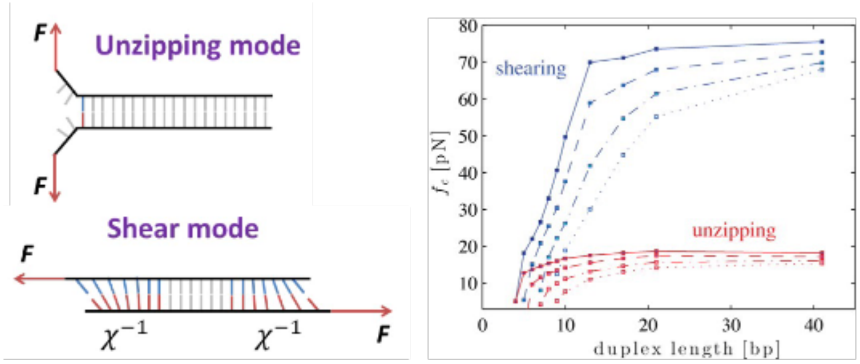

Figure 1.10. Mechanical rupture of DNA duplex. Reprinted from reference 7 and 37 with permission.

1.3.1.3. DNA duplex peeling under force

DNA duplexes can also melt under force that is applied on the same strand (5'-3' pulling), through a force-driven strand separation process known as peeling. Magnetic tweezers characterization showed that for short DNA duplexes under 5'-3' pulling on the same strand, the melting is a two-state system with a transition state consisting of several base pairs (**Figure 1.11**). The application of force contributes to the free energy needed for the DNA to transition from dsDNA to ssDNA. The critical force that induces this transition, T_{tol}, is defined as the critical force at which there is 50% ssDNA at a given time and is dependent on the GC%. For AT-rich short duplexes, the T_{tol} is usually below 65 pN, and peeling occurs before the DNA B-form to S-form transition [40-41]. Specifically, for a 24mer or a 28mer duplex in a magnetic tweezer study, the T_{tol} was found to be ~ 41 pN and ~50 pN for the 24mer and 28mer duplexes, respectively [42].

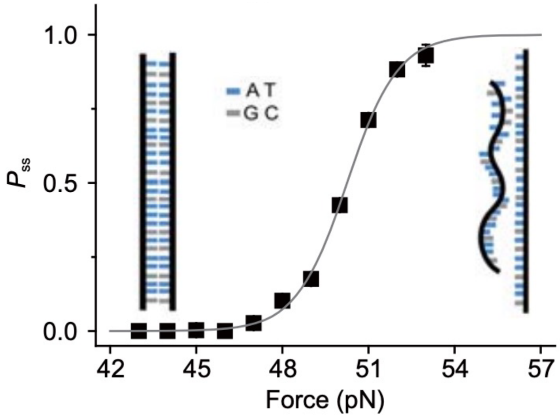

Figure 1.11. Mechanical peeling of DNA duplex. Plot show the transition and T_{tol} for a 28mer DNA duplex. Reprinted from reference 42 with permission.

1.3.2. DNA-based molecular force sensing

Taking advantage of the mechanical melting properties of DNA molecules, DNA-based force probes have been invented to map and study the forces exerted from a receptor on the cell surface to its ligand. Typically, the force probes are comprised of a mechanical melting region, a fluorophore-quencher pair that reports mechanical melting events, and the ligand which the receptor of interest can recognize. These DNA-based molecular probes are often anchored on 2D surfaces to present the ligands to cells. After cells are plated onto these force probe-functionalized surfaces, the receptors recognize, bind, and exert forces to the ligands. As the forces are transmitted through the DNA construct, if the force is greater than the $F_{1/2}$ or T_{tol} of the DNA construct, mechanical melting will occur, resulting in a change in the distance between the fluorophore and quencher, yielding a fluorescent signal to report this mechanical melting event. These probes can be reversible or irreversible depending on the structure of the DNA force-sensing region (**Figure 1.12**).

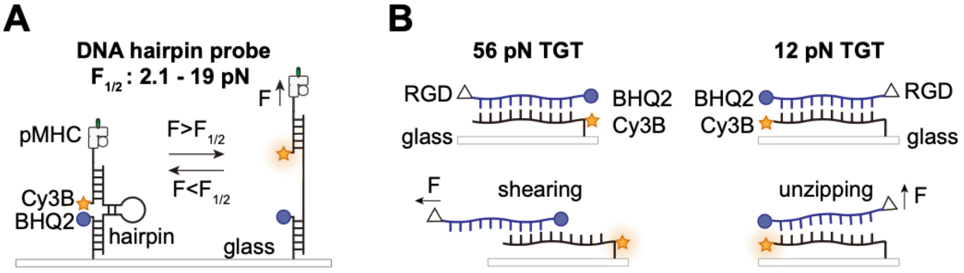

Figure 1.12. Classic reversible and irreversible DNA-based tension probes. (A) DNA hairpin-based reversible tension probe and (B) DNA duplexes as irreversible tension probes.

1.3.2.1. Reversible DNA force probes

DNA hairpin structures are incorporated as the force-sensing module due to their dynamic ability to unfold and refold with or without the presence of the force. DNA hairpin tension probes report the forces exceeding the threshold, $F_{1/2}$. As $F_{1/2}$ is dependent on the ΔG_{unfold} and $\Delta G_{stretch}$ as discussed in **1.3.1.1**, one can easily tune the force threshold that the probes map by tuning the GC% and length of the hairpin stem. The first DNA hairpin tension probes were reported in 2014 by two groups independently. Chen and colleagues reported an all-covalent system by using a single strand DNA with a stem-loop region, with modifications of a fluorophore, a quencher, and a peptide ligand RGD. With this molecular tension probe, they mapped the heterogenous integrin forces in fibroblast focal adhesions [34]. Meanwhile, our lab pioneered a highly modular DNA hairpin tension probe system, comprised of three strands, a top strand with a ligand and a fluorophore, a bottom strand with a quencher and an anchoring moiety, and a hairpin strand that links them together. This multi-strand design provided more flexibility for force mapping as opposed to the single-strand design, as one can easily change the force threshold of the probe by swapping the hairpin strand, which does not require any additional chemical modifications. One benefit of using a reversible force probe is that it provides low force threshold mapping. Our lab reported a small library of DNA hairpin tension probes ranging from 2.1 pN to 19 pN [5, 33]. Whilst providing great temporal resolution of the force dynamics, one disadvantage of the hairpin probes is that it only reports forces in real-time. The force history information is difficult to capture because it refolds within microseconds once force is withdrawn. Another limitation is that the narrow force detection limit is not sufficient for receptors that can produce stronger forces.

1.3.2.2. Irreversible DNA tension probes

Irreversible DNA tension probes do not provide good temporal resolution of the force dynamics; however, they provide information on the receptor force history. Ha and co-workers first reported manipulation of the tension exerted through receptor-ligand binding with tension gauge tethers (TGT). The two geometries, unzipping and shearing, detect and tolerate peak tension of 12 pN and 56 pN, respectively [7]. Compared to hairpin probes, TGTs have a bigger range of force detection, which is tuned by positioning the ligand at different positions throughout the length of the duplex [43]. As a receptor mechanotransduction manipulating tool, the TGT is superior, since the chemical cues it provides to cells are the same, while the mechanical cues are very different. However, as a force reporter, TGTs have two major drawbacks. First, the lowest T_{tol} for TGTs is 12 pN. Though, there have been attempts to reach a lower force regime using a single strand DNA wrapping around the protein SSB, which achieved ~ 4 pN of T_{tol} [44]; the other drawback remains: once TGTs are ruptured, the mechanical signaling is terminated as well, inevitably affecting the function of the cell.

1.3.2.3. Other variations of the probes to answer specific mechanobiology questions

Building on the basic structure of DNA hairpins and TGTs, more DNA structures have been designed to investigate different biophysical questions at the cell-substrate interface. Wang and co-workers further developed the TGT library by positioning the ligand on different bases on the top strand, incorporating fluorophore-quencher pairs, and assembling multiplexing substrates, which further calibrated the integrin forces inside and outside FAs to a narrower rage [43, 45]. To amplify the receptor force readout, a mechanical-triggered isothermal polymerization reaction based on the TGT structure was reported, which has potential in evaluating mechano-modulatory drugs [46]. Additionally, DNA origami structures with multivalent hairpin force probes were reported, capitalizing on the ability of this self-assembly technique to present multiple ligands with precisely controlled spacing, proving to be a great tool to study the relationship between the force and clustering [47]. This method would also allow for investigating the crosstalk between different receptors during mechanotransduction.

To study forces on membranes, DNA force probes were also redesigned to be compatible with supported lipid bilayers (SLB). SLB is a fluid system, which means an increase in intensity cannot be directly attributed to mechanical pulling by the receptors. To solve this issue, two strategies have been reported to distinguish receptor clustering from receptor forces. In 2016, a ratiometric probe was published, which can report TCR clustering and TCR forces simultaneously on a fluid membrane [48]. In 2019, a fluorescent lifetime imaging method was published which was able to distinguish the receptor clustering and force signals, as well as investigated the force during podosome formation on a fluid membrane [49]. While FLIM can be a useful solution for mechanobiology studies in fluid systems, it also has a relatively poor temporal resolution (~60 s), which limited its application to less dynamic receptor forces. Apart from using SLBs to mimic the cell-cell interface, there are also attempts of mapping the force at the cell-cell junction. In 2017, a membrane DNA tension probe was tested at the cell-cell junction. Instead of being anchored on a 2D substrate, the DNA tension probes is anchored to the membrane of a cell through two cholesterol modifications via hydrophobic interaction [50]. Though, it is important to be aware of the stability of cholesterol probe anchoring, which could potentially cause false negative signals. Cholesterol can also become involved in cellular uptake, also potentially causing false signals.

In addition to measuring the magnitude of the receptor forces and percentage opening of the probes, measuring the force orientation provides direct proof to support the hypotheses of whether the force orientation affects receptor mechanotransduction. To measure the receptor force orientation at the molecular level, molecular force microscopy (MFM) was invented by coupling fluorescence polarization microscopy with DNA hairpin probes [51]. Taking advantage of the stacking between the dye Cy3B and the DNA base pairs, MFM successfully reported the axial integrin force alignment during platelets activation, supporting a hypothesis of the involvement of lateral forces during platelets activation. However, one drawback of MFM is that the image acquisition is time-consuming (~3.6 s), which makes it more suitable to measure the orientation of relatively less dynamic forces.

As more and more of the mysteries of receptor mechanics and its role in cell biology have been solved, recent research has been pushing the imaging resolution to the nanometer level for force mapping. Wang and co-workers reported a cellular force nanoscopy (CFN) method in 2020, achieving 50 nm resolution in integrin force mapping [52]. This method utilizes a modified version of a conventional TGT, comprised of a DNase-resistant PNA/DNA duplex rather than a DNA/DNA duplex. The TGT is labeled with a fluorophore-quencher pair (Cy5-BHQ2), thus the Cy5 is dequenched one force is applied. This technique is straightforward and easy to implement with a TIRF microscope by following these steps: first, the dequenched Cy5 is bleached in 0.5-1 s; second, newly ruptured TGT molecules are imaged in the next frame; and third, the just imaged TGTs are bleached. By repeating this cycle, 50 nm resolution integrin force mapping is achieved in both migratory and stationary cells. One pitfall of this technique is that around 3% of the signal is false positive signal, coming from the dissociation of the TGTs during the image acquisition. Another recent paper describes a relatively more complicated but powerful method to achieve super-resolved tension mapping. Leveraging DNA-Points Accumulation for Imaging in Nanoscale Topography (DNA-PAINT) technique, the resolution is further improved to 25 nm [53]. The authors presented a real-time DNA tension probe featuring a strain-free force-sensing region with a cryptic docking site that is advantageous for a complementary imager strand to form a transient binding interaction. By imaging the imager sampling of the mechanically opened probes, a super-resolved tension map can be reconstructed. This method is also adaptable to the TGTs for mapping accumulative tension. Similar to CFN, one of the limitations of tPAINT is the temporal resolution. The other disadvantage is that tPAINT under samples the mechanical events due to the imager on-rate. However, it is still superior given that it provides super-resolved tension mapping in both real-time and the accumulative history.

1.4. Aim and scope of the dissertation

The emergence of DNA nanotechnology has provided the field of mechanobiology with many powerful tools to investigate the receptor mechanics, from detecting the force to manipulating the mechanical signaling. Despite the encouraging advances that have been made, new techniques are required to depict the receptor mechanics and its regulation from more perspectives, and currently our tools lack the ability to harness the receptor mechanics as a biomarker. This dissertation aims to develop a toolbox based on DNA nanotechnology to (1) overcome the limitations of existing DNA-based probes and improve force detection sensitivity; (2) expand the metrics of receptor force measurements from magnitude and orientation to kinetics; and (3) establish high throughput identification of cells with higher receptor mechanical activities.

My PhD training began with one simple experiment: trying to achieve DNA hybridization under (receptor) force. It worked very robustly with immune cell receptors and completely failed with integrins. With this puzzling observation, I was motivated to carefully investigate and understand why, and because of these investigations, I found ways to take advantage of the nuances of DNA hybridization/dehybridization under force to ultimately develop of four new tools that can address the aims of the thesis.

Chapter 2 describes a mechanical information storing probe that allows for toggling between mapping dynamic force and accumulated force, which is particularly useful in mapping transient and weak receptor forces that are difficult to detect [54]. The application of this method in T cells revealed TCR mechanical sampling is correlated with antigen potency and detected programmed cell death receptor 1 (PD1) forces. In **Chapter 3**, I will discuss a method that leverages the mechanical information storing probe from Chapter 2 along with kinetic modeling to infer the average TCR force kinetics in $CD8^+$ T cells that are actively exerting TCR force to antigens. **Chapter 4** will introduce a method, also building on Chapter 2, to identify cells that present mechanically active receptors in a high throughput manner. In **Chapter 5**, I will discuss a new type of DNA tension probe that has risen from the failed application of mechanically selective hybridization, which reveals high magnitude receptor force and can also be used to tag cells that are mechanically active.

Finally, in **Chapter 6**, this dissertation will outline several promising directions for future work and several outlooks for the development and application of DNA nanotechnology in mechanobiology studies.

1.5. References

1. D. Mohammed; M. Versaevel; C. Bruyere; L. Alaimo; M. Luciano; E. Vercruysse; A. Proces; S. Gabriele, Innovative Tools for Mechanobiology: Unraveling Outside-In and Inside-Out Mechanotransduction. *Front Bioeng Biotechnol* **2019,** *7*, 162.

2. T. Iskratsch; H. Wolfenson; M. P. Sheetz, Appreciating force and shape-the rise of mechanotransduction in cell biology. *Nat Rev Mol Cell Biol* **2014,** *15* (12), 825.

3. Y. Chen; L. Ju; M. Rushdi; C. Ge; C. Zhu, Receptor-mediated cell mechanosensing. *Mol Biol Cell* **2017,** *28* (23), 3134.

4. Y. Zhang; Y. Qiu; A. T. Blanchard; Y. Chang; J. M. Brockman; V. P.-Y. Ma; W. A. Lam; K. Salaita, Platelet integrins exhibit anisotropic mechanosensing and harness piconewton forces to mediate platelet aggregation. *Proceedings of the National Academy of Sciences* **2018,** *115* (2), 325.

5. Y. Liu; L. Blanchfield; V. P.-Y. Ma; R. Andargachew; K. Galior; Z. Liu; B. Evavold; K. Salaita, DNA-based nanoparticle tension sensors reveal that T-cell receptors transmit defined pN forces to their antigens for enhanced fidelity. *Proceedings of the National Academy of Sciences* **2016,** *113* (20), 5610.

6. K. M. Spillane; P. Tolar, B cell antigen extraction is regulated by physical properties of antigen-presenting cells. *J Cell Biol* **2017,** *216* (1), 217.

7. X. Wang; T. Ha, Defining single molecular forces required to activate integrin and notch signaling. *Science* **2013,** *340* (6135), 991.

8. Z. Sun; M. Costell; R. Fassler, Integrin activation by talin, kindlin and mechanical forces. *Nat Cell Biol* **2019,** *21* (1), 25.

9. A. Banno; M. H. Ginsberg, Integrin activation. *Biochem Soc Trans* **2008,** *36* (Pt 2), 229.

10. D. A. Calderwood; I. D. Campbell; D. R. Critchley, Talins and kindlins: partners in integrin-mediated adhesion. *Nat Rev Mol Cell Biol* **2013,** *14* (8), 503.

11. L. B. Case; C. M. Waterman, Integration of actin dynamics and cell adhesion by a three-dimensional, mechanosensitive molecular clutch. *Nat Cell Biol* **2015,** *17* (8), 955.

12. F. Martino; A. R. Perestrelo; V. Vinarsky; S. Pagliari; G. Forte, Cellular Mechanotransduction: From Tension to Function. *Front Physiol* **2018,** *9*, 824.

13. K. A. Beningo; K. Hamao; M. Dembo; Y. L. Wang; H. Hosoya, Traction forces of fibroblasts are regulated by the Rho-dependent kinase but not by the myosin light chain kinase. *Arch Biochem Biophys* **2006,** *456* (2), 224.

14. C. Le Clainche; M. F. Carlier, Regulation of actin assembly associated with protrusion and adhesion in cell migration. *Physiol Rev* **2008,** *88* (2), 489.

15. J. Stricker; Y. Aratyn-Schaus; P. W. Oakes; M. L. Gardel, Spatiotemporal constraints on the force-dependent growth of focal adhesions. *Biophys J* **2011,** *100* (12), 2883.

16. P. W. Oakes; Y. Beckham; J. Stricker; M. L. Gardel, Tension is required but not sufficient for focal adhesion maturation without a stress fiber template. *J Cell Biol* **2012,** *196* (3), 363.

17. J. I. Lehtimaki; E. K. Rajakyla; S. Tojkander; P. Lappalainen, Generation of stress fibers through myosin-driven reorganization of the actin cortex. *Elife* **2021,** *10.*

18. E. Kassianidou; C. A. Brand; U. S. Schwarz; S. Kumar, Geometry and network connectivity govern the mechanics of stress fibers. *Proc Natl Acad Sci U S A* **2017,** *114* (10), 2622.

19. A. H. Courtney; W. L. Lo; A. Weiss, TCR Signaling: Mechanisms of Initiation and Propagation. *Trends Biochem Sci* **2018,** *43* (2), 108.

20. J. B. Huppa; M. M. Davis, T-cell-antigen recognition and the immunological synapse. *Nat Rev Immunol* **2003,** *3* (12), 973.

21. S. Valitutti; S. Muller; M. Cella; E. Padovan; A. Lanzavecchia, Serial triggering of many T-cell receptors by a few peptide-MHC complexes. *Nature* **1995,** *375* (6527), 148.

22. J. Hellmeier; R. Platzer; A. S. Eklund; T. Schlichthaerle; A. Karner; V. Motsch; M. C. Schneider; E. Kurz; V. Bamieh; M. Brameshuber; J. Preiner; R. Jungmann; H. Stockinger; G. J. Schutz; J. B. Huppa; E. Sevcsik, DNA origami demonstrate the unique stimulatory power of single pMHCs as T cell antigens. *Proc Natl Acad Sci U S A* **2021,** *118* (4).

23. W. A. Comrie; J. K. Burkhardt, Action and Traction: Cytoskeletal Control of Receptor Triggering at the Immunological Synapse. *Front Immunol* **2016,** *7*, 68.

24. C. Zhu; W. Chen; J. Lou; W. Rittase; K. Li, Mechanosensing through immunoreceptors. *Nat Immunol* **2019,** *20* (10), 1269.

25. R. Basu; B. M. Whitlock; J. Husson; A. Le Floc'h; W. Jin; A. Oyler-Yaniv; F. Dotiwala; G. Giannone; C. Hivroz; N. Biais; J. Lieberman; L. C. Kam; M. Huse, Cytotoxic T Cells Use Mechanical Force to Potentiate Target Cell Killing. *Cell* **2016,** *165* (1), 100.

26. E. Cai; K. Marchuk; P. Beemiller; C. Beppler; M. G. Rubashkin; V. M. Weaver; A. Gerard; T.-L. Liu; B.-C. Chen; E. Betzig, Visualizing dynamic microvillar search and stabilization during ligand detection by T cells. *Science* **2017,** *356* (6338), eaal3118.

27. Y. Feng; E. L. Reinherz; M. J. Lang, alphabeta T Cell Receptor Mechanosensing Forces out Serial Engagement. *Trends Immunol* **2018,** *39* (8), 596.

28. V. P. Y. Ma; K. Salaita, DNA nanotechnology as an emerging tool to study mechanotransduction in living systems. *Small* **2019,** *15* (26), 1900961.

29. A. Stubb; R. F. Laine; M. Miihkinen; H. Hamidi; C. Guzman; R. Henriques; G. Jacquemet; J. Ivaska, Fluctuation-Based Super-Resolution Traction Force Microscopy. *Nano Lett* **2020,** *20* (4), 2230.

30. W. J. Polacheck; C. S. Chen, Measuring cell-generated forces: a guide to the available tools. *Nat Methods* **2016,** *13* (5), 415.

31. D. R. Stabley; C. Jurchenko; S. S. Marshall; K. S. Salaita, Visualizing mechanical tension across membrane receptors with a fluorescent sensor. *Nat Methods* **2011,** *9* (1), 64.

32. Y. Liu; K. Yehl; Y. Narui; K. Salaita, Tension sensing nanoparticles for mechano-imaging at the living/nonliving interface. *Journal of the American Chemical Society* **2013,** *135* (14), 5320.

33. Y. Zhang; C. Ge; C. Zhu; K. Salaita, DNA-based digital tension probes reveal integrin forces during early cell adhesion. *Nature communications* **2014,** *5*, 5167.

34. B. L. Blakely; C. E. Dumelin; B. Trappmann; L. M. McGregor; C. K. Choi; P. C. Anthony; V. K. Duesterberg; B. M. Baker; S. M. Block; D. R. Liu; C. S. Chen, A DNA-based molecular probe for optically reporting cellular traction forces. *Nat Methods* **2014,** *11* (12), 1229.

35. S. Cocco; J. Yan; J. F. Leger; D. Chatenay; J. F. Marko, Overstretching and force-driven strand separation of double-helix DNA. *Phys Rev E Stat Nonlin Soft Matter Phys* **2004,** *70* (1 Pt 1), 011910.

36. M. T. Woodside; W. M. Behnke-Parks; K. Larizadeh; K. Travers; D. Herschlag; S. M. Block, Nanomechanical measurements of the sequence-dependent folding landscapes of single nucleic acid hairpins. *Proceedings of the National Academy of Sciences* **2006,** *103* (16), 6190.

37. M. Mosayebi; A. A. Louis; J. P. Doye; T. E. Ouldridge, Force-Induced Rupture of a DNA Duplex: From Fundamentals to Force Sensors. *ACS Nano* **2015,** *9* (12), 11993.

38. K. Hatch; C. Danilowicz; V. Coljee; M. Prentiss, Demonstration that the shear force required to separate short double-stranded DNA does not increase significantly with sequence length for sequences longer than 25 base pairs. *Phys Rev E Stat Nonlin Soft Matter Phys* **2008,** *78* (1 Pt 1), 011920.

39. S. Cocco; R. Monasson; J. F. Marko, Force and kinetic barriers to unzipping of the DNA double helix. *Proc Natl Acad Sci U S A* **2001,** *98* (15), 8608.

40. X. Zhang; H. Chen; H. Fu; P. S. Doyle; J. Yan, Two distinct overstretched DNA structures revealed by single-molecule thermodynamics measurements. *Proc Natl Acad Sci U S A* **2012,** *109* (21), 8103.

41. X. Zhang; Y. Qu; H. Chen; I. Rouzina; S. Zhang; P. S. Doyle; J. Yan, Interconversion between three overstretched DNA structures. *J Am Chem Soc* **2014,** *136* (45), 16073.

42. Z. J. Yang; G. H. Yuan; W. L. Zhai; J. Yan; H. Chen, The kinetics of force-dependent hybridization and strand-peeling of short DNA fragments. *Science China Physics, Mechanics & Astronomy* **2016,** *59* (8).

43. Y. Wang; D. N. LeVine; M. Gannon; Y. Zhao; A. Sarkar; B. Hoch; X. Wang, Force-activatable biosensor enables single platelet force mapping directly by fluorescence imaging. *Biosens Bioelectron* **2018,** *100*, 192.

44. F. Chowdhury; I. T. Li; T. T. Ngo; B. J. Leslie; B. C. Kim; J. E. Sokoloski; E. Weiland; X. Wang; Y. R. Chemla; T. M. Lohman; T. Ha, Defining Single Molecular Forces Required for Notch Activation Using Nano Yoyo. *Nano Lett* **2016,** *16* (6), 3892.

45. Y. Wang; X. Wang, Integrins outside focal adhesions transmit tensions during stable cell adhesion. *Sci Rep* **2016,** *6*, 36959.

46. V. P. Ma; Y. Liu; K. Yehl; K. Galior; Y. Zhang; K. Salaita, Mechanically Induced Catalytic Amplification Reaction for Readout of Receptor-Mediated Cellular Forces. *Angew Chem Int Ed Engl* **2016,** *55* (18), 5488.

47. P. K. Dutta; Y. Zhang; A. T. Blanchard; C. Ge; M. Rushdi; K. Weiss; C. Zhu; Y. Ke; K. Salaita, Programmable Multivalent DNA-Origami Tension Probes for Reporting Cellular Traction Forces. *Nano Lett* **2018,** *18* (8), 4803.

48. V. P. Ma; Y. Liu; L. Blanchfield; H. Su; B. D. Evavold; K. Salaita, Ratiometric Tension Probes for Mapping Receptor Forces and Clustering at Intermembrane Junctions. *Nano Lett* **2016,** *16* (7), 4552.

49. R. Glazier; J. M. Brockman; E. Bartle; A. L. Mattheyses; O. Destaing; K. Salaita, DNA mechanotechnology reveals that integrin receptors apply pN forces in podosomes on fluid substrates. *Nat Commun* **2019,** *10* (1), 4507.

50. B. Zhao; C. O'Brien; A. Mudiyanselage; N. Li; Y. Bagheri; R. Wu; Y. Sun; M. You, Visualizing Intercellular Tensile Forces by DNA-Based Membrane Molecular Probes. *J Am Chem Soc* **2017,** *139* (50), 18182.

51. J. M. Brockman; A. T. Blanchard; V. M. Pui-Yan; W. D. Derricotte; Y. Zhang; M. E. Fay; W. A. Lam; F. A. Evangelista; A. L. Mattheyses; K. Salaita, Mapping the 3D orientation of piconewton integrin traction forces. *Nat Methods* **2018,** *15* (2), 115.

52. Y. Zhao; K. Pal; Y. Tu; X. Wang, Cellular Force Nanoscopy with 50 nm Resolution Based on Integrin Molecular Tension Imaging and Localization. *J Am Chem Soc* **2020,** *142* (15), 6930.

53. J. M. Brockman; H. Su; A. T. Blanchard; Y. Duan; T. Meyer; M. E. Quach; R. Glazier; A. Bazrafshan; R. L. Bender; A. V. Kellner, Live-cell super-resolved PAINT imaging of piconewton cellular traction forces. *Nature Methods* **2020,** *17* (10), 1018.

54. R. Ma; A. V. Kellner; V. P.-Y. Ma; H. Su; B. R. Deal; J. M. Brockman; K. Salaita, DNA probes that store mechanical information reveal transient piconewton forces applied by T cells. *Proceedings of the National Academy of Sciences* **2019,** *116* (34), 16949.

Chapter 2. DNA probes that store mechanical information reveal transient piconewton forces applied by T cells

Adapted from Rong Ma, Anna V. Kellner, Victor Pui-Yan Ma, Hanquan Su, Brendan R. Deal, Joshua M. Brockman, and Khalid Salaita. DNA probes that store mechanical information reveal transient piconewton forces applied by T cells. PNAS August 20, 2019 116 (34) 16949-1695.

2.1. Introduction

Studying the interplay between mechanical forces and chemical signaling in living cells is challenging. This is due, in part, to the difficulties of detecting the piconewton (pN) forces that deform biomolecules and trigger mechanotransduction pathways. For instance, stretching a molecule by 1 nm using 7 pN of force equates to a free energy change of ~1 kcal/mol, which is slightly greater than thermal energy (k_BT=0.59 kcal/mol). We previously developed molecular tension-based fluorescence microscopy (MTFM) to address the challenge of real-time mapping of the pN forces exerted by live cells [1]. MTFM probes are anchored to a surface and comprised of a "spring-like" element flanked by a fluorophore and quencher and presenting a biological ligand for receptor recognition [2]. The key design requirement for MTFM probes is to maximize fluorophore quenching when the probe is at rest, and to conversely minimize quenching when the probe experiences pN force. MTFM has found a range of applications, revealing the pN forces involved in platelet activation [3], T cell and B cell receptor triggering [4-5], as well as cell adhesion and migration [6].

One fundamental challenge in MTFM pertains to imaging transient mechanical events. This is because MTFM probes rapidly refold (within μs) upon termination of the mechanical input [7]. Hence long-lived molecular forces or forces mediated by high-copy number receptors have been the focus of MTFM studies. Even single molecule imaging of MTFM probes, which is difficult to implement in live cells, fails to capture rare mechanical events or transient mechanical events with a lifetime below that of the fluorescence acquisition time window (>100 ms) [8]. One potential solution is to use the tension gauge tether technology, which employs DNA-duplex probes that are irreversibly denatured at specific thresholds of forces [9]. However, the minimum detectable force threshold is ~12 pN applied for a duration of 2 s; hence, the tension gauge tether approach is not appropriate for detecting weak, or short-lived mechanical events [9].

Thus, there is a significant need to develop new probes to detect infrequent or short-lived mechanical events actively generated by cells. Such rare mechanical events are especially important to mechano-immunology. For example, single molecule mechanical stimulation through the T cell receptor (TCR) peptide-major histocompatibility complex (pMHC) bond is sufficient to trigger T cells [10]. Moreover, single molecule force spectroscopy experiments show that the TCR-pMHC bond lifetime ranges from tens of ms to 1 s, as a function of the applied force (1-20 pN) and the identity of the TCR-antigen pair [10-13]. Therefore, developing molecular probes that can visualize rare and transient pN forces will provide deeper insights into mechano-immunology.

Herein we demonstrate the concept of dynamic mechanical information storage to record and erase molecular force signals (**Figure 2.1A**). To achieve this goal, we employ the most sensitive class of MTFM probes, stem-loop DNA hairpins that function as a reversible digital switch (real-time closed, **Figure 2.1A**) [4, 6]. DNA MTFM probes are highly modular, and the equilibrium force that leads to a 50% probability of hairpin unfolding (real-time open, **Figure 2.1A**), $F_{1/2}$, can be tuned by adjusting the GC content and length of the stem-loop structure [6, 14-15]. DNA MTFM probes unfold and rapidly refold in response to molecular forces applied by cell receptors. In our approach, storage of mechanical events is mediated by a “locking” oligonucleotide that selectively hybridizes to mechanically unfolded hairpins and prevents refolding (**Figure 2.1B**). Therefore, mechanical unfolding of probes is irreversible upon addition of the locking strand (locked, **Figure 2.1A**). The locking strand can be modified with a fluorophore, Atto647N (**Figure A2.1**), to report the accumulation of mechanical events that equal or exceed $F_{1/2}$. This accumulated mechanical signal can subsequently be erased by an "unlocking" strand that triggers a toehold-mediated strand displacement reaction (**Figure 2.1A**).

Using this mechanical information storage strategy, we demonstrate the ability to perform multiple cycles of storing and erasing TCR forces, as well as mapping tension in static and migratory primary CD8$^+$ T cells. This method reveals the mechanical sampling dynamics of TCRs challenged with the antigenic pMHC, along with near-cognate pMHC ligands displaying single amino acid mutations. The results demonstrate that the TCR mechanically samples antigenic pMHCs with forces >4.7 pN, and the frequency as well as area coverage of mechanical sampling is sensitive to single amino acid mutations. Finally, the locking MTFM probes show that the programmed cell death receptor 1 (PD1), an immune checkpoint inhibitor, transmits pN forces to its ligand in primary T cells. To the best of our knowledge, this is the first report of pN force transmission through the PD1-PDL2 complex, which underscores the power of mechanical information storage in capturing fleeting mechanical events generated by low abundance receptors.

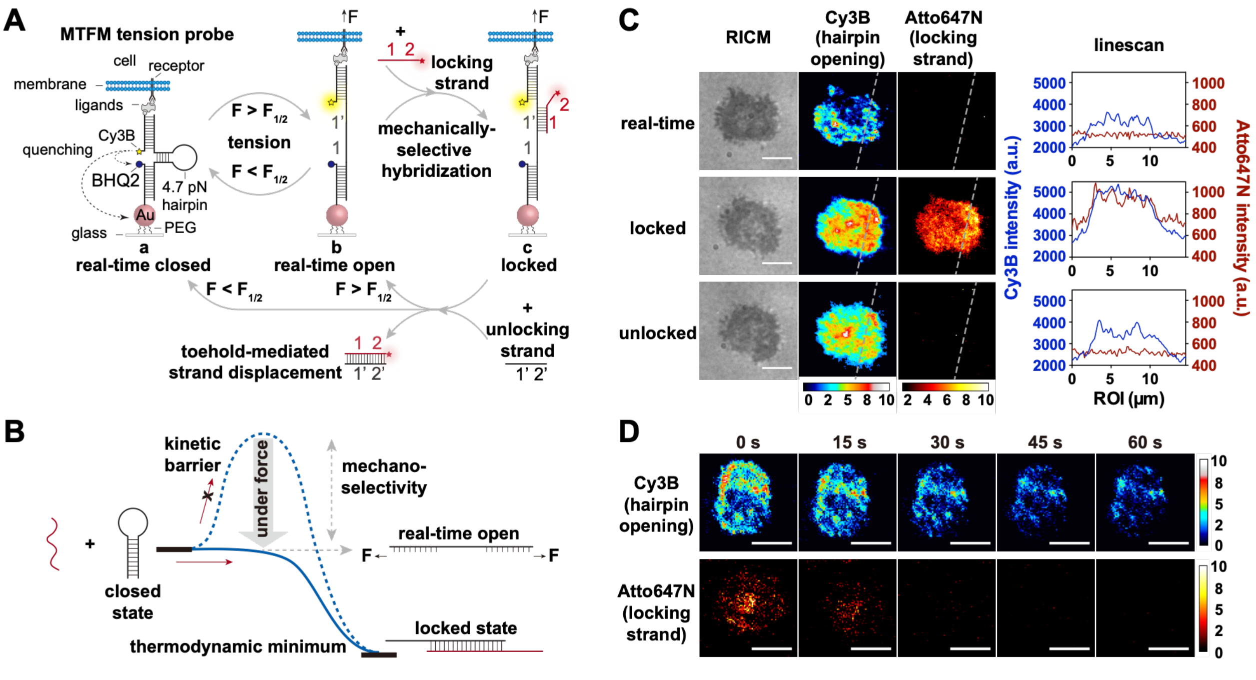

Figure 2.1. Mechanical information storage system concepts and demonstration of mechanical information writing and erasing. (A) Schematic depicting the concept of mechanical information storage. (B) Idealized energy diagram showing how mechanical forces dampen the kinetic barrier to locking strand binding, thus affording mechano-selectivity. (C) RICM, Cy3B, and Atto647N TIRF images of a single OT-1 cell before and after adding the locking strand and after unlocking (toehold mediated displacement). The dashed line in the fluorescence images corresponds to the raw intensity linescan profiles shown to the right. (Scale bar, 5 µm.) (D) Representative cells showing the kinetics of toehold-mediated unlocking, which was visualized by the loss of signal in both the Cy3B and Atto647N channels from 2 different experiments. Images in the upper row were acquired with unlabeled locking probe, and the images in the lower row were acquired with Atto647N labeled locking probe. (Scale bar, 5 µm.) The colored bars display the contrasts used to display each set of fluorescence images.

2.2. Results and Discussion

2.2.1. Preparation and Characterization of DNA hairpin tension probe substrate

We prepared gold nanoparticle MTFM tension probe surfaces as described previously (**Figure A2.2**) [4]. Atomic force microscopy and fluorescence microscopy (**Figure A2.3**) showed that the tension probe substrates were uniform and displayed an average of 1000 ± 89 gold nanoparticles/µm^2, with approximately 4.4 DNA tension probes per gold particle [4].

2.2.2. Hybridization between the DNA hairpin tension probes and the locking strand in a cell-free system

To achieve mechanical information storage, we first screened a small library of oligonucleotides to identify appropriate candidates for mechanically selective hybridization. Ideally, the locking oligonucleotide must rapidly bind to the unfolded hairpin and also display thermodynamic stability such that it remains bound to the probe for the duration of the experiment. Since the binding target is a stem-loop hairpin, these two properties are at odds, as the most thermodynamically stable locking strand is a full complement, which will also form a hairpin itself, thus hindering the rate of locking. Conversely, shorter locking strands that lack the full stem enhance the rate of locking but reduce thermodynamic stability. Based on these criteria, we designed five different locking oligonucleotides that ranged in length from 25mer to 13mer to screen (**Table A2.1**). Based on this screen, we used the 17mer as the locking strand, due to its favorable binding (**Figure A2.4**). To estimate mechano-selectivity, we compared the differential binding of locking strand to MTFM probe at rest to that of an unstructured sequence (mimicking the unfolded state of MTFM probe) and found a greater than two orders of magnitude difference (Supplementary note, **Figure A2.5**).

2.2.3. Unlocking the tension probes with toehold-mediated strand displacement in a cell-free system

For unlocking experiments, we engineered an 8 nt toehold with 50% GC content at the 3' end of the locking strand. The addition of unlocking strand triggered a rapid toehold-mediated strand displacement reaction that released locking strands from the DNA probes, resetting the probes to the real-time closed state (**Figure A2.6A, B**).

2.2.4. Confirming mechanically selective hybridization and toehold-mediated unlocking of the probes with T cells

To test the locking/unlocking concept in live cells, naïve OT-1 T cells were allowed to adhere and spread on MTFM probe surfaces presenting antiCD3ε antibodies. Cells generated tension signal as the TCR engaged the antibody and transmitted forces to the probes (real-time, **Figure 2.1C**). Subsequently, the Atto647N-tagged locking strand was added for 10 min, washed, and the same T cells were imaged, confirming binding (locked, **Figure 2.1C**). Importantly, the Cy3B hairpin signal increased after the locking strand was introduced (linescan, **Figure 2.1C**), indicating that the locking strand led to the accumulation of opened hairpins. We found significant co-localization between the Cy3B (hairpin opening) and the Atto647N (locking strand) signals, as evident from linescan analysis and the Pearson's correlation coefficient of 0.72 ± 0.096 (n=20 cells). Since the excess locking strand was rinsed away before re-imaging, we anticipate that some mechanical hairpin unfolding events will not be accompanied by locking strand hybridization. We next tested "erasing" the stored cellular mechanical information. This process was triggered by adding 200 nM unlocking strand to the sample for 2-3 min, and confirmed by imaging the same group of T cells (unlocked, **Figure 2.1C**). The unlocking process was rapid and reached completion within 60 s (**Figure 2.1D**, **Figure A2.6C**, n=31 cells). Control experiments using tension probes with a scrambled stem-loop confirmed the specificity of locking real-time tension (**Figure A2.7A, B, C**). Time-lapse videos confirmed the unlocking of stored information was due to toehold-mediated strand displacement (**Movie A2.1**) rather than photobleaching (**Movie A2.2**), and was sequence-specific (**Figure A2.7D, E, F**, **Movie A2.3 and A2.4**).

2.2.5. Confirming the stability of locked probes

Control experiments using latrunculin B (5 μM, 15 min), a cytoskeletal inhibitor, confirmed that the locked tension was maintained even when receptor forces were minimized (**Figure A2.8**).

2.2.6. Multiple rounds of mechanical information storage of TCR forces

One advantage of this strategy is the ability to arbitrarily toggle between the locked and unlocked states of the probe, thus selecting different time windows for integrating the force signal. Accordingly, we performed multiple rounds of mechanical information storage and erasing. TCR-antiCD3ε forces were first imaged (real-time tension, **Figure 2.2A**), and 200 nM locking strand was subsequently added to accumulate tension signal for 10 min. Excess locking strand was then washed away, and stored tension images were acquired (1^{st} cycle locked, **Figure 2.2A**). The stored tension signal was then erased with 100 nM unlocking strand for 3 min (1^{st} cycle unlocked, **Figure 2.2A**). This procedure was repeated for two additional cycles, and the hairpin opening and locking strand signal for the same naïve OT-1 cell was imaged. To quantify how locking and unlocking modulated the Cy3B tension signal, we repeated the same experiment using an unlabeled locking strand that eliminates potential bleed-through and thus reduces the number of washes required for these measurements. Statistically significant changes were observed in integrated Cy3B intensity upon addition of locking and unlocking strand (**Figure 2.2B**, n=27 cells), corresponding to the accumulation of tension or erasing of the stored tension. The increasing levels of locked tension signal at later wash cycles may reflect the mechanosensitive nature of the TCR which experiences shear forces during addition and washing of the oligonucleotide probes. Both inadvertent washing-induced activation of T cells and also T cell fatigue may be minimized in future studies by using microfluidics.

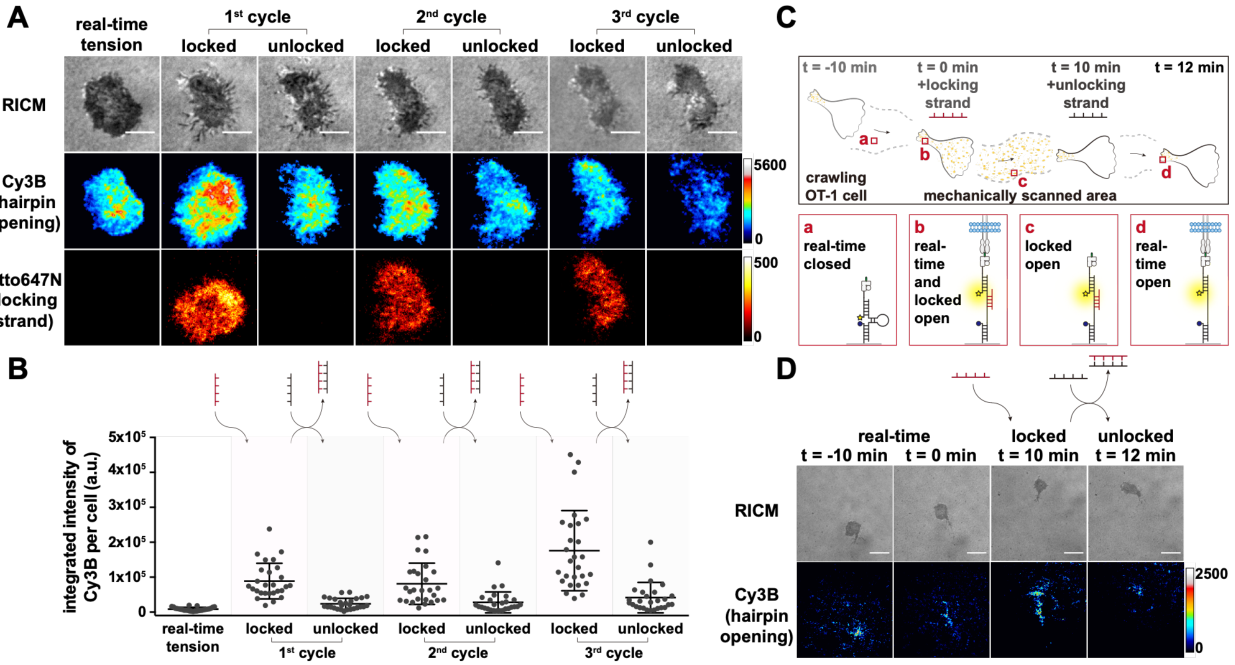

Figure 2.2. Demonstration of repeated rounds of tension locking and unlocking and tracking the transient mechanical events occurring under migratory cells. (A) Representative RICM, Cy3B (hairpin opening), and Atto647N (locking strand) images of a single OT-1 CD8+ T cell that underwent 3 rounds of mechanical information storage and erasing. (Scale bar, 5 μm.) Locking was driven with a 200 nM solution of oligo for a duration of 10 min, while unlocking was triggered using 100 nM unlocking probe for a duration of 3 min. The Atto647N signal drops to background levels upon addition of the unlocking strand. The colored bars display the contrasts used to display each set of fluorescence images. (B) Plot displaying the Cy3B (hairpin opening) integrated intensity per cell for a population of cells (n = 27 cells) that underwent 3 cycles of locking and unlocking as described in A, except for using an unlabeled locking strand instead of a Atto647N labeled locking strand. Error bars represent SD. There was a statistically significant shift in the integrated intensity based on Student's t tests when comparing locked to unlocked groups, $P < 0.0001$. (C) Schematic showing how mechanical information storage was used to map mechanical sampling/scanning of pMHC antigen during cell migration. (D) Representative RICM and tension images of a single T cell crawling on an ICAM-1/pMHC N4 surface. The first 2 images correspond to 2 time points acquired in the real-time state (before locking). The third image was collected

after adding the locking strand for 10 min (revealing tension history), and the fourth image shows the tension signal after unlocking. (Scale bar, 10 μm.)

2.2.7. Mechanical information storage of TCR forces in migratory T cells

We next investigated the potential of mechanical information storage to map TCR forces produced by a migratory T cell (**Figure 2.2C**). To trigger the migration, we engineered surfaces presenting ICAM-1 molecules along with the antigenic N4 pMHC (peptide: SII**N**FEKL), which is a commonly studied OT-1 TCR antigen [16]. ICAM-1 binds to lymphocyte function-associated antigen 1 (LFA-1) which is crucial in T cell activation, adhesion and crawling [17]. Therefore, the co-presentation of these two ligands triggered a highly migratory phenotype of OT-1 cells (**Movie A2.5**). The TCR tension was primarily located at the trailing edge of the cells and was highly transient, dynamically following the cellular trajectory along the substrate (real-time, **Figure 2.2D**, **Movie A2.5**). Motile T cells show a distinct TCR force map compared to static cells exclusively stimulated with N4 pMHC; the latter formed a ring-like tension pattern that evolved to distribute across the cell-substrate contact area (**Figure 2.3A**) [4]. Upon addition of the locking strand, the TCR tension signal was enhanced and also extended across the T cell track, revealing the spatial distribution of pMHC ligands scanned with F>4.7 pN over 10 min (locked, **Figure 2.2D**). Interestingly, these images show that the T cell mechanically scanned a significant fraction of antigen (81 ± 28% over its initial contact area, n=10 cells) within a 10 min migration time window. Thus, the dynamic T cell synapse (kinapse) represents a zone of TCR mechanosensing [18-20]. Upon addition of the unlocking strand, probes "reset" back to the real-time state, and exclusively showed tension at the trailing cell edge of the cell (unlocked state, **Figure 2.2D**). Taken together, these experiments show the utility of the locking/unlocking strategy to visualize the molecular forces associated with static and migratory T cells across different time scales.

2.2.8. TCR force signal enhancement by the mechanical information storage

Given that mechano-locking enhances TCR-pMHC tension signal by accumulating pulling events that are >4.7 pN, we next aimed to determine the degree of enhancement and its accumulation dynamics. OT-1 T cells were allowed to engage real-time tension probes and then incubated with unlabeled locking strand (200 nM). The unlabeled locking strand was beneficial here because it eliminated bleed-through from the Atto647N tag. Additionally, avoiding the rinsing steps accelerates the experiments and reduces perturbation of cells. **Figure 2.3A** shows a time course for TCR-N4 pMHC tension signal accumulation for three cells upon addition of the locking strand. Interestingly, the tension signal was concentrated at the central and peripheral region of the cell-substrate interface and accumulated over time after lock strand addition (**Figure A2.9**). Analysis of kinetics for n=16 cells showed that the signal approached saturation by t=10 min (**Figure 2.3B**). Notably, the enhancement of the integrated N4 tension signal per cell was approximately 189-fold in this experiment. Tension occupancy, which is the fraction of the cell contact area showing tension signal, reached 91% in 10 min. The tension occupancy is an indication of the area that is mechanically scanned by the TCR with F>4.7 pN in search for antigen. The kinetics of the tension occupancy increase is in agreement with a recent report showing that T cell microvilli search for cognate antigen at a consistent coverage [21].

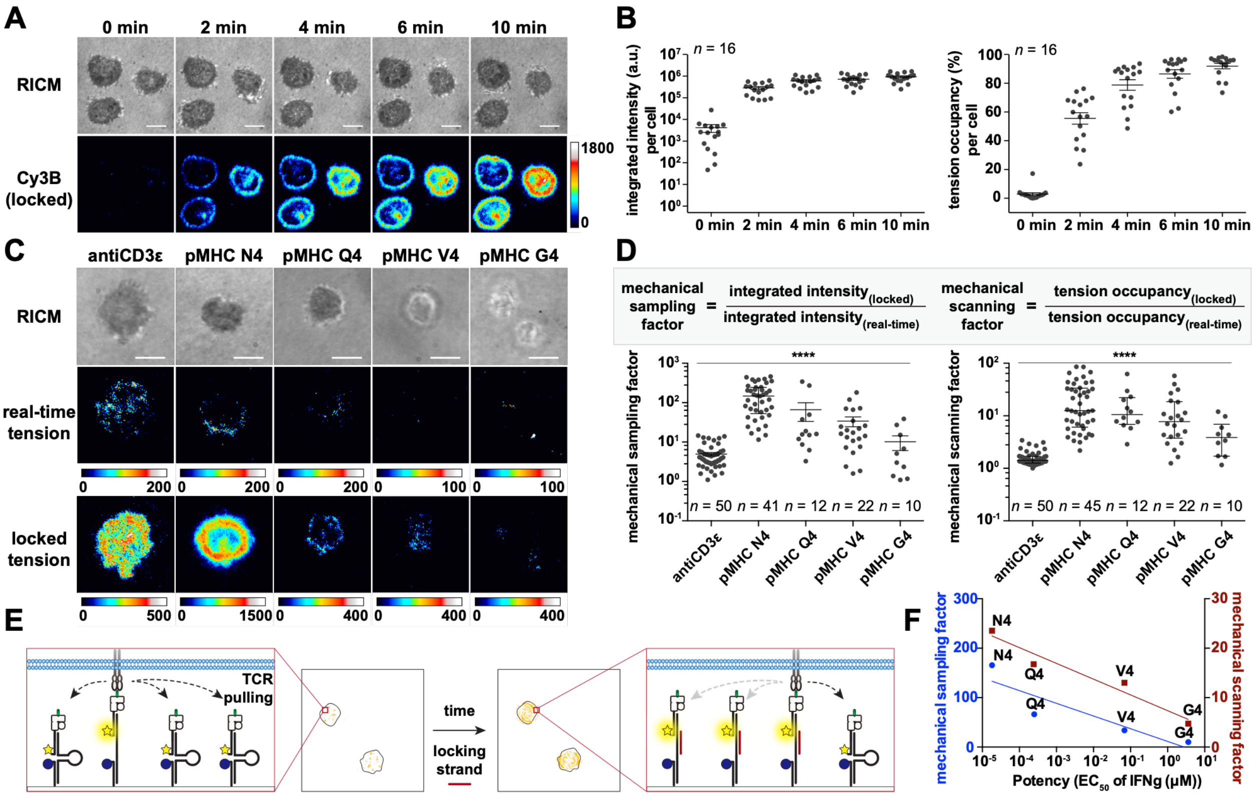

Figure 2.3. Kinetics of locking and detection and analysis of TCR forces with altered peptide ligands. (A) Time-lapse showing RICM and Cy3B tension signal for 3 representative cells after adding locking strand to probes presenting N4 ligand. (Scale bar, 5 μm.) (B) Plots of integrated tension signal and tension occupancy of individual cells as a function of time (n = 16 cells from the same animal). Error bars represent the SEM. (C) Representative images of single cells that were imaged using probes in the real-time and locked state when presented with antiCD3ε, pMHC N4, Q4, V4, and G4. Note the colored bars at the bottom of each image indicate the range of display values and differ for each group depending on the intensity of the signal. (Scale bar, 5 μm.) (D) Definition and plots showing sampling and scanning factor for different ligands. Error bars represent the SEM. Statistical significance was analyzed with a 1-way ANOVA (****$P < 0.0001$). The number of analyzed cells in each group is indicated in the plots. (E) Schematic showing the concept of mechanical sampling and scanning. (F) Correlation between the mechanical sampling and scanning factor and the potency of the ligand. EC50 values were obtained from literature (24).

2.2.9. Detection and analysis of the TCR forces with altered peptide ligands

We next sought to investigate how T cells differentially mechanically sample their cognate and near cognate ligands over time. The TCR-pMHC interaction is highly specific, allowing T cells to discriminate between single amino acid mutants of the cognate pMHC despite their similar μM-range 3D affinity [22]. Single molecule force spectroscopy measurements suggest that the stability of the TCR-pMHC complex at differing levels of mechanical strain provides a mechanism to enhance antigen discrimination [11]. We tested a panel of well-characterized altered peptide ligands, as well as antiCD3ε against OT-1 cells. **Figure 2.3C** shows representative TCR tension maps of naïve OT-1 cells challenged with the cognate N4 pMHC and single amino acid mutants of the 4th position of SII<u>X</u>FEKL, where X=Q, V, and G. In the real-time state, cells produced the greatest tension signal with antiCD3ε, followed by N4, with the mutant pMHC antigens producing weak or non-detectable tension signal. This result is consistent with our prior work with V4 [4] and also with the reported bond lifetimes for mutant ligands [10]. For example, independent of CD8, TCR-pMHC N4 binding displays catch-bond behavior, with an average bond lifetime of 100 ms at zero force and 800 ms at 10 pN. However, the TCR exhibits slip-bond behavior with the mutant pMHC G4 (SII<u>G</u>FEKL), displaying an average bond lifetime of 300 ms at zero force and <100 ms at 10 pN [10, 22]. Such short-lived mechanical events are difficult to visualize with real-time probe imaged with conventional MTFM probes. Upon addition of the locking strand, the integrated tension signal was significantly enhanced in all the tested antigens due to the accumulation of mechanical events over a time window of 10 min. Though mechanical events mediated between TCRs and weak antigens are transient and previously undetectable, the addition of the locking strand amplified the tension signal and rendered it distinguishable (locked tension, **Figure 2.3C**). The less potent pMHC Q4 produced a ring-pattern that could be observed after locking, though it was much less pronounced compared to the N4 antigen. With pMHC V4 and G4, the observed tension did not show the typical ring-pattern and was more disorganized. The mutant antigens showed significantly weaker integrated tension and tension occupancy, which can be attributed, in part, to TCR-pMHC bond failure as well as the lack of T cell triggering.

We noticed that the signal accumulation levels differed when cells were presented with antibody, cognate pMHC, and altered peptide ligands. To quantify these differences on a per cell basis, we defined two parameters: the mechanical sampling factor, which is the fold enhancement in integrated tension signal; and the mechanical scanning factor, which reflects the fold increase in tension occupancy (**Figure 2.3D**). These factors reflect the frequency of TCR binding to antigens, applying $F>4.7$ pN, dissociating, and then sampling new ligands (**Figure 2.3E**). Interestingly, the integrated tension signal and the tension occupancy varied significantly when the OT-1 cells were exposed to different antigens (**Figure A2.10**). Plots in **Figure 3D** show the mechanical sampling and mechanical scanning factors for different TCR ligands averaged from $n>10$ cells per group. Surprisingly, the average mechanical sampling factor was only 5 ± 0.5 (mean ± S.E.M.) for antiCD3ε whereas for N4 it was 165 ± 21, followed by 66 ± 32, 33 ± 9, and 10 ± 4 for the Q4, V4, and G4 antigens, respectively (**Figure 2.3D**, **Figure A2.10A**). Although the real-time tension with antiCD3ε was the greatest among all tested ligands (**Figure 2.3C**), it failed to accumulate as fast as N4, implying less frequent mechanical sampling by the TCRs, which is likely partially due to the slow k_{off} of the antibody. The difference in 2D kinetics of TCR-ligand interactions is likely an important contributor to the significant difference in mechanical sampling factor across the panel of altered peptide ligands. For example, independent of CD8 engagement, the TCR-pMHC N4 interaction has an effective 2D on-rate $A_c k_{on}=1.7\times10^{-3}$ $\mu m^4 s^{-1}$ at 25 °C [22]. This rapid on-rate enables T cells to search for and sample antigens at high speed, and quickly accumulate sufficient antigen stimulation for further signaling. In contrast, for less potent pMHC G4, $A_c k_{on}=4.7\times10^{-5}$ $\mu m^4 s^{-1}$ [22] which leads to slower binding, and thus contributes to a smaller mechanical sampling factor. There has been long standing speculation that the rapid kinetics of TCR-antigen binding provides an advantage in terms of maximizing sampling of antigen, and our results confirm this notion through the mechanical sampling factor for N4.

The mechanical scanning factor, which is a measure of the increase in tension occupancy, and is related to cytoskeleton coordination of TCRs, showed similar trends. Prior to locking, the tension occupancy for the antiCD3ε and N4 ligands was 60.8 ± 2.1% (mean ± S.E.M.) and 8.3 ± 1.1%, respectively (real-time, **Figure 2.3C**, **Figure A2.10B**). After locking, the tension occupancy increased to 88.7 ± 1.2% and 90.6 ± 1.4% for antiCD3ε and N4, respectively (locked, **Figure 2.3C**, **Figure A2.10B**), leading to a scanning factor of 1.6 ± 0.1 (mean ± S.E.M.) for antiCD3ε and 23.6 ± 3.3 for N4. Within 10 minutes of contacting the surface, cells leveraged the short-lived TCR-pMHC N4 bond to mechanically scan almost the entire contact area, significantly faster than the cells on antiCD3ε substrate, though they both can activate T cells effectively. Moreover, the locked tension signal showed a ring pattern with puncta at its center (pMHC N4, **Figure 2.3C**), demonstrating that the most frequent pulling events were arranged and focused at the edge and the center of the cells. This pattern resembles the architecture of the immunological synapse. With the altered peptide ligands, the decreased scanning factor (**Figure 2.3D**), together with the reduced contact area (pMHC Q4, V4, G4, **Figure 2.3C**), suggest weaker cytoskeleton engagement, which might be an outcome of reduced cell triggering. These direct measurements of TCR mechanical sampling and scanning agree well with previous single-molecule force spectroscopy measurements, where forces were applied externally to determine 2D kinetics and affinity [22]. We also found that the mechanical sampling and scanning factors were both highly correlated to the potency of these antigens (as measured using published cytokine production assays) [23-24], further underscoring the potential of these mechanical parameters as readouts of T cell activation (**Figure 2.3F**).

2.2.10. Detection and analysis of the PD1 forces

Although TCR-pMHC affinities are weak (K_d~μM), T cells tend to express high copy numbers of the TCR. The reported density of TCRs in naïve OT-1 cells is ~130-200 molecules/μm^2 [22]. To demonstrate mapping of forces generated by low abundance receptors, we next investigated mechanotransduction of the programmed cell death receptor 1 (PD1). PD1 is a co-inhibitory receptor that downregulates T cell activation when it encounters its ligands, programmed cell death ligand 1 (PDL1) and/or ligand 2 (PDL2) [25]. PD1 density is low in naïve OT-1 $CD8^+$ cells, with 0.2 molecules per μm^2 (24 ± 1 copies per cell), and 6.8 molecules per μm^2 (671 ± 16 copies per cell) in antibody-stimulated activated cells [26]. Hence, we activated naïve OT-1 cells using the N4 peptide for 48 h, and the activated cells were imaged on tension probes presenting either antiPD1 antibody or murine PDL2. TCR-antiCD3ε forces were also quantified as a positive control. Without the locking strand, the PD1-antiPD1 and PD1-mPDL2 tension was very weak or non-distinguishable from noise (real-time, **Figure 2.4A**). However, the PD1 tension signal was enhanced upon addition of the locking strand (1 μM, introduced 30 min after cell plating) (locked, **Figure 2.4A**). In contrast to TCR forces, PD1-mPDL2 tension was less abundant and more punctate and did not display a typical ring-pattern characteristic for TCR ligands. The integrated tension intensity and tension occupancy were quantified before and after incubation with the locking strand (**Figure A2.11**). Both parameters were weaker for the mPDL2 ligand compared to the PD1 antibody, likely reflective of their relative affinities [27]. Even upon addition of the locking strand, there was modest signal enhancement compared to that of the TCR antigens. Employing similar parameters defined in **Figure 2.3D**, we found that the mechanical sampling factor was 6.4 ± 1.5 for mPDL2 and 20.8 ± 2.9 for antiPD1 (**Figure 2.4B**). The mechanical scanning factor was 2.9 ± 0.4 for mPDL2 and 6.4 ± 0.8 for antiPD1 (**Figure 2.4C**). These values imply that PD1 forces were less dynamic when T cells were stimulated with mPDL2 compared to antiPD1. It is not clear how the cytoskeleton coordinates the mechanical sampling and scanning features of PD1, but given that PD1-PDL2 binding mediates dampening of T cell activity and adhesion [28], it is plausible that this difference reflects differential T cell activation upon stimulation with PDL2 versus antiPD1. Taken together, the mechanical information storage approach clearly shows that PD1 transmits F>4.7 pN to its ligand upon surface engagement. Future studies are needed to determine whether and how mechanical forces modulate PD1 signaling.

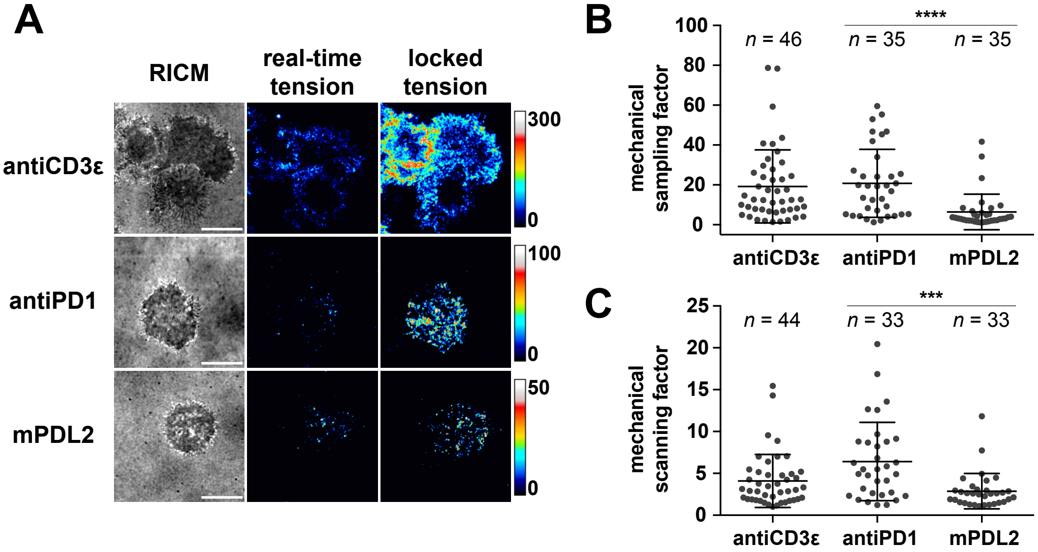

Figure 2.4. Detection and analysis of the PD1 forces. (A) Representative RICM and tension images of activated OT-1 cells on antiCD3ε, antiPD1, and mPDL2-functionalized tension probes in the real-time and locked state (10 min duration). (Scale bar, 10 μm.) Colored bars indicated the display values used for each set of fluorescence images. (B and C) Plots of mechanical sampling factor and mechanical scanning factor for antiCD3ε, antiPD1, and mPDL2 in activated OT-1 cells. Error bars represent SD (statistical significance was analyzed with a Student's t test; ***$P < 0.001$; ****$P < 0.0001$).

2.3. Conclusion

This work implements a strategy that can switch between mapping the real-time receptor force and accumulated force history, and overcomes the shortcomings in mapping weak and transient mechanical events that are characteristic of immune receptor interactions. By employing multiple tension locking and unlocking cycles, we demonstrate the utility of this technique for studying both static and migratory cell immune receptor mechanics. This method was further applied to visualize and analyze TCR forces upon engagement to cognate antigen and altered peptide ligands. With this technique, we were able to define mechanical sampling/scanning factors that correlated with ligand potency. Moreover, this strategy revealed PD1 receptor mechanics, featuring a punctate pattern with a less dynamic sampling profile than the TCR. Mechanical locking represents a significant improvement in sensitivity for molecular tension probes and therefore, mechanical locking may become the standard in the field when studying mechano-immunology. It is important to also note that there are two potential limitations of mechanical information storage. First, the signal enhancement comes at a cost of losing temporal information, thus this method poorly captures the oscillatory dynamics of T cell forces [29-30]. Second, the addition of locking strand slightly tilts the energy landscape of hairpins towards the open state, which will reduce the effective $F_{1/2}$ in a concentration-dependent manner. Nonetheless, this work demonstrates a powerful strategy to investigate weak, transient, and less abundant mechanical events, which is expected to be widely useful for studying the mechanobiology of immune cells.

2.4. Supplementary note

The selectivity of lock strand binding to unfolded hairpins over folded ones was measured by using model surfaces that either presented the folded MTFM probe or an unstructured single stranded DNA sequence. The unstructured sequence included a complementary region to the 17mer, thus providing a model for the opened state of the MTFM hairpin probes (**Figure A2.5A**). The hybridization of locking strand to the unstructured sequence saturated in seconds (**Figure A2.5B**). In contrast, lock strand hybridization to the closed hairpin tension probe did not saturate even after 8 h of incubation. Our observed rates of binding to a stem-loop hairpin is in agreement with previous reports, where binding kinetics displayed a fast regime representing "kissing" at the loop site, and a slow regime of intermolecular base pairing with the stem [31]. Hybridization yield was also shown to be significantly lowered when targeting a hairpin structure compared to an unstructured sequence [31-32].

Assuming pseudo first-order binding kinetics, we fit the data using one-phase association and obtained the observed rate constants, $k_{\mathrm{obs}} = 0.22 \pm 0.09\ \mathrm{s}^{-1}$ (mean ± SD) and $4.5\times10^{-4} \pm 8.1\times10^{-5}\ \mathrm{s}^{-1}$ for the unstructured and hairpin probes, respectively. These values are likely an underestimate, as the mixing dead-time was significant relative to the rapid binding to the unstructured probe. These observed rate constants correspond to k_{hyb} of $\sim1.09\times10^{6}\ \mathrm{M}^{-1}\mathrm{s}^{-1}$ and $\sim2.24\times10^{3}\ \mathrm{M}^{-1}\mathrm{s}^{-1}$ for the for unstructured and hairpin probe, respectively. This represents a 487-fold difference in binding rates, thus providing an estimate of the lock binding selectively between mechanically unfolded and folded probes. (**Figure 2.1C**).

This analysis ignores the effect of tension on k_{hyb}, which is a reasonable assumption given that optical tweezers measurements show that k_{hyb} is not impaired when the load is less than 20 pN [33]. Interestingly, weak forces applied to a ssDNA slightly promote hybridization, as tension helps with aligning the strand at initial encounter [33]. Conversely, mechanical stretching of DNA with large values of tension is expected to hinder hybridization. This is because forming the B-form duplex becomes less energetically favorable. Indeed, it was found that when $F \approx 41$ pN for a 24mer, this created a barrier to hybridization. However, our past work quantifying TCR-pMHC N4 forces showed that TCR force values fail to unfold DNA hairpins with a $F_{1/2} = 19$ pN. Given that TCR forces are below 19 pN, our estimates of mechano-selectivity are justified here [4, 34].

Another important consideration is the role of the lock strand concentration in capturing transient unfolding events. If the rate of k_{hyb} is slow relative to the lifetime of the mechanical event, then mechanical information storage will fail. At high concentration of lock strand, the vast majority of hairpin unfolding events will lead to lock binding and mechanical information storage. We recognize that quantitative analysis of the kinetics of tension signal accumulation as a function of lock strand concentration will likely provide a direct measurement of force lifetimes (τ_{force}), but this is beyond the scope of this current study and will be pursued in subsequent work.

2.5. Materials and methods

2.5.1. Oligonucleotides

All oligonucleotides were custom synthesized by Integrated DNA Technologies (Coralville, IA), except for the BHQ2 strand, which was synthesized by Biosearch Technologies (Novato, CA). **Table A2.1** includes the names and sequences for all oligonucleotides used in this work. Structures of the modifications are shown in **Figure A2.1A**.

Table A2.1. **List of oligonucleotides used in Chapter 2**

sequence ID	description	sequence (5’ to 3’)
4.7 pN hp	hairpin strand in MTFM	GTG AAA TAC CGC ACA GAT GCG TTT GTA TAA ATG TTT TTT TCA TTT ATA CTTTAA GAG CGC CAC GTA GCC CAG C
A21B	top strand in MTFM	/5AmMC6/ - CGC ATC TGT GCG GTA TTT CAC TTT - /3Bio/
Cy3B strand	Cy3B labeled A21B	Cy3B - CGC ATC TGT GCG GTA TTT CAC TTT - /3Bio/
BHQ2 strand	bottom and quencher strand in MTFM	/5-ThioC6-5/ - TTT GCT GGG CTA CGT GGC GCT CTT - /3BHQ_2/
scrambled 4.7 pN hp	scrambled hairpin strand in MTFM	GTG AAA TAC CGC ACA GAT GCG TTT GTA AAT ATG TGG TGG TCA TAT TTA CTT TAA GAG CGC CAC GTA GCC CAG C

13mer	partial complement to 4.7 pN hp	AA AAC ATT TAT AC
15mer	partial complement to 4.7 pN hp	AAA AAA CAT TTA TAC
17mer	partial complement to 4.7 pN hp	GAA AAA AAC ATT TAT AC
21mer	partial complement 4.7 pN hp	AAA TGA AAA AAA CAT TTA TAC
25mer	full complement to 4.7 pN hp	GTA TAA ATG AAA AAA ACA TTT ATA C
unstructured sequence	mimic 17mer binding site at hairpin open state	GT ATA AAT GTT TTT TTC CCA GCG TGA T /3ThioMC3-D/
17mer locking strand (non-fluorescent)	complement to partial hairpin	GAA AAA AAC ATT TAT ACC CTA CCT A /3AmMO/
17mer locking strand	non-fluorescent locking strand labeled with Atto647N	GAA AAA AAC ATT TAT ACC CTA CCT A-Atto647N
unlocking strand	full complement to 17mer locking strand	TAG GTA GGG TAT AAA TGT TTT TTT C

scrambled unlocking1	17mer region scrambled unlocking strand	TAG GTA GGC ACG CTG ATT AGT GTG G
scrambled unlocking2	fully scrambled unlocking strand	TTA TCA TTG ACG CTG ATT AGT GTG G

2.5.2. Reagents

(3-Aminopropyl)triethoxysilane was purchased from Acros (Cat# AC430941000, Pittsburgh, PA). LA-PEG-SC (Cat# HE039023-3.4K) and mPEG-SC (Cat# MF001023-2K) were purchased from Biochempeg (Watertown, MA). Sulfo-NHS acetate (Cat# 26777) was purchased from Thermo Fisher Scientific (Waltham, MA). Custom synthesized 8.8 nm diameter tannic acid modified gold nanoparticles were obtained from Nanocomposix (San Diego, CA). Ethanol (Cat# 459836), hydrogen peroxide (Cat# H1009), bovine serum albumin (BSA) (Cat# 10735078001), latruculin B (Cat# L5288, >80%), 3-hydroxypicolinic acid (3-HPA, Cat# 56197), Atto647N NHS ester (Cat# 18373-1MG-F), and Hank's balanced salts (H1387) were purchased from Sigma Aldrich (St. Louis, MO). Dulbecco's phosphate-buffered saline (DPBS, Cat# 21-031-CM), and Dulbecco's Modified Eagle's Medium (DMEM, 10-013-CV) were acquired from Corning. Cy3B NHS ester (Cat# PA63101) was purchased from GE Healthcare (Pittsburgh, PA). NTA-SAM reagent was purchased from Dojindo Molecular Technologies (Rockville, MD). Red blood cell lysis buffer (Cat# 00-4333-57), biotinylated anti-mouse CD3ε (Cat# 13-0031-82), and biotinylated anti-mouse PD1 (Cat# PA5-35009) were purchased from eBioscience (San Diego, CA). Biotinylated pMHC ovalbumin (SIINFEKL) was obtained from the NIH Tetramer Core Facility at Emory University, which has been described in detail in our previous work [4]. Biotinylated pMHC ovalbumin mutants (SIIQFEKL, SIIVFEKL, SIIGFEKL) and biotinylated murine PDL2 were kindly provided by Dr. Cheng Zhu's lab at Georgia Institute of Technology.

No. 2 round glass coverslips (Cat# 48382-085) were purchased from VWR (Radnor, PA). Teflon racks (Cat# C14784) were obtained from Thermo Fisher Scientific. P2 size exclusion gel (Cat#1504118) was purchased from Bio-Rad (Hercules, CA). 3 mL syringes were purchased from BD bioscience (San Jose, CA). Cell strainers (Cat# 15-1100) were bought from Biologix (Shandong, China). Nanosep MF centrifugal devices (Cat# ODM02C35) with bio-inert membrane were bought from Pall laboratory (Port Washington, NY). Midi MACS (LS) startup kit (Cat# 130-042-301) (separator, columns, stand), and mouse CD8$^+$ T cell isolation kit (Cat# 130-104-075) were purchased from Miltenyi Biotec (Bergisch Gladbach, Germany).

2.5.3. Cells

The OT-1 CD8$^+$ T cell is a well-established system to study T cell biology. OT-1 transgenic mice were housed and bred in the Division of Animal Resources Facility at Emory University under the Institutional Animal Care and Use Committee. Naïve OT-1 T cells that express the CD8 co-receptor and specifically recognize chicken ovalbumin epitope 257–264 (SIINFEKL) were isolated and enriched from the spleen of a sacrificed mouse using MACS separation with the CD8$^+$ T cell isolation kit according to the manufacturer's instructions. DPBS buffer supplemented with 0.5% BSA and 2 mM EDTA was used as a buffer for the purification process. The purified CD8$^+$ naïve OT-1 cells were kept in R10 medium (RPMI with 10% FBS, 2 mM L-glutamine, penicillin G (100 U/mL), streptomycin (100 µg/mL, and 20 mM HEPES) at 4 °C before imaging on the same day. Activated OT-1 T cells were used for PD1 tension experiments. To activate OT-1 T cells, red blood cells from the splenocyte suspension were lysed using red blood cell lysis buffer following manufacturer's instructions, after which the cell suspension (2x10^6 cells/mL) was pulsed with 10 nM of SIINFEKL peptide in R10 medium at 37 °C for activation. After 2 h of incubation, the cells were washed in warm R10 medium once and plated in a 24 well plate at a density of 2x10^6 cells per well. After 48 h, the activated OT-1 cells were purified using the MACS CD8$^+$ T cell isolation kit and imaged.

2.5.4. Equipment

The major equipment that was used in this study include: Barnstead Nanopure water purifying system (Thermo Fisher), High-performance liquid chromatography (Agilent 1100), Nanodrop 2000 UV-Vis Spectrophotometer (Thermo Scientific), Matrix-assisted laser desorption/ionization time-of-flight mass spectrometer (MALDI-TOF-MS, Voyager STR), Inverted microscope system (Nikon Eclipse Ti) equipped with an EMCCD, total internal reflection fluorescence (TIRF) microscopy components TIRF 488 nm, TIRF 561 nm, TIRF 647 nm, a perfect focus system for maintaining focus during timelapse imaging, and reflection interference contrast microscopy (RICM).

2.5.5. Labeling oligonucleotides with dyes

Oligonucleotide-dye conjugates (Cy3B strand, 17mer locking strand) were prepared by coupling the terminal amine on the DNA strand with activated NHS-ester of the organic dye. Briefly, 50 μg (an excess quantity) of NHS dye was dissolved in 10 μL of DMSO, and reacted with 10 nmol of oligonucleotide in 1×PBS with 0.1 M $NaHCO_3$ overnight at 4 °C. After the reaction, byproducts, salts, and unreacted dye in the mixture were removed by P2 gel filtration with Nanosep MF centrifugal devices at 14000 rpm for 1 min. The product was further purified by reverse-phase HPLC with an Agilent AdvanceBio Oligonucleotide C18 column (653950-702, 4.6 x 150 mm, 2.7 μm). The mobile phase A: 0.1 M TEAA and B: ACN were used for a linear gradient elution of 10-100% B over 50 min at a flow rate of 0.5 mL/min (**Figure A2.1B**). The desired product was characterized by MALDI-TOF-MS (**Figure A2.1C, D**). 3-HPA was dissolved in 50% ACN/H_2O containing 0.1% TFA and 5 mg/mL ammonium citrate as matrix to acquire MALDI-TOF-MS spectra. The concentration of the strands was determined by UV-Vis using a Nanodrop instrument.

2.5.6. Biotinylated dimeric ICAM-1 expression

HEK293FT cells for lentivirus production were maintained in complete DMEM supplemented with 10% FBS, penicillin G (100 U/mL), and streptomycin (100 µg/mL) at 37 °C with 5% CO_2. Lentivirus particles were produced with HEK293FT cells by co-transfection of the pLEX transfer plasmid encoding the soluble dimeric ICAM-1 sequence with the 2nd generation packaging plasmids pMD2.G and psPAX2 (gifts from Didier Trono, Addgene plasmid #12259 and #12260) using linear polyethylenimine (MW = 25,000). The particles were harvested from the supernatant 48-72 h post-transfection, filtered and concentrated into ~200 µL in DMEM with 20% FBS by ultracentrifugation and stored at -80 °C before use. For lentiviral transduction, ~20,000 TB-15 cells (a variant of HEK293T cells stably expressing BirA biotinylating enzyme, a gift from Prof. John Altman and Dr. Richard Willis from the NIH Tetramer Core Facility at Emory University) were seeded onto a 96 well cell culture plate. On the next day, ~50 µL of concentrated lentivirus particles were added to the cells. After 6 h of infection, the media was exchanged to complete DMEM. Transduced cells were expanded to appropriate density before adaptation to suspension culture in a shaking incubator where the cells were maintained in FreeStyle 293 expression media (8% CO_2, shaking speed = 125 rpm). Soluble ICAM-1 was collected from the supernatant every 3 days and purified using Ni-NTA agarose affinity resin (Thermo Fisher Scientific). ICAM-1 quality was confirmed using SDS-PAGE and fluorescence imaging. The concentration of the recombinant ICAM-1 protein was quantified using Nanodrop and adjusted to 1 mg/mL and stored at -80 °C before use.

2.5.7. Surface preparation

Preparation of MTFM probes on Gold Nanoparticle Surfaces. Gold nanoparticle MTFM probe surfaces were prepared as described previously [4] and as illustrated in **Figure A2.2**. Note that we have made slight modifications to previously published methods [4]. Briefly, glass slides were placed in a Teflon rack and rinsed with 40 mL of Nanopure water 3 times. Then the rack holding the slides was placed in a beaker with 1:1 (v/v) solution of ethanol:Nanopure water and sonicated for 20 min. After sonication, the slides were washed 6 times with 40 mL of Nanopure water to remove any remaining organic solvents. Next, 40 mL of freshly made piranha solution (3:1 mixture (by volume) of H_2SO_4 and H_2O_2, CAUTION: highly explosive if mixed with organics) was prepared. The rack carrying slides was submerged in piranha solution for 30 minutes. After 30 min, the slides were washed intensively with 40 mL of Nanopure water 6 times, followed by another 3 washes with 40 mL of ethanol, until water was removed. Next, slides were incubated in 3% APTES in 40 mL of ethanol for 1 h at room temperature, after which the surfaces were washed with 40 mL of ethanol 3 times and baked in oven at 80 °C for 20 min. Then, the amine-modified glass coverslips were placed in petri dishes lined with parafilm with 300 μL of 0.5% w/v lipoic acid-PEG-NHS and 2.5% w/v mPEG-NHS in 0.1 M $NaHCO_3$ on each slide for 1 h at room temperature. Subsequently, the samples were rinsed with Nanopure water and incubated with 0.1 M $NaHCO_3$ containing 0.5 mg/mL of sulfo-NHS acetate for 30 min in order to passivate unreacted amine groups. Gold nanoparticles (8.8 nm, tannic acid modified) at 20 nM were subsequently added to surfaces for 30 minutes after intensive washes with Nanopure water. Meanwhile, 4.7 pN hp, Cy3B, and BHQ2 strands that form the molecular tension probe constructs were mixed and annealed at a ratio of 1.1:1:1 in 1 M NaCl at a 300 nM concentration. After annealing, an additional 2.7 μM of BHQ2 strand was added to the DNA solution for additional quenching. After 30 min of surface incubation with gold nanoparticles at room temperature and three washes with Nanopure water, the annealed DNA solution containing tension probes and quencher was added to surfaces and allowed to be immobilized overnight. After washing excess probes away with PBS on the second day, 40 μg/mL of streptavidin in PBS was added to the surfaces and incubated for 1 h. After washing slides with PBS, 40 μg/mL biotinylated antibodies (antiCD3ε or antiPD1) or pMHC ligands were allowed to bind to tension probes via biotin-streptavidin interactions for 1 h at room temperature in PBS. Finally, the slides were rinsed with PBS, assembled in imaging chambers, and immediately used for imaging. Surface quality was confirmed every time before conducting the experiment as shown in **Figure A2.3**.

Co-presenting ligands on surfaces modified with MTFM probes. Gold nanoparticles at 10 nM were added to surfaces modified with mPEG and lipoic acid PEG and allowed to react for 30 min. After washing 3 times with Nanopure water and twice with ethanol, 100 μL 0.2 mM NTA-SAM in ethanol was added to each surface and incubated at room temperature for 1 h in a sealed petri dish. The excess NTA-SAM was washed away with ethanol 3 times, followed by another 3 washes with Nanopure water. Gold nanoparticles at 20 nM were then added to surfaces again and incubated at room temperature for 30 min. Meanwhile the DNA tension probes were annealed as described previously. After hybridization, the probes were allowed to anchor on gold particles overnight at 4 °C. On the following day, 10 mM $NiCl_2$ in PBS was added to surfaces for 10 min and washed away with PBS. Dimeric ICAM-1 with His-tag was immobilized on surfaces by incubating surfaces with 10 μg/mL solution in PBS. After washing with PBS, streptavidin and biotinylated pMHC N4 were added to surfaces sequentially as previously described [4].

2.5.8. Microscopy

Atomic force microscopy. The density of AuNPs on the functionalized substrate was measured by an atomic force microscope with an anti-vibration stage (MFP-3D, Asylum Research, CA).

Silicon AFM tips (MikroMasch) were used to scan the sample in tapping mode with a force constant (5.4-16 N/m) at 1 Hz.

Fluorescence microscopy. Imaging was conducted with a Nikon Eclipse Ti inverted microscope driven by the NIS Elements software. The microscope was integrated with an evolve electron multiplying charge coupled device (Photometrics), an Intensilight epifluorescence source (Nikon), a CFI Apo 100× NA 1.49 objective (Nikon), a TIRF launcher with three laser lines: 488 nm (50 mW), 561 nm (50 mW), and 640 nm (40 mW), and a Nikon Perfect Focus System which allows the capture of multipoint and time-lapse images without loss of focus. All of the experiments were performed using reflection interference contrast microscopy (RICM) and the following Chroma filter cubes: TIRF 488, quad band TIRF 405/488/561/647, TRITC, FITC, Cy5. Imaging was performed using Hank's Balanced Salts supplemented with 0.35 g/L $NaHCO_3$ and 10 mM HEPES (Cell imaging media). All imaging data was acquired at room temperature.

Imaging in cell-free systems. Surfaces presenting hairpin tension probes were fabricated the same way as described in section 3.3.1, but without streptavidin and ligands. Surfaces presenting unstructured sequence were prepared similarly, except for using the same amount of unstructured sequence instead of DNA tension probe construct. The surfaces were imaged and incubated with locking oligonucleotides at 200 nM. Time-lapse data was acquired at 5 xy-coordinates (6710.8 μm^2 for epi measurements (**Figure A2.4**) and 163.84 μm^2 for TIRF measurements (**Figure A2.5**) at each coordinate) on each surface and averaged for processing after subtracting CCD background. The in-situ hybridization experiment was performed in PBS without cells and was repeated 3 times.

Mechanically selective hybridization and toehold-mediated strand displacement. Naïve $CD8^+$ OT-1 cells were purified from a transgenic OT-1 mouse 1 h before imaging. Purified OT-1 cells were added to surface presenting antiCD3ε and allowed to attach for 10 min. After cells started to produce tension continuously on surfaces, the locking strand was added (final concentration 200 nM) to surfaces in cell imaging media (CIM) for mechanically selective hybridization. After a specific time, typically 10 min, cells were gently rinsed with 1 mL PBS three times and imaged in fresh CIM (for raw representative data and imaging process see **Figure A2.12B, D**). A 4.7 pN hairpin with a scrambled stem-loop was used as control to demonstrate the specificity of mechanically selective hybridization. Linescans of raw data were used to show overlapping tension signals after the addition of locking strand. Unlocking strand was then added at 100 nM or 200 nM to erase the recorded tension signal. Images and videos (for videos 100 nM unlocking strand was used to better capture the erasing) were acquired for further analysis. Two scrambled unlocking controls were included to demonstrate the specificity of erasing the mechanical information.

Latrunculin B inhibition. Aliquoted latrunculin B stock was reconstituted with DMSO at 25 mg/mL and stored at -20 °C. Naïve OT-1 cells were treated with latrunculin B for 15 min at 5 μM, then imaged after gently replacing with fresh CIM.

Multiple rounds of TCR mechanical information locking/unlocking. 200 nM of fluorescent or non-fluorescent locking strand was used to record naïve OT-1 tension history against antiCD3ε from time t to t+10 min. Note imaging typically started 30-40 min after plating the cells. After gentle washing, images were acquired in both fluorescence channels. This procedure was repeated two additional times. Statistical analysis was carried out by comparing raw integrated density of individual cells for multiple rounds of locking and unlocking using a Student's *t*-test.

Migration tension tracks. Naïve OT-1 cells were plated on tension probe modified surfaces co-presenting pMHC N4 and dimeric ICAM-1 (See methods). A migratory phenotype was observed and the real-time tension during migration was imaged (**Movie A2.5**, for raw representative data please see **Figure A2.12A**). Locking strand was added at 200 nM at t ~ 30 min to map the migration tension track for 10 min. Then real-time tension probes were regenerated using an unlocking strand. Images were thresholded with the mean of background + 2*SD.

Tension against pMHC OVA ligands. Naïve OT-1 cells were plated on tension probe surfaces presenting pMHC N4, Q4, V4 or G4, for 40 min. Images of tension signal accumulation against pMHC N4 upon addition of locking strand were acquired at 0, 2, 4, 6, 10 min. Real-time hairpin mechanical opening was imaged, as well as the locked open hairpins after introducing non-fluorescence locking strand (200 nM) for 10 min (for raw representative data please see **Figure A2.12B**). Radial profile analysis of TCR-pMHC N4 tension accumulation was performed using the ImageJ "radial profile analysis" plugin (**Figure A2.9C**). Integrated intensity and tension occupancy of each cell that attached to the surface were quantified before and after the addition of the locking strand (for data process please see **Figure A2.12E**). Note that TCR-altered peptide ligands tension was observed after locking with more cells than reported in **Figure 2.3** (n = 65 for Q4, n = 111 for V4, and n = 28 for G4, cells were from 3 mice), but to calculate the mechanical sampling and scanning factor, only cells (n> 10 in each group from 3 mice) that showed non-zero values before locking were included in the analysis. Statistical analysis was carried out by one-way ANOVA.

PD1 tension. Activated OT-1 cells were plated on tension probe surfaces presenting anti-PD1 or murine PDL2 for 30 min. Images were acquired with or without 10 min of incubation with 1 μM of 15mer locking strand (for raw representative data please see **Figure A2.12C**). A shorter strand at higher concentration was selected to minimize the background signal increase during the locking process; the 15mer is assumed to have a higher k_{hyb} to the unfolded hairpin than folded hairpins. Integrated intensity and tension occupancy of each cell adhered to the surfaces were quantified before and after the addition of the locking strand. Statistical analysis on mechanical sampling and scanning factor was carried out using a Student's *t*-test.

2.6. Appendix

Figure A2.1. **Characterization of modified oligonucleotides**. (A) Structures of oligonucleotide modifications used in the current work. (B) Representative HPLC traces and (C) MALDI-TOF-MS spectra of labeled oligonucleotides. The gray arrow in the UV-vis traces indicate the relevant peaks associated with the relevant MALDI-TOF spectra shown in B. (D) Calculated mass and peaks found using MALDI-TOF-MS.

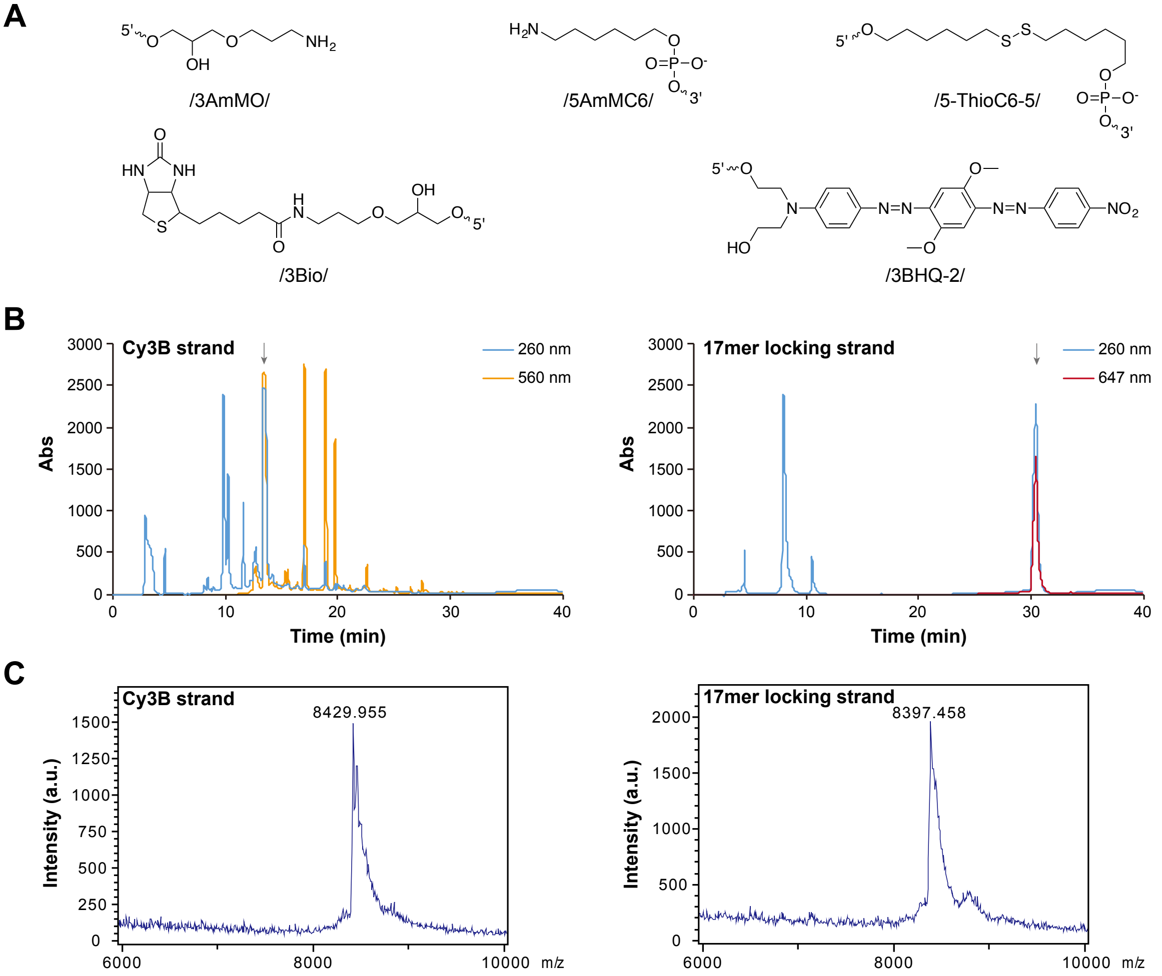

D

sample	calculated mass	m/z found	error
A21B	7917.4	8054.55	1.7%
Cy3B strand	8577.4	8429.995	1.7%
17mer locking strand (non-fluorescent)	7797.2	7802.687	0.07%
17mer locking strand (labeled with Atto647N)	8540.2	8397.458	1.7%

Figure A2.2. Preparation of the surfaces with MTFM probes.

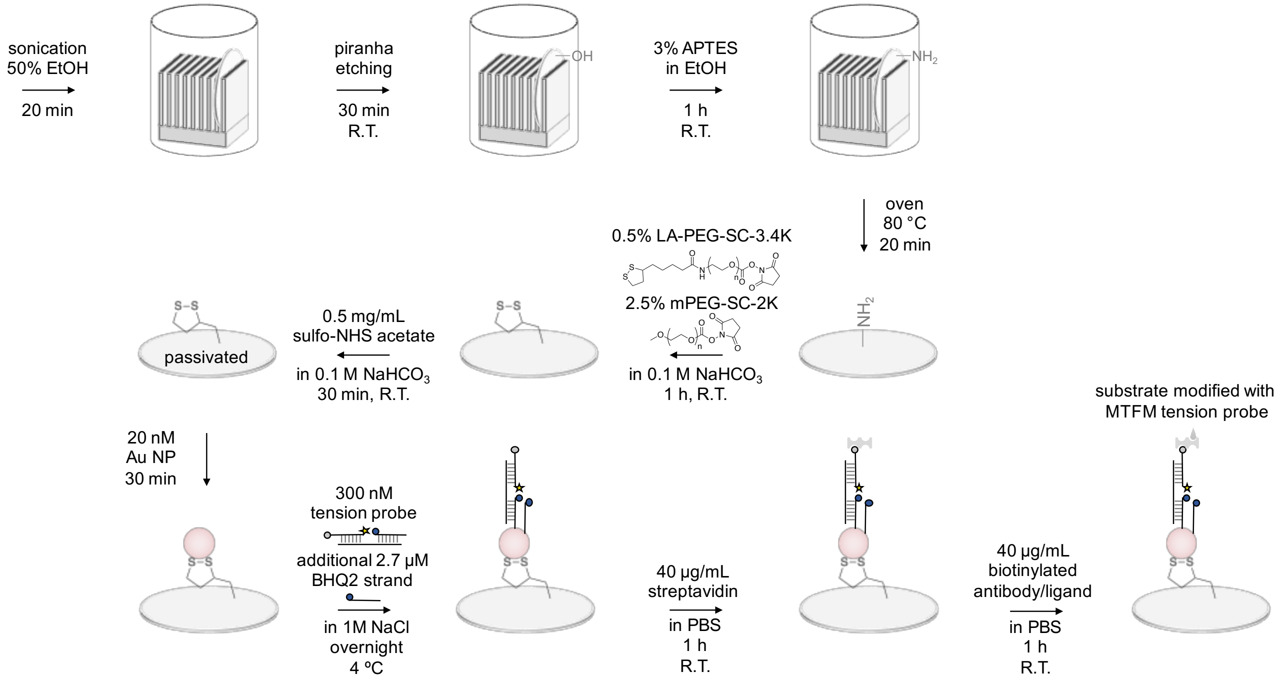

Figure A2.3. Characterization of the functionalized surfaces. (A) AFM image and (B) RICM and epifluorescence images of the surfaces functionalized with nanoparticle-MTFM probes. Scale bar = 10 µm. Density of gold nanoparticle on the surface was estimated to be 1000 ± 89 particles/µm^2 by automated particle counting using ImageJ (*n*=3 samples). Epifluorescence and RICM images show homogeneous coating of nanoparticle-MTFM probes on the surface.

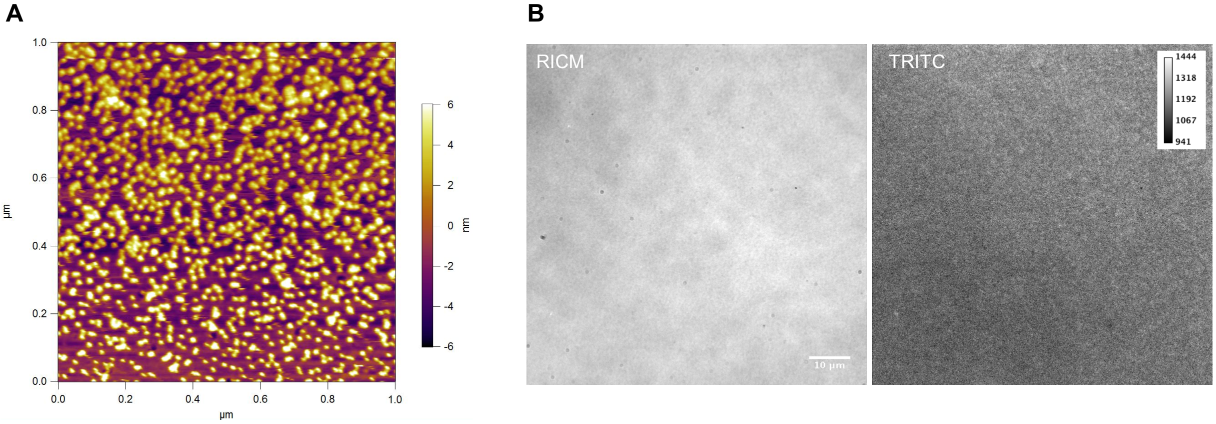

Figure A2.4. Testing different locking oligonucleotides. (A) Illustration of tension probe and locking oligonucleotides ranging from 13mer to 25mer, as well as duplex alignment after hybridization. The stem-loop region is indicated in blue, locking oligonucleotides are in black and the 17mer lock used in the present work is shown in red. The calculated *ΔG* values for hybridization are listed below each locking strand. The *ΔG* values were determined using IDT's nearest neighbor thermodynamic analysis with Na^+= 140 mM, Mg^{2+}= 0.2 mM at 25 °C. (B) Fluorescence measurements of in-situ hybridization kinetics between the immobilized MTFM probes and the locking oligonucleotides at 200 nM. Locking oligonucleotides were added to surfaces presenting the MTFM tension probes at room temperature and allowed to bind to the hairpin for >1 h. Hybridization was monitored by the increase in fluorescence due to hairpin opening. Among the locking oligonucleotides tested, we found that the 17mer displayed optimal hybridization to the MTFM probes.

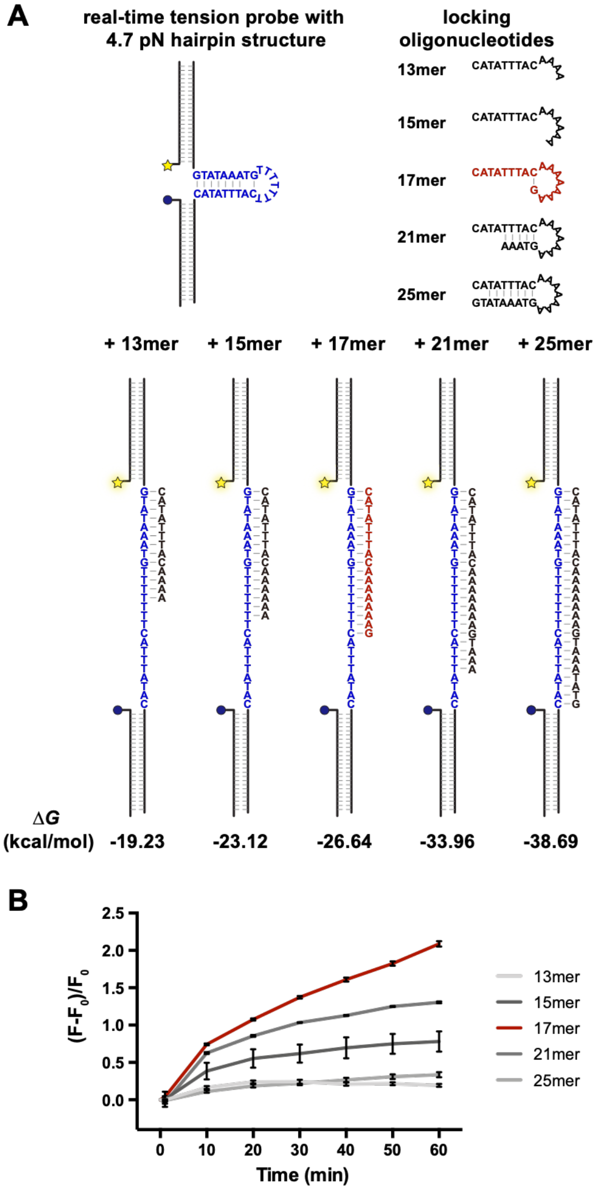

Figure A2.5. Characterizing locking strand hybridization kinetics. (A) Schematic of the engineered substrates presenting either an unstructured sequence (in red box) or a MTFM hairpin tension probes (in blue box). A 10-nt random region was incorporated in the unstructured sequence to reduce the quenching of Atto647N from gold particles after the binding. (B) TIRF microscopy measurements of in-situ hybridization kinetics of 200 nM of locking strand to the immobilized unstructured sequence (red) or MTFM hairpin tension probes (blue). Hybridization was monitored using the Atto647N fluorescence from the 17mer locking strand. The plot shows the average of 5 kinetic runs of 3 replicates. The error bars represent the SD, and the grey curves represent fitting curves. The binding to the unstructured sequence saturated in seconds and was normalized to the maximum fluorescence measurements. Although lock binding to hairpin probes did not saturate by 8 h, this was used to normalize the data and provide a conservative estimate of hybridization kinetics. Assuming pseudo first-order binding kinetics, we fit the data using one-phase association and obtained the $k_{\mathrm{obs}} = 0.22 \pm 0.09\ \mathrm{s}^{-1}$ (mean ± SD, R^2 = 0.9454, 0.8777, and 0.909 for three runs) and $4.5\times10^{-4} \pm 8.1\times10^{-5}\ \mathrm{s}^{-1}$ ((mean ± SD, R^2 = 0.964, 0.9531, and 0.9773 for three runs), which correspond to the k_{hyb} of ~$1.09\times10^{6}\ \mathrm{M}^{-1}\mathrm{s}^{-1}$ and ~$2.24\times10^{3}\ \mathrm{M}^{-1}\mathrm{s}^{-1}$ for the for unstructured and hairpin probe, respectively.

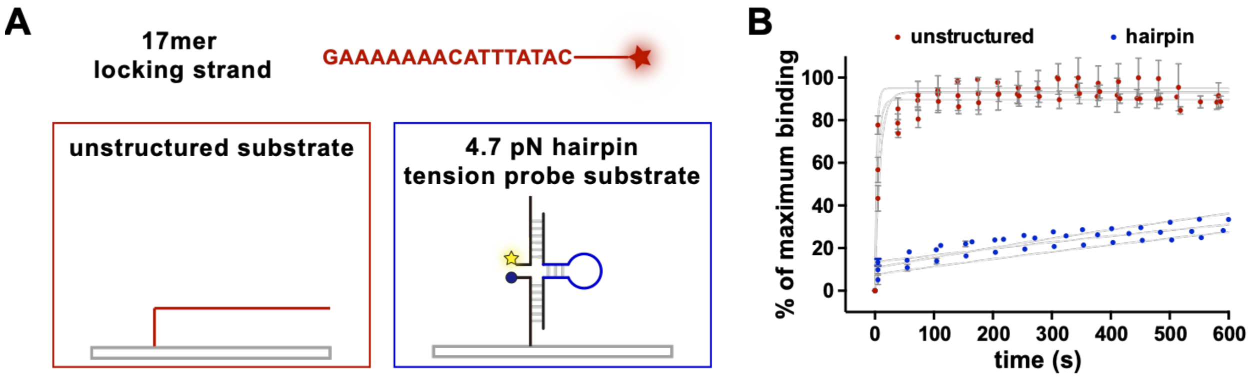

Figure A2.6. Toehold-mediated displacement reaction (unlocking). (A) Schematic shows unlocking of the probes via a toehold-mediated strand displacement reaction. (B) Fluorescence traces showing the kinetic profile of toehold-mediated strand displacement when the unlocking strand was held constant at 200 nM in a cell-free system. The MTFM tension probe was annealed with the locking strand (17mer) before immobilization onto the surface. (C) Fluorescence traces measuring the unlocking kinetics for cells incubated with 200 nM unlocking strand. Naïve OT-1 cells were allowed to produce tension against antiCD3ε on tension probe substrates. The mechanically opened probes were locked with 200 nM locking strand over 10 min. After rinsing away excess locking strand, the unlocking strand was added at a final concentration of 200 nM, and the tension signal for the same cells was measured as a function of time. The average fluorescence intensity within each cell was averaged from *n*=31 cells, and the error bars represent the standard deviation. The kinetics were assumed to be pseudo first-order, and was simplified and fitted into a one-phase association model. The observed rate constant k_{obs} was 0.066 ± 0.0039 s^{-1} (mean ± SD), R^2=0.8034.

The unlocking strand could potentially bind to one stem of the hairpin, but it is rather unfavorable. This is because the region of complementarity is only 9 bp long (ΔG = -12.06 kcal/mol at 140 mM Na^+). The T_m for this 9 bp duplex at these conditions is 13.9 °C (IDT Oligoanalyzer). Accordingly, this binding is not a significant concern in our current assay.

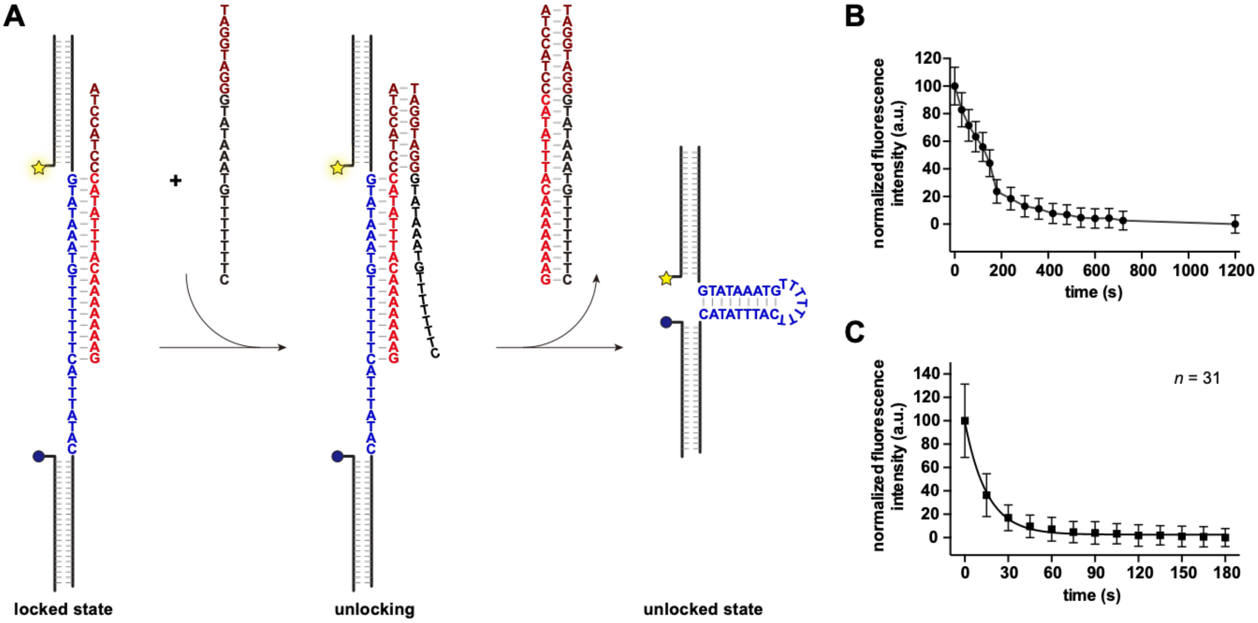

Figure A2.7. Controls testing specificity of locking and unlocking reactions. (A) Schematic of control where the stem-loop of the hairpin in the MTFM probe was scrambled. We assumed that the mechanical properties of the scrambled hairpin were similar to that of the original sequence [14]. Sequence shown in grey box was scrambled. (B) Fluorescence images of OT1 cells engaging antiCD3ε MTFM probes. The same cell was imaged before and after the addition of the locking strand. The mechanical hairpin openings were not accompanied by the locking signal. Only when the lock sequence is complementary to the hairpin can the tension signal be locked, thus demonstrating specificity of mechanically selective hybridization. Scale bar = 5 µm. (C) Linescan analysis from regions highlighted in images from (B) showing lack of co-localization between hairpin opening (Cy3B) and mechanically selective hybridization (Atto647N). (D) Schematic of experiment used to demonstrate the specificity of unlocking, where we introduced scrambled unlock sequences to the locked tension probe. Sequences shown in grey box were scrambled. We used two types of controls: the first had a scrambled the 17mer recognition region (scrambled unlocking1), while the second completely scrambled sequence (scrambled unlocking2). (E) Controls showing that the unlocking process was not triggered with the scrambled sequences. Only the sequence-specific complement and a toehold can initiate the unlocking. Scale bar = 5 µm. (F) Plots showing the quantitative tension signal measurements of cells in Cy3B and Atto647N channel (mean ± SD). Dunnett's multiple comparisons test using the locked signals as control showed no significant differences with or without the presence of scrambled unlocking strands.

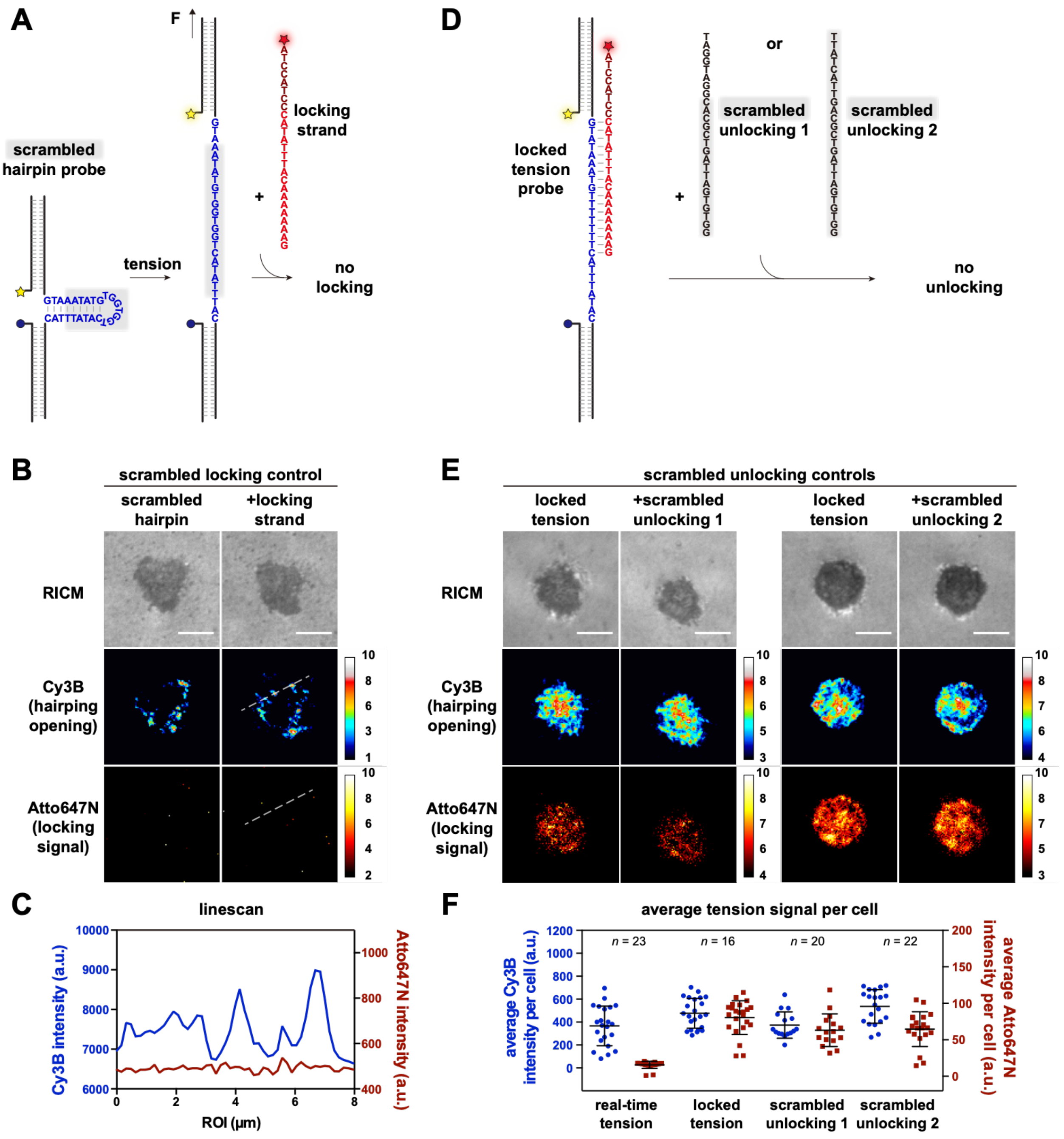
A
scrambled hairpin probe
GTAAATATG
TGGTGGT
CATTTATAC
tension
F
GTAAATATGTGGTGGTCATATTTAC
+
ATCCATCCCATATTTACAAAAAAAG
locking strand
no locking
D
locked tension probe
GTATAAATGTTTTTTCATTTATAC
ATCCATCCCATATTTACAAAAAAAG
+
TAGGTAGGCACGCTGATTAGTGTGG
scrambled unlocking 1
or
TTATCATTGACGCTGATTAGTGTGG
scrambled unlocking 2
no unlocking
B
scrambled locking control
scrambled hairpin
+locking strand
RICM
Cy3B (hairping opening)
Atto647N (locking signal)
10
8
6
3
1
10
8
6
4
2
E
scrambled unlocking controls
locked tension
+scrambled unlocking 1
locked tension
+scrambled unlocking 2
RICM
Cy3B (hairping opening)
Atto647N (locking signal)
10
8
6
5
3
10
8
7
6
4
10
8
7
6
4
10
8
7
5
3
C
linescan
Cy3B intensity (a.u.)
10000
9000
8000
7000
6000
Atto647N intensity (a.u.)
1000
800
600
400
0
2
4
6
8
ROI (µm)
F
average tension signal per cell
average Cy3B intensity per cell (a.u.)
1200
1000
800
600
400
200
0
average Atto647N intensity per cell (a.u.)
200
150
100
50
0
n = 23
n = 16
n = 20
n = 22
real-time tension
locked tension
scrambled unlocking 1
scrambled unlocking 2

Figure A2.8. Locked probe maintains tension signal after inhibiting actin polymerization. To demonstrate that the locked probe is irreversibly open; cells were treated with Latrunculin B to inhibit actin polymerization and ablate tension signal. Specifically, naïve OT-1 cells generating forces were incubated without (left panel) or with (right panel) 200 nM of locking strand for 10 min, washed and imaged, followed by 5 µM of latrunculin B treatment for 15 min. Cells were washed and imaged again in fresh cell imaging media. Latrunculin B treatment abolished most real-time tension signal, whereas locked probes maintained tension signal. This demonstrates that mechanically selective hybridization (with 17mer) is irreversible for the experimental time window tested. Scale bar = 5 µm.

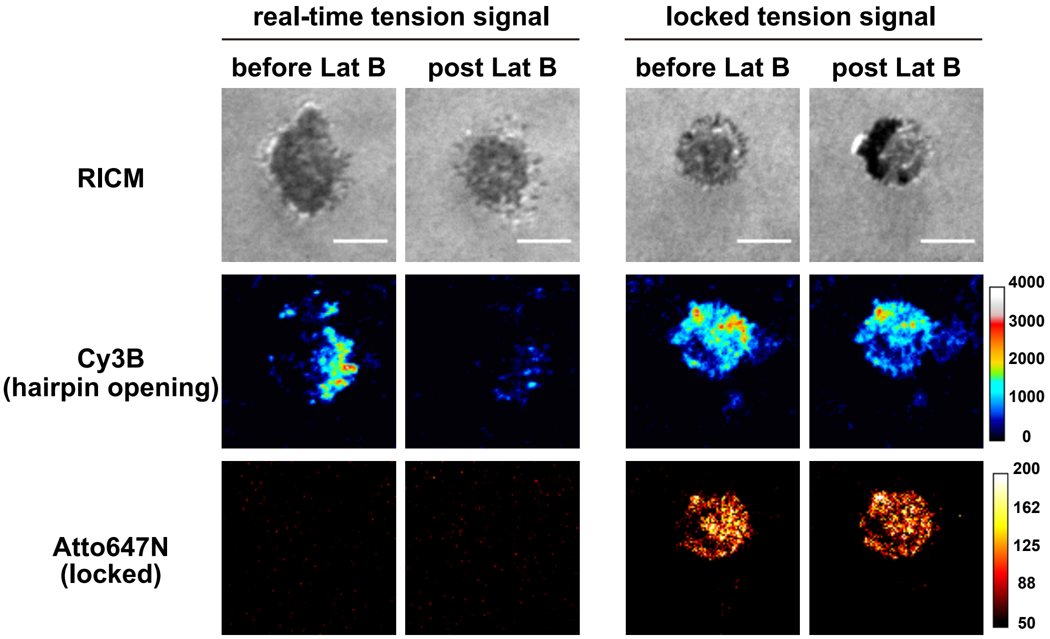

Figure A2.9. Radial profile analysis of TCR-pMHC N4 tension accumulation. (A) Radial profile analysis of tension accumulation in individual cells (*n*=16, from **Figure 2.3*A***). The central and peripheral region of the cells had higher accumulated tension signal. (B) The spatial distribution of locked tension signal is displayed using a heatmap, which shows how TCR-pMHC tension accumulates more frequently at the center and at the periphery of the junction. Moreover, the peripheral pulling zone seems to move inward while also expanding. (C) Radial profile analysis method.

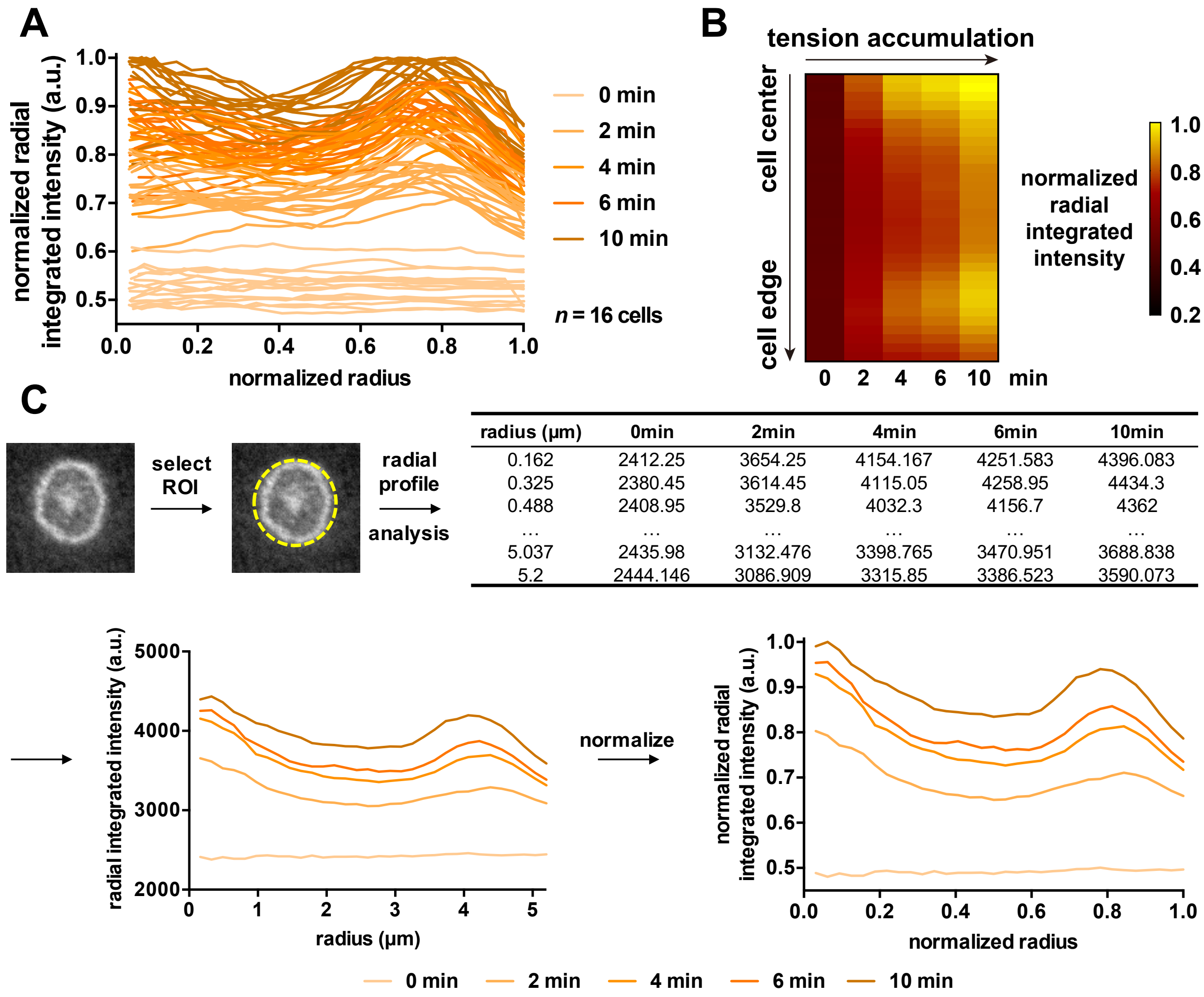

radius (μm)	0min	2min	4min	6min	10min
0.162	2412.25	3654.25	4154.167	4251.583	4396.083
0.325	2380.45	3614.45	4115.05	4258.95	4434.3
0.488	2408.95	3529.8	4032.3	4156.7	4362
…	…	…	…	…	…
5.037	2435.98	3132.476	3398.765	3470.951	3688.838
5.2	2444.146	3086.909	3315.85	3386.523	3590.073

Figure A2.10. Plots of integrated tension signal and tension occupancy for a panel of TCR ligands. Plots represent integrated tension signal (A) and tension occupancy (B) produced by the TCR in naïve OT-1 cells that were challenged with tension probes presenting antiCD3ε, pMHC N4, Q4, V4, and G4 in the real-time or locked state. Each plot displays data from at least 10 cells obtained from 3 different animals. Each data point represents the same cell that was imaged before and after locking. For Q4, V4, and G4, since the ligands were mutant and triggered weak activation and cell spreading, only cells that attached were analyzed. This represents a small sub-population of the total number of cells that were plated. This observation is consistent with previous reports [11]. Y-axis is displayed on a log scale for (A) integrated intensity, and a linear scale for (B) tension occupancy.

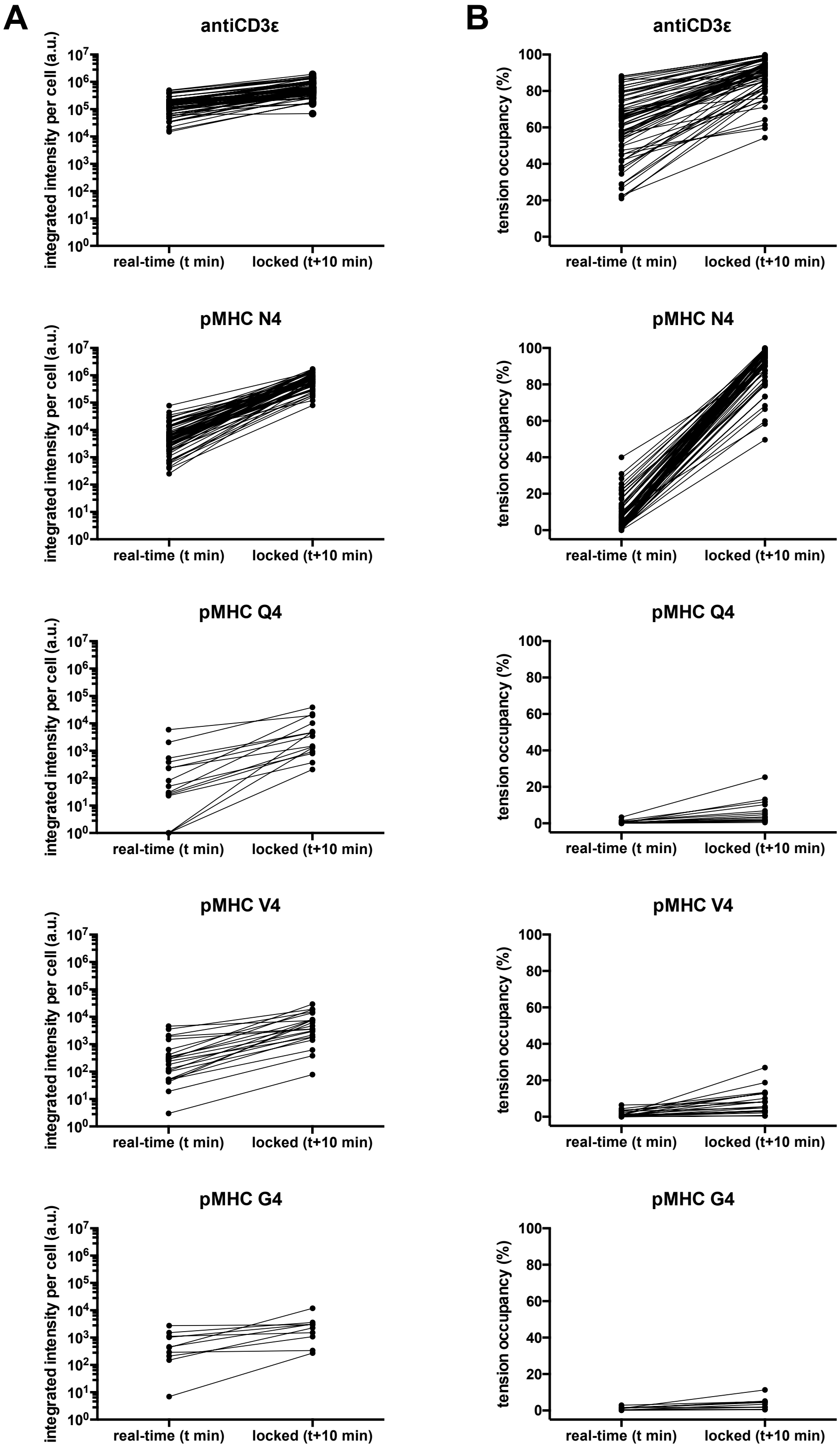
A
B
antiCD3ε
pMHC N4
pMHC Q4
pMHC V4
pMHC G4
integrated intensity per cell (a.u.)
10^0
10^1
10^2
10^3
10^4
10^5
10^6
10^7
tension occupancy (%)
0
20
40
60
80
100
real-time (t min)
locked (t+10 min)

Figure A2.11. Locking strategy reveals force transmission through the programmed cell death receptor 1 (PD1). (A) Integrated tension signal and (B) tension occupancy acquired from activated OT-1 against antiCD3ε, antiPD1, and mPDL2 in the real-time and locked state. The same cell was imaged before and after locking. Data in each group was acquired from >29 cells obtained from 3 mice. Y-axis is on a log scale for (A) integrated intensity and a linear scale for (B) tension occupancy.

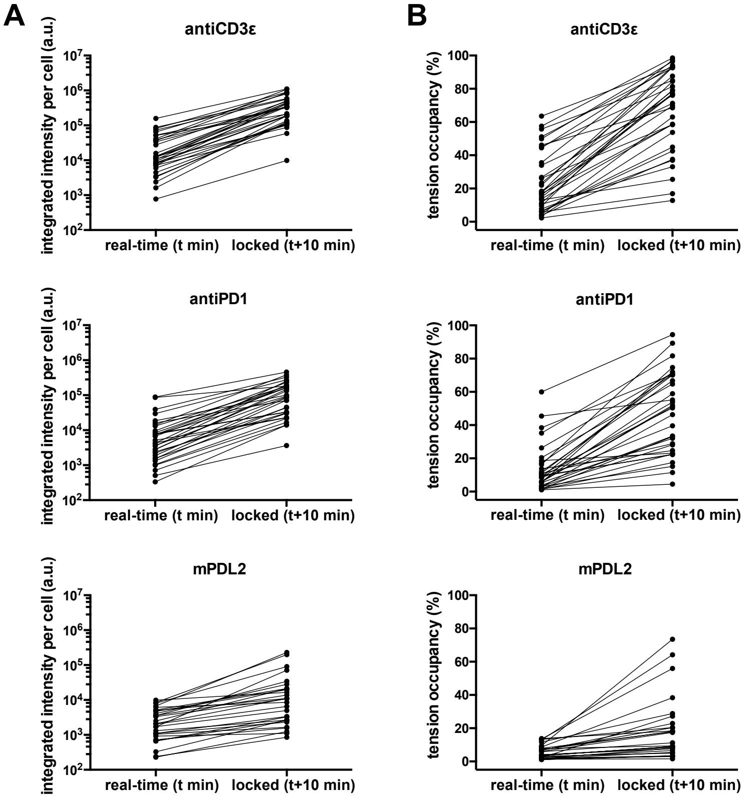

Figure A2.12. Representative raw data and flow chart illustrating data analysis procedure. All imaging data was processed with Fiji ImageJ software. (A) Raw representative data of the locked tension track (t = 10 min, [locking strand] = 200 nM) produced by migratory OT-1 cells on MTFM tension probe substrate co-presenting pMHC N4 and ICAM-1. Scale bar = 10 µm. (B) Raw representative RICM, TIRF and epifluorescence images showing TCR-pMHC N4 tension enhancement before and after locking. Note calibration bars are in different scale. Scale bar = 10 µm. (C) Raw representative RICM and TIRF images showing PD1-antiPD1 and PD1-mPDL2 hardly distinguishable real-time tension and enhanced locked tension produced by activated OT-1 cells. Scale bar = 10 µm. (D) TIRF image processing routine on a representative naïve OT-1 cell producing TCR tension against antiCD3ε. (Mean of background + 2×SD of background and mean of background + 3×SD of background were both used for thresholding in this paper.) (E) Quantitative image analysis routine to determine tension occupancy and integrated intensity of TCR-pMHC N4 tension signals produced by individual OT-1 cells.

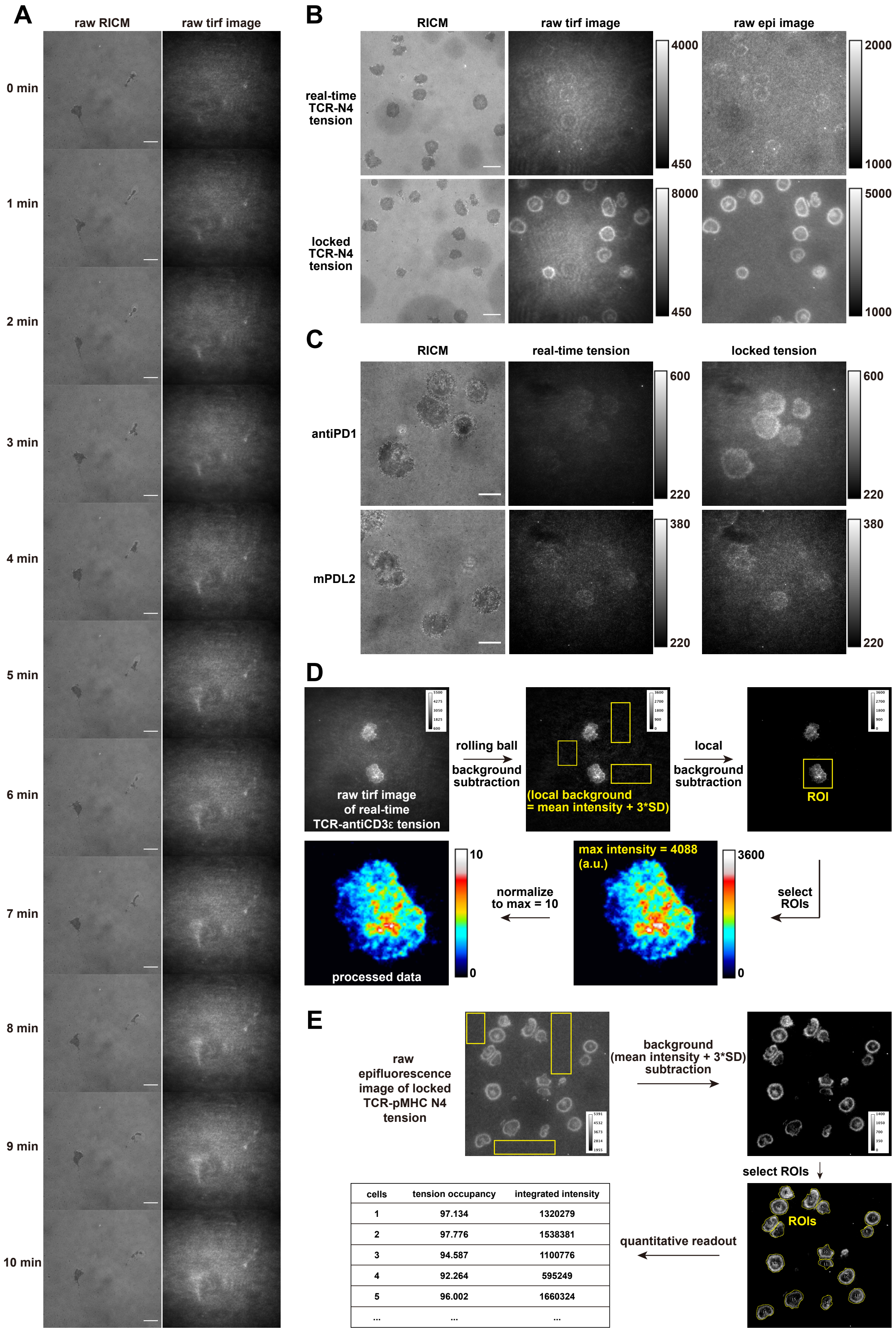

cells	tension occupancy	integrated intensity
1	97.134	1320279
2	97.776	1538381
3	94.587	1100776
4	92.264	595249
5	96.002	1660324
...	...	...

Movie A2.1. Erasing the stored mechanical information with the unlocking strand. Raw time-lapse of OT-1 cells showing the erasing of the stored mechanical information with the unlocking strand in 2 min. Locking strand signal in TIRF quickly diminished after 100 nM of unlocking strand was added to the system. Scale bar (in white) = 10 μm.

Movie A2.2. Erasing of stored mechanical information was not due to photobleaching of Atto647N dye on the locking strand. Raw time-lapse of showing a OT-1 cell with remained locking strand signal in TIRF under same exposure to laser as cells in **Movie S1** in 2 min. Scale bar (in white) = 10 μm.

Movie A2.3. Control showing failed unlocking with scrambled unlocking strand 1. A raw 2-min time-lapse of OT-1 cells showing with the addition of 100 nM of scrambled unlocking strand 1, the stored tension signal in TIRF was not erased. Scale bar (in white) = 10 μm.

Movie A2.4. Control showing failed unlocking with scrambled unlocking strand 2. A raw 2-min time-lapse of OT-1 cells showing with the addition of 100 nM of scrambled unlocking strand 2, the stored tension signal in TIRF was not erased. Scale bar (in white) = 10 μm.

Movie A2.5. Real-time TCR-pMHC N4 tension during the migration of an OT-1 cell. A 12-min time-lapse of RICM and TIRF showing a naïve OT-1 cell crawling over the substrate and producing transient tension when dimeric ICAM-1 was co-presented with pMHC N4. Note the TCR tension was highly dynamic and mostly located at the trailing edge. Scale bar = 10 μm.

2.7. References

1. D. R. Stabley; C. Jurchenko; S. S. Marshall; K. S. Salaita, Visualizing mechanical tension across membrane receptors with a fluorescent sensor. *Nat Methods* **2011,** *9* (1), 64.

2. Y. Liu; K. Galior; V. P. Ma; K. Salaita, Molecular Tension Probes for Imaging Forces at the Cell Surface. *Acc Chem Res* **2017,** *50* (12), 2915.

3. Y. Zhang; Y. Qiu; A. T. Blanchard; Y. Chang; J. M. Brockman; V. P.-Y. Ma; W. A. Lam; K. Salaita, Platelet integrins exhibit anisotropic mechanosensing and harness piconewton forces to mediate platelet aggregation. *Proc. Natl. Acad. Sci. USA* **2018,** *115* (2), 325.

4. Y. Liu; L. Blanchfield; V. P.-Y. Ma; R. Andargachew; K. Galior; Z. Liu; B. Evavold; K. Salaita, DNA-based nanoparticle tension sensors reveal that T-cell receptors transmit defined pN forces to their antigens for enhanced fidelity. *Proc. Natl. Acad. Sci. USA* **2016,** *113* (20), 5610.

5. K. M. Spillane; P. Tolar, B cell antigen extraction is regulated by physical properties of antigen-presenting cells. *J. Cell Biol.* **2017,** *216* (1), 217.

6. Y. Zhang; C. Ge; C. Zhu; K. Salaita, DNA-based digital tension probes reveal integrin forces during early cell adhesion. *Nat. Commun.* **2014,** *5*, 5167.

7. Y. Yin; X. S. Zhao, Kinetics and dynamics of DNA hybridization. *Acc. Chem. Res.* **2011,** *44* (11), 1172.

8. M. F. Juette; D. S. Terry; M. R. Wasserman; Z. Zhou; R. B. Altman; Q. Zheng; S. C. Blanchard, The bright future of single-molecule fluorescence imaging. *Curr. Opin. Chem. Biol.* **2014,** *20*, 103.

9. X. Wang; T. Ha, Defining single molecular forces required to activate integrin and notch signaling. *Science* **2013,** *340* (6135), 991.

10. B. Liu; W. Chen; B. D. Evavold; C. Zhu, Accumulation of dynamic catch bonds between TCR and agonist peptide-MHC triggers T cell signaling. *Cell* **2014,** *157* (2), 357.

11. J. Hong; C. Ge; P. Jothikumar; Z. Yuan; B. Liu; K. Bai; K. Li; W. Rittase; M. Shinzawa; Y. Zhang, A TCR mechanotransduction signaling loop induces negative selection in the thymus. *Nat. Immunol.* **2018,** *19* (12), 1379.

12. D. K. Das; Y. Feng; R. J. Mallis; X. Li; D. B. Keskin; R. E. Hussey; S. K. Brady; J. H. Wang; G. Wagner; E. L. Reinherz; M. J. Lang, Force-dependent transition in the T-cell receptor beta-subunit allosterically regulates peptide discrimination and pMHC bond lifetime. *Proc. Natl. Acad. Sci. U. S. A.* **2015,** *112* (5), 1517.

13. L. V. Sibener; R. A. Fernandes; E. M. Kolawole; C. B. Carbone; F. Liu; D. McAffee; M. E. Birnbaum; X. Yang; L. F. Su; W. Yu; S. Dong; M. H. Gee; K. M. Jude; M. M. Davis; J. T. Groves; W. A. Goddard, 3rd; J. R. Heath; B. D. Evavold; R. D. Vale; K. C. Garcia, Isolation of a Structural Mechanism for Uncoupling T Cell Receptor Signaling from Peptide-MHC Binding. *Cell* **2018,** *174* (3), 672.

14. M. T. Woodside; W. M. Behnke-Parks; K. Larizadeh; K. Travers; D. Herschlag; S. M. Block, Nanomechanical measurements of the sequence-dependent folding landscapes of single nucleic acid hairpins. *Proc. Natl. Acad. Sci. USA* **2006,** *103* (16), 6190.

15. B. L. Blakely; C. E. Dumelin; B. Trappmann; L. M. McGregor; C. K. Choi; P. C. Anthony; V. K. Duesterberg; B. M. Baker; S. M. Block; D. R. Liu; C. S. Chen, A DNA-based molecular probe for optically reporting cellular traction forces. *Nat Methods* **2014,** *11* (12), 1229.

16. S. R. Clarke; M. Barnden; C. Kurts; F. R. Carbone; J. F. Miller; W. R. Heath, Characterization of the ovalbumin-specific TCR transgenic line OT-I: MHC elements for positive and negative selection. *Immunol. Cell Biol.* **2000,** *78* (2), 110.

17. B. L. Walling; M. Kim, LFA-1 in T cell migration and differentiation. *Front. Immunol.* **2018,** *9*.

18. V. Mayya; E. Judokusumo; E. A. Shah; C. G. Peel; W. Neiswanger; D. Depoil; D. A. Blair; C. H. Wiggins; L. C. Kam; M. L. Dustin, Durable interactions of T cells with T cell receptor stimuli in the absence of a stable immunological synapse. *Cell Rep.* **2018,** *22* (2), 340.

19. G. A. Azar; F. Lemaître; E. A. Robey; P. Bousso, Subcellular dynamics of T cell immunological synapses and kinapses in lymph nodes. *Proc. Natl. Acad. Sci. USA* **2010,** *107* (8), 3675.

20. M. L. Dustin, T-cell activation through immunological synapses and kinapses. *Immunol. Rev.* **2008,** *221* (1), 77.

21. E. Cai; K. Marchuk; P. Beemiller; C. Beppler; M. G. Rubashkin; V. M. Weaver; A. Gerard; T.-L. Liu; B.-C. Chen; E. Betzig, Visualizing dynamic microvillar search and stabilization during ligand detection by T cells. *Science* **2017,** *356* (6338), eaal3118.

22. J. Huang; V. I. Zarnitsyna; B. Liu; L. J. Edwards; N. Jiang; B. D. Evavold; C. Zhu, The kinetics of two-dimensional TCR and pMHC interactions determine T-cell responsiveness. *Nature* **2010,** *464* (7290), 932.

23. C. Godinho-Silva; S. Marques; D. Fontinha; H. Veiga-Fernandes; P. G. Stevenson; J. P. Simas, Defining immune engagement thresholds for in vivo control of virus-driven lymphoproliferation. *PLoS Pathog.* **2014,** *10* (6), e1004220.

24. S. G. Oberle; L. Hanna-El-Daher; V. Chennupati; S. Enouz; S. Scherer; M. Prlic; D. Zehn, A minimum epitope overlap between infections strongly narrows the emerging T cell repertoire. *Cell Rep.* **2016,** *17* (3), 627.

25. A. H. Sharpe; K. E. Pauken, The diverse functions of the PD1 inhibitory pathway. *Nat. Rev. Immunol.* **2018,** *18* (3), 153.

26. E. Hui; J. Cheung; J. Zhu; X. Su; M. J. Taylor; H. A. Wallweber; D. K. Sasmal; J. Huang; J. M. Kim; I. Mellman, T cell costimulatory receptor CD28 is a primary target for PD-1–mediated inhibition. *Science* **2017,** *355* (6332), 1428.

27. K. Li; X. Cheng; A. Tilevik; S. J. Davis; C. Zhu, In situ and in silico kinetic analyses of programmed cell death-1 (PD-1) receptor, programmed cell death ligands, and B7-1 protein interaction network. *J. Biol. Chem.* **2017,** *292* (16), 6799.

28. I. Azoulay-Alfaguter; M. Strazza; A. Pedoeem; A. Mor, The coreceptor programmed death 1 inhibits T-cell adhesion by regulating Rap1. *J. Allergy Clin. Immunol.* **2015,** *135* (2), 564.

29. C. A. Hartzell; K. I. Jankowska; J. K. Burkhardt; R. S. Lewis, Calcium influx through CRAC channels controls actin organization and dynamics at the immune synapse. *eLife* **2016,** *5*.

30. T. N. Sims; T. J. Soos; H. S. Xenias; B. Dubin-Thaler; J. M. Hofman; J. C. Waite; T. O. Cameron; V. K. Thomas; R. Varma; C. H. Wiggins; M. P. Sheetz; D. R. Littman; M. L. Dustin,

Opposing effects of PKCtheta and WASp on symmetry breaking and relocation of the immunological synapse. *Cell* **2007,** *129* (4), 773.

31. Y. Gao; L. K. Wolf; R. M. Georgiadis, Secondary structure effects on DNA hybridization kinetics: a solution versus surface comparison. *Nucleic Acids Res.* **2006,** *34* (11), 3370.

32. J. X. Zhang; J. Z. Fang; W. Duan; L. R. Wu; A. W. Zhang; N. Dalchau; B. Yordanov; R. Petersen; A. Phillips; D. Y. Zhang, Predicting DNA hybridization kinetics from sequence. *Nat. Chem.* **2018,** *10* (1), 91.

33. K. D. Whitley; M. J. Comstock; Y. R. Chemla, Elasticity of the transition state for oligonucleotide hybridization. *Nucleic Acids Res.* **2016,** *45* (2), 547.

34. Z. Yang; G. Yuan; W. Zhai; J. Yan; H. Chen, The kinetics of force-dependent hybridization and strand-peeling of short DNA fragments. *Sci China Phys Mech.* **2016,** *59* (8), 680013.

Chapter 3. Investigating the TCR force regulatory network with DNA tension probes and ensemble measurement of TCR-pMHC force lifetime based on DNA hybridization kinetics

Partially adapted from Rong Ma, Anna V. Kellner, Yuesong Hu, Brendan R. Deal, Aaron T. Blanchard, Khalid Salaita. DNA Tension Probes to Map the Transient Piconewton Receptor Forces by Immune Cells. J. Vis. Exp. Mar 20, 2021, 169, e62348.

3.1. Introduction

Immune cells defend against pathogens and cancer cells by crawling across the surfaces of target cells, continuously scanning for antigens on the target cell surface. Recognition of the antigen is mediated by binding between the T cell receptor (TCR) and the peptide-major histocompatibility complex MHC (pMHC) expressed on the surface of target cells [1]. Because TCR-pMHC recognition occurs at the junction between two mobile cells, it has long been hypothesized that this interaction experiences mechanical forces. Moreover, this hypothesis led to the mechano-sensor model of T cell activation, which suggests that the TCR forces also contribute to its function [2-3]. Studies using traction force microscopy and micropillar arrays have observed traction forces in T cells, which are correlated with the functional output, such as target cell killing in cytotoxic T cells [4]. Complementing these bulk methods, single molecule force spectroscopy studies with molecular-level resolution have shown that the TCR triggering is very sensitive to two key components: the magnitude and the duration of the TCR-pMHC binding under force [5]. The unmatched sensitivity offered by these methods suggest strong correlation between the TCR-pMHC bond lifetimes and T cell activation, especially the lifetimes when ~10 pN of force was applied to T cells. However, this force is externally applied to a single TCR-pMHC binding, with an experimenter actively manipulating the magnitude and loading rate of the force, and thus does not fully capture what the T cells do when encountering antigens in a biological setting.

To visualize molecular TCR forces generated by T cells, our lab pioneered the development of DNA-based hairpin tension probes, which use fluorophore-quencher pairs to report on the mechanical extension and unfolding of DNA hairpins under force (closed and open state, **Figure 3.1A**) [6]. Briefly, a DNA hairpin is hybridized to a fluorescent ligand strand on one arm and a quencher anchor strand on the other arm, and then immobilized on a glass substrate. In the absence of mechanical force, the hairpin is closed, and thus the fluorescence is quenched. However, when a mechanical force greater than the $F_{1/2}$ (the force at equilibrium that leads to a 50% probability of unfolding) is applied, the hairpin mechanically melts, and a fluorescent signal is generated. This DNA-based tension probe provides high signal to noise ratio and force sensitivity, which is easily tuned from a few pN up to ~20 pN, and maps the tension in real-time [7]. This technology revealed that the T cells generate defined forces (<19 pN) through TCR to mechanically challenge its antigen [6]. We further improved the force detection of this technology by building a mechanical information storing DNA-based tension probe (locked state, **Figure 3.1A**) [8]. When a DNA tension probe is mechanically unfolded, it exposes a cryptic binding site. With the addition of a complementary lock oligonucleotide that preferably and irreversibly binds to the cryptic site, the mechanically unfolded hairpins are locked open and allow the fluorescent tension signal to accumulate for facile tension mapping (**Figure 3.1A, Figure A3.1A**) [8]. With this upgrade, transient TCR forces > 4.7 pN against altered peptide ligands were visualized and were found to be correlated with the ligand potency.

Given that single-molecule force spectroscopy studies predict that the TCR-pMHC lifetime under force is a critical parameter in the T cell response, it is highly desirable to develop tools that can measure the innate TCR force durations when T cells actively engage antigenic peptides. In principle, one may be able to determine force duration using single molecule methods, but this may not be possible given the dynamic nature of TCR forces and the reported need for TCR microclusters formation to drive T cell triggering.

To tackle this challenge, we sought to find and use a relatively more understood and characterized kinetic reference to measure the time duration of receptor forces. Building on the mechanical information storing DNA probes, we decided to employ DNA hybridization kinetics as the benchmark for TCR force lifetime. Given the simple rules of DNA base-pairing, the intensive studies on DNA hybridization kinetics, and the fast rate (~10^6 $M^{-1}s^{-1}$), DNA hybridization kinetics is an ideal benchmark to study the short durations of mechanical forces applied by T cells [9-10].

The principal concept in the mechanical information storing DNA probes is that a lock oligonucleotide selectively and irreversibly hybridizes to a DNA hairpin while a DNA hairpin is unfolded by a force greater than 4.7 pN. For a lock oligo to bind the cryptic site at appreciable rates and with high probability, hybridization must be fast enough to occur before the force is terminated and the DNA hairpin refolds (k_{close}) and rapidly hides the cryptic binding site within microseconds. According to pseudo first-order kinetics, the rate of locking k_{lock} is proportional to the lock oligonucleotide concentration and the hybridization on-rate constant. Thus, by titrating the concentration of the lock, one can precisely tune the hybridization rate and the time it takes the lock to hybridize to mechanically opened hairpins ($1/k_{\mathrm{lock}}$). Therefore, since locking probability significantly increases when $1/k_{\mathrm{lock}}$ is faster than $1/k_{\mathrm{close}}$ and since $1/k_{\mathrm{lock}}$ is easily tuned by changing the lock concentration, the rate and degree of locking at different concentrations can be used to derive the k_{close} (**Figure 3.1C**). When T cells pull on the DNA hairpins, the duration of hairpin opening is essentially the force duration, since the hairpin refolding time (~microseconds) is negligible compared to the range of TCR-pMHC bond lifetimes (~milliseconds to seconds) reported from single-molecule force spectroscopy measurements [11]. Therefore, the k_{close} that can be derived from locking kinetics is equivalent to TCR force off-rate, and the TCR force duration $\tau_{\mathrm{force}} = 1/k_{\mathrm{close}}$.

In this paper, we describe the establishment and application of this method to measure the TCR force kinetics in OT-1 $CD8^+$ T cells (**Figure 3.1D**). As a proof-of-concept, we estimate the force lifetimes for TCR forces applied on antiCD3ε, the cognate antigen pMHC N4, as well as an altered peptide ligand pMHC Q4. Furthermore, we applied this method to investigate the effect of co-receptor engagement on TCR force lifetime, by co-presenting either the adhesion molecule Intercellular Adhesion Molecule 1 (ICAM-1) to Lymphocyte function-associated antigen 1 (LFA-1), or a co-stimulatory ligand B7-1 to CD28. Moreover, we also applied this method to investigate the cytoskeletal contribution to TCR forces and their duration. We find that the force against antiCD3ε has the longest lifetime (29 ± 3.9 s), whereas the TCR-pMHC N4 force has an average lifetime of 6.8 ± 0.9 s and the TCR-pMHC Q4 has an average lifetime around 0.1 s. With the engagement of LFA-1-ICAM-1 interaction at the cell-substrate junction, the TCR force off-rate becomes slightly faster, resulting in a shorter TCR force lifetime (3.2 ± 0.5 s). With the engagement of CD28-B7-1 interaction, TCR samples pMHC N4 more frequently (increased force on-rate), with a lifetime decreased to 1.4 ± 0.3 s. When the cytoskeleton network was disrupted with small molecule inhibitors, we observed no significant changes in force on-rate and force lifetime at the whole cell level, however, we did notice spatial difference in the force accumulation upon inhibition of different networks. Taken together, we developed a method based on DNA nanotechnology that is complementary to single-molecule force spectroscopy to evaluate the TCR force kinetics and applied it to reveal the effect of different pathways in TCR force regulation.

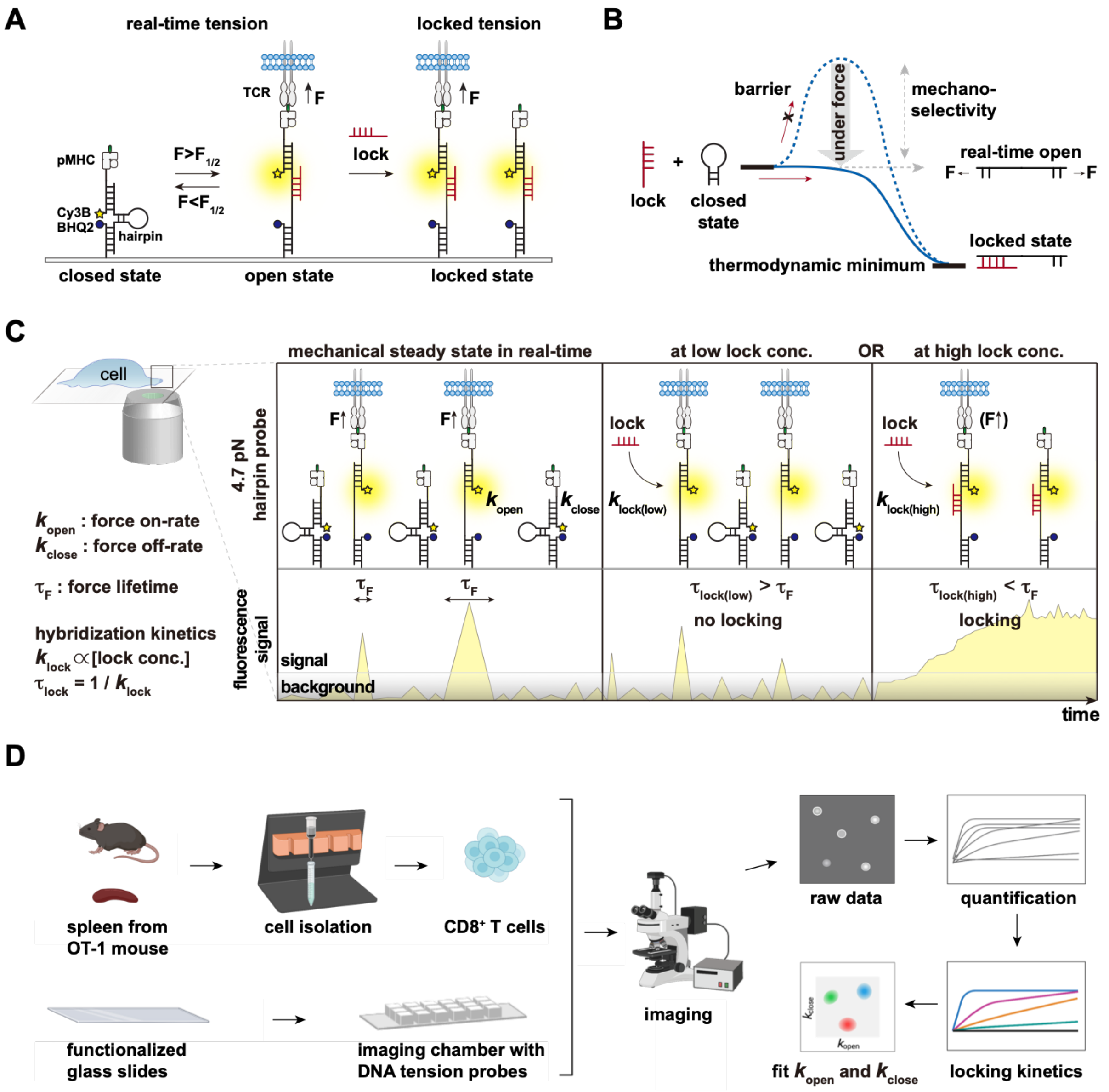

Figure 3.1. Schematics and workflow of the force lifetime ensemble measurements. Scheme showing the concept of using hybridization kinetics as a kinetic reference to measure force lifetimes. (A) Schematic shows the closed and open states of a DNA hairpin probe when the lock is absent. As the lock binds to the mechanically opened hairpin, the hairpin stays in the open state. (B) Energy diagram shows that the force removes the energy barrier and facilitates the selective hybridization. (C) Schematic showing the principle of the approach. When a T cell is imaged under a microscope, the TCR force pulls open the hairpin probes when the F > 4.7 pN; and when the force terminates, the hairpin refolds. The k_{open} represents the force on-rate and k_{close} represents the force off-rate. The duration of the force is $\tau_F = 1/ k_{close}$. If the lock is added at low concentration, due to hybridization kinetics, the rate it binds to the cryptic binding site on the hairpin is slower than the rate of force off-rate, which would result in no locking. If the lock is added at high concentration, the rate for it to bind is faster that the rate of force off-rate, which would result in

locking and signal accumulation as the cells pull on more ligands. (D) Workflow of the force lifetime ensemble measurements.

3.2. Establishing a model that describes the system

DNA hairpins can be treated as digital switches that are either in the opened or closed conformation (two-state system) [12]. In the specific context of DNA hairpin-based tension sensors, the hairpins exist primarily in the fluorescent opened state when $F > F_{1/2}$ and exist primarily in the quenched closed state when $F < F_{1/2}$. At $F = F_{1/2}$, the hairpins spend equal amounts of time in the closed and opened states. The reversible transitions between opened (O) and closed states (C) can be described using the first-order rate constants k_{open} and k_{close}. The constant k_{open} represents force-mediated transitions of probes from a closed state to an opened state and depends on many factors including the rate of association between TCR and tension probe ligands, the surface density of receptors on the cell membrane, and the loading rate of the cellular machinery. The constant k_{close} represents the transition of probes from an opened state to a closed state, which can be caused by either 1) rupture of the receptor ligand bond, or 2) decrease in F below $F_{1/2}$ without ligand rupture. Accordingly, the inverse of k_{close} can be described as the force lifetime, τ_{force} (note this definition is different than bond lifetime). The introduction of a locking strand causes opened strands to irreversibly transition to a locked state (L) in a lock concentration-dependent manner with a first order rate constant k_{lock}. This whole process is a two-step chemical reaction with a reversible first step, which can be described as:

$$C \underset{k_{close}}{\overset{k_{open}}{\rightleftharpoons}} O \overset{k_{lock}}{\rightarrow} L.$$

We use this chemical equation to derive an equation for fluorescence intensity as a function of time. Importantly, this derivation only works under the condition of a mechanical steady state

(**Figure A3.1C**), meaning the k_{open}, k_{close}, and k_{lock} are constant in time such that the chemical equation can accurately describe the population of tension probes as a function of time. Physically this assumption means that the ensemble interaction between the cell and the DNA tension probe substrate via receptor-ligand binding is constant throughout the duration of acquisitions; all physical properties that govern k_{open}, k_{close}, and k_{lock}, including receptor and ligand density, receptor-ligand association rate, the concentration of locking strand beneath the cell, and the force loading rate, are all constant in time. At mechanical steady state, at t = 0 (before locking), the initial fractions of probes in the opened and closed states (denoted O_0 and C_0 respectively) has already reached a pseudo-equilibrium such that $O_0/C_0 = k_{open}/k_{close}$.

According to the chemical equation defined above, the analytical solution for the rate of reaction can be described using a form derived by previous literature [13] and rearranged to

$$I_f = \frac{k_{close}}{k_{open}}\left(1 - \frac{\left(1-\frac{(k_C-2k_{open})}{\sqrt{-\Delta_C}}\right)}{2}\mathrm{e}^{\frac{(\sqrt{-\Delta_C}-k_F)}{2}t} + \frac{\left(1+\frac{(k_C-2k_{open})}{\sqrt{-\Delta_C}}\right)}{2}\mathrm{e}^{\frac{(-\sqrt{-\Delta_C}-k_F)}{2}t}\right) \qquad (1),$$

where $k_F = k_{open} + k_{close} + k_{lock}$, $k_c = k_{open} - k_{close} - k_{lock}$, $\Delta_c = \sqrt{-k_c{}^2 - 4k_{open}k_{close}}$.

In this way the rate of reaction can be described by I_f, the fold-increase in fluorescence intensity from the DNA tension probes. By fitting equation (1) to locking time-lapse series acquired at different concentrations, we can drive k_{open}, k_{close}, and k_{lock} (see method for deriving the analytical equation). We tested whether our model describes this chemical reaction by plugging in mock values of k_{open} and k_{close}, and k_{lock} to predict the locking kinetics (**Figure A3.2**). Assuming the lock rate constant k_{lock} is 1.09×10^{6} $\text{M}^{-1}\text{s}^{-1}$ [8-9], we obtained the locking kinetics with 6 different lock concentrations ranging from 5 µM to 0 µM while k_{open} and k_{close} are varied. When the k_{open} is fixed at 0.01 s^{-1}, and k_{close} is varied from 0.05 s^{-1} to 5 s^{-1}, our model predicted the fold increase in integrated fluorescence intensity would vary from around 5 up to hundreds (**Figure A3.2A**). At 0.05 s^{-1}, the model predicts that all the concentrations of locks would have similar level of locking kinetics, whereas at 5 s^{-1}, the 5 μM lock would generate highest level of locking over time and the lower concentrations of the lock would have minimal fold-increase compare to the high concentrations. This prediction is also reflected as we plot the predicted fold-increase in fluorescence intensity versus concentration, which the longer lifetimes of the force would generate locking signal profiles that saturate at lower concentrations comparing to shorter lifetimes. When the k_{close} is fixed at 0.5 s^{-1}, and k_{open} is varied from 0.05 s^{-1} to 0.002 s^{-1}, our model predicted the fold increase in integrated fluorescence intensity would vary from around 10 to over a hundred with little or distinct resolution between different concentrations (**Figure A3.2B**). With this model established, next we acquired experimental data of TCR tension signal locking kinetics with OT-1 naïve $CD8^+$ T cells for model fit and analysis.

3.3. Results and Discussion

3.3.1. TCR force lifetime measurement with antiCD3ε, pMHC N4 and pMHC Q4

As a proof of concept, we first applied this method to antiCD3ε, the cognate peptide ligand for the OT-1 system, the ovalbumin peptide pMHC N4 (SII<u>N</u>FEKL), and an altered peptide ligand pMHC Q4 (SII<u>Q</u>FEKL). Briefly, DNA tension probes were prepared (**Figure A3.3**) and functionalized on a glass coverslip, and the coverslip was attached to multi-well imaging chambers (**Figure A3.4**). The tension probes were then conjugated to a ligand to present either antiCD3ε, pMHC N4, or pMHC Q4. The $CD8^+$ naïve T cells were isolated from OT-1 mouse spleens and allowed to attach and spread on DNA tension probes ($F_{1/2}$ = 4.7 pN) substrate for 30 min (**Figure 3.1D**). Tension signals were first imaged in real-time with a fluorescence microscope to confirm that the cells reached mechanical steady state (**Figure A3.1C**). Before adding the lock, the tension profile for OT-1 cells on antiCD3ε was the strongest among the three, and the OT-1 cells on pMHC Q4 DNA tension probes generated very weak real-time tension signal, which is consistent with what we have observed previously [8]. Next, as an initial proof-of-concept, Atto647N labeled lock oligonucleotide was added to the cells and colocalization analysis of the Cy3B tension signal and Atto647N lock signal was performed to confirm that the lock hybridized selectively to the mechanically opened hairpins (**Figure A3.1**).

The unlabeled lock was then introduced to cells at 0, 50 nM, 100 nM, 500 nM, 1 µM, and 5 µM in parallel wells. Next, time-lapses were acquired as the lock hybridized to the mechanically unfolded hairpin probes (**Figure 3.2A, Figure A3.5, Movie A3.1**). Upon addition of the lock, the tension signals were accumulated in cells on antiCD3ε, pMHC N4 and pMHC Q4, each revealing distinct tension accumulation characteristics. For force against antiCD3ε, there was less significant differences for the accumulation from a lower lock concentration to higher concentration. However, TCR force against the pMHC N4 showed a dramatic difference in the accumulated tension signals at different concentrations (**Figure 3.2B, Figure A3.5**, **Movie A3.2**). For force against pMHC Q4, only high concentrations of the lock resulted in substantial signal accumulation (**Figure 3.2B, Figure A3.5, Movie A3.3**). The signal accumulation profile was plotted by extracting raw integrated intensity of the tension signal per cell in the time-lapses, (**Figure A3.6A**) and normalizing to the real-time signal of the same cell (t=0 min) for quantitative analysis (**Figure A3.6B**). Locking kinetics in **Figure 3.2C** shows the average locked/real-time tension per cell from three mice at each concentration of the lock with antiCD3ε, pMHC N4, or pMHC Q4. The locked/real-time tension of TCR forces against antiCD3ε saturated at a low concentration of ~0.5 µM lock, whereas for the forces against pMHC N4, the locked/real-time tension started saturating at higher concentrations of the lock, ~5 μM. For forces against pMHC Q4, there was no saturation observed, even at 5 μM of the lock. Since the binding between CD3ε and antiCD3ε (clone: 2C11) is usually considered to have a higher affinity compared to TCR-pMHC binding, it is likely that the relatively slower binding off-rate would result in less mechanical resampling, which is reflected in the smallest fold-increase of tension signal. The TCR-pMHC N4 has a much higher fold increase in intensity followed by Q4, consistent with what we observed before [4]. Unlike antiCD3 ε and pMHC N4, from the quantitative analysis, TCR-pMHC Q4 forces did not accumulate with 0.05 μM lock, implying the force off-rate is fast enough that the lock failed to bind with the necessary rate at 0.05 μM.

Overall, the experimental locking kinetic profiles agreed very well with the trend of the locking kinetics predicted by our model (**Figure A3.2**). Next, we fit the experimental data using our model, and derived the force kinetic parameters for antiCD3ε, pMHC N4, and pMHC Q4. Note that the k_{open}, k_{close}, and k_{lock} values that are obtained from the model report the mean of hundreds of bootstrapping iteratives of sampling hundreds of cells from the locking profiles in each condition (**Figure 3.2E, F Figure A3.7**). We find that the forces exerted to antiCD3ε have an average force lifetime of 29 ± 3.9 s, whereas TCR forces against pMHC N4 have an average force lifetime of 6.8 ± 0.9 s (**Figure 3.2E, F, Figure A3.7**). According to the single-molecule force spectroscopy studies, the bond lifetimes for pMHC Q4 (independent of CD8-MHC binding) is only slightly shorter compared to N4 at 10 pN [5]. However, in our measurement, with the MHC-CD8 binding, the TCR forces against Q4 has an average lifetime that is around 0.1 s. Note that the fitted data is obtained from 5 and 7 mice for antiCD3ε and pMHC N4, respectively. While the locking kinetics profile with Q4 was obtained and averaged from data collected with 3 mice, we were only able to fit with data collected from 1 mouse. This is because the Q4 dataset did not show the trend of saturation, which made the model fit poorly constrained.

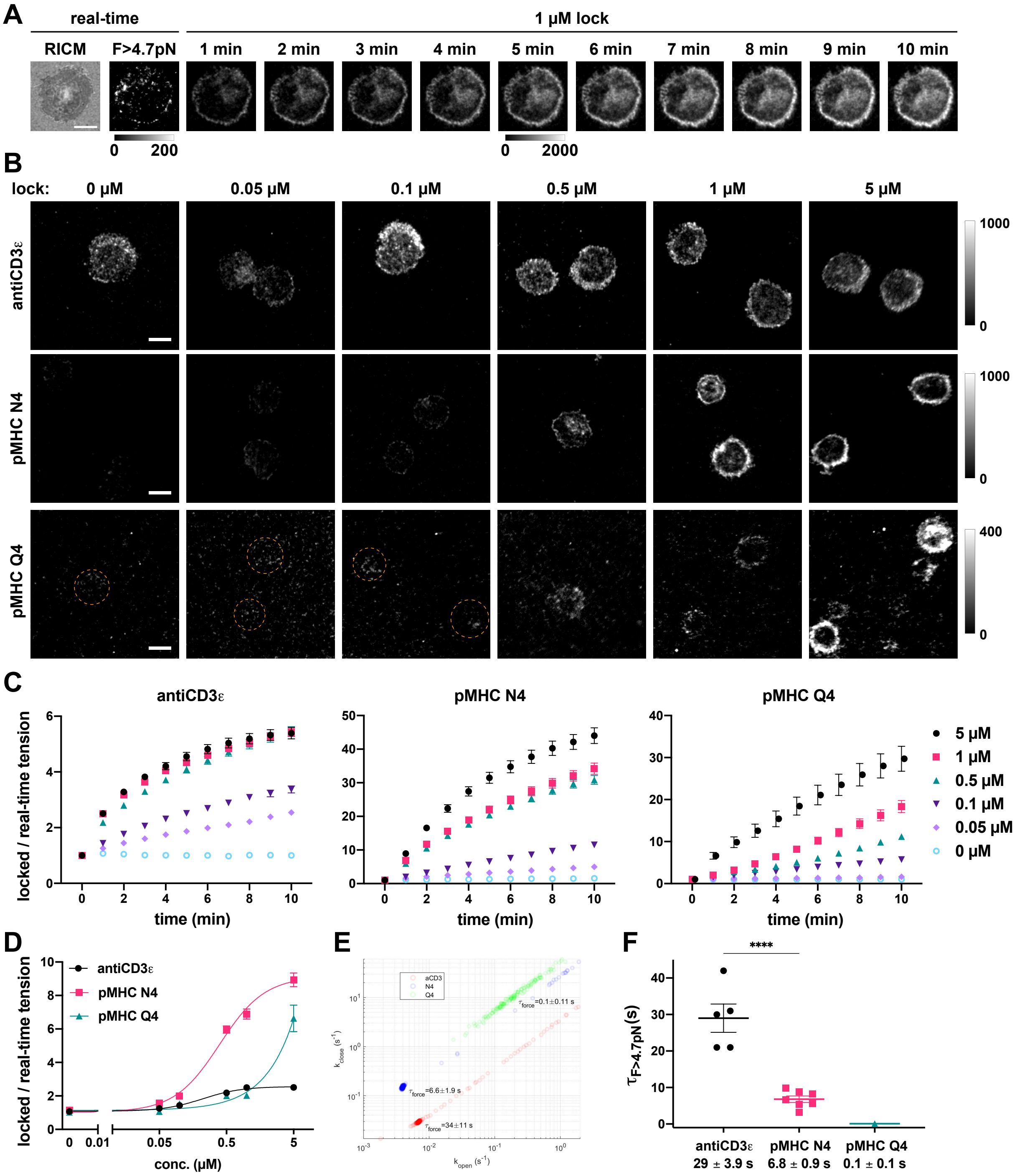

Figure 3.2. Force lifetime measurements with antiCD3e, cognate antigen pMHC N4, and altered peptide ligand pMHC Q4. (A) Representative microscopy images of an OT-1 CD8$^+$ naïve T cell producing tension signal against pMHC N4 on a DNA hairpin tension probe substrate.

Time lapse images show the significant tension signal accumulation in Cy3B channel after the addition of 1 μM 15mer lock. (B) Representative microscopy images of tension signal produced by OT-1 $CD8^+$ naïve T cells on tension probe substrates presenting antiCD3ε, pMHC N4, and pMHC Q4 in real-time (0 μM) and at different lock concentrations (0.05, 0.1, 0.5, 1, 5 μM) after incubating with the lock for 1 min. (C) Locking kinetics of TCR forces applied by OT-1 CD8+ naïve T cells to antiCD3ε, pMHC N4, and pMHC Q4, represented by locked/real-time integrated intensity of tension signal per cell (mean ± SEM). Data shows the average from 99-268 cells from 3 mice per concentration for each condition. (D) Locked/real-time tension per cell vs. concentration of lock with different ligands after 1 min of locking. Data shows the average from 99-268 cells from 3 mice per concentration for each condition. (E) Representative model fit of the locking kinetics to derive the k_{open}, k_{close} and τ_{force}. (F) TCR force lifetime measurements (mean ± SEM) for antiCD3ε (5 mice), pMHC N4 (7 mice), and pMHC Q4 (1 mouse) from model fit. Statistical analysis to quantify significant differences between antiCD3ε and pMHC N4 was performed with Student *t*-test (**** $P < 0.0001$).

3.3.2. Effect of co-receptor engagement on TCR force and force lifetimes

As the T cell activation upon TCR triggering is delicately dictated by multiple receptors acting cooperatively, we sought to investigate whether the engagement of other co-receptors would affect the lifetimes of TCR forces (**Figure 3.3A**). Since CD28 is a critical co-stimulatory receptor upon binding to its ligand B7-1 or B7-2 [14], we suspected that the engagement of CD28 would affect the TCR forces, including their on-rate and lifetime [15]. Another co-receptor on T cell surfaces that we suspected was involved in tuning the TCR force kinetics is LFA-1. LFA-1 binds to the adhesion molecule ICAM-1 and facilitates adhesion and migration and has been suspected of involvement in mechanical crosstalk with TCR [16]. A previous report using conventional DNA hairpin probes ($F_{1/2}$ = 19 pN) showed that the LFA-1-ICAM-1 binding can slightly increase the magnitude of TCR-pMHC forces. Without LFA-1 engagement, OT-1 $CD8^+$ naïve T cells failed to generate TCR forces greater than 19 pN, but with LFA-1 engagement, TCR tension signal that was greater than 19 pN can be observed at the focal zone [6]. Therefore, we sought to further investigate the impact of ICAM-1 and pMHC co-presentation on the force by measuring the force lifetime.

In order to examine the TCR force signal with co-receptor engagement, we engineered our DNA tension probe substrate so that it can present the co-receptor ligands directly on the gold particle surface, orthogonal to the pMHC on the tension probes, to avoid any signal interference (**Figure A3.8**). The OT-1 CD8$^+$ naïve T cells were isolated and plated onto the pMHC N4 DNA tension probe substrates co-presenting either B7-1 or ICAM-1 and allowed to spread for 30 min. Once the majority of cells reached mechanical steady state, the force transmitted through TCR to pMHC N4 was imaged before and after the addition of the lock in parallel wells. Time-lapses of tension signal accumulation were then acquired to obtain the locking kinetics.

The results show that real-time TCR force tension signal with the presence of CD28-B7-1 interaction was sparser compared to that without CD28-B7-1 interaction and mostly located at the periphery of the cell, forming a clear ring pattern (0 min, **Figure A3.9A**). Moreover, both the real-time tension area and contact area decreased compared to cells on pMHC N4 only (**Figure A3.10**). In contrast, cells on substrates that allowed LFA-1-ICAM-1 interaction showed a highly migratory phenotype (RICM, **Figure A3.9B**), with a larger cumulative (over 10 min) contact area but decreased tension area (**Figure A3.10**). The real-time tension was mostly located at the focal zone of the migrating cells (0 min, **Figure A3.9B**), in agreement with a previous report [6]. Quantitative analysis of cells on the substrate co-presenting B7-1 or ICAM-1 both showed decreased integrated intensity of real-time tension compared to cells on a substrate that only presented pMHC N4 (**Figure 3.3B**).

The locking kinetics of the TCR forces were extracted and normalized from the time-lapses (**Figure A3.11**). The average fold-increase of tension signal for TCR forces with CD28 engagement was over a hundred at the high concentrations of the lock after 10 minutes, in stark contrast to the minimal fold-increase at 0.05 μM, implying the TCR force off-rate mostly outcompeted the rate of locking at the lowest concentration (**Figure 3.3C, Figure A3.9, Figure A3.12, Movie A3.4**). The locking kinetics of TCR forces with LFA-1 engagement showed around a hundred-fold increase over the time course, slightly less than that with CD28 engagement (**Figure 3.3C, Figure A3.9**, **Figure A3.12, Movie A3.5**). After 1 min of locking, the TCR forces with engaged CD28 showed much more frequent mechanical sampling compared to cells on pMHC N4 alone or with LFA-1 engagement (**Figure 3.3C, Figure 3.3D**). By fitting the data collected from 3 mice into our model, we found that the TCR force on-rate when B7-1 was co-presented was significantly higher than that of pMHC N4 alone or with LFA-1 engagement (**Figure 3.3E**). While facilitating more frequent mechanical pulling against pMHC, CD28 engagement also resulted in a faster force off-rate, with the TCR lifetime decreased to 1.4 ± 0.3 s (**Figure 3.3F**). When LFA-1 was engaged, the TCR forces showed a subtle decrease in force on-rate compared to cells without LFA-1 engagement (not statistically significant, **Figure 3.3E**), and the TCR force lifetime decreased to 3.2 ± 0.5 s (**Figure 3.3F**).

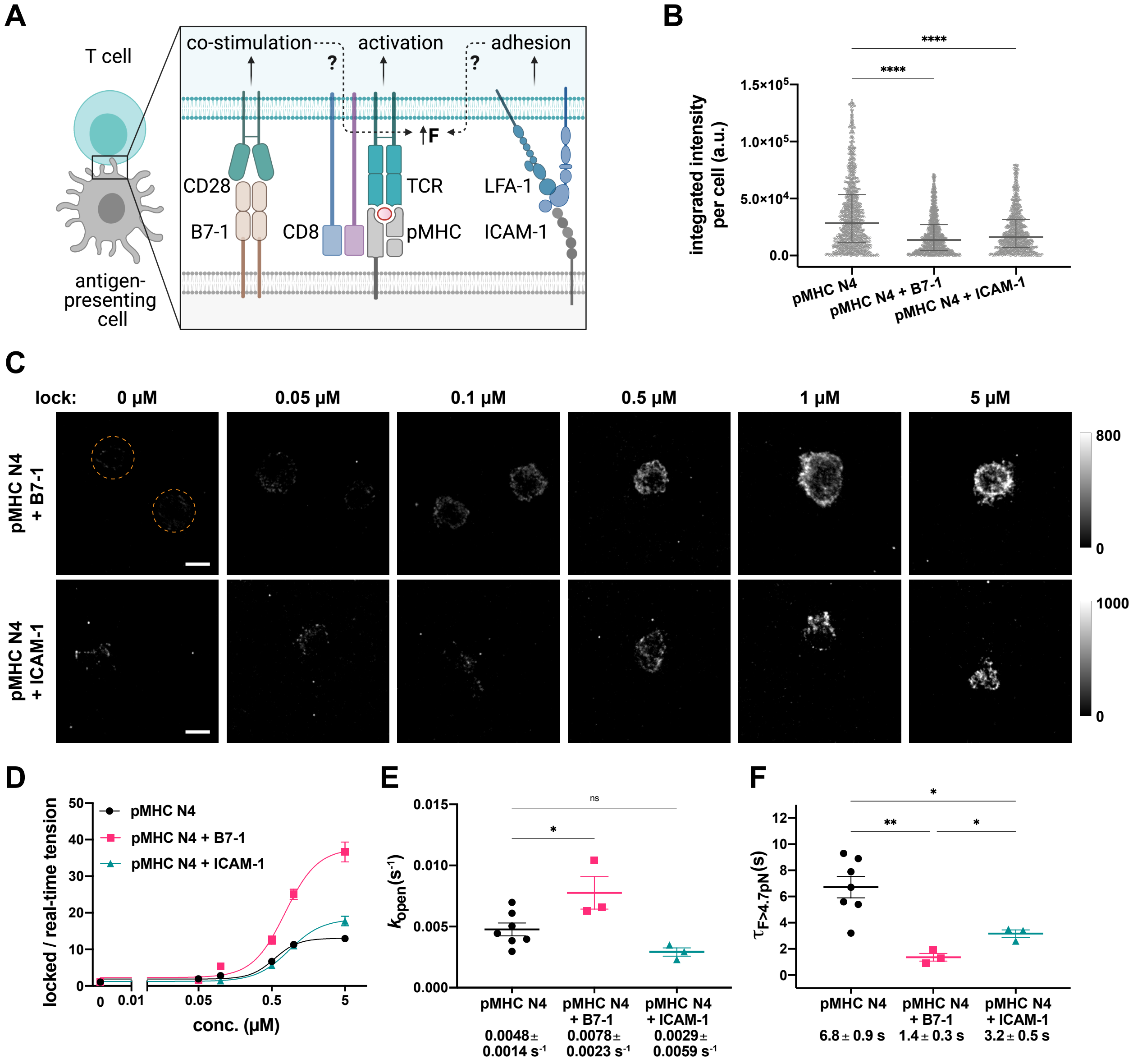

Figure 3.3. The **effect of co-receptor engagement on TCR force and force lifetimes.** (A) Scheme showing the functional role of CD28 and LFA-1 in T cells. (B) Quantitative analysis of real-time TCR forces > 4.7 pN in cells with just TCR-pMHC N4 binding, or with additional CD28-B7-1 and LFA-1-ICAM-1 binding. (C) Representative microscopy images of TCR forces with CD28 or LFA-1 engagement in real-time and after locking for 1 min at different concentrations. (D) Locking profiles at 1 min for TCR forces applied by OT-1 CD8^{+} naïve T cells to pMHC N4, and with CD28-B7-1 or LFA-1-ICAM-1 interaction, represented by locked/real-time integrated intensity of tension signal per cell (mean ± SEM). Data shows the average from cells (n=71-149 for B7-1, 81-125 for ICAM-1) isolated from 3 mice per concentration for each condition at each concentration. (E) The k_{open} (mean ± SEM) obtained from model fitting of the TCR forces. (F) TCR force lifetime measurements (mean ± SEM) for pMHC N4 (7 mice), pMHC N4 with B7-1 (3 mice), and pMHC N4 with ICAM-1 (3 mice) from model fit. Statistical analysis to quantify

significant differences between groups was performed with Brown-Forsythe and Welch ANOVA and Dunnett's T3 multiple comparisons test (ns $P > 0.05$, * $P < 0.05$, ** $P < 0.01$, **** $P < 0.0001$).

These force kinetic measurements obtained following B7-1 or ICAM-1 co-presentation were intriguing in the context of previous studies. As reported in single molecule force spectroscopy studies and according to the catch-bond model, the lifetime of TCR-pMHC binding at ~10 pN force is one of the major inputs that contributes to the antigen discrimination cascade and that triggers T cell activation [17-18]. However, if the T cell-APC interface lacks CD28 engagement, the activation is only partial with TCR-pMHC interaction alone, and leads to either apoptosis or an anergy state [19]. Thus, as a co-stimulatory receptor, CD28 is required for T cells to achieve full activation and was also found to contribute to greater traction force in primary $CD4^+$ T cells on pMHC and anti-CD28 coated micropillars [15]. Therefore, we expected to observe a prolonged TCR force lifetime when B7-1 was co-presented, yet, counterintuitively, our results showed a significant decrease of TCR force lifetimes. Interestingly, this decrease was accompanied by a significant increase in the frequency of TCR mechanical sampling of pMHC. This could be a collective effect of both the CD28 signaling pathway and actin remodeling independent of TCR [20]. CD28 can bind to filamin A and interact with F-actin, and also bind to adapter proteins GRB-2 and Vav1, which further regulate cytoskeletal arrangements [21]. Though the individual TCR pulling events have a shorter lifetime, they collectively have an increased force on-rate and dynamics that might lead the overall traction force to appear stronger on force sensing platforms with poorer molecular-level force sensitivity, such as traction force microscopy and micropillar. This observation of increased force on-rate with the presence of CD28 resonates with the observations that repeated force application triggers stronger TCR early signaling. Studies using biomembrane force probe (BFP) and AFM to apply cyclic forces to T cells triggered Ca^{2+} influx significantly higher than that of constant force [17, 22]. It is argued that the mechanosensing induced TCR conformational change of ~10 nm by 15 pN (~150 pN·nm work), roughly equal to 37 K_BT, greater than the thermal energy driven binding (K_BT: 4.3 pN·nm). As the reversible TCR conformational transition is needed to provide multiple chances for energy transfer to initiate activation, the decrease in force lifetime and increase in force on-rate when CD28 is engaged, could be a result of a "sweet spot" that T cells delicately modulate to achieve maximum activation [23].

LFA-1-ICAM-1 is the primary adhesive interaction for T cell-APC contact, and is responsible for T cell migration and for assisting in T cell activation and differentiation [24]. Upon binding to ICAM-1, through "outside-in" signaling, LFA-1 engaged Crk-associated complexes regulate actin polymerization and mediate a T cell's mechanosensing [25]. Therefore, our findings of the decreased TCR lifetime (and slight but not statistically significant decreases of force on-rate) were unexpected. However, a report on integrin engagement modulation of TCR early signaling shows diminished pY319 on Zap-70 and decrease in total phosphorylation upon LFA-1 engagement. This resonates with our findings, since we find less total TCR force ($F > 4.7$ pN) events per cell with LFA-1 engagement compared to that of TCR-pMHC N4 alone (**Figure A3.12B**). If the phosphorylation of the ITAMs is a force-dependent process, this observation would explain why the there was less tyrosine phosphorylation for cells with LFA-1 engagement. Additionally, we noticed that the TCR tension was primarily located at the focal zone/trailing edge in real-time and at low lock concentrations (0, 0.05, 0.1 μM, **Figure 3.3C**), in agreement with previous reports. However, when a high concentration of lock was added, resulting in binding to briefly unfolded hairpins, TCR forces at the leading edge were locked and visualized (0.5, 1, 5 μM, **Figure 3.3C, Figure A3.9, Movie A3.5**). This result suggested that the TCR force lifetime at the leading edge was long enough for the high concentration lock to bind, but short enough that low concentration of the lock was too slow to bind. In contrast, the TCR forces at the focal zone were observed in real-time with both 4.7 pN and 19 pN hairpin [6, 8], and at low concentration of the lock, suggesting a relative longer lifetime. This result shows that the TCR force magnitude differs within an individual cell and its lifetime is specifically regulated and spatially distributed. Moreover, it indicates that the TCR forces with higher magnitude likely have a longer lifetime, which is in agreement with the catch-bond model [3].

3.3.3. The effect of cytoskeleton network on TCR force and force lifetime

Actin networks have been identified as an important player in mediating T cell signaling, and its dynamic re-organization and association with tensile forces may regulate the maintenance of the immune synapse [21, 26-27]. Many drug inhibitors have been designed that are each able to impact the actin network in unique ways. Though previous studies with micropillars and traction force microscopy have reported on the effect of these inhibitors on the T cell traction forces, these less sensitive force detection methods do not provide molecular resolution of the force [28]. Our previous attempt to address the impact of the actin network reported on TCR forces following the treatment of a few inhibitors [6]; however, the experiments are performed with cells on antiCD3ε substrates rather than pMHC substrates, and missed the opportunity to analyze the force dynamics due to the limitation of the conventional DNA hairpin probes. To fill the gap, we sought to investigate the effect of cytoskeleton networks on the molecular forces generated by the T cells and transmitted through TCR with this method. We chose an Arp2/3 complex inhibitor CK666 to assess the impact of branched actin network and the actin foci on the TCR forces and force lifetime, as it affects the Arp2/3 complex conformational change and thus the actin nucleation [29]. Blebbistatin (Blebb) was also chosen to inhibit myosin IIA and study the impact of the actomyosin network in TCR forces

[30]. Moreover, jasplakinolide (Jas) was used to stabilize actin filaments and arrest actin retrograde flow [31]. Briefly, OT-1 CD8+ naïve T cells were plated on the 4.7 pN DNA tension probe substrates that present the pMHC N4 and allowed to spread for 30 min so that many of the cells could reach mechanical steady state. Cells were imaged (t = 0 min), and then treated with 50 µM CK666, 50 µM Blebb, or 1 µM Jas for 5 min to target the different cytoskeletal networks, or a negative control of 0.5% DMSO. Real-time TCR tension of the same cells was imaged during the drug treatment (t = 2.5 and 5 min with drug), and then the lock was added to the cells at different concentrations in parallel wells. Time-lapses were acquired to obtain the locking kinetics and perform model fit with drug treatment.

Upon CK666 treatment, TCR-pMHC force showed a diminished real-time tension (real-time tension, **Figure A3.14**), which occurred across the whole cell contact area, and most noticeably at the ring (actin cortex). On the other hand, the F > 4.7 pN real-time tension map for cells treated with Blebb and Jas did not show much difference before and after the treatment (real-time tension, **Figure A3.15** and **Figure A3.16**), similar to the DMSO control (real-time, tension **Figure A.3.17**) Quantitative analysis showed that the real-time tension signal decreased by 60-70% for cells incubated with CK666 and increased by 20-30% for cells treated with Blebb and Jas (**Figure 3.4B, Figure A3.18**). As lock was added to the inhibitor-treated cells, accumulation of tension signal was observed (**Figure 3.4A,** locked tension, **Figure A3.14, Figure A3.15, Figure A3.16, Figure A3.17**). Quantitatively, the ensemble locking kinetics did not reveal statistically significant differences of the force on-rate and lifetime (**Figure 3.4B, C**; **Figure A3.19, Figure A3.20**), however, we observed very different patterns of tension accumulation. For cells treated with CK666, tension accumulated at the cortex, or the lamellipodia-like-dSMAC (distal supramolecular activation cluster region). Though it was diminished in the real-time observation, this pattern was revealed with higher lock concentrations. Alternatively, the lamella-like-pSMAC-like (peripheral SMAC) and cSMAC-like (central SMAC) regions showed significantly less accumulated tension (**Figure 3.4A, C**; locked tension, **Figure A3.14, Movie A3.6**). The contact area of the cell treated with CK666 also increased after 15 min of data acquisition, with the cell mechanical sampling pattern at the cortex becoming less organized (locked tension, **Figure A3.14, Figure A3.18**). For cells treated with Blebb, substantial tension accumulation at the pSMAC-like and cSMAC-like region was observed, as well as tension at the cell cortex (**Figure 3.4A, C**; locked tension, **Figure A3.15, Movie A3.7**). Following Jas treatment, most cells showed tension accumulation at the cortex and the pSMAC-like region, but not so much at the cSMAC-like region (**Figure 3.4A, C**; locked tension, **Figure A3.16, Movie A3.8**). In contrast, most of the cells incubated with DMSO showed a "bull's eye" tension accumulation pattern similar to cells with no treatment, with a ring at the cortex, less noticeable tension at the pSMAC-like region, and a clear center at the cSMAC-like region (**Figure 3.4A, C**; locked tension, **Figure A3.17, Movie A3.9**), consistent with our previous report [6, 8].

It is a slightly unexpected that treatment with this panel of inhibitors targeting different cytoskeletal networks did not show any statistically significant differences in the force on-rate and lifetime. Though, this could be due to several reasons: (1) the sensitivity of the assay is not high enough to resolve the differences; (2) the inhibitors only perturbed parts of the cytoskeletal networks, which was not a whole cell level of modulation like CD28 or LFA-1; (3) the inhibited/remaining network did not profoundly change the TCR force kinetics. Nonetheless, we can semi-quantitatively or qualitatively discuss the results with the spatial differences in TCR tension we observed upon different network inhibition.

According to literature, upon activation T cells have ~70% Arp2/3-nucleated actin filament and 30% formin-nucleated actin filament [32]. The inhibition of Arp2/3 depleted 60-70% real-time tension (**Figure 3.4B, Figure A3.18**), suggesting that the Arp2/3 pathway was responsible for around 70% of TCR-pMHC pulling forces that are greater than 4.7 pN, and nearly all the Arp2/3 nucleated branch actin was contributing to the TCR pulling force. Overall, the tension accumulation we observed following CK666 treatment was a lot less compared to cells with no treatment or treatment with DMSO (**Figure 3.4A, B, D, Figure A3.14, Figure A3.17)**, and this remaining tension accumulation at the cortex/dSMAC-like region might come from formin-related activities [32-33]. It was evident that the inhibition of formin reduces the phosphorylation of the transmembrane signaling hub LAT (linker for activation of T cells), and inhibits the formation of the actin ring, but it does not impact pY Zap70 [34]. Since LAT is associated with other regulators of the cytoskeleton, it is therefore possible that the remaining tension signal is related to formin. Our result also showed that the remaining tension ring was more asymmetric compared to the ring exhibited by untreated cells, though the mechanism accounting for the loss of ring integrity is unclear presently. Notably, though the tension accumulation at the ring was significantly lower following CK666 treatment compared to non-treated cells or cells treated with the other inhibitors, the locked/real-time only showed a small difference (**Figure 3.4B, Figure A3.19**), with a non-statistically significant decrease in force on-rate and lifetime. This suggests that the non-Arp2/3 related TCR force has similar kinetics to the TCR force kinetics when all of the cytoskeletal network is engaged. Moreover, Arp2/3 is also found to mediate actin foci formation from branched actin, which is closely associated with TCR microclusters [35]. Since cells with inhibited Arp2/3 did not show any significant new mechanical sampling in the pSMAC-like and dSMAC-like regions compared to what we frequently see in cells with no treatment or DMSO, it implies that the Arp2/3 actin foci might contribute significantly to the molecular TCR-pMHC forces at these regions.

The inhibition of myosin II can cause a rather disorganized actomyosin network, which further leads to reduced centralization of the LFA-1 and TCR microclusters [36]. With Blebb treatment, we noticed that the dip in tension signal at the pSMAC-like region usually observed with control cells was less pronounced, and the force pattern of the three regions became less resolved due to the accumulated tension signal in the pSMAC-like region (**Figure 3.4A, D, Figure A.3.15**). This result reflects that the inhibited myosin II failed to drive TCR microclusters toward the cSMAC-like region [30, 37]. Interestingly, the inhibited myosin II did not show total 4.7 pN tension signal decrease, suggesting that it does not contribute significantly to the molecular forces transmitted through the TCR to the pMHC (**Figure A3.19**). This finding is consistent with a previous paper using traction force microscopy [28, 31]. Additionally, a previous report showed inhibition of myosin II light chain kinase (MLCK) using the ML-7 inhibitor completely changed the spatial pattern of real-time tension signal and reduced contact area. The mapped TCR force pattern upon ML-7 treatment resembled shrinking arcs/ring of the actomyosin network, yet there was no overall decrease in tension signal intensity [6]. Taken together, it is possible the role of myosin II in molecular TCR forces is more related to providing the integrity of the cytoskeletal networks which regulate the TCR spatial distribution rather than generating the force that is transmitted through TCR-pMHC binding.

Actin retrograde flow is also shown to regulate the TCR microcluster movement to the cSMAC-like region [38]. In the context of mechanosensing and mechanotransduction, actin flow is widely assumed to be the main driver of TCR-pMHC bond breaking. A previous report on perturbation of actin retrograde flow showed diminished T cell traction force upon treatment [31]. However, our results suggest that the abrogation of actin flow did not significantly impact the TCR forces. Though the real-time forces increased slightly within 5 min, the accumulated tension offered further evidence that there was no significant difference in total mechanical sampling compared to cells treated with DMSO quantitatively (**Figure A3.14, Figure A3.19**). We also did not observe any statistically significant difference in the on-rate or off-rate of the forces (**Figure A3.20)**, which suggests that the actin retrograde flow is not the primary mechanism that drives TCR-pMHC force interactions. Conveniently, it is reported that the arrest of actin flow did not affect the pY319 on ZAP70, but instead decreased pY783 on signaling molecule PLCγ1, which directly caused decreased Ca^{2+} signaling and TCR microclusters centralization [38]. Our result resonates with this report, as the TCR force that samples pMHC not being significantly affected also suggests that Zap70 phosphorylation could be intact. Overall, since there is a discrepancy in the phosphorylation status of Zap70 and PLC γ1, it is reasonable to assume that there is unclear cytoskeleton coordination responsible for the mechanosensing and mechanotransduction bridging the Zap70 and PLC γ1 activation steps, likely at LAT multi-molecular signaling complexes which could form as a result of actin retrograde flow [39].

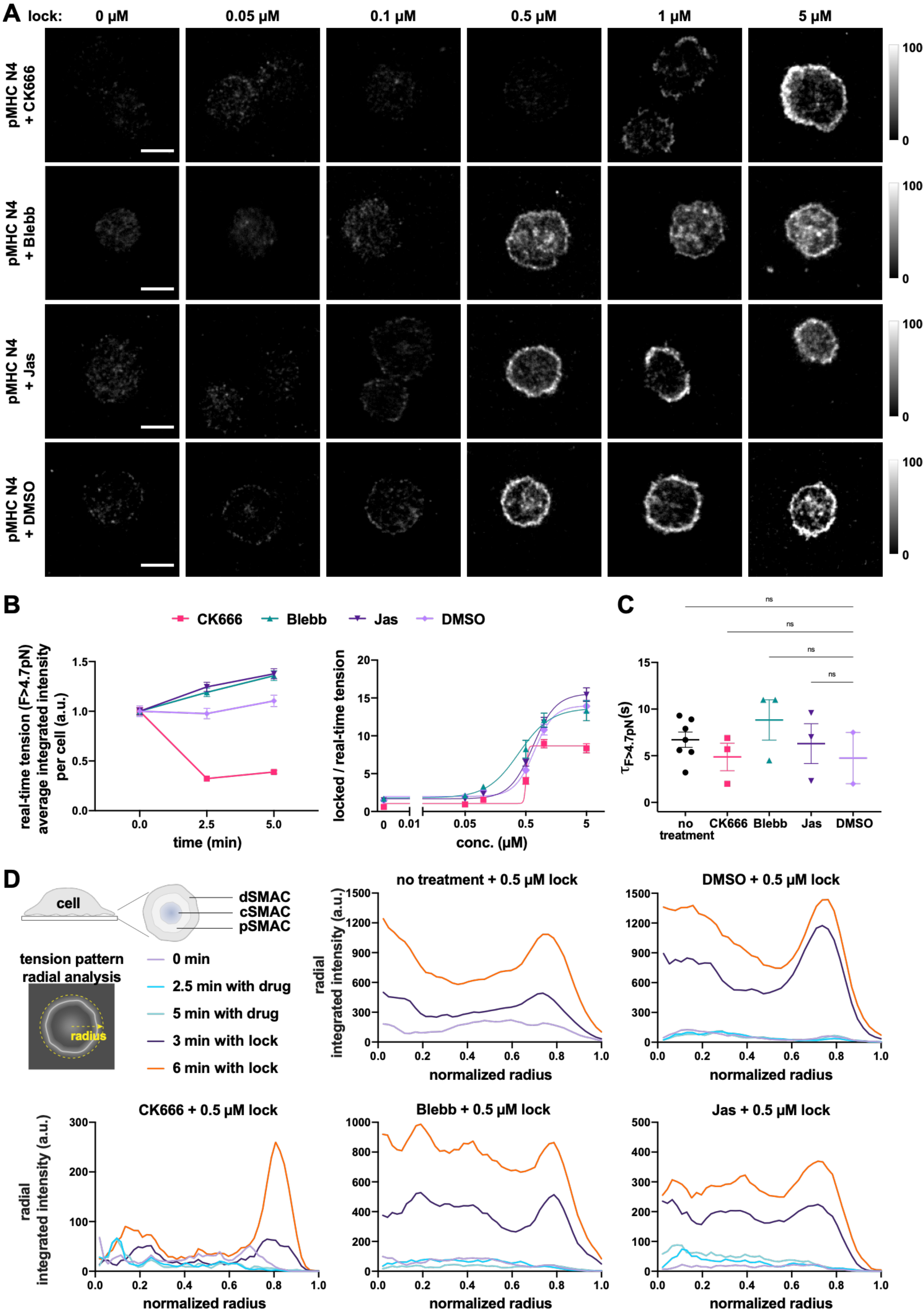
A
lock:
0 μM
0.05 μM
0.1 μM
0.5 μM
1 μM
5 μM
pMHC N4 + CK666
pMHC N4 + Blebb
pMHC N4 + Jas
pMHC N4 + DMSO
1000
0
B
CK666
Blebb
Jas
DMSO
real-time tension (F>4.7pN) average integrated intensity per cell (a.u.)
1.5
1.0
0.5
0.0
0.0
2.5
5.0
time (min)
locked / real-time tension
20
15
10
5
0
0
0.01
0.05
0.5
5
conc. (μM)
C
ns
ns
ns
ns
τF>4.7pN(s)
15
10
5
0
no treatment
CK666
Blebb
Jas
DMSO
D
cell
dSMAC
cSMAC
pSMAC
tension pattern radial analysis
radius
0 min
2.5 min with drug
5 min with drug
3 min with lock
6 min with lock
no treatment + 0.5 μM lock
DMSO + 0.5 μM lock
radial integrated intensity (a.u.)
1500
1200
900
600
300
0
0.0
0.2
0.4
0.6
0.8
1.0
normalized radius
CK666 + 0.5 μM lock
Blebb + 0.5 μM lock
Jas + 0.5 μM lock
300
200
100
0
1000
800
600
400
200
0
500
400
300
200
100
0

Figure 3.4 The effect of cytoskeletal coordination on TCR force and force lifetimes. (A) Representative microscopy images of TCR forces treated with inhibitors in real-time and after locking for 1 min at different concentrations. (B) Left: Quantitative analysis of real-time TCR forces > 4.7 pN of cells under different treatment. Data was averaged from 3 mice, total n > 150 cells per condition. Right: Locking profiles at 1 min for TCR forces applied by OT-1 $CD8^+$ naïve T cells to pMHC N4 with different treatment, represented by locked/real-time integrated intensity of tension signal per cell (mean ± SEM). Data shows the average from cells isolated from 3 mice per concentration for each condition at each concentration. (C) TCR force lifetime measurements (mean ± SEM) for pMHC N4 (7 mice) of cells with no treatment (7 mice), CK666 treatment (3 mice), Blebb treatment (3 mice), Jas treatment (3 mice), and DMSO treatment (2 mice) from model fit. Statistical analysis to quantify significant differences between groups was performed with Brown-Forsythe and Welch ANOVA and Dunnett's T3 multiple comparisons test (ns, $P > 0.05$). (D) Radial profile analysis of representative cells under different conditions.

3.4. Conclusion

In this chapter, we took advantage of rapid hybridization kinetics by using lock oligonucleotide hybridization as a reference to measure the force kinetics of T cell-exerted molecular forces through TCR to pMHC. Using this technique, we measured that the lifetime of TCR forces during cognate antigen binding was ~ 6.8 s, while during antiCD3ε binding it was significantly longer at ~29 s. The engagement of coreceptor CD28 and LFA-1 was also found to significantly change the force kinetics. The TCR-pMHC force lifetime with CD28 decreased to 1.4 s but was coupled with an increased force on-rate, resulting in more frequent mechanical sampling. With LFA-1 engagement, the TCR forces showed decreased lifetime in the migratory cells, and the lifetime at the leading edge was found to be shorter than that at the focal zone. Importantly, TCR density measurements confirmed that these force kinetics results were not due to changes in TCR density under different conditions, as the total TCR density was not altered (**Figure A3.21**). Future work should also extend to inhibitory co-receptors like CTLA-4 and PD-1 in order to explore if they actively regulate the force kinetics to prevent T cell activation.

The effect of cytoskeleton network was also evaluated using a small panel of inhibitors. We found that the TCR force cannot be attributed to one single network. The Arp2/3 pathway is a primary contributor to TCR force transmission, however, there are other mechanisms that could be involved. Moreover, we observed that myosin II and actin retrograde flow are not key regulators of the TCR molecular force towards pMHC, and that these networks do not significantly alter the TCR force kinetics.

Piecing together the results we obtained on TCR molecular pulling, it is possible that there are alternative mechanisms that actively drive the mechanical sampling of the antigen separate from the Arp2/3 pathway. More de-convolution of this complicated but delicate process is needed through the use of different perturbation methods. For example, TCR forces from cells incubated with the formin inhibitor SMIFH2 should be tested to confirm that it generates the remaining force transmission observed after Arp2/3 inhibition. The TCR force kinetics should also be examined together with pCasL, a mechanosensing protein that accompanies cytoskeleton tension and only gets phosphorylated after local stretching [26].

Furthermore, this method to measure force lifetimes has proven to be a powerful tool and should also be extended to DNA hairpin probes with a $F_{1/2}$ of 12 pN in order to observe potential catch-bond behavior. If observed, the presence of catch-bond behavior when cells actively mechanically sample antigen can confirm the findings from single-molecule force spectroscopy and offer crucial support to the mechanosensing models of T cell triggering.

3.5. Materials and methods

3.5.1. Oligonucleotides

The oligonucleotides used in this study were custom synthesized from Integrated DNA Technologies and listed in **Table A3.1**.

Table A3.1. List of oligonucleotides used in Chapter 3.

oligonucleotide	5'	sequence (5' to 3')	3'
amine ligand strand (A21B)	/5AmMC6/	CGC ATC TGT GCG GTA TTT CAC TTT	/3Bio/
Cy3B ligand strand (A21B Cy3B)	Cy3B	CGC ATC TGT GCG GTA TTT CAC TTT	/3Bio/
Cy5B ligand strand (A21B Cy5B)	Cy5B	CGC ATC TGT GCG GTA TTT CAC TTT	/3Bio/
BHQ2 anchor strand	/5ThiolMC6-D/	TTT GCT GGG CTA CGT GGC GCT CTT	/3BHQ_2/
4.7 pN hairpin strand	-	GTG AAA TAC CGC ACA GAT GCG TTT GTA TAA ATG TTT TTT TCA TTT ATA CTT TAA GAG CGC CAC GTA GCC CAG C	-
12 pN hairpin strand	-	GTG AAA TAC CGC ACA GAT GCG TTT GGG TTA ACA TCT AGA TTC TAT TTT TAG AAT CTA GAT GTT AAC CCT TTA AGA GCG CCA CGT AGC CCA GC	-
4.7 pN hp 15mer lock	-	AAA AAA CAT TTA TAC	-
4.7 pN hp 15mer lock NH2	-	AAA AAA CAT TTA TAC	/3AmMO/
12 pN hp 18mer lock	-	AGA ATC TAG ATG TTA ACC	-
12 pN hp 18mer lock NH2	-	AGA ATC TAG ATG TTA ACC	/3AmMO/

3.5.2. Reagents

Table A3.2. List of reagents used in Chapter 3.

Material	Company	Catalog Number	Remarks
Biotin anti-mouse CD3ε Antibody (2C11)	Biolegend	100304	antibody/ ligand
Biotinylated pMHC ovalbumin (SIINFEKL)	NIH Tetramer Core Facility	NA	
Biotinylated pMHC ovalbumin (SIIQFEKL)	NIH Tetramer Core Facility	NA	
Recombinant Mouse B7-1/CD80 Fc Chimera His-tag Protein, CF	R&D systems	740-B1-100	
ICAM-1 Protein, Mouse, Recombinant (His & hFc Tag)	Sinobiological	50440-M03H	
PD-L1 Protein, Mouse, Recombinant (ECD, His & hFc Tag)	Sinobiological	50010-M03H	
Ultra-LEAF™ Purified anti-mouse TCR β chain Antibody (H57)	Biolegend	109253	
PE Rat Anti-Mouse Vα2 TCR, Clone B20.1	BD Pharmingen	553289	
Rat IgG2a kappa Isotype Control (eBR2a), PE	eBioscience	12-4321-41	
Ultra-LEAF™ Purified anti-mouse CD3 Antibody (17A2)	Biolegend	100239	
Anti-Mouse CD8a (Ly 2) Purified (Clone CT-CD8a) (rat IgG2a)	Cedarlane	CL168AP	
Alexa Fluor® 488 anti-mouse CD8a Antibody	Biolegend	100723	
Alexa fluor 647 conjugated anti-TCR antibody (H57-597)	Life technologies	HM3621	
Alexa Fluor® 647 anti-mouse CD279 (PD-1) Antibody	Biolegend	109118	
10x Red blood cell lysis buffer	Biolegend	00-4333-57	cell preparation
Dulbecco's phosphate-buffered saline (DPBS)	Corning	21-031-CM	
Hank's balanced salts (HBSS)	Sigma	H8264	
BD Syringes only with Luer-Lok	BD bioscience	309657	
Cell strainers	Biologix	15-1100	
Midi MACS (LS) startup kit	Miltenyi Biotec	130-042-301	
Mouse CD8+ T cell isolation kit	Miltenyi Biotec	130-104-075	
Ovalbumin (257-264) chicken	Sigma	S7951-1MG	
Atto647N NHS ester	Sigma	18373-1MG-F	oligo preparation materials
Cy3B NHS ester	GE Healthcare	PA63101	
3-Hydroxypicolinic acid (3-HPA)	Sigma	56197	
Nanosep MF centrifugal devices	Pall laboratory	ODM02C35	
P2 gel	Bio-rad	1504118	
Triethylammonium acetate buffer	Sigma	90358	
mPEG-SC	Biochempeg	MF001023-2K	surface preparation materials
(3-Aminopropyl)triethoxysilane	Acros	AC430941000	
8.8 nm gold nanoparticles, tannic acid	Nanocomposix	customized order	
Coverslip Mini-Rack, teflon	Thermo Fisher Scientific	C14784	
Ethanol	Sigma	459836	
Hydrogen peroxide	Sigma	H1009	
LA-PEG-SC	Biochempeg	HE039023-3.4K	
NTA terminal-SAM formation reagent	Dojindo Molecular Technologies	N475-10	
Sufuric acid	EMD Millipore Corporation	SX1244-6	
Sulfo-NHS acetate	Thermo Fisher Scientific	26777	
Wash-N-Dry™ Slide Rack	Sigma	Z758108	
Glass Coverslips for sticky-Slides 25 / 75 mm	Ibidi	10812	
Sticky-slide 18 Well	Ibidi	81818	inhibitors
Jasplakinolide	Thermo Fisher	J7473	
Blebbistatin	Sigma	B0560	
CK666	Sigma	SML0006	
Latrunculin B	Sigma	L5288	
PP1 Analog IV, 3-IB-PP1 - Calbiochem (Csk inhibitor)	Sigma	529598-10MG	
LCK inhibitor	Cayman	15135	
ML-7 (MLCK inhibitor)	Abcam	ab120848	
Y27632	Sigma	Y0503	
Cytochalasin D	Sigma	C8273	
Bovine serum albumin	Sigma	735078001	general
Attofluor Cell Chamber, for microscopy	Thermo Fisher Scientific	A7816	
PE Phycoerythrin Fluorescence Quantitation Kit	BD Quantibrite	340495	
Dimethyl Sulfoxide (DMSO)	EMD-Millipore	M1096780100	
Sodium azide	Sigma	S2002	
UltraPure™ 0.5M EDTA, pH 8.0	Thermo Fisher	15575020	
SiR-Actin Kit	Cytoskeleton	CY-SC001	
Formaldehyde solution	Sigma	252549	
Triton™ X-100	Sigma	X100	

3.5.3. Equipment

Table A3.3. List of equipment used in Chapter 3.

Equipment	Company
Barnstead Nanopure water purifying system	Thermo Fisher
AdvanceBio Oligonucleotide C18 column, 4.6 x 150 mm, 2.7 µm	Agilent
High-performance liquid chromatography	Agilent 1100
Matrix-assisted laser desorption/ionization time-of-flight mass spectrometer (MALDI-TOF-MS)	Voyager STR
Nanodrop 2000 UV-Vis Spectrophotometer	Thermo Fisher
CFI60 Apochromat TIRF 100X Oil Immersion Objective Lens, N.A. 1.49	Nikon
Prime 95B-25MM Back-illuminated sCMOS Camera. 1608x1608,30fps	Photometrics
Nikon Ti2-E Motorized Research Microscope	Nikon
Ti2-ND-P Perfect Focus System 4	Nikon
SOLA SE II 365 Light Engine	Nikon
NIS Elements software	Nikon
C-FL Surface Reflection Interference Contrast (SRIC) Cube	CHROMA
CF-L AT CY5/Alexa Fluor 647/Draq 5 Filter Set	CHROMA
C-FL DS Red Hard Coat, High Signal-to-Noise, Zero Shift Filter Set	CHROMA
CytoFLEX V0-B3-R1 Flow Cytometer	BECKMAN COULTER

3.5.4. Oligonucleotide preparation

The amine ligand strand (A21B) was dissolved at a final concentration of 1 mM in water. First, 10 μL of the A21B stock was mixed with 10 μL of 10x PBS, 10 μL of 1 M $NaHCO_3$, and 60 μL of water. Then, an aliquot of 50 μg Cy3B NHS ester was dissolved in DMSO immediately before use and added to the mixture. The mixture was allowed to react at room temperature for 1 h or 4 °C overnight. After the reaction, by-products, excess dye, and salts were removed by P2 desalting gel filtration.

3.5.5. HPLC

The product was purified by a C18 column designated for oligonucleotide purification, with solvent A: 0.1 M TEAA in H2O and B: ACN as the mobile phase for a linear gradient elution 10-100% B over 50 min at a flow rate of 0.5 mL/min. The purified product was dried and reconstituted in water. Concentration of the oligo-dye conjugate was determined using absorbance at 260 nm.

3.5.6. Transgenic mice and T cell preparation

The OT-1 transgenic mice are housed at the Division of Animal Resources Facility at Emory University. All the experiments were approved and performed under the Institutional Animal Care and Use Committee (IACUC) protocol. OT-1 $CD8^+$ naïve T cells were purified from the spleens of sacrificed mice using the MACS mouse $CD8^+$ T cell isolation kit with a MACS separator following manufacturer's instruction. Briefly, non $CD8^+$ T cells are removed with magnetic depleting antibody cocktail and the remaining untouched $CD8^+$ T cells were isolated and enriched. Purified OT-1 $CD8^+$ naïve T cells were resuspended in HBSS at 2 x 10^6 cells/mL and kept on ice prior to use.

3.5.7. Substrate preparation

4.7 pN DNA tension probe surfaces. Coverslips (25 x 75 mm) were placed on a Wash-N-Dry rack in a tall 200 mL beaker and rinsed in Nanopure water three times to get rid of dust. The coverslips were further cleaned by sonication for 15 min in ethanol, and another 15 min in water. After sonication, the liquid was discarded and the beaker with the rack and coverslips in it was washed with Nanopure water at least 6 times to remove any remaining organic solvent. Fresh piranha solution was prepared by gently mixing sulfuric acid and hydrogen peroxide at a ratio of 3:1. CAUTION: LARGE AMOUNTS OF ORGANIC SUBSTANCES COULD REACT VIGOROUSLY WITH PIRANHA SOLUTION AND MAY CAUSE EXPLOSION. The rack that holds the coverslips was transferred to the beaker containing piranha solution for etching. After 30 min of piranha etching, the rack holding the coverslips was transferred to a clean 200 mL beaker with Nanopure water and rinsed again with water at least 6 times. The rack holding the coverslips was then immersed in ethanol three times to remove water, after which, the rack was immersed in 3% aminopropyl triethoxy silane (APTES) (v/v) in 200 mL of ethanol for 1 h at room temperature. After the reaction, the coverslips were rinsed at least 6 times by submerging them into 200 mL of ethanol, then baked-dry in an oven at 80 °C for 20 min. After cooling, the amine-modified coverslips were placed in a plastic petri dish. Subsequently, 1 mL of 0.5% w/v LA-PEG-SC and 2.5% w/v mPEG-SC in 0.1 M $NaHCO_3$ was added onto a coverslip and allowed to incubate for 1 h at room temperature. After the reaction, surfaces were rinsed three times with Nanopure water. Then, 300 µL of 0.1 M $NaHCO_3$ containing 10 mg/mL of sulfo-NHS acetate was added to the coverslip for passivation for 30 min, and afterwards the excess was washed away with water. Coverslips functionalized with lipoic acid PEG and passivated with mPEG and sulfo-NHS-acetate were assembled onto the 18-well sticky slides. Then, 80 µL of gold nanoparticles (Au NPs, 8.8

nm, tannic acid, 0.05 mg/mL) was added to each well and allowed to incubate for 30 min at room temperature, after which each well was rinsed with water. During the incubation with gold particles, the 4.7 pN hairpin, Cy3B ligand strand, and BHQ2 anchor strand that form the molecular tension probes were mixed and annealed (heated to 95 ºC and cooled to room temperature) at a ratio of 1.1:1:1 in 1 M NaCl at 300 nM. Additional BHQ2 strand was added to the annealed DNA solution to make the total ratio between BHQ2 strand and Cy3B strand 10:1 to ensure maximum quenching. Then, 40 µL of the DNA probes was added to each well and the imaging chamber was sealed with scotch tape and kept in the dark and at 4 ºC overnight. On the second day, the excess probes were washed off with 1× PBS. Streptavidin (40 µg/mL in PBS) was added to each well and incubated for 30 min at room temperature, and the excess was washed away with PBS. Finally, 50 µL of biotinylated antibody (40 µg/mL) or ligand (10 µg/mL) was added to each well in 1× PBS and allowed to incubate for 30 min at room temperature, and afterwards the excess was rinsed away with PBS.

4.7 pN DNA tension probe surfaces for ligand co-presentation. The surface preparation is identical to the procedure described above until the end of sulfo-NHS acetate passivation. The Au NPs were first added at 0.025 mg/mL to the glass slide for 30 min (to cover the whole surface), and the excess was rinsed away with water after incubation. Then, NTA-SAM was added at 0.2 mM in ethanol and incubated overnight on the 25 × 75 mm glass slide. On the second day, the excess was washed away, and the glass slide was air-dried before assembled to the 18-well sticky slides. Then, 50 µL of 40 mM $NiCl_2$ was added to each well and allowed to incubate for 1 h, and afterwards the excess was washed away with water. Au NPs were added again at 0.05 mg/mL for 30 min (80 µL/well), and afterwards the excess was rinsed away with water. The annealed DNA tension probe and streptavidin were functionalized onto the substrate as described previously. At the final step, the biotinylated ligand (10 µg/mL) and the his-tag containing ligand (either B7-1 or ICAM-1, 10 µg/mL) were added together as a mixture to each well and incubated at room temperature for 30 min. The excess was rinsed away with PBS after incubation.

3.5.8. Microscopy

General imaging procedure with cells. The purified OT-1 CD8$^+$ cells were plated at 4×10^4 cells/well and allowed to spread for 30 min to reach the mechanical steady state. RICM images of the cells and the real-time tension signals in Cy3B channel were acquired. A serial dilution of the lock oligonucleotide was prepared in HBSS to give 10 µM, 2 µM, 1µM, 0.2 µM, 0.1 µM, and 0 µM solutions. Immediately after acquiring the real-time tension signal, 50 µL lock was gently added to a well containing 50 µL HBSS. This procedure was repeated for each lock concentration and time-lapses of the tension were collected accordingly.

Treatment with inhibitors. The purified OT-1 CD8$^+$ cells were plated at 4×10^4 cells/well and allowed to spread for 30 min. RICM images of the cells and the real-time tension signals in Cy3B channel were acquired. Stock solutions (200×) of the inhibitors were prepared in DMSO. Cells were treated with either CK666 (50 µM), Blebbistatin (50 µM), Jasplakinolide (1 µM), or 0.5% DMSO (control) for 5 min.

Treatment with antibodies. The purified OT-1 CD8$^+$ cells were plated at 4×10^4 cells/well and allowed to spread for 15 min. BSA (0.1% w/v) was first added to cells for 5 min, followed by the addition of 10 µg/mL TCR b chain antibody H57. After 10 min of incubation, real-time tension images and time-lapses with the lock were acquired.

3.5.9. Flow cytometry

OT-1 CD8$^+$ T cells with no treatment or treated with inhibitors/antibodies were suspended in 100 µL pre-chilled FACS buffer (1xPBS without Ca2+ and Mg2+, 5 mM EDTA, 1% BSA, 25 mM

HEPES, 0.02% sodium azide) at 10^6 cells/mL and kept on ice for 5 min (to block non-specific binding). PE-anti TCR Va2 (clone B20.1) was added to cells at a final concentration of 10 µg/mL and incubated on ice for 30 min in dark. After incubation, cells were spun down at 250xg for 5 min, rinsed with FACS buffer twice, resuspended in FACS buffer, and run on a flow cytometer. Cells stained with an isotype control antibody were also analyzed and the geometric mean of the isotype control group was subtracted from the geometric mean of each experimental group. BD QuantiBrite PE standard beads with known quantities of PE molecules were used to quantify the number of PE molecules per μm^2. Briefly, the beads were reconstituted in 0.5 mL FACS buffer, vortexed for 5-10 s, and used to generate a standard curve relating the geometric mean fluorescence value to the number of PE molecules per cell. The number of PE molecules per μm^2 was then obtained by dividing the number of PE molecules per cell by the surface area (110 μm^2) of an OT-1 $CD8^+$ naïve T-cell [5].

3.5.10. Data analysis

Image analysis was performed using Fiji software, and the quantitative analysis was performed using Microsoft Excel and GraphPad Prism. Briefly, after acquiring fluorescence images of tension signal, the drift in the time-lapses were corrected, and the camera background was subtracted. The fluorescence background produced by the DNA tension probe substrates was subtracted using the average + 3*SD of three different local background regions. ROIs of cells on either background-subtracted images or RICM images were drawn with Fiji freehand selections tool. The area and raw integrated intensity of the cell ROIs were measured and then plotted in Prism. The locked/real-time tension per cell was obtained by normalizing the raw integrated intensity over time to the raw integrated intensity at real-time (t = 0 min). The locked/real-time was plotted from the averaged data obtained from at least 3 mice for each condition at each concentration of the lock.

3.5.11. Model

DNA hairpins can be treated as digital switches that are either in the opened or closed conformation[40-41]. In the specific context of DNA hairpin-based tension sensors, the hairpins exist primarily in the fluorescent opened state when $F > F_{1/2}$ and exist primarily in the quenched closed state when $F < F_{1/2}$. At $F = F_{1/2}$, the hairpins spend equal amounts of time in the closed and opened states. Upon opening, the fluorescence intensity increases by a fixed amount such that (in the absence of a locking strand) the background-subtracted fluorescent intensity is directly proportional to the fraction of probes in an opened state. This fraction is denoted by O, while the fraction of probes in a closed state is denoted by C.

Reversible transitions between opened and closed states can be described using the first-order rate constants k_{open} and k_{close}. The k_{open} represents force-mediated transitions of probes from a closed state to an open state and depends on many factors including the rate of association between receptors and tension probe ligands, the surface density of receptors on the cell membrane, and the loading rate of the cellular machinery. k_{close} represents the transition of opened tension probes from an opened state to a closed state, which can be caused by either 1) rupture of the receptor-ligand bond, or 2) decrease in F below $F_{1/2}$ without ligand rupture. Accordingly, the inverse of k_{close} represents the force lifetime, τ_{force}, rather than the bond lifetime.

The introduction of a locking strand causes opened strands to irreversibly transition to a locked state. The fraction of probes in a locked state (regardless of whether they are engaged by a receptor) is described by L. Transitions from the opened state to the locked state are described by the lock concentration-dependent first order rate constant k_{lock}. Together, these processes can be represented using a simple chemical equation:

$$C \underset{k_{close}}{\overset{k_{open}}{\rightleftharpoons}} O \overset{k_{lock}}{\rightarrow} L$$

Below, we will use this chemical equation to derive an equation for fluorescence intensity as a function of time.

Importantly, this derivation only works under the condition of a mechanical steady state. By mechanical steady state, we mean that k_{open}, k_{close}, and k_{lock} are constant in time such that the chemical equation can accurately describe the population of tension probes as a function of time. Physically, this means that the cell's interaction with the surface via receptor-ligand interactions is constant throughout the duration of acquisitions; all physical properties that govern k_{open}, k_{close}, and k_{lock} – including receptor surface density, receptor-ligand association rate, the concentration of locking strand beneath the cell, and the force loading rate – are all constant in time. We also make a pre-equilibrium assumption that dictates that at $t = 0$, the initial fractions of probes in the opened and closed states (denoted O_0 and C_0 respectively) has already reached a pseudo-equilibrium such that $O_0/C_0 = k_{open}/k_{close}$.

According to the chemical equation defined above, the analytical solution for the fraction of unopened, unlocked probes can be described using a form derived by Park and Park [13]:

$$C(t) = C_0 \mathrm{e}^{-\frac{k_F}{2}t} \left[\cosh\left(\frac{\sqrt{-\Delta_c}}{2}t\right) - \frac{\left(k_c - 2k_{close}\frac{O_o}{C_0}\right)}{\sqrt{-\Delta_c}} \sinh\left(\frac{\sqrt{-\Delta_c}}{2}t\right) \right] \tag{1}$$

where $k_F = k_{open} + k_{close} + k_{lock}$, $k_c = k_{open} - k_{close} - k_{lock}$, $\Delta_c = \sqrt{-k_c{}^2 - 4k_{open}k_{close}}$ and cosh and sinh are the hyperbolic cosine and sine functions. The total fraction of opened, bright probes, including all locked probes (L) and opened unlocked probes (O), is equal to $1 - C$. This quantity is directly proportional to the fluorescence intensity:

$$I(t) = a\big(1 - C(t)\big) \tag{2}$$

where a is an arbitrary scaling constant. $I(t)$ can be built into equation (1) by subtracting both sides of equation (1) from 1 and multiplying by a:

$$a\big(1 - C(t)\big) = a - aC_0\mathrm{e}^{-\frac{k_F}{2}t}\left[\cosh\left(\frac{\sqrt{-\Delta_c}}{2}t\right) - \frac{\left(k_c - 2k_{close}\frac{O_o}{C_0}\right)}{\sqrt{-\Delta_c}}\sinh\left(\frac{\sqrt{-\Delta_c}}{2}t\right)\right] \quad (3).$$

Combining (2) and (3) yields:

$$I(t) = a - aC_0\mathrm{e}^{-\frac{k_F}{2}t}\left[\cosh\left(\frac{\sqrt{-\Delta_c}}{2}t\right) - \frac{\left(k_c - 2k_{close}\frac{O_o}{C_0}\right)}{\sqrt{-\Delta_c}}\sinh\left(\frac{\sqrt{-\Delta_c}}{2}t\right)\right] \tag{4}$$

The pre-equilibrium assumption can be applied to show that processes of probe opening and closing are at equilibrium:

$$k_{open}C_0 = k_{close}O_0 \tag{5}$$

Where O_0 is the fraction of probes in an open state at $t = 0$. At $t = 0$, $k_{lock} = 0$ so no tension probes are locked (i.e., $L_0 = 0$). I_0 (the fluorescence intensity at $t = 0$) can be defined using O_0:

$$I_0 = aO_0 \quad (6).$$

Re-arranging equations (5) an (6) and combining yields:

$$a = \frac{I_0}{C_0}\left(\frac{k_{close}}{k_{open}}\right) \quad (7).$$

Combining (4) and (7) and yields:

$$I(t) = I_0\left(\frac{k_{close}}{k_{open}}\right)\left(\frac{1}{C_0} - \mathrm{e}^{-\frac{k_F}{2}t}\left[\cosh\left(\frac{\sqrt{-\Delta_c}}{2}t\right) - \frac{\left(k_c - 2k_{open}\right)}{\sqrt{-\Delta_c}}\sinh\left(\frac{\sqrt{-\Delta_c}}{2}t\right)\right]\right) \quad (8).$$

Finally, we can represent C_0 using an alternative form:

$$C_0 = 1 - O_0 \tag{9}$$

which, when combined with equation (5) yields:

$$\frac{1-C_0}{C_0}=\frac{k_{open}}{k_{close}} \qquad (10).$$

This equation can be re-arranged to obtain

$$\frac{1}{C_0}=\frac{k_{open}}{k_{close}}+1 \qquad (11),$$

which can be combined with equation (7) to obtain

$$I(t)=I_0\left(\frac{k_{close}}{k_{open}}\right)\left(\frac{k_{open}}{k_{close}}+1-\mathrm{e}^{-\frac{k_F}{2}t}\left[\cosh\left(\frac{\sqrt{-\Delta_c}}{2}t\right)-\frac{\left(k_c-2k_{open}\right)}{\sqrt{-\Delta_c}}\sinh\left(\frac{\sqrt{-\Delta_c}}{2}t\right)\right]\right) (12).$$

It is possible to validate this equation in one way by showing that $I(t)=I_0$ when $k_{lock}=0$. Instead of representing intensity, we can represent the fold-increase in intensity, $I_f=I/I_0-1$, as

$$I_f=\frac{k_{close}}{k_{open}}\left(1-\mathrm{e}^{-\frac{k_F}{2}t}\left[\cosh\left(\frac{\sqrt{-\Delta_c}}{2}t\right)-\frac{\left(k_c-2k_{open}\right)}{\sqrt{-\Delta_c}}\sinh\left(\frac{\sqrt{-\Delta_c}}{2}t\right)\right]\right) \qquad (13).$$

For numerical stability, we apply the identities $\cosh(x)=\exp(x)+\exp(-x)$ and $\sinh(x)=\exp(x)-\exp(-x)$ to equation (13) and re-arrange to obtain:

$$I_f=\frac{k_{close}}{k_{open}}\left(1-\frac{\left(1-\frac{\left(k_c-2k_{open}\right)}{\sqrt{-\Delta_c}}\right)}{2}\mathrm{e}^{\frac{\left(\sqrt{-\Delta_c}-k_F\right)}{2}t}+\frac{\left(1+\frac{\left(k_c-2k_{open}\right)}{\sqrt{-\Delta_c}}\right)}{2}\mathrm{e}^{\frac{\left(-\sqrt{-\Delta_c}-k_F\right)}{2}t}\right) (14)$$

We started by fitting equation (14) to data acquired with T cells spreading on surfaces coated with tension probes linked to pMHC ligands with different conditions or treatment. We fit equation (14) to datasets cooperatively using MATLAB's built-in fminunc() function and least-squares residuals fitting. Fitting was performed with ~300 bootstrapping iterations; for each iteration, hundreds of intensity time-lapses and the I_f were randomly drawn from the set of ~100 cells.

3.6. Appendix

Figure A3.1. The basis of mechanically selective hybridization and mechanical steady state. (A) Representative microscopy images of an OT-1 CD8+ T cell producing tension > 4.7 pN on an antiCD3ε DNA tension probe substrate. 200 nM of a 15mer lock-Atto647N strand was added and allowed to hybridize for 10 min. The locked tension was imaged in both Cy3B and Atto647N channel. Scale bar = 5 µm. (B) Co-localization of the lock and the tension signal from mechanically unfolded hairpins using the linescan drawn in (A). (C) Mechanical steady state of OT-1 CD8+ naïve T cells on the DNA tension probe substrate presenting pMHC N4. Most of OT-1 cells reached mechanical steady state 30 min after plating.

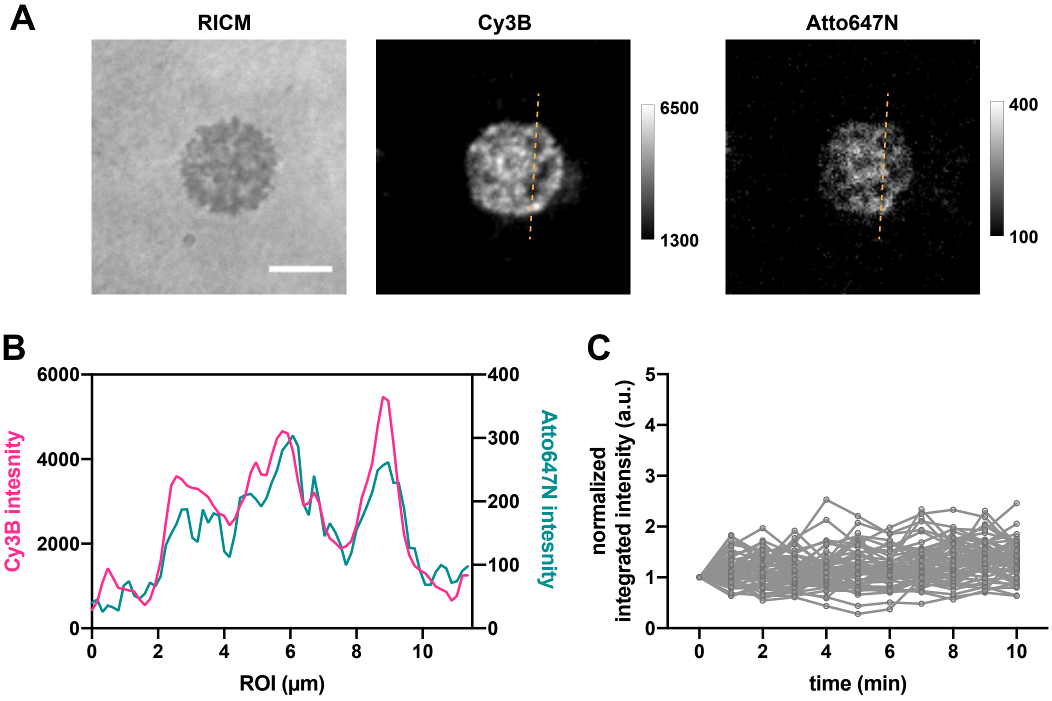

Figure A3.2. Model predictions of the locking kinetics with mock k_{open} and k_{close} values. (A) Locking kinetics profile when force off-rate (inverse of lifetime) is varied and force on-rate is kept constant at 0.01 s^{-1}. (B) Locking kinetics profile when force on-rate (force sampling frequency) is varied and force off-rate is kept constant at 0.5 s^{-1}. For all predictions, k_{hyb} is assumed to be 1.09×10^6 M^{-1} s^{-1}.

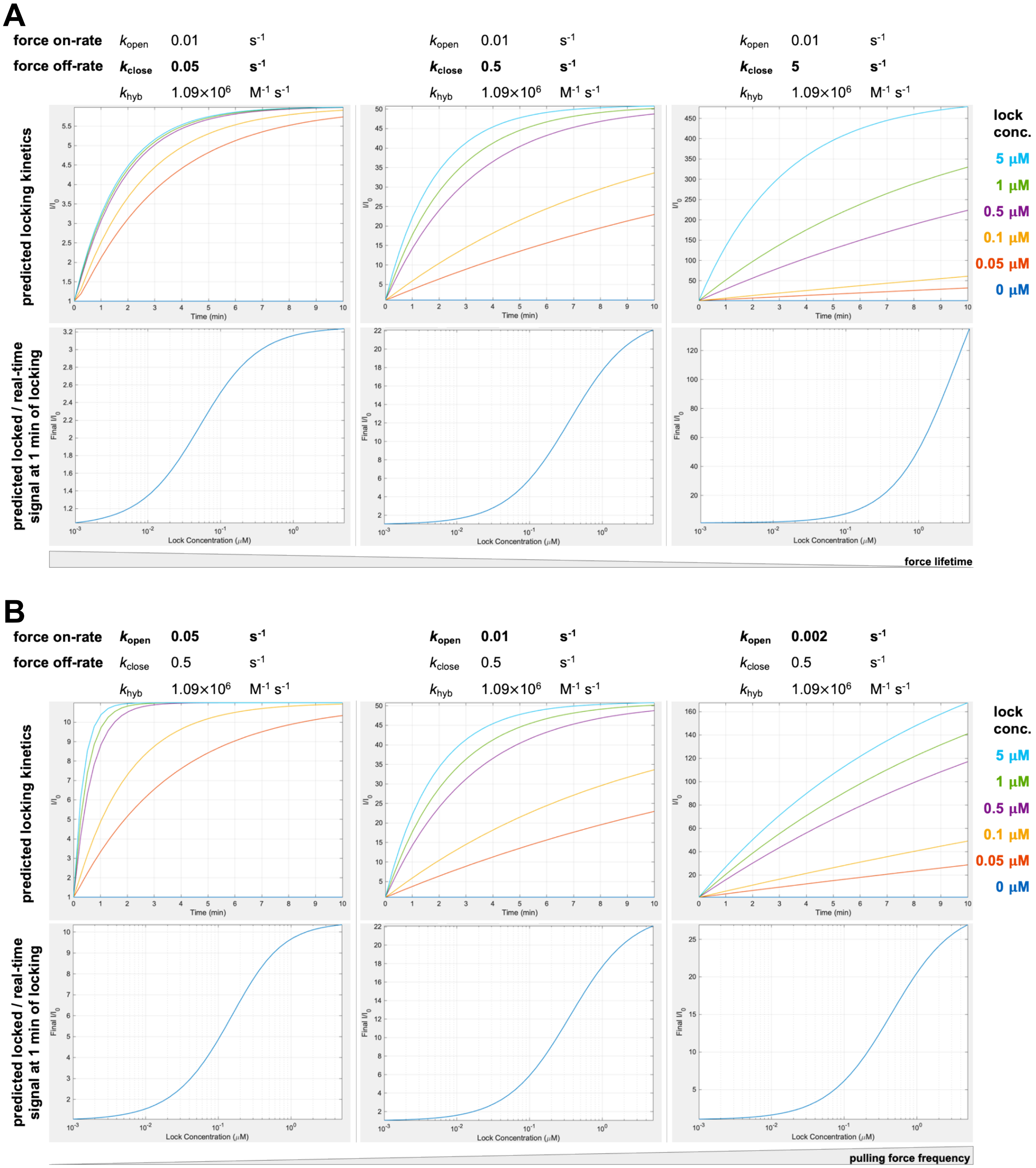

Figure A3.3. Oligonucleotide preparation. HPLC traces show that the oligonucleotides were successfully conjugated with Cy3B or Atto647N fluorescent dyes and purified for this study.

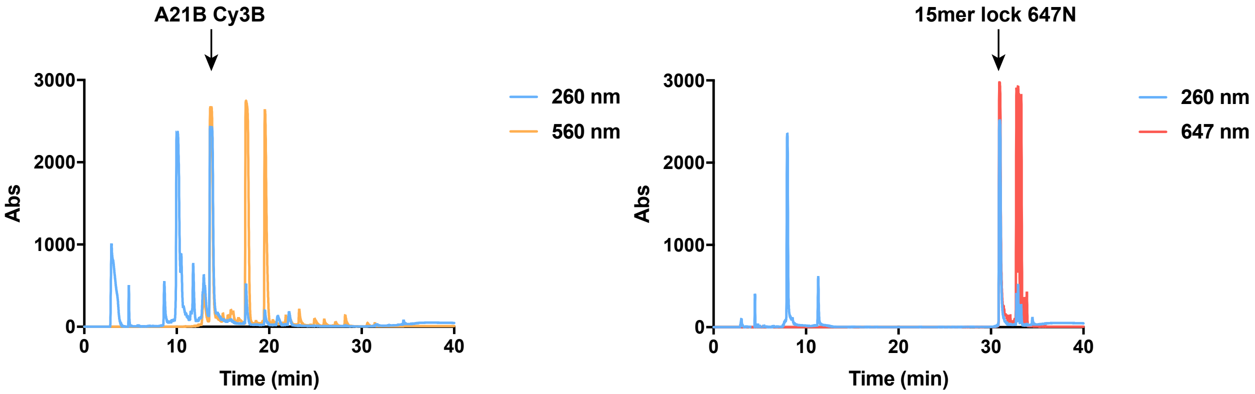

Figure A3.4. Illustration of the surface preparation procedures.

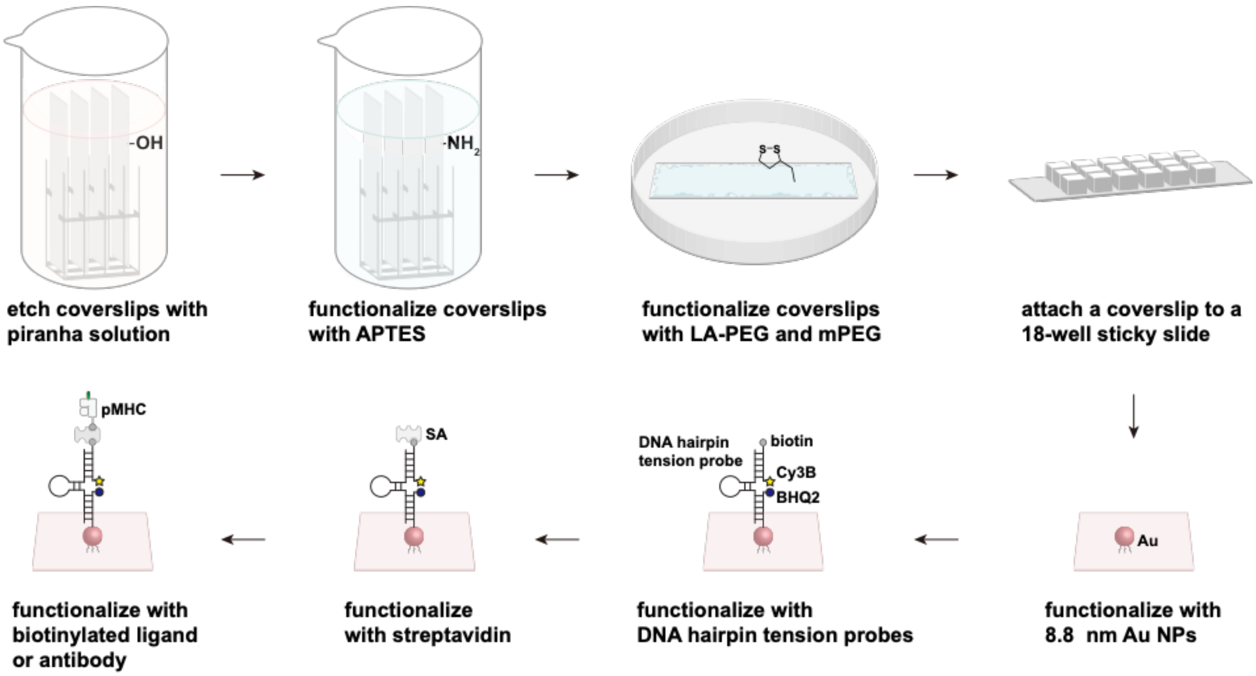

Figure A3.5. **Representative microscopy images of tension against antiCD3ε, pMHC N4 and pMHC Q4 before and after adding the lock at different concentrations.** OT-1 T cells cells were plated on DNA hairpin tension probe substrates presenting either antiCD3ε, pMHC N4, or pMHC Q4. RICM and real-time tension signal images are shown prior to the addition of different concentrations of the lock. Locked-tension signal images of the same cells are then shown 1 min and 10 min after addition of the lock.

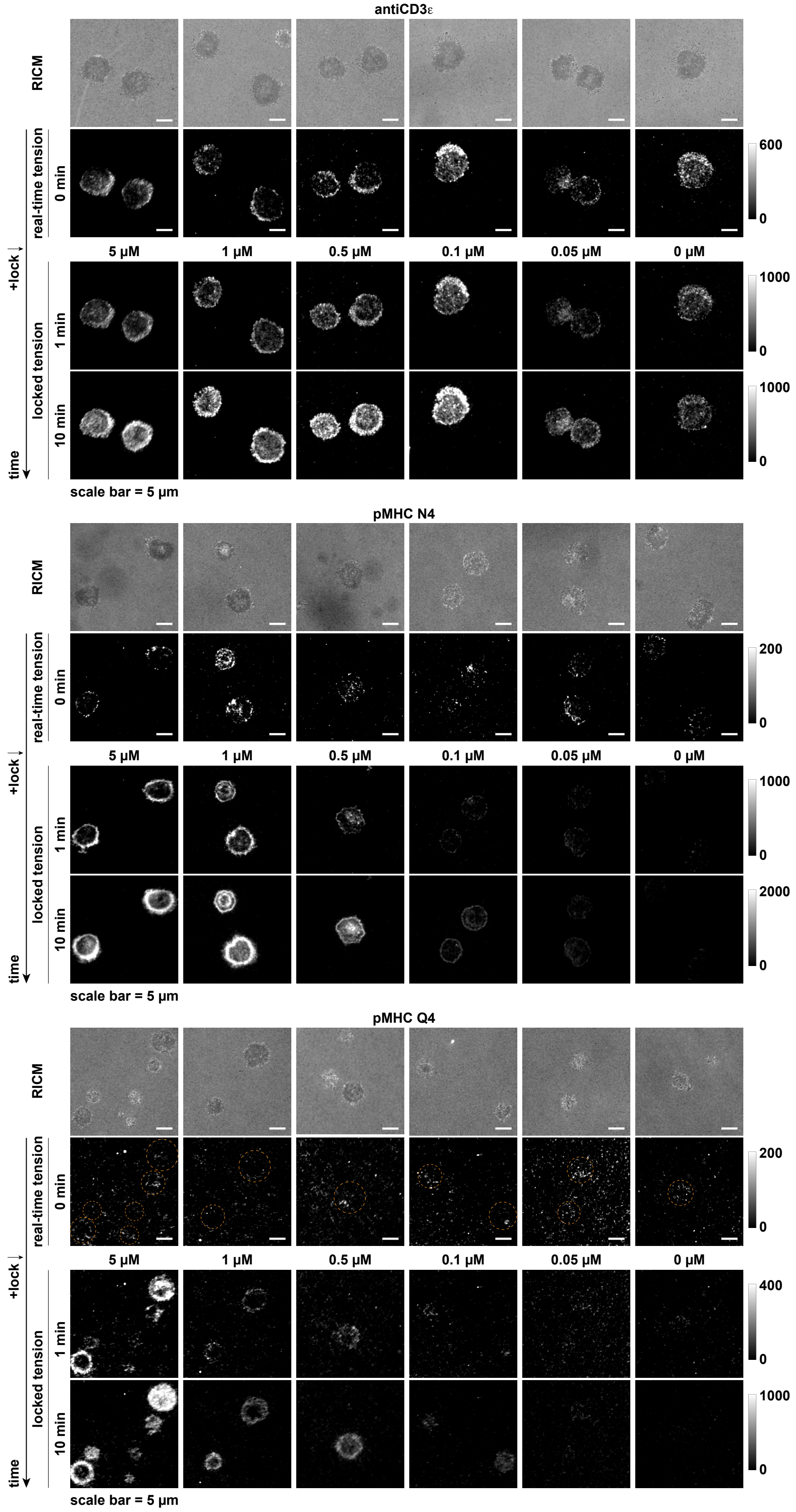
antiCD3ε
RICM
real-time tension
0 min
+lock
locked tension
1 min
10 min
time
5 µM
1 µM
0.5 µM
0.1 µM
0.05 µM
0 µM
600
0
1000
0
1000
0
scale bar = 5 µm
pMHC N4
RICM
real-time tension
0 min
+lock
locked tension
1 min
10 min
time
5 µM
1 µM
0.5 µM
0.1 µM
0.05 µM
0 µM
200
0
1000
0
2000
0
scale bar = 5 µm
pMHC Q4
RICM
real-time tension
0 min
+lock
locked tension
1 min
10 min
time
5 µM
1 µM
0.5 µM
0.1 µM
0.05 µM
0 µM
200
0
400
0
1000
0
scale bar = 5 µm

Figure A3.6. Representative quantification of the TCR tension signal on pMHC N4. (A) Raw integrated intensity of the tension signal over time after addition of different concentration of the lock. (B) Normalized integrated intensity over time after addition of different concentration of the lock. Data for each concentration was collected from 3 mice.

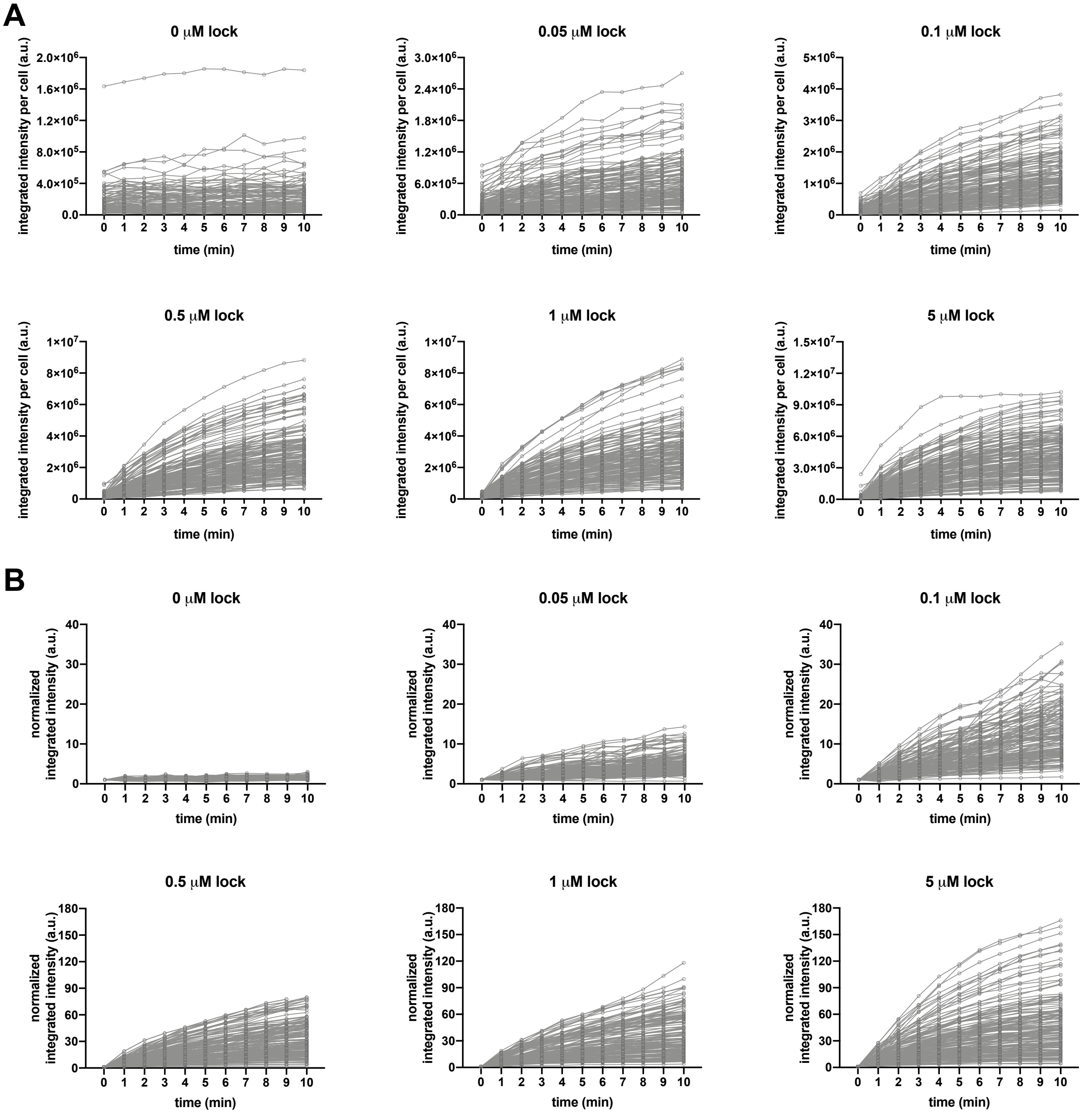

Figure A3.7. Model fit with the locking kinetics data from each mouse for surfaces with different ligands. Several representative plots showing the model fitting results for k_{close}, k_{open}, and force lifetime of TCR forces on antiCD3ε, pMHC N4, or pMHC Q4. Each representative plot contains data from an individual mice spleen.

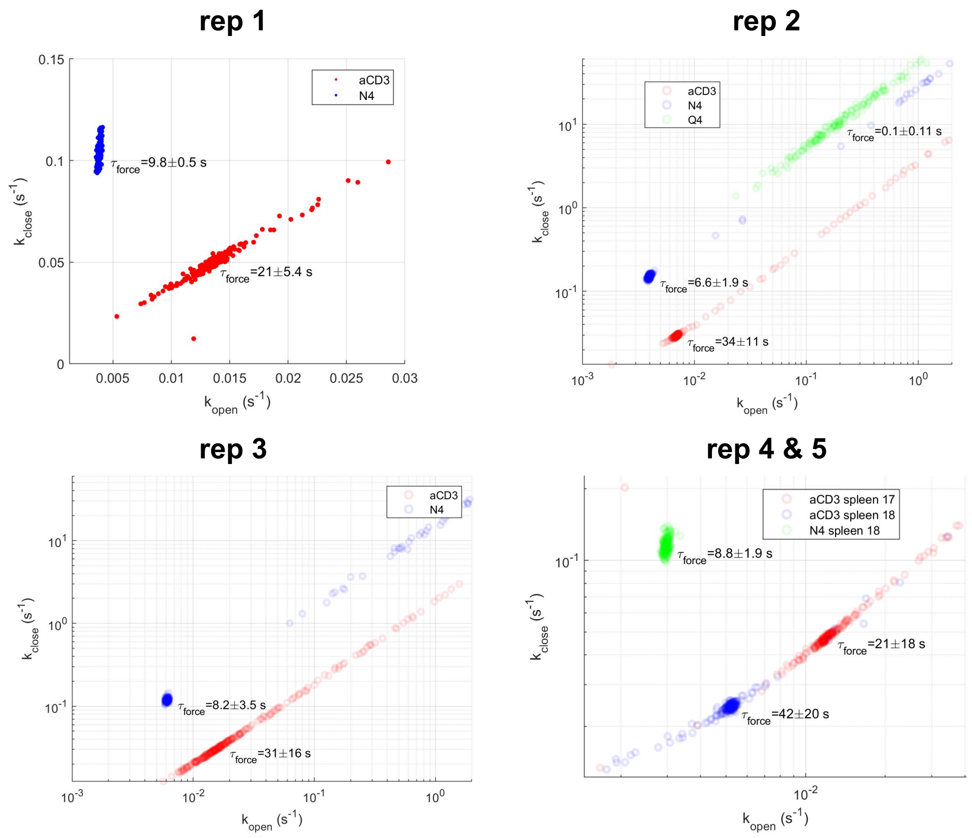

Figure A3.8. Surface preparation procedure for co-presenting co-receptor ligands.

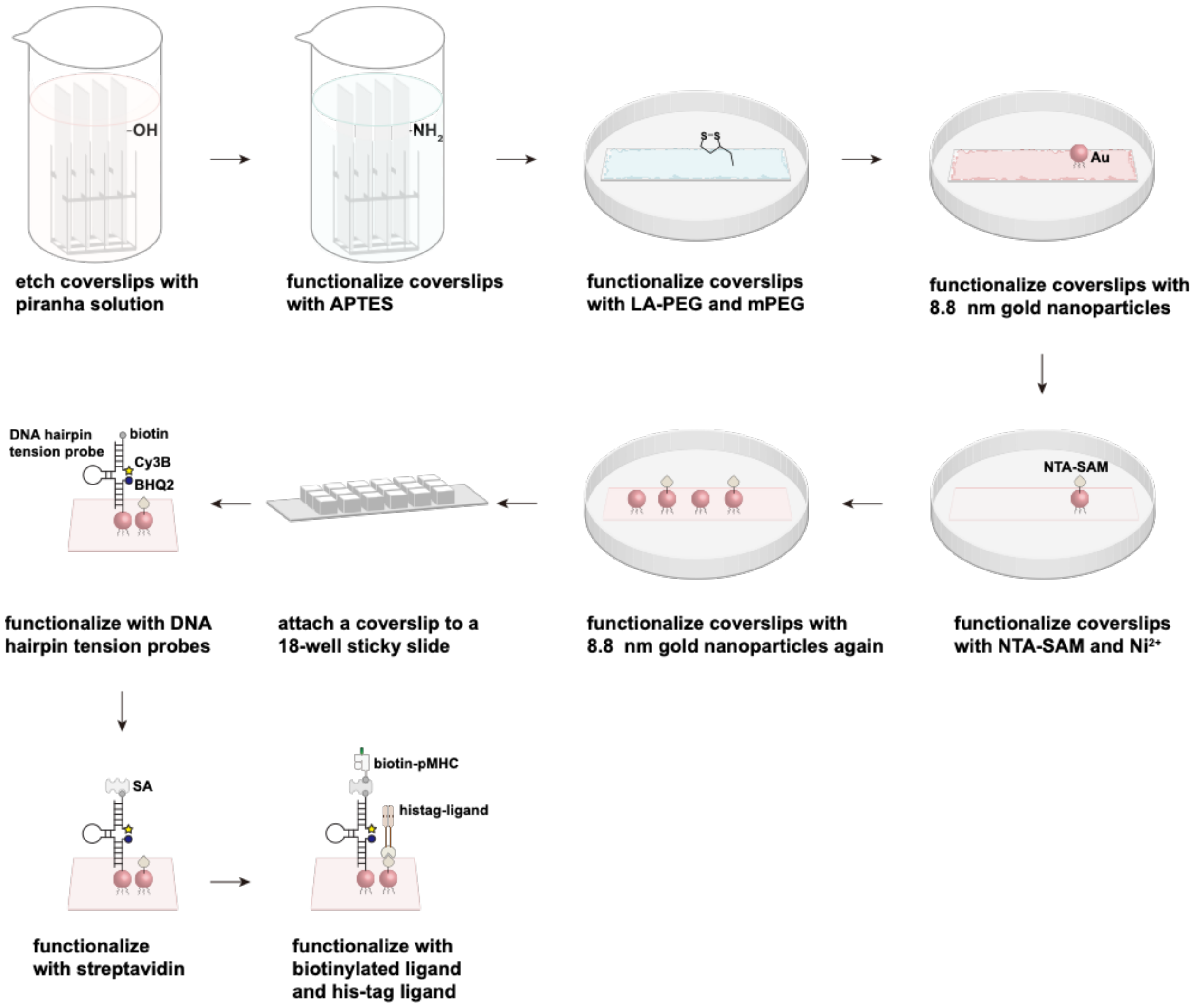

Figure A3.9. Representative microscopy images of TCR tension signal before and after adding the lock at different concentrations while co-presenting B7-1 or ICAM-1. OT-1 T cells cells were plated on DNA hairpin tension probe substrates presenting co-presenting pMHC N4 and B7-1 or ICAM-1. RICM and real-time tension signal images are shown prior to the addition of different concentrations of the lock. Locked-tension signal images of the same cells are then shown 1 min and 10 min after addition of the lock.

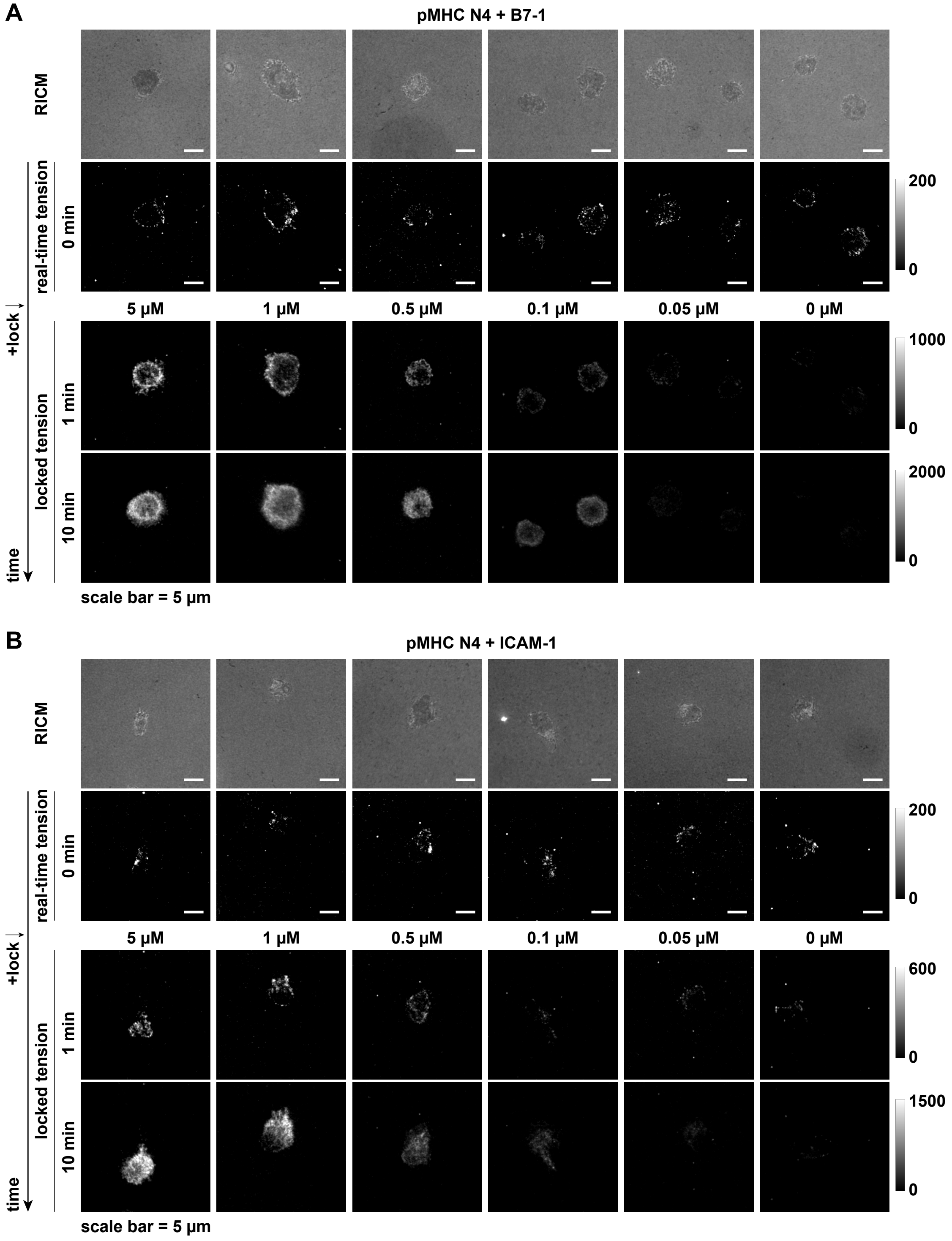

Figure A3.10. Effect of co-receptor engagement on real-time tension area and contact area over 10 min. Real-time tension area and contact area for cells plated on pMHC N4, pMHC N4 + B7-1, or pMHC N4 + ICAM-1 surfaces were calculated by quantifying the total area of all the pixels with a fluorescent value exceeding a baseline threshold value the contact area and the total area that the cell contacted over a 10-minute time interval. Plots show the area of each individual cell from each group (n= 1202, 1097, and 1254 cells for N4, N4 + B7-1, and N4 + ICAM-1, respectively) along with the median value +/- 25% indicated by the overlayed lines. Statistical analysis to determine significant differences between each group were performed using the Brown-Forsythe ANOVA and Games-Howell's multiple comparisons test (**** P < 0.0001).

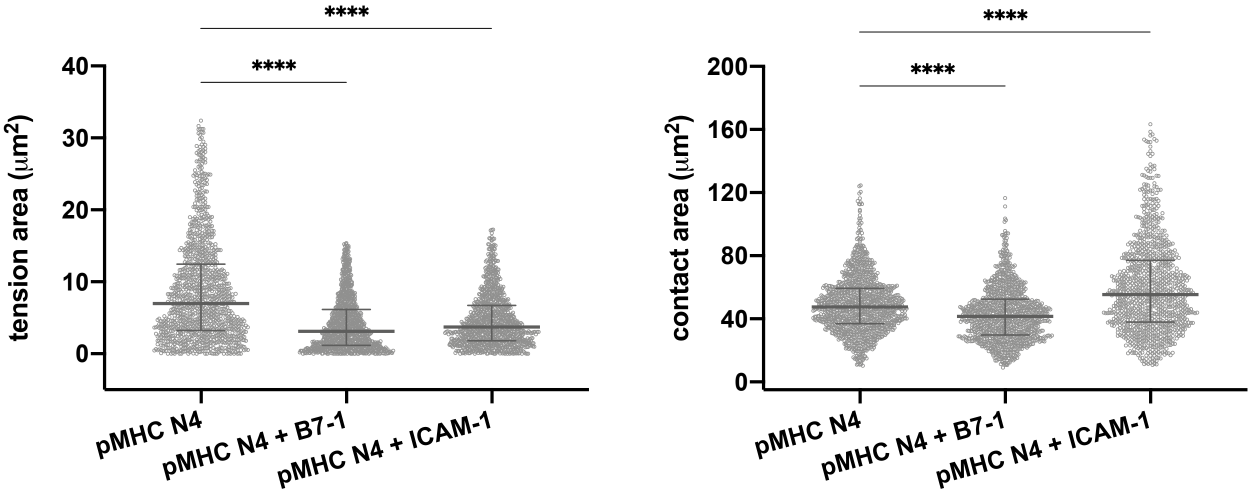

Figure A3.11. Quantification of the TCR tension signal on pMHC N4 DNA tension probe substrate co-presenting B7-1 or ICAM-1. (A) Plots show normalized integrated intensity over time of TCR force with the presence of B7-1 after addition of different concentration of the lock. Each curve represents an individual cell. Data for each concentration was collected from 3 mice. (B) Plots show normalized integrated intensity over time of TCR force with the presence of ICAM-1 after addition of different concentration of the lock. Data for each concentration was collected from 3 mice.

pMHC N4 + B7-1

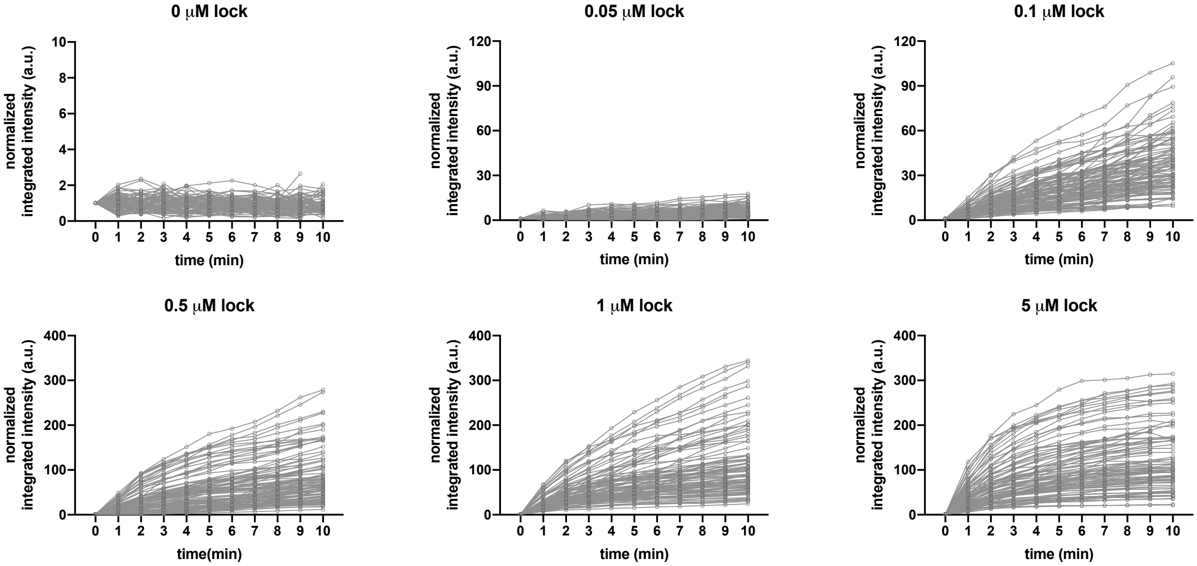

pMHC N4 + ICAM-1

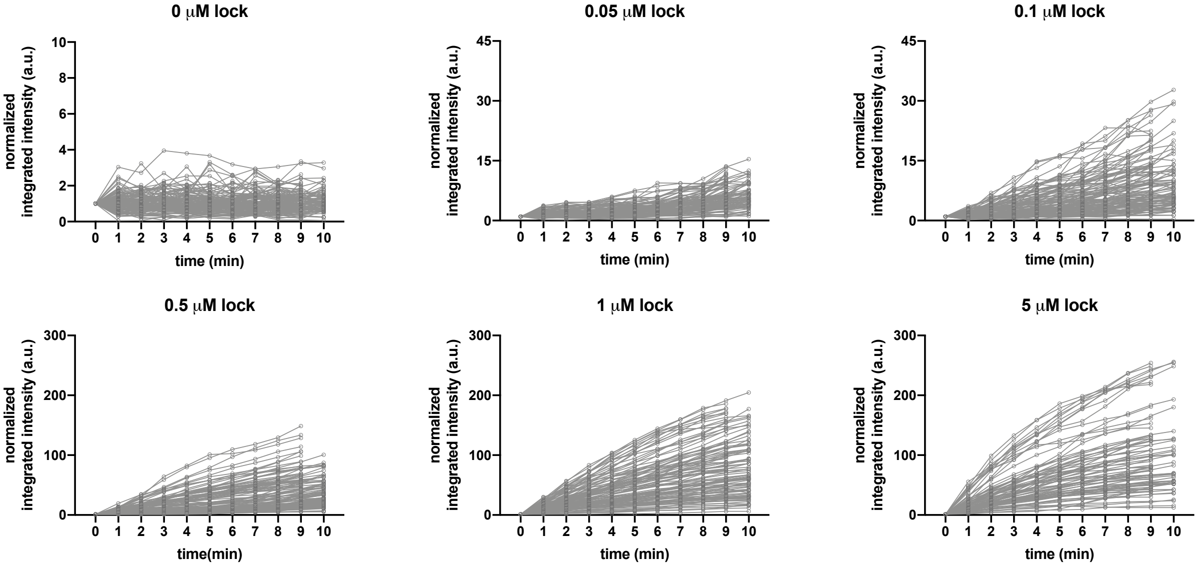

Figure A3.12. Locking kinetics of TCR forces applied by OT-1 CD8+ naïve T cells to pMHC N4 in the presence of B7-1 or ICAM-1. (A) Data is represented by locked/real-time integrated intensity of tension signal per cell (mean ± SEM). Data shows the average from 71-149 cells from 3 mice per concentration for B7-1 and 81-125 cells from 3 mice per concentration for ICAM-1. The locked/real-time integrated intensity represents the frequency of mechanical sampling. (B) Plots show integrated intensity of tension signal per cell (median ± interquartile range) after 1 min of locking at different lock concentrations for cells that were incubated on pMHC N4 substrate alone or with the presence of B7-1 and ICAM-1. The integrated intensity represent total mechanical sampling per cell within 1 min. Statistical analysis was performed with Brown-Forsythe ANOVA and Games-Howell's multiple comparisons test (ns $P > 0.05$, * $P < 0.05$, **** $P < 0.0001$).

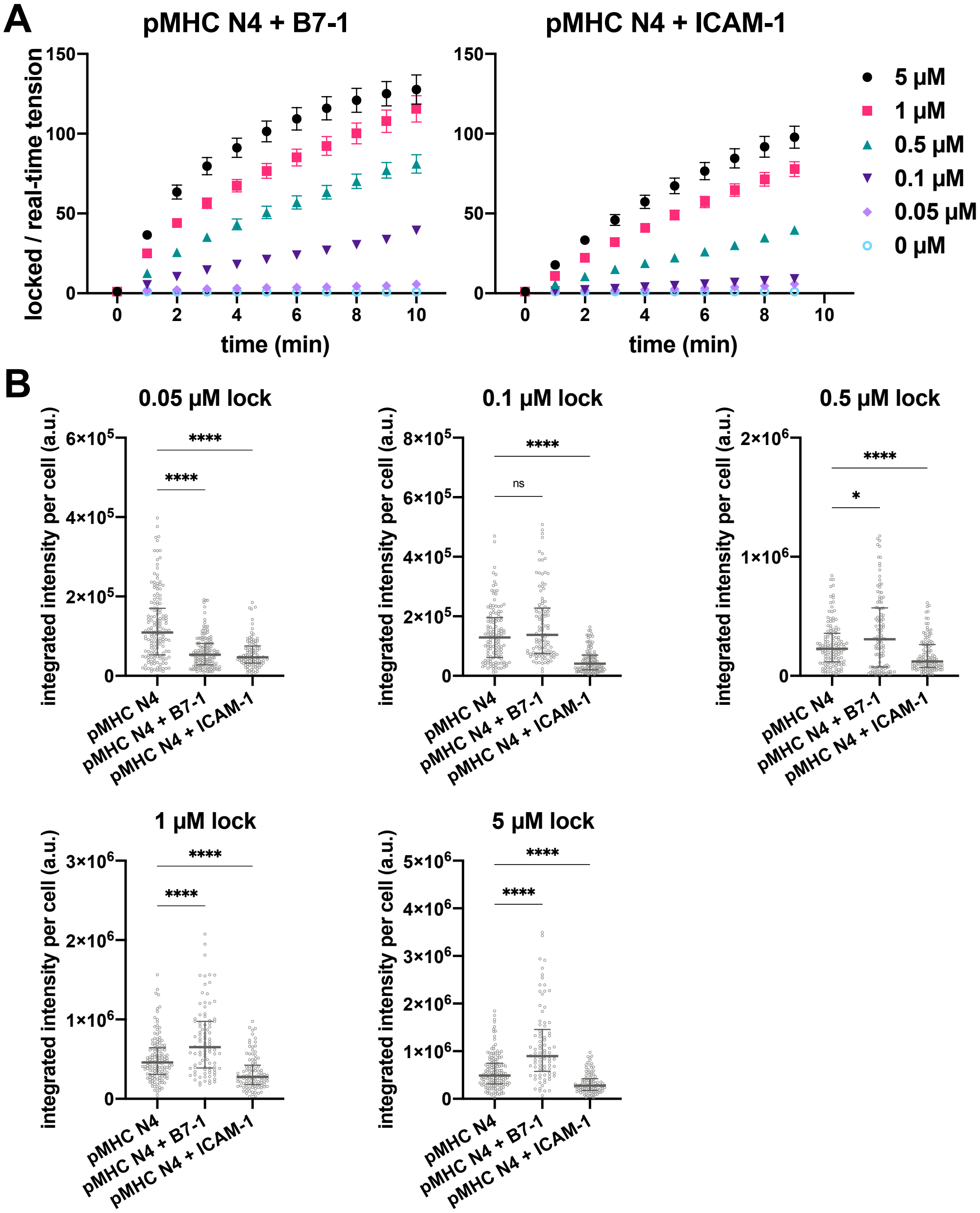

Figure A3.13. Model fit with the locking kinetics data from individual mice for surfaces with different co-receptors. Plots showing the model fitting results for k_{close}, k_{open}, and force lifetime of TCR forces on pMHC N4 DNA tension probes alone, or co-presenting either B7-1 or ICAM-1. Each representative plot contains data from an individual mice spleen.

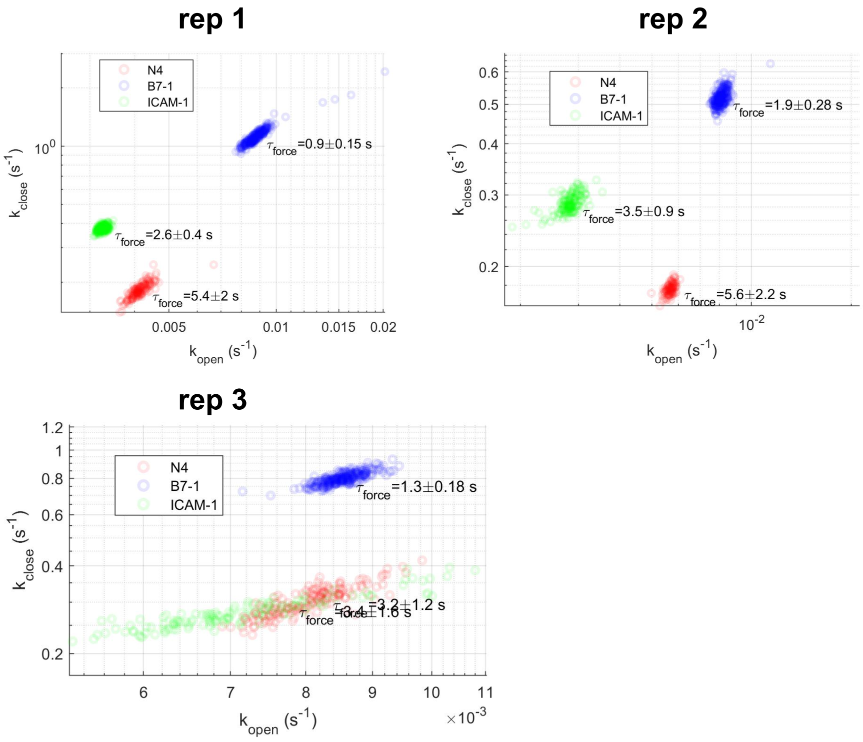

Figure A3.14. Representative microscopy images of TCR real-time and locked tension with CK666 treatment. OT-1 T cells were plated on DNA hairpin tension probe substrates presenting pMHC N4 and then treated with 50 µM of CK666 after reaching mechanical steady state. Real-time tension signal images are shown over a 5 min interval following CK666 addition prior to the addition of different concentrations of the lock. Locked-tension signal images of the same cells are then shown 1 min and 10 min after addition of the lock.

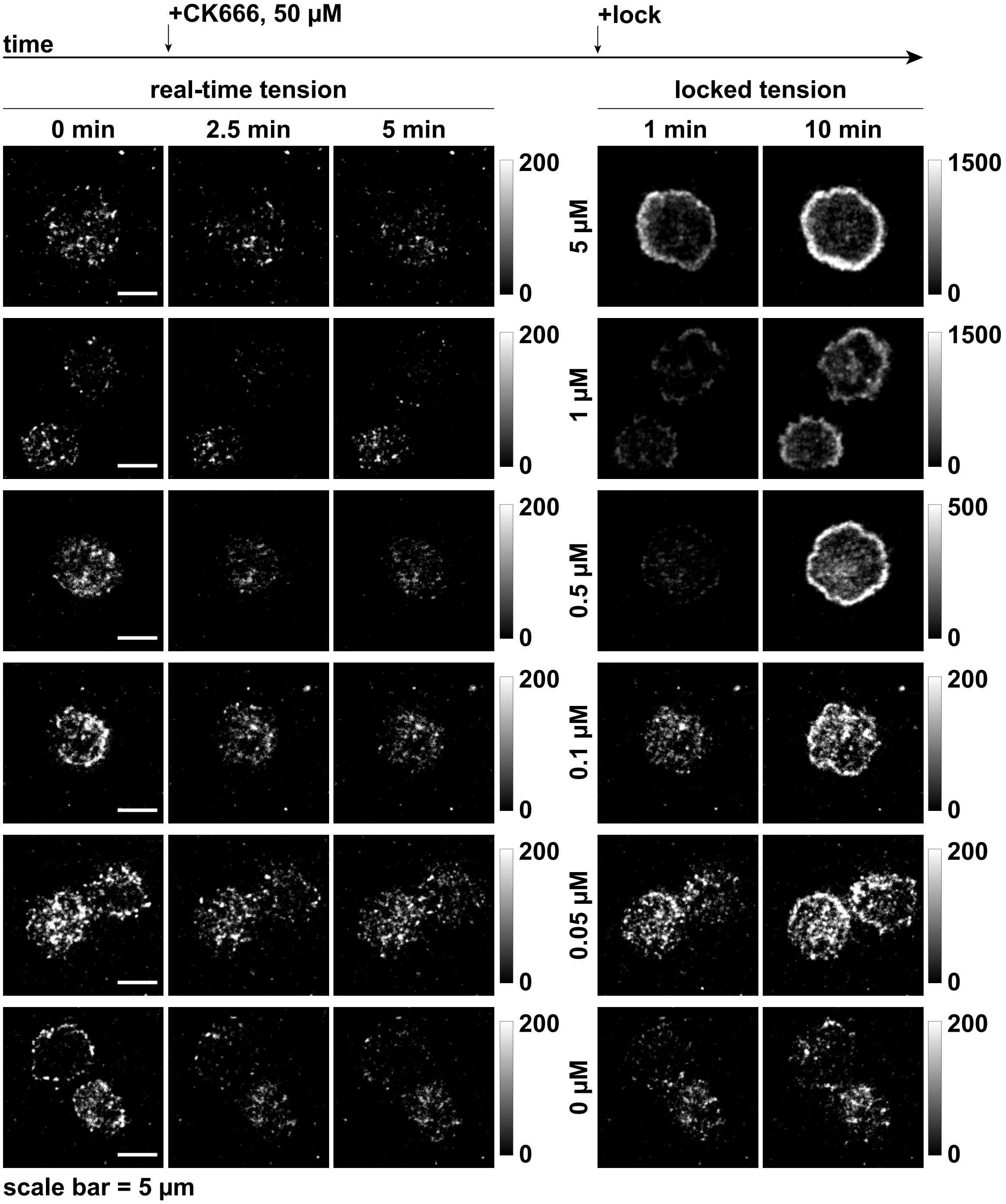

Figure A3.15. Representative microscopy images of TCR real-time and locked tension with Blebb treatment. OT-1 T cells were plated on DNA hairpin tension probe substrates presenting pMHC N4 and then treated with 50 μM of Blebbistatin after reaching mechanical steady state. Real-time tension signal images are shown over a 5 min interval following Blebbistatin addition prior to the addition of different concentrations of the lock. Locked-tension signal images of the same cells are then shown 1 min and 10 min after addition of the lock.

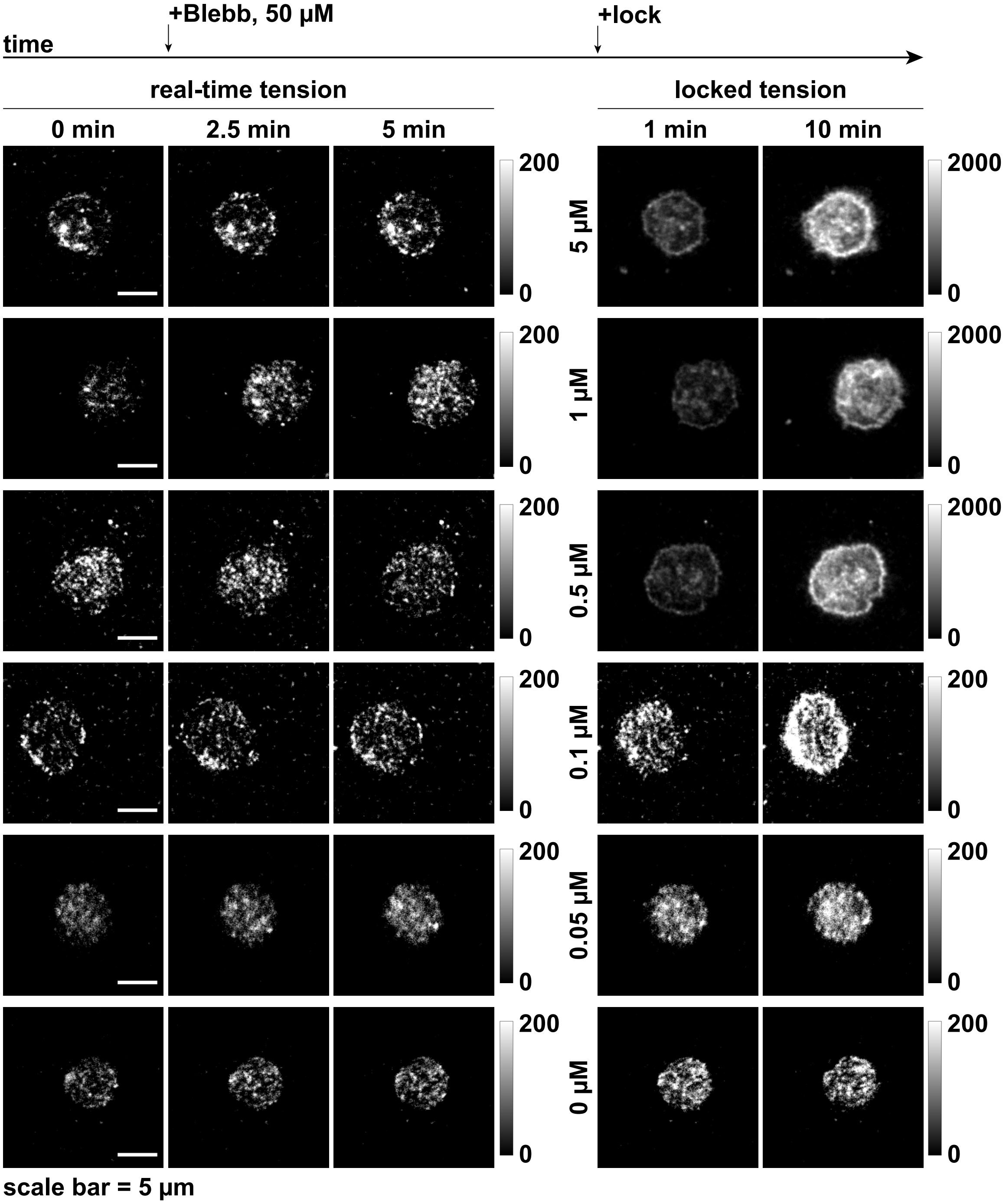

Figure A3.16. Representative microscopy images of TCR real-time and locked tension with Jas treatment. OT-1 T cells were plated on DNA hairpin tension probe substrates presenting pMHC N4 and then treated with 1 μM of Jasplakinolide after reaching mechanical steady state. Real-time tension signal images are shown over a 5 min interval following Jasplakinolide addition prior to the addition of different concentrations of the lock. Locked-tension signal images of the same cells are then shown 1 min and 10 min after addition of the lock.

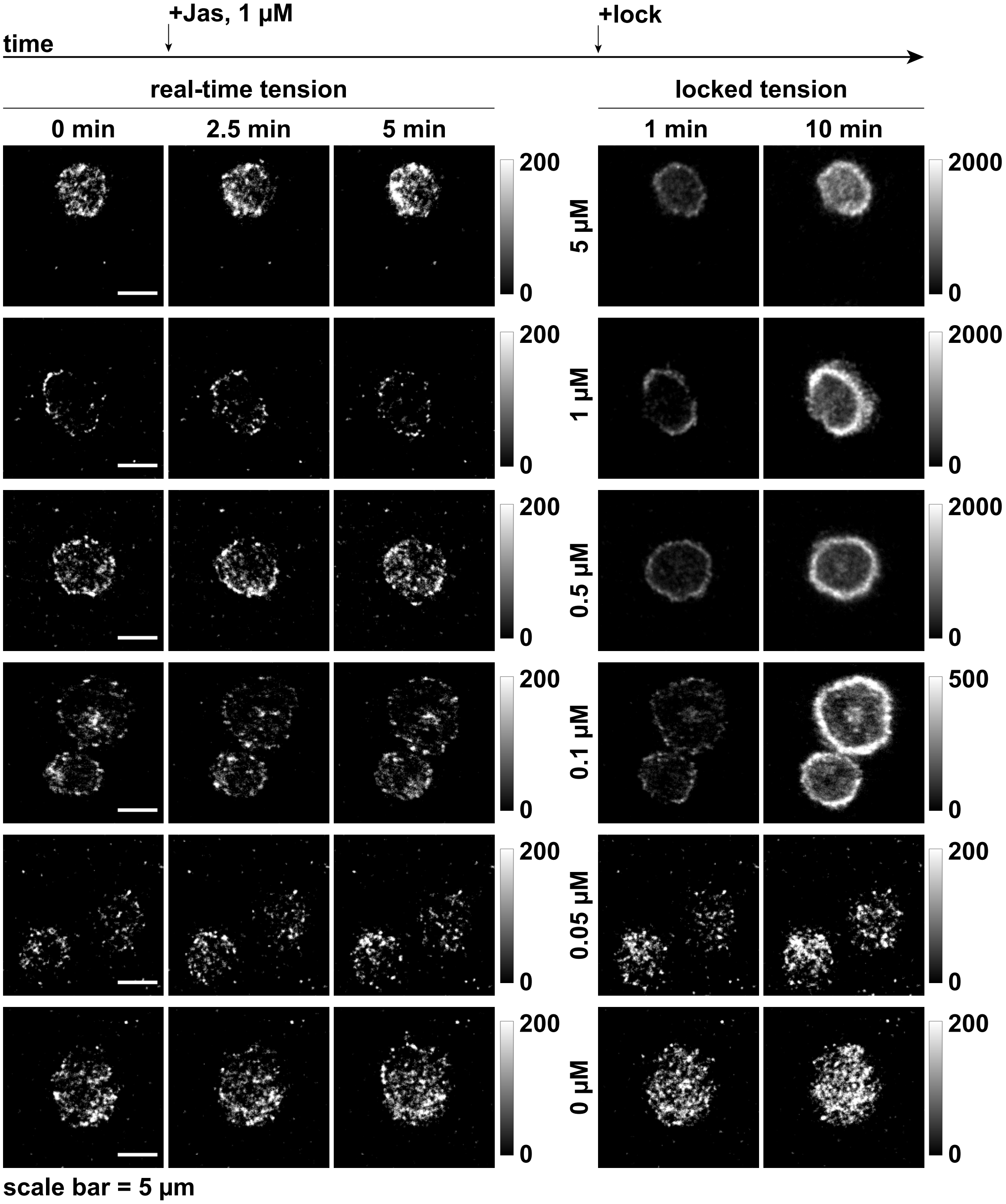

Figure A3.17. Representative microscopy images of TCR real-time and locked tension with DMSO treatment. OT-1 T cells were plated on DNA hairpin tension probe substrates presenting pMHC N4 and then treated with 0.5% DMSO after reaching mechanical steady state as a negative control to confirm that the effects of the drug treatments were not a result of DMSO addition. Real-time tension signal images are shown over a 5 min interval following DMSO addition prior to the addition of different concentrations of the lock. Locked-tension signal images of the same cells are then shown 1 min and 10 min after addition of the lock.

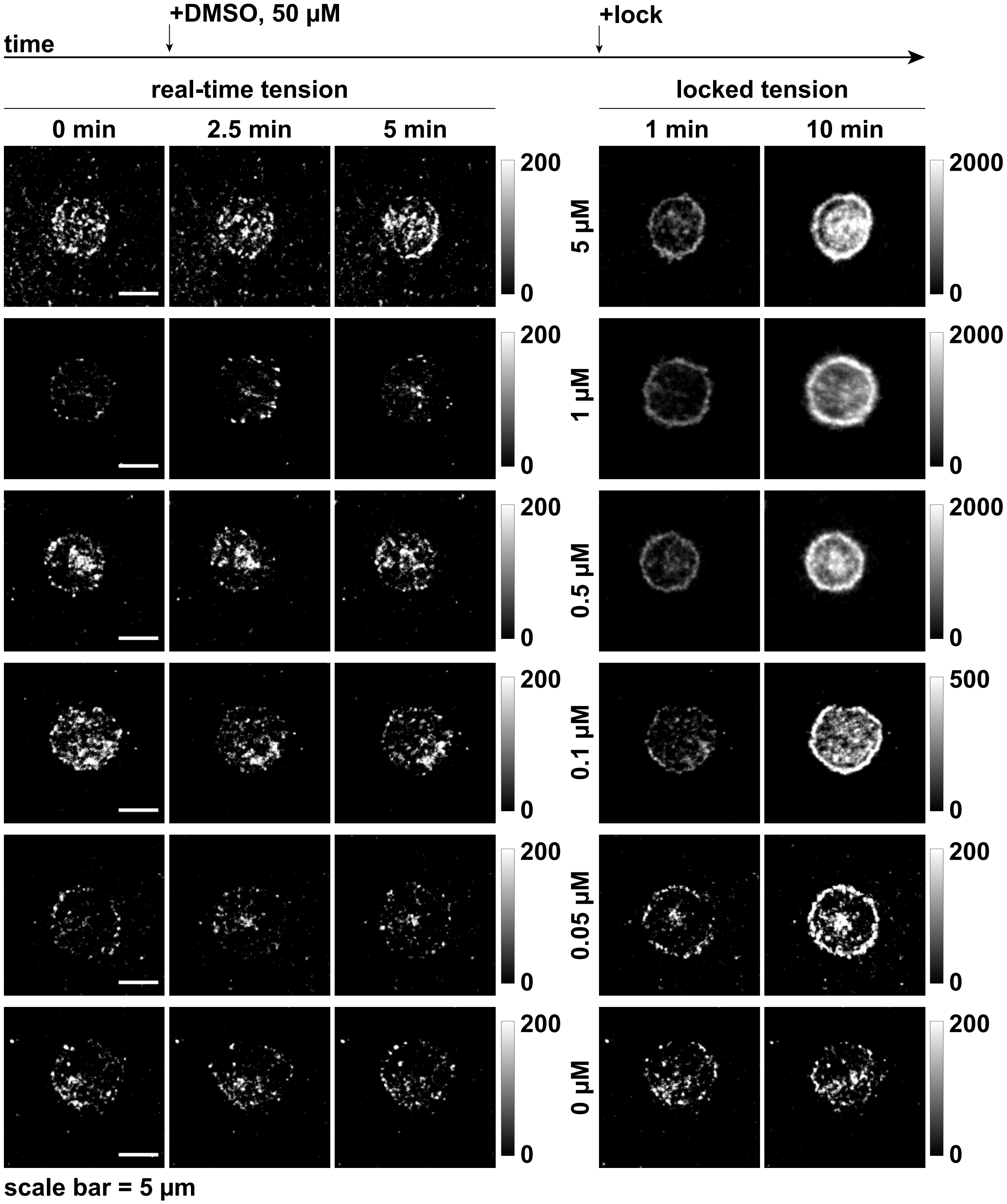

Figure A3.18. Effect of cytoskeleton network inhibitors on real-time TCR forces and contact area. (A) Plot shows the quantification of real-time tension signal (F>4.7 pN) that OT-1 CD8+ T cells generated against pMHC N4 after 5 min of 0.5% DMSO, 50 µM CK666, 50 µM Blebb, or 1 µM Jas treatment. Integrated intensity of tension signal per cell was normalized to that of the same cell before the addition of the drug. Bars represent mean ± SEM. Statistical analysis was performed with one-way ANOVA and Dunnett's multiple comparisons test. Experiments were performed with 3 mice with a total n > 406 cells per condition. (B) Plot shows the contact area of OT-1 CD8+ T cells on the pMHC DNA tension probe substrate during 10 min of image acquisition. Bars represent mean ± SEM. Statistical analysis was performed with one-way ANOVA and Dunnett's multiple comparisons test (ns P > 0.05, * P < 0.05, **** P < 0.0001). Experiments were performed with 3 mice with a total n > 1042 cells per condition.

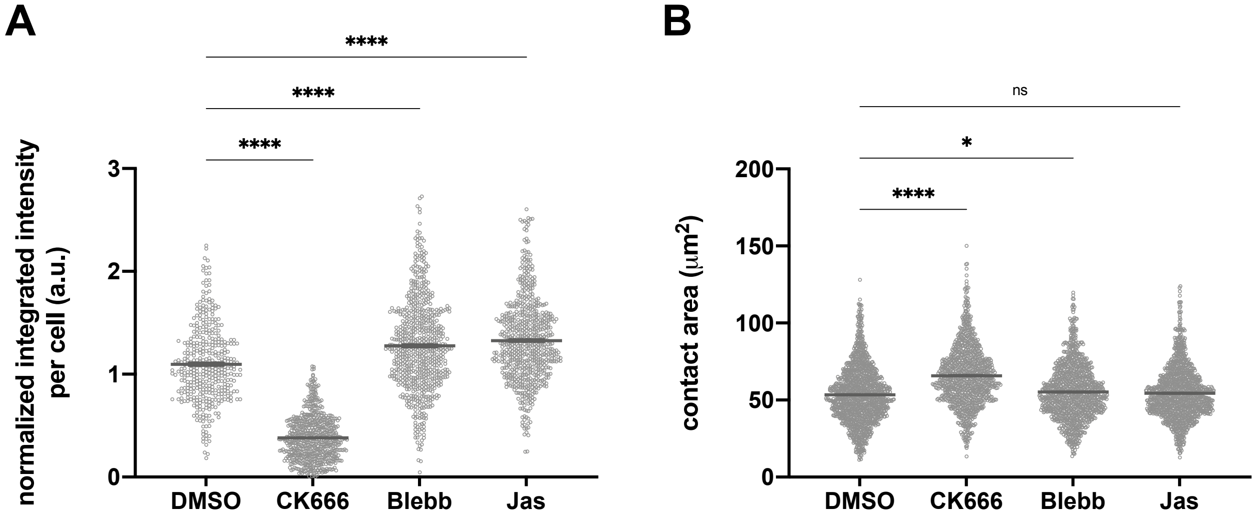

Figure A3.19. Locking kinetics of the TCR tension signal on pMHC N4 with CK666, Blebb, Jas, and DMSO treatment. (A) OT-1 CD8$^+$ T cells were plated on DNA tension probes substrate presenting pMHC N4. After reaching mechanical steady state, 50 µM CK666, 50 µM Blebb, 1 µM Jas, or 0.5% DMSO was added, and the real-time tension signal was captured at t = 0 min (before drug), 2.5 min (with drug) and 5 min (+lock). Time-lapses were acquired when the lock was added at a final concentration of either 5 µM, 1 µM, 0.5 µM, 0.1 µM, 0.05 µM or 0 µM. The tension signal was normalized to that of the same cell at t = 0 min. Plots show data (mean ± SEM) obtained from 3 independent experiments (total cells: CK666, n = 120-145; Blebb, n = 66-154; Jas, n = 82-156; DMSO, n=130-195 for each concentration of lock.) (B) Plot shows the integrated intensity of accumulated tension at 5 µM lock after 5 min of locking. Statistical analysis was performed with Brown-Forsythe ANOVA and Games-Howell's multiple comparisons test (ns $P > 0.05$, **** $P < 0.0001$).

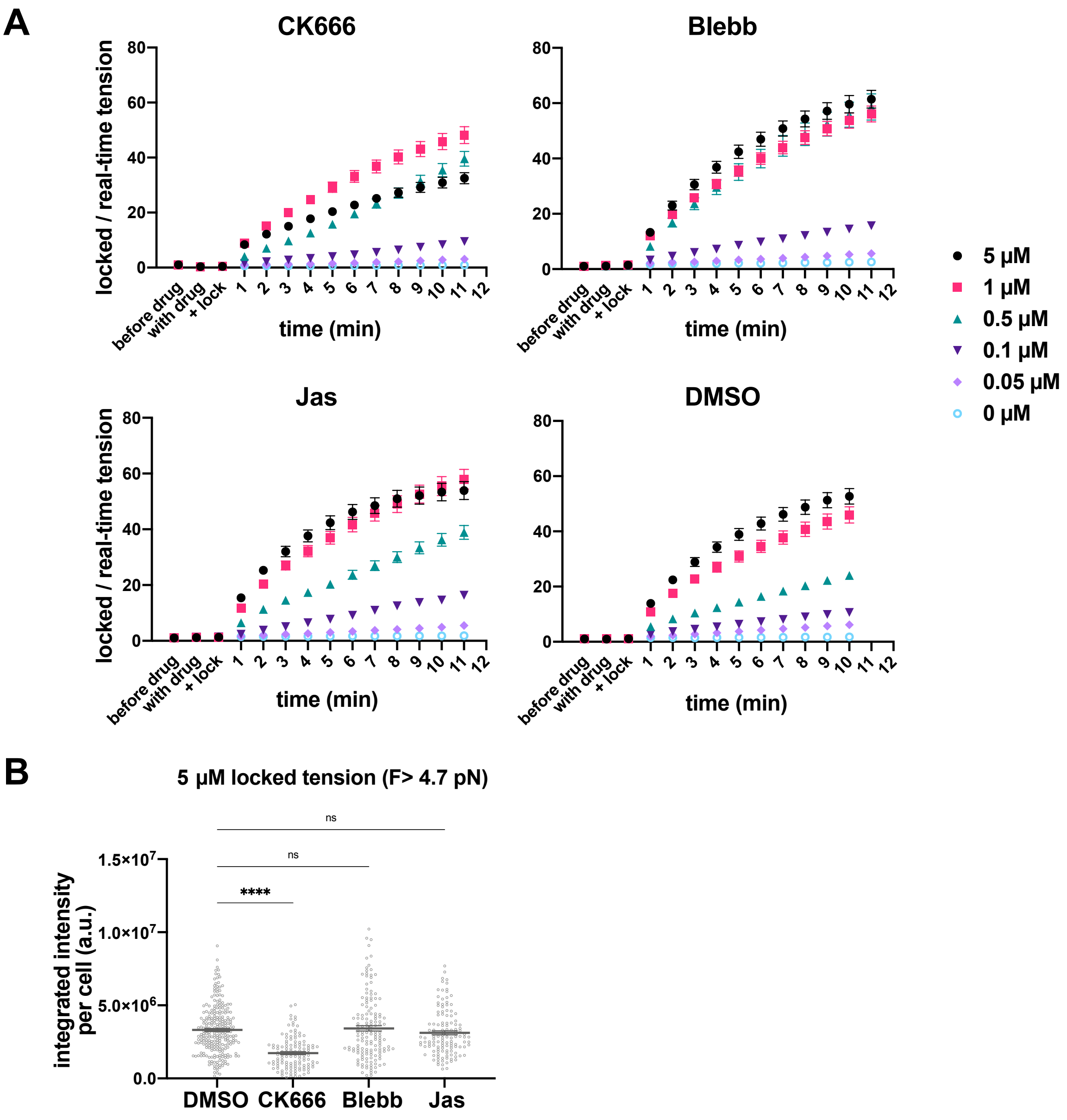

Figure A3.20. Model fit with the locking kinetics data from individual mice for cells treated with drug inhibitors. (A) Plot showing the model fitting results for k_{close}, k_{open}, and force lifetime of TCR forces on on pMHC N4 DNA tension probes of cells treated with Blebbistatin or Jasplakinolide. Each replicate contains data from an individual mice spleen. (B) k_{open} values obtained from model fitting for TCR forces following no treatment or treatment with CK666, Blebbistatin, or Jaspakinolide. Error bars represent mean +/- SEM and statistical analysis to test for significant differences between each group was performed using the ANOVA and Dunnett's multiple comparisons test (ns, P > 0.05).

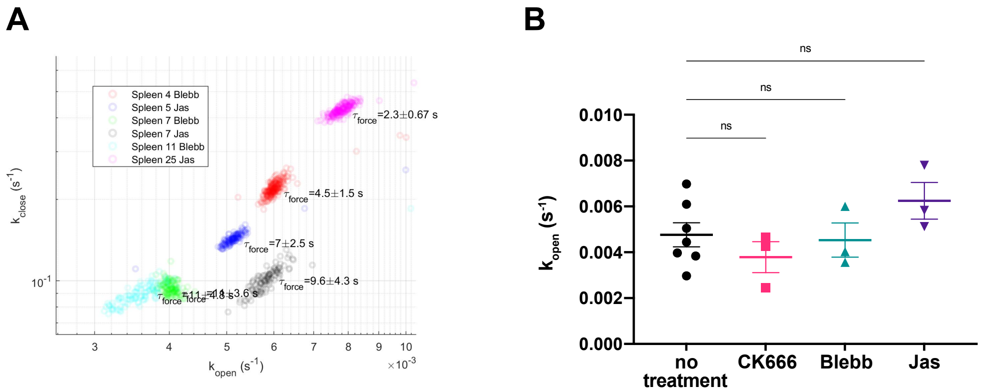

Figure A3.21. Representative flow cytometry data showing TCR density is not affected by the experimental conditions. (A) OT-1 CD8$^+$ T cell TCR density after incubation on glass slides coated with pMHC N4, pMHC N4 + B7-1, or pMHC N4 + ICAM-1. (B) OT-1 CD8$^+$ T cell TCR density after incubation in solution for 5 min with drug inhibitors. Cells were stained with a PE-TCR antibody, and the fluorescence of the cells were measured with a flow cytometer. An isotype antibody was included as a negative control. PE molecules/um^2 were calculated using a standard curve generated from flow cytometry analysis of microparticles labeled with known quantities of PE molecules. Experiments were performed with 2 biological replicates.

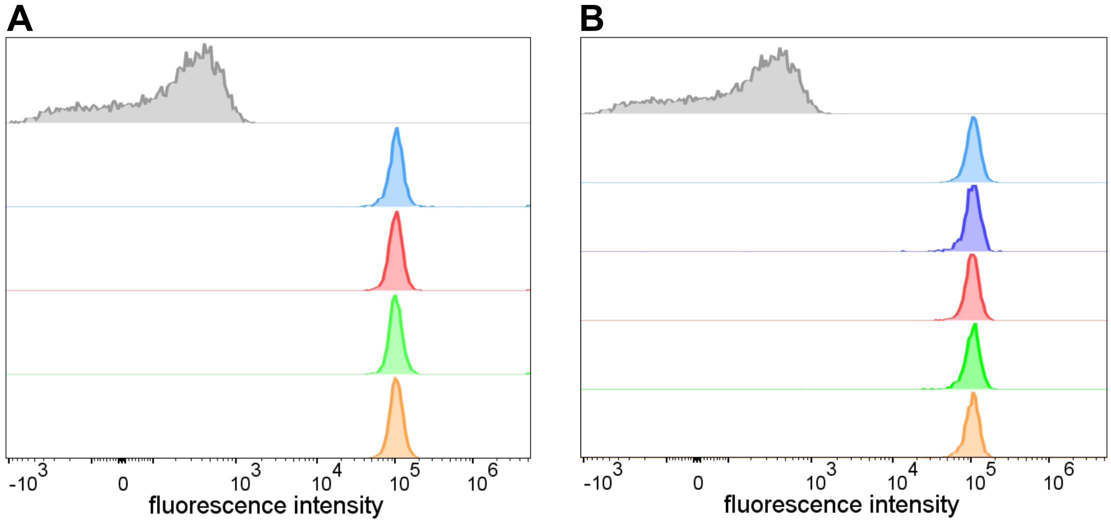

	SampleID	PE molecules/um2
⬜	OT1 CD8+, isotype control	
🟦	OT1 CD8+, cells only	174.3
🟥	OT1 CD8+, pMHC N4	173.2
🟩	OT1 CD8+, pMHC N4 + B7-1	174.3
🟧	OT1 CD8+, pMHC N4 + ICAM-1	174.5

	SampleID	PE molecules/um2
⬜	OT1 CD8+, isotype control	
🟦	OT1 CD8+, cells only	178.4
🟪	OT1 CD8+, DMSO, 0.5% 5min	171.2
🟥	OT1 CD8+, CK666, 50 uM 5min	171.1
🟩	OT1 CD8+, Jas, 1 uM 5min	170.2
🟧	OT1 CD8+, Blebb, 50 uM 5 min	170.3

Movie A3.1. Locking kinetics of OT-1 TCR force with antiCD3ε with 5, 1, 0.5, 0.1, 0.05, 0 µM lock.

Movie A3.2. Locking kinetics of OT-1 TCR force with pMHC N4 with 5, 1, 0.5, 0.1, 0.05, 0 µM lock.

Movie A3.3. Locking kinetics of OT-1 TCR force with pMHC Q4 with 5, 1, 0.5, 0.1, 0.05, 0 µM lock.

Movie A3.4. Locking kinetics of OT-1 TCR force with CD28-B7-1 engagement with 5, 1, 0.5, 0.1, 0.05, 0 µM lock.

Movie A3.5. Locking kinetics of OT-1 TCR force with LFA-1-ICAM-1 engagement with 5, 1, 0.5, 0.1, 0.05, 0 µM lock.

Movie A3.6. Locking kinetics of OT-1 TCR force with CK666 inhibition of Arp2/3 with 5, 1, 0.5, 0.1, 0.05, 0 µM lock.

Movie A3.7. Locking kinetics of OT-1 TCR force with Blebb inhibition of myosin II with 5, 1, 0.5, 0.1, 0.05, 0 µM lock.

Movie A3.8. Locking kinetics of OT-1 TCR force with Jas arresting actin flow with 5, 1, 0.5, 0.1, 0.05, 0 µM lock.

Movie A3.9. Locking kinetics of OT-1 TCR force with DMSO control with 5, 1, 0.5, 0.1, 0.05, 0 µM lock.

Scale bar = 5 µm.

3.7. References

1. A. H. Courtney; W. L. Lo; A. Weiss, TCR Signaling: Mechanisms of Initiation and Propagation. *Trends Biochem Sci* **2018,** *43* (2), 108.

2. D. L. Harrison; Y. Fang; J. Huang, T-Cell Mechanobiology: Force Sensation, Potentiation, and Translation. *Front Phys* **2019,** *7*.

3. C. Zhu; W. Chen; J. Lou; W. Rittase; K. Li, Mechanosensing through immunoreceptors. *Nat Immunol* **2019,** *20* (10), 1269.

4. R. Basu; B. M. Whitlock; J. Husson; A. Le Floc'h; W. Jin; A. Oyler-Yaniv; F. Dotiwala; G. Giannone; C. Hivroz; N. Biais; J. Lieberman; L. C. Kam; M. Huse, Cytotoxic T Cells Use Mechanical Force to Potentiate Target Cell Killing. *Cell* **2016,** *165* (1), 100.

5. J. Huang; V. I. Zarnitsyna; B. Liu; L. J. Edwards; N. Jiang; B. D. Evavold; C. Zhu, The kinetics of two-dimensional TCR and pMHC interactions determine T-cell responsiveness. *Nature* **2010,** *464* (7290), 932.

6. Y. Liu; L. Blanchfield; V. P.-Y. Ma; R. Andargachew; K. Galior; Z. Liu; B. Evavold; K. Salaita, DNA-based nanoparticle tension sensors reveal that T-cell receptors transmit defined pN forces to their antigens for enhanced fidelity. *Proceedings of the National Academy of Sciences* **2016,** *113* (20), 5610.

7. V. P. Y. Ma; K. Salaita, DNA nanotechnology as an emerging tool to study mechanotransduction in living systems. *Small* **2019,** *15* (26), 1900961.

8. R. Ma; A. V. Kellner; V. P.-Y. Ma; H. Su; B. R. Deal; J. M. Brockman; K. Salaita, DNA probes that store mechanical information reveal transient piconewton forces applied by T cells. *Proceedings of the National Academy of Sciences* **2019,** *116* (34), 16949.

9. Y. Yin; X. S. Zhao, Kinetics and dynamics of DNA hybridization. *Accounts of chemical research* **2011,** *44* (11), 1172.

10. J. X. Zhang; J. Z. Fang; W. Duan; L. R. Wu; A. W. Zhang; N. Dalchau; B. Yordanov; R. Petersen; A. Phillips; D. Y. Zhang, Predicting DNA hybridization kinetics from sequence. *Nature chemistry* **2018,** *10* (1), 91.

11. K. Neupane; D. A. Foster; D. R. Dee; H. Yu; F. Wang; M. T. Woodside, Direct observation of transition paths during the folding of proteins and nucleic acids. *Science* **2016,** *352* (6282), 239.

12. M. T. Woodside; W. M. Behnke-Parks; K. Larizadeh; K. Travers; D. Herschlag; S. M. Block, Nanomechanical measurements of the sequence-dependent folding landscapes of single nucleic acid hairpins. *Proceedings of the National Academy of Sciences* **2006,** *103* (16), 6190.

13. B. S. Park; T. J. Park, Chemical Kinetics of Consecutive and Parallel Reactions Both with a Reversible First Step. *Bull. Korean Chem. Soc.* **2015,** *36* (9), 2221.

14. J. H. Esensten; Y. A. Helou; G. Chopra; A. Weiss; J. A. Bluestone, CD28 Costimulation: From Mechanism to Therapy. *Immunity* **2016,** *44* (5), 973.

15. K. T. Bashour; A. Gondarenko; H. Chen; K. Shen; X. Liu; M. Huse; J. C. Hone; L. C. Kam, CD28 and CD3 have complementary roles in T-cell traction forces. *Proc Natl Acad Sci U S A* **2014,** *111* (6), 2241.

16. B. L. Walling; M. Kim, LFA-1 in T Cell Migration and Differentiation. *Front Immunol* **2018,** *9*, 952.

17. B. Liu; W. Chen; B. D. Evavold; C. Zhu, Accumulation of dynamic catch bonds between TCR and agonist peptide-MHC triggers T cell signaling. *Cell* **2014,** *157* (2), 357.

18. J. Hong; C. Ge; P. Jothikumar; Z. Yuan; B. Liu; K. Bai; K. Li; W. Rittase; M. Shinzawa; Y. Zhang, A TCR mechanotransduction signaling loop induces negative selection in the thymus. *Nature Immunology* **2018,** *19* (12), 1379.

19. M. L. Alegre; K. A. Frauwirth; C. B. Thompson, T-cell regulation by CD28 and CTLA-4. *Nat Rev Immunol* **2001,** *1* (3), 220.

20. L. I. Salazar-Fontana; V. Barr; L. E. Samelson; B. E. Bierer, CD28 engagement promotes actin polymerization through the activation of the small Rho GTPase Cdc42 in human T cells. *J Immunol* **2003,** *171* (5), 2225.

21. W. A. Comrie; J. K. Burkhardt, Action and Traction: Cytoskeletal Control of Receptor Triggering at the Immunological Synapse. *Front Immunol* **2016,** *7*, 68.

22. K. H. Hu; M. J. Butte, T cell activation requires force generation. *J Cell Biol* **2016,** *213* (5), 535.

23. Y. Feng; E. L. Reinherz; M. J. Lang, alphabeta T Cell Receptor Mechanosensing Forces out Serial Engagement. *Trends Immunol* **2018,** *39* (8), 596.

24. N. H. Roy; S. H. J. Kim; A. Buffone, Jr.; D. Blumenthal; B. Huang; S. Agarwal; P. L. Schwartzberg; D. A. Hammer; J. K. Burkhardt, LFA-1 signals to promote actin polymerization and upstream migration in T cells. *J Cell Sci* **2020,** *133* (17).

25. N. H. Roy; J. L. MacKay; T. F. Robertson; D. A. Hammer; J. K. Burkhardt, Crk adaptor proteins mediate actin-dependent T cell migration and mechanosensing induced by the integrin LFA-1. *Science signaling* **2018,** *11* (560).

26. S. Kumari; M. Mak; Y. C. Poh; M. Tohme; N. Watson; M. Melo; E. Janssen; M. Dustin; R. Geha; D. J. Irvine, Cytoskeletal tension actively sustains the migratory T-cell synaptic contact. *EMBO J* **2020,** *39* (5), e102783.

27. N. H. Roy; J. K. Burkhardt, The Actin Cytoskeleton: A Mechanical Intermediate for Signal Integration at the Immunological Synapse. *Front Cell Dev Biol* **2018,** *6*, 116.

28. K. L. Hui; L. Balagopalan; L. E. Samelson; A. Upadhyaya, Cytoskeletal forces during signaling activation in Jurkat T-cells. *Mol Biol Cell* **2015,** *26* (4), 685.

29. K. I. Jankowska; J. K. Burkhardt, Analyzing Actin Dynamics at the Immunological Synapse. *Methods Mol Biol* **2017,** *1584*, 7.

30. T. Ilani; G. Vasiliver-Shamis; S. Vardhana; A. Bretscher; M. L. Dustin, T cell antigen receptor signaling and immunological synapse stability require myosin IIA. *Nat Immunol* **2009,** *10* (5), 531.

31. H. Colin-York; Y. Javanmardi; M. Skamrahl; S. Kumari; V. T. Chang; S. Khuon; A. Taylor; T. L. Chew; E. Betzig; E. Moeendarbary; V. Cerundolo; C. Eggeling; M. Fritzsche, Cytoskeletal Control of Antigen-Dependent T Cell Activation. *Cell Rep* **2019,** *26* (12), 3369.

32. M. Fritzsche; R. A. Fernandes; V. T. Chang; H. Colin-York; M. P. Clausen; J. H. Felce; S. Galiani; C. Erlenkamper; A. M. Santos; J. M. Heddleston; I. Pedroza-Pacheco; D. Waithe; J. B. de la Serna; B. C. Lagerholm; T. L. Liu; T. L. Chew; E. Betzig; S. J. Davis; C. Eggeling, Cytoskeletal actin dynamics shape a ramifying actin network underpinning immunological synapse formation. *Sci Adv* **2017,** *3* (6), e1603032.

33. S. Murugesan; J. Hong; J. Yi; D. Li; J. R. Beach; L. Shao; J. Meinhardt; G. Madison; X. Wu; E. Betzig; J. A. Hammer, Formin-generated actomyosin arcs propel T cell receptor microcluster movement at the immune synapse. *J Cell Biol* **2016,** *215* (3), 383.

34. D. Thumkeo; Y. Katsura; Y. Nishimura; P. Kanchanawong; K. Tohyama; T. Ishizaki; S. Kitajima; C. Takahashi; T. Hirata; N. Watanabe; M. F. Krummel; S. Narumiya, mDia1/3-

dependent actin polymerization spatiotemporally controls LAT phosphorylation by Zap70 at the immune synapse. *Sci Adv* **2020,** *6* (1), eaay2432.

35. S. Kumari; D. Depoil; R. Martinelli; E. Judokusumo; G. Carmona; F. B. Gertler; L. C. Kam; C. V. Carman; J. K. Burkhardt; D. J. Irvine; M. L. Dustin, Actin foci facilitate activation of the phospholipase C-gamma in primary T lymphocytes via the WASP pathway. *Elife* **2015,** *4*.

36. D. Blumenthal; J. K. Burkhardt, Multiple actin networks coordinate mechanotransduction at the immunological synapse. *J Cell Biol* **2020,** *219* (2).

37. J. Hong; S. Murugesan; E. Betzig; J. A. Hammer, Contractile actomyosin arcs promote the activation of primary mouse T cells in a ligand-dependent manner. *PLoS One* **2017,** *12* (8), e0183174.

38. A. Babich; S. Li; R. S. O'Connor; M. C. Milone; B. D. Freedman; J. K. Burkhardt, F-actin polymerization and retrograde flow drive sustained PLCgamma1 signaling during T cell activation. *J Cell Biol* **2012,** *197* (6), 775.

39. J. A. Ditlev; A. R. Vega; D. V. Koster; X. Su; T. Tani; A. M. Lakoduk; R. D. Vale; S. Mayor; K. Jaqaman; M. K. Rosen, A composition-dependent molecular clutch between T cell signaling condensates and actin. *Elife* **2019,** *8*.

40. Y. Zhang; C. Ge; C. Zhu; K. Salaita, DNA-based digital tension probes reveal integrin forces during early cell adhesion. *Nat Commun* **2014,** *5*, 5167.

41. M. T. Woodside; W. M. Behnke-Parks; K. Larizadeh; K. Travers; D. Herschlag; S. M. Block, Nanomechanical measurements of the sequence-dependent folding landscapes of single nucleic acid hairpins. *Proc. Natl. Acad. Sci. U. S. A.* **2006,** *103* (16), 6190.

Chapter 4. Towards the identification of mechanically active T cells, TCRs, and antigens with mechanically selective proximity tagging

Partially adapted from Rong Ma, Anna V. Kellner, Yuesong Hu, Brendan R. Deal, Aaron T. Blanchard, Khalid Salaita. DNA Tension Probes to Map the Transient Piconewton Receptor Forces by Immune Cells. J. Vis. Exp. Mar 20, 2021, 169, e62348.

4.1. Introduction

T cells defend against infections and cancer by constantly searching for self and foreign antigens. Upon T cell receptor (TCR)-antigen binding, T cells recognize the antigen, become activated, and initiate killing. Multiple hypotheses of how the TCR can discriminate different peptide-major major histocompatibility complexes (pMHC) have been discussed within the field in the past decades, including kinetic proofreading, serial engagement, receptor clustering and segregation, etc [1-2]. Among these hypotheses, growing evidence in the past few years suggest that T cells use mechanical forces to challenge the antigens [3-5]. When force was applied to T cells externally and transmitted through the TCR-pMHC interaction, significant increases in Ca^{2+} influx was observed compared to cells that have the same binding but without force application, indicating force stimulation can yield early T cell activation. Our lab confirmed the presence of the mechanical forces exerted by T cells during TCR-pMHC binding with molecular tension probes [6-7]. The DNA-based tension probe is comprised of a fluorescent strand for pMHC presentation, a quencher anchoring stand for immobilization, and a hairpin strand to join them together (**Figure 4.1**). The tension probes are anchored on a planar surface and present pMHC molecules for T cells to scan. The hairpin is unfolded and extended once a T cell binds and pulls on the pMHC molecule, separating the fluorophore and the quencher and generating a fluorescent signal. With this technique, we observed forces between 4.7 pN and 19 pN are transmitted from the TCR to the pMHC upon binding in primary mouse $CD8^+$ T cells. Interestingly, the forces are not just a by-product of the TCR-pMHC binding. When T cells are introduced to an environment that is chemically identical (a DNA-coated surface presenting the cognate peptide antigen) but mechanically different, meaning forces greater than 12 pN are instantaneously terminated, the activation level is reduced dramatically due to a lack of force transmission during the interaction

[6]. Moreover, when different TCR-pMHC binding interactions have similar affinities, the interactions that are able to persist longer under force induce greater T cell activation responses [8-9], supporting the role of the TCR mechanics in antigen discrimination and T cell activation. Furthermore, when altered peptide ligands (APL) were presented to T cells in place of the cognate antigen, the T cell mechanical sampling of the APLs had strong correlation with the potency of the APLs, despite the APLs all having similar affinity to the same TCR in solution [10]. This implies that the TCR-pMHC force is also related to antigen immunogenicity [11]. Compared to the conventional technique of tetramer staining, which is based on the in-solution (3-dimensional) affinity between the TCR and the pMHC [12], the binding and the TCR forces at the 2-dimensional interface is a more faithful marker to identify potent TCR-pMHC interactions. Due to the vast therapeutic implications for effectively predicting and identifying immunogenic antigens, as well as the specific T cells that can recognize them, TCR mechanics should be taken into consideration and employed, particularly in the development of cancer immunotherapies [13]. However, current techniques to detect these receptor forces are mostly microscopy-based, which is low-throughput and does not offer a solution to isolate the mechanically active T cells and TCRs for downstream analysis. Thus, a method which can identify and isolate the T cells that possess TCRs with mechanically active TCR-pMHC binding is highly desired.

To identify T cells with potent TCR-pMHC interactions using TCR mechanics as a marker, a major challenge is to mark the cells while they are dynamically exerting forces to test the antigens. Therefore, biocompatible and rapid reactions with good mechanical selectivity are required to achieve this goal. Accordingly, we decided to develop a proximity tagging-based technique to specifically tag the mechanically active cells. Proximity tagging techniques, which were originally developed to study protein-protein interactions (PPIs) [14], utilize enzymes to generate small reagents, which can covalently tag the neighbors in close proximity of a protein of interest. Normally, the enzyme is introduced by a “bait” protein, and upon addition of the enzyme’s substrate, the proteins near the “bait” are chemically tagged as the enzyme-generated reactive tagging molecules diffuse. Due to the short half-life of the unstable enzyme-catalyzed tagging molecule, only proteins within certain distance are labeled [15-17]. To date, peroxidases are the most common enzymes that have been used to study PPIs [17-18]. It catalyzes the oxidation of tyramine or phenolic aryl azide derivatives, which then attack the exposed aromatic side chains (mainly tyrosines) on proximal proteins that are within ~20 nm of the radius [17]. Usually, the enzyme-generated tagging molecule contains a reactive moiety for tagging, and a biotin moiety for isolation and downstream identification [14]. In the past few years, the ability of ascorbate peroxidase (APEX) to label PPIs within 1 min has been demonstrated in both in vitro and in vivo systems. This rapid time span of tagging with peroxidase is ideal to fill the existing gap in the labeling of highly dynamic T cells.

Thus, we combined the mechanical information storage approach discussed in Chapters 2 and 3 with the proximity labeling techniques to design a system capable of labeling T cells with mechanically active TCRs (**Figure 4.1**). In this design, a lock oligonucleotide that is complementary to the stem of the DNA hairpin tension probe is functionalized with a proximity biotinylation enzyme called horseradish peroxidase (HRP). The lock selectively and rapidly hybridizes to mechanically unfolded hairpins [10], enabling the delivery of HRP to mechanically active TCRs. Upon addition of the HRP substrate, hydrogen peroxide and biotin-phenol, the proximal proteins are tagged by oxidized biotin-phenol radicals, which can be detected by fluorescence microscopy. Finally, the mechanically active cells that are tagged with biotin can be collected from the substrate, stained with fluorescent streptavidin, and identified by flow cytometry.

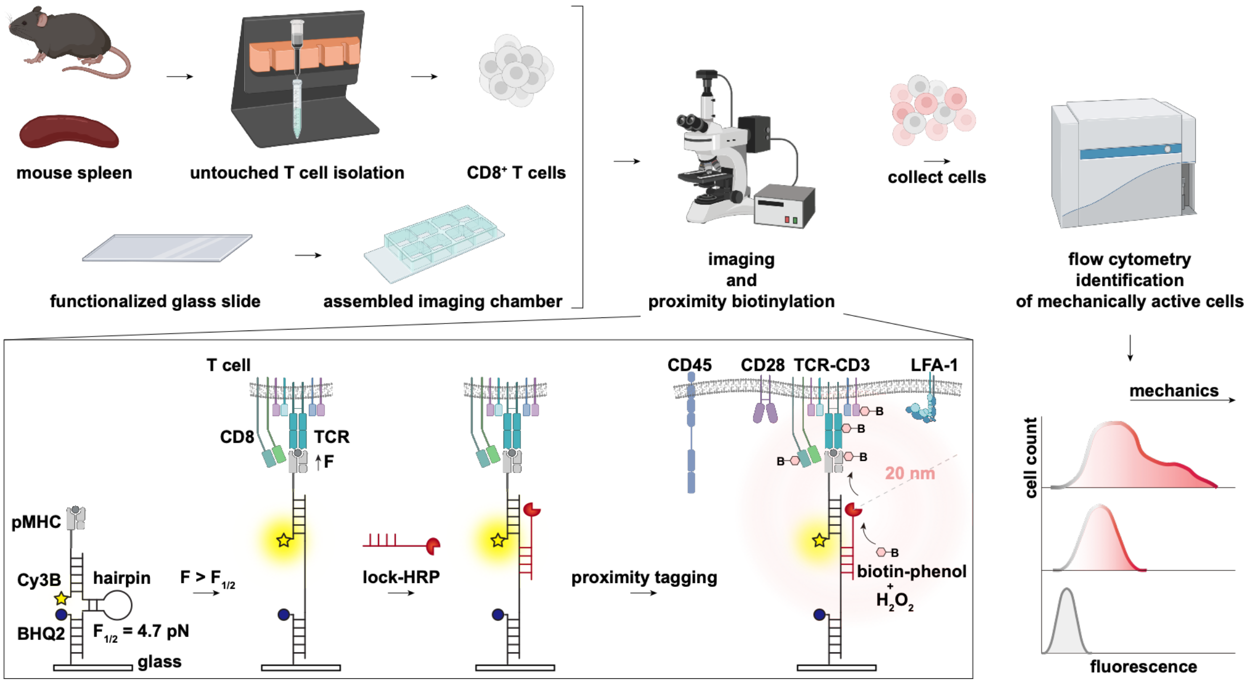

Figure 4.1. **Workflow and scheme of the selective proximity biotinylation of mechanically active TCRs and T cells.** Briefly, untouched naïve CD8$^+$ T cells were isolated from an OT-1 transgenic mouse spleen and plated on a glass slide that is functionalized with DNA tension probes. With the addition of the lock-HRP to solution, the mechanically unfolded DNA hairpins became accompanied with a lock-HRP almost instantaneously. Then, when supplied with H_2O_2 and the HRP substrate biotin-phenol, the membrane proteins in close proximity to the HRP were covalently tagged, allowing for flow cytometry identification of the mechanically active T cells.

4.2. Results and Discussion

4.2.1. Hybridization on 2D substrate is not affected by the presence of proximity labeling enzyme

We first tested whether conjugation of HRP to the lock would affect binding to the DNA hairpin probe on the 2D substrate. Given the relatively bulky size of the enzyme (several nm), hybridization to the probes that are confined on a 2D surface may be hindered. Horseradish peroxidase (HRP) was chosen as the proximity labeling enzyme in this study for three reasons:

The peroxidase has a short labeling time comparing to biotin ligase, which takes hours [16] [15], it is more commercially available compared to the recently developed APEX enzymes, and it has been demonstrated that HRP can be coupled to antibodies that target cell membrane proteins to study protein-protein interactions [18].

The gold nanoparticle DNA tension probes substrate was prepared as described (**Figure A4.1**) [6]. To better visualize the effect of the enzyme, we chose a 17mer complement as the lock for this assay, as it drives significant background opening of the hairpin when mechanical force is absent (**Figure A4.2**) [10]. The HRP was conjugated to the 17mer lock through its 3' end using sulfo-SMCC heterobifunctional crosslinking (**Figure A4.3**). The hybridization of the lock-HRP to the hairpin stem-loop region was compared to that of the lock alone and to that of the non-crosslinked lock and HRP added simultaneously (**Figure 4.2**). The fluorescence increase of DNA hairpin tension probes was used as an indication of hybridization rate between the lock and the hairpin. The conjugation of the HRP did not show significant impact on the hybridization between the lock and the hairpin stem-loop in the cell-free system (**Figure 4.2**). Due to the possibility of the enzyme non-specifically sticking to the DNA probe substrate, a scrambled DNA tension probe substrate incubated with the lock-HRP was included as a control, further revealing minimal non-specific binding.

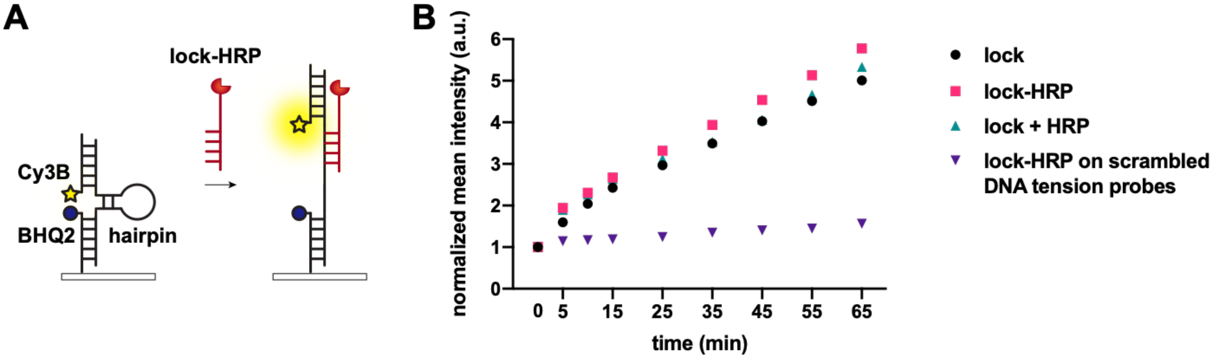

Figure 4.2. Effect of the conjugation of lock and HRP on in-situ hybridization. (A) Schematic of the hybridization in cell-free system. (B) Normalized fluorescence intensity (mean±SD) of the

Cy3B signal increase over time with the addition of either 200 nM lock, the lock-HRP, or the non-crosslinked lock and HRP together. Fluorescence intensity from 5 positions of the substrates was measured over time, averaged, and normalized to the initial t = 0 min intensity. The lock conjugated with HRP showed a similar hybridization rate compared to the lock alone in the cell-free system.

4.2.2. Mechanically selective proximity biotinylation

After confirming that the lock-HRP can hybridize to the hairpin on the 2D surface, we tested the concept of mechanically selective proximity biotinylation with naïve CD8$^+$ T cells from OT-1 transgenic mice. The OT-1 CD8$^+$ T cells, isolated from the spleen of the mice, specifically recognize a peptide epitope from ovalbumin, SIINFEKL. The cells were plated onto DNA tension probe substrates that present antiCD3ε, which the CD3 epsilon chain from the TCR complex binds to. 20 minutes after plating the cells, the tension signal was observed and imaged, before the subsequent addition of the lock-HRP. As the lock binds preferably and irreversibly to the mechanically unfolded hairpins at an extraordinary rate, we first labeled the lock-HRP with Alexa647 to confirm the co-localization of the tension signal and the lock-HRP signal (**Figure 4.3**). As HRP only has 6 lysine residues that are available for conjugation, the yield of lock-HRP-Alexa647 conjugation was below 1:1 when performed after the lock-HRP conjugation, resulting in low fluorescence signal in Alexa647 channel. Yet, importantly, the Alexa647 lock-HRP signal overlaps with the tension signal in Cy3B, showing strong co-localization. Since we confirmed that the lock-HRP accompanied mechanically unfolded hairpins, biotin-phenol and H_2O_2 were added for proximity labelling, after which the cells were fixed and stained with Alexa 488 labeled streptavidin (SA488) to detect the mechanically selective proximity biotinylation. A negative control, where H_2O_2 was withheld, indicated minimal non-specific binding and uptake of biotin-phenol (**Figure 4.3C**). Proximity tagging with the addition of non-crosslinked lock and HRP, as well as a lock-HRP on a scrambled hairpin probe substrate were used to control for non-specific biotinylation in the system (**Figure A4.4**). Both negative controls showed minimal background tagging as well.

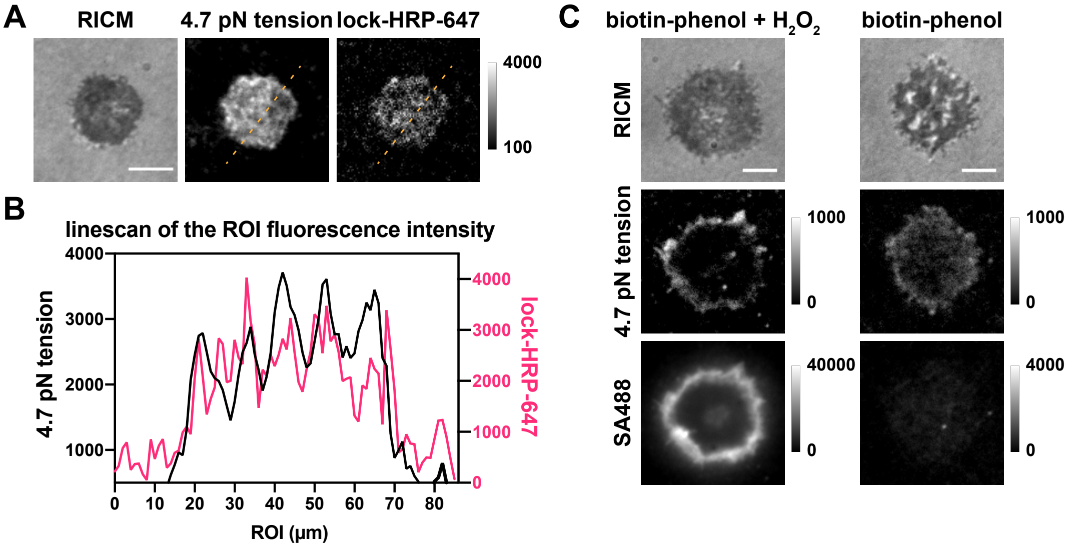

Figure 4.3. The mechanically selective hybridization and proximity biotinylation with lock-HRP. (A) Mechanically selective hybridization between the lock-HRP-647 and the DNA tension probes as OT-1 T cells unfolded the hairpin probes that presented antiCD3ε. Images of the tension signal and the lock-HRP-647 signal were acquired 10 min after the addition of 100 nM lock-HRP. (B) Linescan of the ROI (raw data) shows the overlapping fluorescence tension signal and lock-HRP-647 signal, confirming that the lock-HRP-647 was able to hybridize selectively to the mechanically unfolded hairpins. (C) Microscopy images of the biotinylated mechanically active T cells. OT-1 T cells were plated on DNA tension probes that presented antiCD3ε, after real-time tension signal in Cy3B channel was observed, lock-HRP was added at 100 nM for 10 min, followed by gentle rinses and proximity labelling. The tagged cell membrane proteins were detected by SA488 after fixing. A negative control without H_2O_2 was included. Scale bar = 5 µm.

The microscopy results showed that mechanically selective proximity tagging is achievable with the OT-1 T cells. This implies that the membrane proteins that actively engaged in TCR mechanics were likely biotinylated, as well as the mechanically active TCR itself. It is possible that the SA488 detected biotinylation is a result of background tagging on the HRP, streptavidin, and antiCD3ε that are present on the substrate near the mechanically active TCR. However, the SA488 did not completely co-localize with the tension signal, implying that membrane proteins were likely biotinylated and reorganized at the interface during the experiment. To further confirm the labeling of the cells, we next sought to collect the cells from the substrates following proximity labelling and use flow cytometry to confirm the biotinylation on the cell surface and identify the mechanically active T cells.

4.2.3. High throughput detection of the biotinylated mechanically active T cells

We used flow cytometry as a readout and used fluorescently labeled streptavidin to stain for the mechanically active OT-1 cells that carry the biotin tags on the cell surface. Flow cytometry is commonly used in immunology and allows for the sorting of subpopulations out of biological samples based on the fluorescence of each cell, offering us an opportunity to further expand the utility of our mechanically selective proximity tagging method. One challenge to establishing the workflow of detecting the tagged cells with flow cytometry is the harvesting the cells from the DNA tension probe substrate. Ideally, the collection of labeled cells should have a high cell recovery yield while keeping the cells untouched. We first hypothesized that we could take advantage of the enzymatic vulnerability of the DNA tension probe substrate by using DNase to cleave the probes, thus releasing the cells from the substrate. However, cells that went through the proximity labeling procedures remained bound to the surface after DNase incubation (**Figure A4.5**), potentially a result of changes to the DNA structure in the oxidative environment [19]. Therefore, we employed an alternative approach and harvested the cells by gently scraping them off from the glass slides after quenching the labeling process. To accommodate the scraping approach, the DNA tension probe substrate preparation procedure was modified to avoid any use of gold particles, which could interfere with or quench the fluorescence signal of the cells on the flow cytometer, and instead utilized SMCC crosslinking chemistry (**Figure A4.1**). After performing proximity biotinylation on the substrate, OT-1 cells were washed and incubated on ice with Alexa647 labeled streptavidin (SA647) for 10 min, after which they were washed again and run through a flow cytometer (**Figure A4.7**). **Figure 4.4** shows the results when OT-1 T cells were allowed to mechanically interact with substrates presenting either antiCD3ε, its cognate antigen pMHC N4, or an altered peptide ligand, pMHC Q4. As the binding of CD8 to the MHC was identified as a main contributor to the TCR forces, we tested whether there would be less labeling if CD8-MHC binding was blocked through the use of a CD8 antibody CTCD8a. The cells incubated with the non-crosslinked lock and the HRP were used as a negative control for non-specific proximity tagging. The cells on the pMHC N4 DNA tension probe substrate showed the highest tagging level, followed by pMHC Q4, and then antiCD3ε. Though the highest real-time tension signal is often observed with cells on the antiCD3ε substrate, the lock-HRP technique would result in the most hybridization with the cells that have the most frequent mechanical pulling events with forces greater than 4.7 pN [10]. Therefore, the level of tagging is consistent with microscopy observations of the frequency of mechanical pulling events (Chapter 3). When CD8-MHC binding was blocked, the level of tagging decreased significantly, in agreement with the previous report on the TCR force with CD8 blockade. Overall, the labeling levels across the different treatment groups showed strong correlation with the TCR mechanics. Moreover, the percentage of the cells that showed positive biotinylation in each sample also agreed with the potency of the TCR interaction with pMHC. We noticed highly heterogeneous levels of mechanical activity that led to distinct subpopulations in the flow cytometry readout, with many cells containing lower tagging levels and many cells showing higher tagging levels (**Figure 4.4B**), strongly agreeing with the heterogenous distribution in mechanical activity from microscopy data (**Figure A4.6**). This observation raises another interesting question: what contributes to the dramatic differences in T cell mechanical responses to the same antigen? Furthermore, can we take advantage of this tool that we developed to identify the mechanisms behind it? In the extended studies, the T cells with higher mechanical activities should be sorted out using fluorescence-activated cell sorting (FACS) and techniques such as single cell RNA sequencing should be used to identify the genes that are responsible for the higher receptor mechanics in certain cells and that help the T cell discriminate between antigens and contribute to T cell activation [11, 20-22].

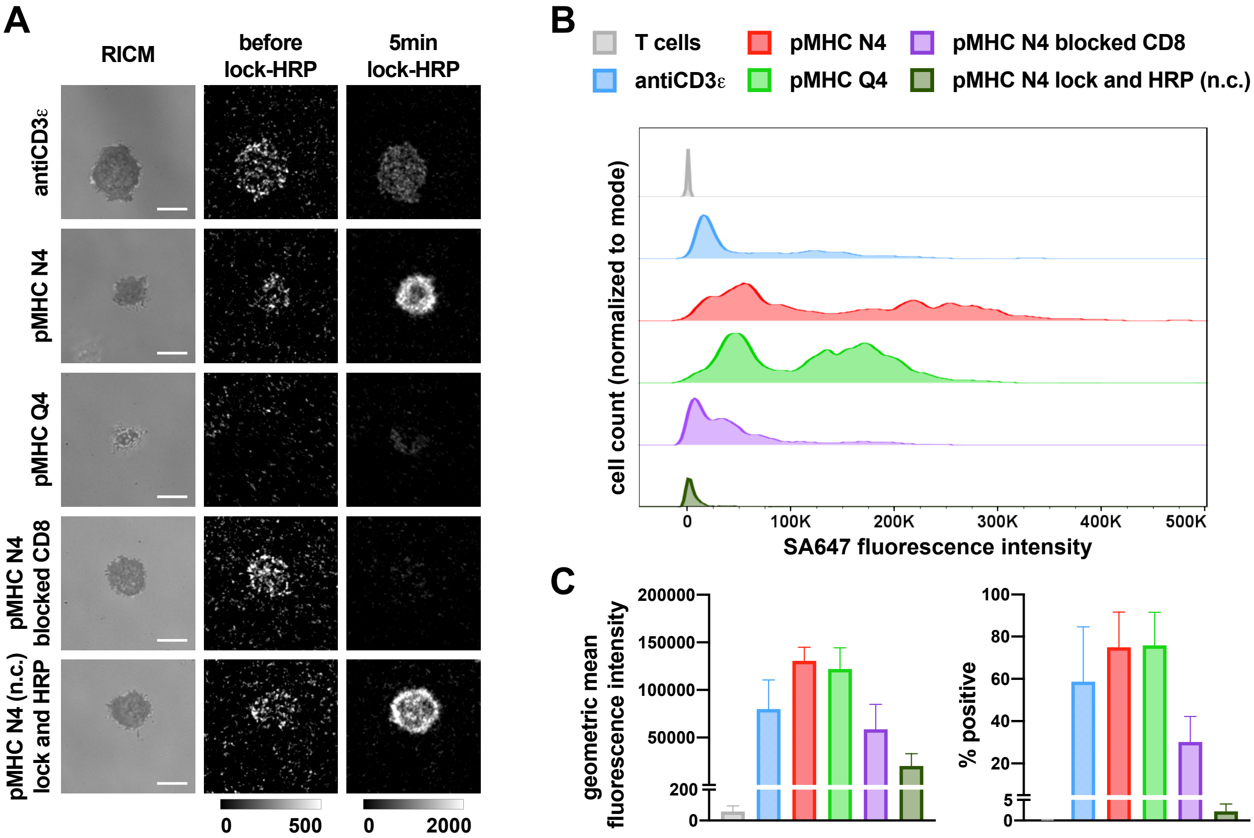

Figure 4.4. Mechanically selective hybridization, proximity biotinylation, and flow cytometry analysis of OT-1 T cells against different ligands. (A) Microscopy images of OT-1 cells spread on DNA tension probe substrates presenting either antiCD3ε, pMHC N4, or pMHC Q4. Real-time Cy3B signals of TCR forces were acquired, followed by the addition of 250 nM lock-HRP and image acquisition of the accumulated tension signal in Cy3B channel after 5 min. The T cells with blocked CD8 and the T cells on pMHC N4 substrate incubated with the lock and HRP were included as controls. (B) Representative flow cytometry detection of the OT-1 cells with mechanically active TCRs. After image acquisition, proximity biotinylation was performed, after which the cells were rinsed, collected, and stained with SA647. Three biological replicates were performed with each generating consistent data. Scale bar = 5 µm. (C) Average geometric mean fluorescence intensity of the cells and % positive of the cells from 2 biological replicates. Error bars represent SD. (We are only showing the average and SD from 2 replicates due to instrument setting differences for the 3rd replicate.)

4.3. Conclusion

This work developed a platform that selectively labels T cells with mechanically active TCR-pMHC interactions. By integrating DNA nanotechnology with a chemical biology technique proximity labelling, we successfully labeled OT-1 T cells that exerted forces on its ligands, and the level of labeling agrees with the functional outcome of the interaction.

With this tool at hand, it is plausible to pursue the next step of sorting the mechanically active T cells and analyze the contributors of their activity with techniques such as single cell RNA sequencing. Moreover, it is very likely that the mechanically active TCRs and the recognized antigens would be labeled with biotin moieties, which could be further pulled down for MS analysis and identification. This method potentially would enable the field to move from observing the force during T cell triggering to a translational step of taking advantage of the force to predict T cell response, as well as identify antigens for personalized cancer immunotherapies [13].

4.4. Materials and methods

4.4.1. Oligonucleotides

The oligonucleotides used in this study are listed in **Table A4.1.**

Table A4.1. List of oligonucleotides used in Chapter 4.

oligo name	5'	sequence (5' to 3')	3'
amine ligand strand (A21B)	/5AmMC6/	CGC ATC TGT GCG GTA TTT CAC TTT	/3Bio/
Cy3B ligand strand (A21B Cy3B)	Cy3B	CGC ATC TGT GCG GTA TTT CAC TTT	/3Bio/
BHQ2 anchor strand	/5ThiolMC6-D/	TTT GCT GGG CTA CGT GGC GCT CTT	/3BHQ_2/
4.7 pN hairpin strand	---	GTG AAA TAC CGC ACA GAT GCG TTT GTA TAA ATG TTT TTT TCA TTT ATA CTT TAA GAG CGC CAC GTA GCC CAG C	---
4.7 pN hp 15mer lock	---	AAA AAA CAT TTA TAC	---
4.7 pN hp 15mer lock thiol	---	AAA AAA CAT TTA TAC CCT ACC TA	/3ThioMC3-D/
scrambled 4.7 pN hairpin strand	---	GTG AAA TAC CGC ACA GAT GCG TTT GTA AAT ATG TGG TGG TCA TAT TTA CTT TAA GAG CGC CAC GTA GCC CAG C	---
4.7 pN hp 17mer lock	---	GAA AAA AAC ATT TAT AC	---
4.7 pN hp 17mer lock thiol	---	GAA AAA AAC ATT TAT ACC CTA	/3ThioMC3-D/

4.4.2. Reagents

The reagents used in this study are listed in **Table A4.2.**

Table A4.2. List of reagents used in Chapter 4.

Name of Material/ Equipment	Company	Catalog Number
Biotin anti-mouse CD3ε Antibody (2C11)	Biolegend	100304
Biotinylated pMHC ovalbumin (SIINFEKL)	NIH Tetramer Core Facility	NA
Biotinylated pMHC ovalbumin (SIIQFEKL)	NIH Tetramer Core Facility	NA
Anti-Mouse CD8a (Ly 2) Purified (Clone CT-CD8a) (rat IgG2a)	Cedarlane	CL168AP
10x Red blood cell lysis buffer	Biolegend	00-4333-57
Dulbecco's phosphate-buffered saline (DPBS)	Corning	21-031-CM
Hank’s balanced salts (HBSS)	Sigma	H8264
BD Syringes only with Luer-Lok	BD bioscience	309657
Cell strainers	Biologix	15-1100
Midi MACS (LS) startup kit	Miltenyi Biotec	130-042-301
Mouse CD8+ T cell isolation kit	Miltenyi Biotec	130-104-075
Ovalbumin (257-264) chicken	Sigma	S7951-1MG
Atto647N NHS ester	Sigma	18373-1MG-F
Alexa Fluor™ 488 NHS Ester	Thermo Fisher	A20100
Alexa Fluor™ 647 NHS Ester	Thermo Fisher	A20006
Cy3B NHS ester	GE Healthcare	PA63101
3-Hydroxypicolinic acid (3-HPA)	Sigma	56197
Nanosep MF centrifugal devices	Pall laboratory	ODM02C35
P2 gel	Bio-rad	1504118
Triethylammonium acetate buffer	Sigma	90358
mPEG-SC	Biochempeg	MF001023-2K
(3-Aminopropyl)triethoxysilane	Acros	AC430941000
8.8 nm gold nanoparticles, tannic acid	Nanocomposix	customized order
Coverslip Mini-Rack, teflon	Thermo Fisher Scientific	C14784
Ethanol	Sigma	459836
Hydrogen peroxide	Sigma	H1009
LA-PEG-SC	Biochempeg	HE039023-3.4K
Sufuric acid	EMD Millipore Corporation	SX1244-6
SMCC (succinimidyl 4-(N-maleimidomethyl)cyclohexane-1-carboxylate)	Thermo Fisher	22360
Sulfo-NHS acetate	Thermo Fisher Scientific	26777
Wash-N-Dry™ Slide Rack	Sigma	Z758108
Glass Coverslips for sticky-Slides 25 / 75 mm	Ibidi	10812
Sticky-slide 18 Well	Ibidi	81818
Bovine serum albumin	Sigma	735078001
Attofluor Cell Chamber, for microscopy	Thermo Fisher Scientific	A7816
Dimethyl Sulfoxide (DMSO)	EMD-Millipore	M1096780100
Sodium azide	Sigma	S2002
UltraPure™ 0.5M EDTA, pH 8.0	Thermo Fisher	15575020
Formaldehyde solution	Sigma	252549
Triton™ X-100	Sigma	X100
Sulfo-SMCC (sulfosuccinimidyl 4-(N-maleimidomethyl)cyclohexane-1-carboxylate)	Thermo Fisher	22322
Streptavidin	Thermo Fisher	434302
Biotinyl tyramide	Sigma	SML2135
Sodium ascorbate	Sigma	Y0000039
Amicon® Ultra 0.5 mL Centrifugal Filters	Sigma	UFC503024
Horseradish peroxidase (HRP)	Sigma	P8250
Bond-Breaker™ TCEP Solution, Neutral pH	Thermo Fisher	77720

4.4.3. Equipment

The equipment used in this study is listed in **Table A4.3.**

Table A4.3. List of equipment used in Chapter 4.

Equipment	Company
Barnstead Nanopure water purifying system	Thermo Fisher
AdvanceBio Oligonucleotide C18 column, 4.6 x 150 mm, 2.7 μm	Agilent
High-performance liquid chromatography	Agilent 1100
Matrix-assisted laser desorption/ionization time-of-flight mass spectrometer (MALDI-TOF-MS)	Voyager STR
Nanodrop 2000 UV-Vis Spectrophotometer	Thermo Fisher
CFI60 Apochromat TIRF 100X Oil Immersion Objective Lens, N.A. 1.49	Nikon
Prime 95B-25MM Back-illuminated sCMOS Camera. 1608x1608,30fps	Photometrics
Evolve electron multiplying charge coupled device (EMCCD)	Photometrics
Nikon Ti2-E Motorized Research Microscope	Nikon
Nikon Eclipse Ti inverted microscope	Nikon
Ti2-ND-P Perfect Focus System 4	Nikon
SOLA SE II 365 Light Engine	Nikon
NIS Elements software	Nikon
C-FL Surface Reflection Interference Contrast (SRIC) Cube	CHROMA
CF-L AT CY5/Alexa Fluor 647/Draq 5 Filter Set	CHROMA
C-FL DS Red Hard Coat, High Signal-to-Noise, Zero Shift Filter Set	CHROMA
CF-L AT FITC Filter Set	
Quad band TIRF 405/488/561/647 Cube	CHROMA
TIRF launcher with three lasers:488 nm (50 mW), 561 nm (50 mW), and 640 nm (40 mW)	Coherent
CytoFLEX V0-B3-R1 Flow Cytometer	BECKMAN COULTER

4.4.4. Mice and cells

Briefly, OT-1 transgenic mice were housed and bred in the Division of Animal Resources Facility at Emory University under the Institutional Animal Care and Use Committee. OT-1 T cells that express the CD8 co-receptor and specifically recognize chicken ovalbumin epitope 257–264 (SIINFEKL) were isolated and enriched from the spleen of a sacrificed mouse using MACS system and CD8$^+$ T cell isolation kit according to the manufacturer's instruction. DPBS buffer supplemented with 0.5% BSA and 2 mM EDTA was used for the purification process as described following the manufacturer's instruction. The purified CD8$^+$ naïve OT-1 cells were kept in HBSS at 2×10^6 cells/mL on ice before imaging.

4.4.5. Oligonucleotide preparation

Oligo-dye conjugation. Cy3B ligand strand and lock-647N were prepared by NHS reaction. Briefly, 50 μg (excess amount) of NHS dye was dissolved in 10 μL of DMSO and reacted with 10 nmol of oligonucleotide in 1× PBS containing 0.1 M $NaHCO_3$ overnight at 4 °C or 1 h at room temperature (**Figure A4.3**). After the reaction, byproduct, salts, and unreacted dye in the mixture were removed by P2 gel filtration using Nanosep MF centrifugal devices. The product was further purified by reverse-phase HPLC equipped with Agilent AdvanceBio Oligonucleotide C18 column (653950-702, 4.6 × 150 mm, 2.7 μm). The mobile phase A: 0.1 M TEAA and B: ACN were used for a linear gradient elution of 10-100% B over 50 min at a flow rate of 0.5 mL/min (**Figure A4.3**). The desired product was characterized by MALDI-TOF-MS (data not shown) and the concentration of the oligo-dye is determined by UV-Vis using absorbance at 260 nm (data not shown).

Lock-HRP conjugation. Lock-HRP was prepared by conjugating the thiol lock strand with HRP using a crosslinker sulfo-SMCC (**Figure A4.3**). HRP was dissolved in 1× PBS at 5 mg/mL and the lysine residues were allowed to react with 10-fold excess of sulfo-SMCC at room temperature for 30 min. Excess amount of the crosslinker was removed using a desalting column with PBS-hydrated P4 gel twice. Meanwhile, the disulfide group on the thiol lock strand was reduced by mixing 200× TCEP and 10 nmol thiol lock strand at room temperature for 15 min. The reduced thiol strand was then mixed with maleimide-activated HRP at room temperature and allowed to react for 1 h. The product was purified with Amicon filter 30 (kD) to remove any unreacted thiol strand.

For microscopy experiments, the lock-HRP was then labeled with Alexa 647 NHS ester on remaining lysine residues. This lock-HRP-647 was purified by P4 gel purification. The lock-HRP and lock-HRP-647 were characterized with UV-Vis, and the concentration of the stock was calculated with the absorbance at 260 nm after correction (**Figure A4.3**). We found that precise control over the ratio of DNA: HRP: Alexa647 is difficult to achieve. However, the ratio is not a major issue as the free HRP is washed away before proximity biotinylation, and the HRP molecule conjugated to more than one lock is unlikely to affect the biotinylation result.

4.4.6. Fluorescence labeling of streptavidin

Streptavidin was labeled with Alexa 488 NHS ester or Alexa 647 NHS ester. Briefly, 100 µg streptavidin was reconstituted in 100 µL 1× PBS and added to a 50 µg dye aliquot. The mixture was allowed to react for 30 min at room temperature. The product was purified with P4 gel filtration hydrated with PBS to remove unreacted dye and by-products. The SA488 and SA647 were characterized using UV-Vis and the concentration was determined by the absorbance at 280 nm.

4.4.7. Substrate preparation

Amine modified glass slides. Glass slides (25×75 mm) were rinsed with water three times and placed onto a Wet-N-Dry rack in a 200 mL tall beaker. The glass slides were submerged in ethanol and sonicated to clean for 15 min. Then the ethanol was disposed of, and the slides were submerged in water and sonicated to clean for another 15 min. The cleaned glass slides were washed with water for 6 times to remove any residual ethanol and dust. Piranha solution (200 mL) was prepared in a clean 200 mL beaker by mixing sulfuric acid and H_2O_2 at a ratio of 3:1 v/v. (CAUTION: Piranha solution is highly reactive and hazardous. It may explode if H_2O_2 exceeds 50% or if it is mixed with organic solvents.) After gentle mixing, the rack that held the slides was transferred to the beaker containing the fresh piranha solution and etched for 30 min at room temperature. After etching, the rack that held the glass slides was transferred to a new beaker and rinsed with 200 mL water 6 times, followed by another 3 washes with 200 mL ethanol. APTES solution (200mL) was then prepared at 3% w/v in ethanol in a 200 mL beaker, and the rack was submerged in the APTES solution and sealed with parafilm to react for 1 h at room temperature. After the reaction, the rack holding the slides was transferred to a new beaker and washed with ethanol 6 times. The slides were then baked dry for 20 min. The amine modified glass slides are stored at -20 °C until use (**Figure A4.1**).

Gold particle DNA-tension probe substrate. An amine modified glass slide was placed in a petri dish, of which the bottom is covered with parafilm. Lipoic acid-PEG NHS (6 mg) and mPEG NHS (30 mg) were weighed and dissolved in 1.2 mL 0.1 M $NaHCO_3$ immediately before adding to the amine glass slide and allowed to react for 1 h at room temperature. After the reaction, the glass slide was rinsed with water and incubated with 10 mg/mL sulfo-NHS acetate in 0.1M $NaHCO_3$ for 30 min at room temperature for passivation, and then washed with water. Afterwards, the lipoic acid PEG functionalized glass slide was air dried and assembled with a sticky-slide chamber. Gold nanoparticles were added to the wells at 0.05 mg/mL (80 µL/well) and allowed to immobilize for 30 min at room temperature in the dark. Meanwhile, DNA tension probes were annealed by heating a 1.1:1:1 mixture of the 4.7 pN hairpin, Cy3B ligand strand, and BHQ2 anchor strand at 300 nM in 1M NaCl to 95 °C for 5 min, and gradually cooling down to 20 °C over 20 min. After the gold particle immobilization, the unbound particles were washed away with sufficient water. DNA tension probes were mixed with another 9-fold excess BHQ2 anchor strand (total final concentration of BHQ2 anchor strand is 3 µM) after annealing and added to each well (40 µL/well) for overnight incubation. On the second day, the excess unbound DNA probe was washed away with PBS and streptavidin (40 µg/mL, 50 µL/well) was added to the wells for 30 min incubation at room temperature. Each well was then washed with PBS and the biotin-antibody (40 µg/mL, 50 µL/mL) or biotin-ligand (10 µg/mL, 50 µL/well) was added to the surfaces and incubated for 30 min at room temperature. After the immobilization of the ligand, the wells were washed with PBS and ready for imaging (**Figure A4.1**).

Maleimide DNA-tension probe substrate. An amine modified glass slide was placed in a petri dish, of which the bottom is covered with parafilm. SMCC (4 mg) was weighed and dissolved in 400 µL DMSO immediately before adding to the amine glass slide and allowed to react for 30 min at room temperature. Meanwhile, DNA tension probes were annealed by heating the 1.1:1:1 mixture of the 4.7 pN hairpin, Cy3B ligand strand, and BHQ2 anchor strand at 100 nM in 1× PBS (pH = 6.8) to 95 °C for 5 min, and gradually cooling down to 20 °C in 20 min. After the SMCC reaction, the glass slide was rinsed with ethanol and incubated with 400 µL 10 mg/mL sulfo-NHS acetate in DMSO for 30 min at room temperature for passivation, and then rinsed with ethanol. In the meantime, 200-fold molar excess of TCEP was added to the annealed DNA tension probes for

15 min to reduce the thiol on the BHQ2 anchor strand. After the passivation, the maleimide activated glass slide was air dried and assembled with a sticky-slide chamber. The reduced DNA tension probe (40 µL/well at 100 nM) was added to the wells and incubated for 1 h at room temperature. After the immobilization of the DNA tension probes, the wells were washed with 1× PBS and were further passivated with 0.5% BSA in PBS for 5 min at room temperature. Then, streptavidin (50 µg/mL, 50 µL/well) was added to the wells for 30 min incubation at room temperature, after which the wells were washed with PBS and incubated with biotin-antibody (40 µg/mL, 50 µL/well) or biotin-ligand (10 µg/mL, 50 µL/well) for 30 min at room temperature. After the incubation, the wells were washed with PBS and ready for experiments (**Figure A4.1**).

4.4.8. Microscopy

Cell free system. Background fluorescence intensity was measured before adding the locks. Lock and lock-HRP strands were added at 200 nM in HBSS to measure the hybridization. Time-lapse data was acquired in Cy3B channel at 5 positions (81.92 µm×81.92 µm at each position) of each surface and averaged for processing.

Imaging with OT-1 cells. Purified OT-1 cells were added to surface and allowed to attach for around 20 min. After cells started to produce tension, lock and the lock-HRP at 200 nM was added in HBSS for mechanically selective hybridization. After 10 min of incubation, cells were gently rinsed with HBSS and imaged in RICM, Cy3B and 647 channels.

Data analysis. Fluorescence images of the Cy3B signal were process by subtracting the camera background, and the fluorescence background of the closed DNA probes using the mean of the local background and 2*SD. The mean intensity was used to for the quantitative analysis in the cell-free system. The raw integrated intensity was used for the quantitative analysis of the TCR tension.

4.4.9. Proximity biotinylation and flow cytometry

A stock solution of biotin-phenol was prepared in DMSO at 500 mM and sonicated for 1 min before use. After mechanical-selective hybridization was confirmed, biotin-phenol was added to the imaging chamber at 250 µM with or without 1 mM of H_2O_2. After 1 min of incubation, sodium ascorbate was added at 10 mM to quench the free radicals. Cells were immediately gently rinsed with HBSS three times.

For microscopy experiments, cells were fixed in 4% formaldehyde for 30 min, followed by blocking non-specific binding with 0.1% BSA in PBS. Streptavidin488 was added to cells at 50 nM for 30 min to detect biotinylation. After washing with PBS three times, cells were imaged for the SA488 signal.

For flow cytometry experiments, sodium ascorbate was added immediately after the proximity tagging process, and the cells were gently rinsed three times with HBSS. Ice-cold FACS buffer was gently added, and the cells were quickly scraped into pre-chilled 1.5 mL tubes and kept on ice for 5 min to block the non-specific binding. The SA647 was then added at 50 nM and allowed to incubate for 15 min to detect cell biotinylation. Finally, the cells were spun down and washed twice in ice-cold FACS buffer prior to flow cytometry detection. Flow cytometry experiments were carried out and data was acquired from biological replicates. Using FlowJo, Live OT-1 T cell singlets were isolated by gating based on forward and side scatter area first and then based on forward and side scatter height. The geometric mean fluorescence intensity of each sample was calculated and the percent of cells with positive fluorescence was calculated by creating a vertical gate on the fluorescence histogram of the negative control so that ~99.5% of the cells would have fluorescent values less than the value of the gate.

4.5. Appendix

Figure A4.1. Preparation of the DNA tension probes substrates. (A) The preparation of gold particle DNA tension probes substrate. (B) The preparation of maleimide DNA tension probes substrate.

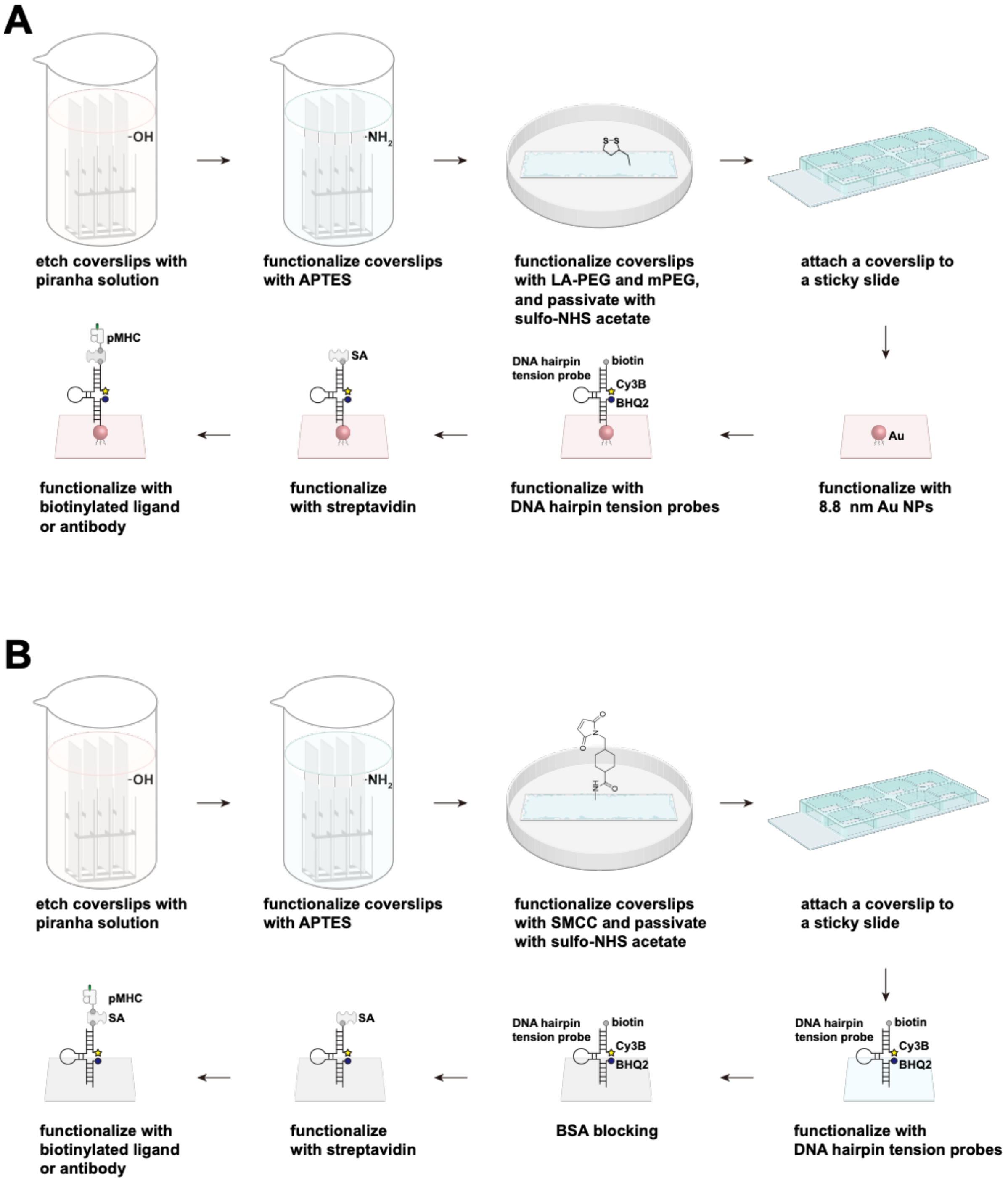

Figure A4.2. Schematic of the binding between the lock and the 4.7 pN DNA tension probes. The 17mer is more thermodynamically favorable to open the hairpins, and thus it was chosen in order to confirm that the hybridization between the lock and the DNA stem-loop is not affected by conjugation to HRP.

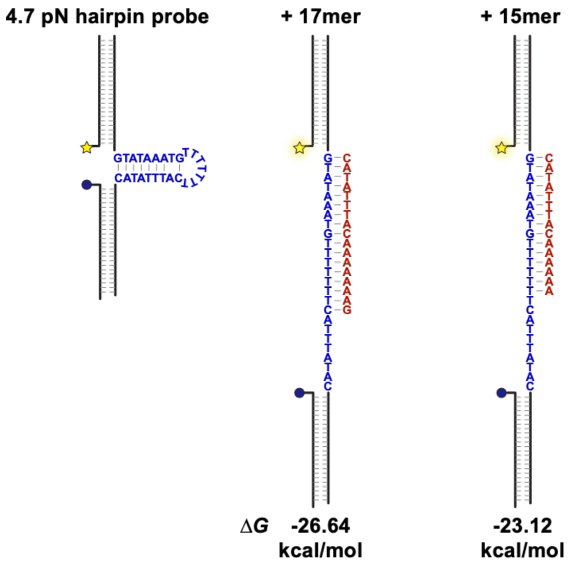

Figure A4.3. Preparation of oligonucleotides. (A) The general reaction to conjugate amine oligonucleotide with Atto647N NHS. (B) The reaction scheme to conjugate the thiol lock with HRP. (C) The reaction scheme to conjugate the thiol lock with HRP and Alexa647 NHS. (D) HPLC trace of A21B Cy3B and lock-647N. The products are marked with arrows. (E) UV-Vis spectra of lock-HRP-Alexa647.

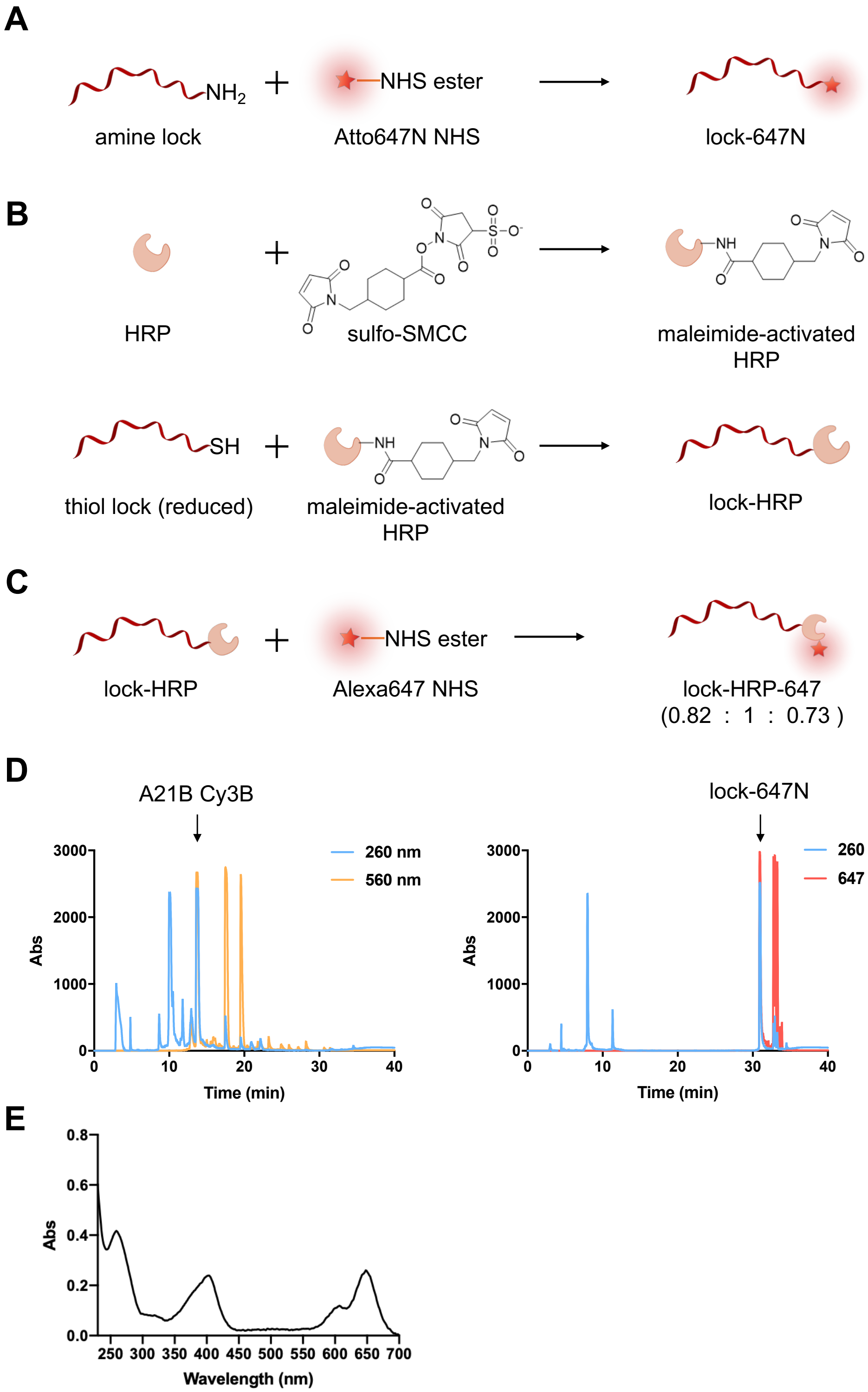

Figure A4.4. Control for the proximity tagging of T cells with mechanically active TCRs. OT-1 cells were plated on a DNA tension probe substrate presenting antiCD3ε and allowed to spread for 20 min. After adding the lock-HRP at 100 nM for 10 min, the cells were gently rinsed and supplemented with biotin-phenol and H_2O_2 for proximity biotinylation for 1 min. Then the cells were gently rinsed again and fixed in 4% formaldehyde for 30 min and blocked with 0.1% BSA and stained with SA488. The cells were then imaged in Cy3B channel (indicates tension signal before biotinylation) and Alexa488 channel (indicates biotinylation). Cells on a scrambled 4.7 pN DNA tension probe and cells incubated with non-crosslinked lock and HRP at the same concentration were used as controls for mechanical selectivity of the biotinylation. Only the 4.7 pN DNA tension probe with the complementary lock-HRP showed strong biotinylation. Scale bar = 5 μm.

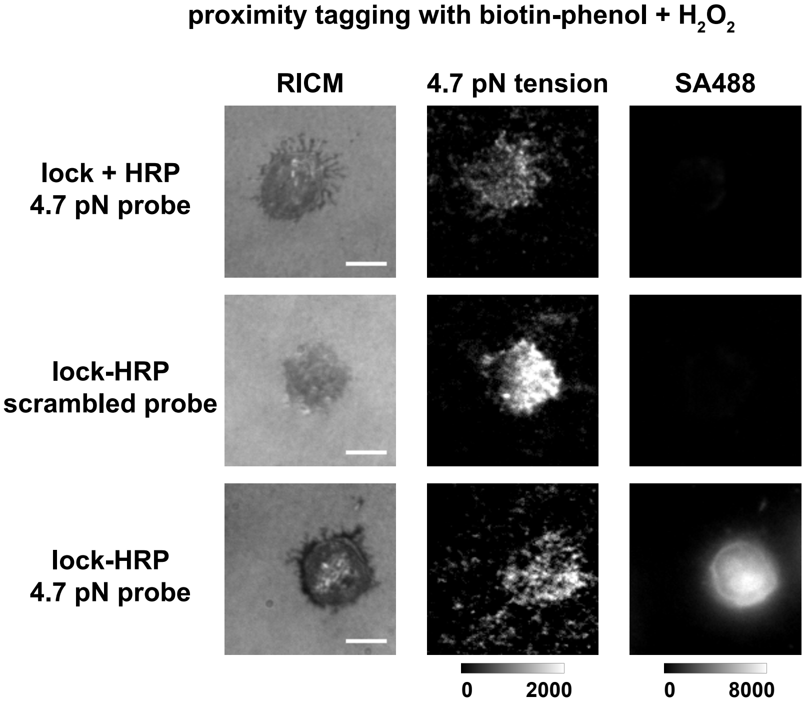

Figure A4.5. Collecting T cells after mechanically selective proximity biotinylation. (A) OT-1 cells on DNA tension probe substrate before and after DNase treatment for 5 min at room temperature. Cells that went through proximity tagging procedure failed to detach from the surface. It was possible that the phenol-radical attacked the guanines, and with the chemical addition, the oligonucleotide might be more resistant to nucleases [19]. (B) Bright field images of cells with H_2O_2 and without H_2O_2 treatment. (C) RICM of OT-1 cells showing scraping is an efficient and effective cell collection method. Scale bar = 10 μm.

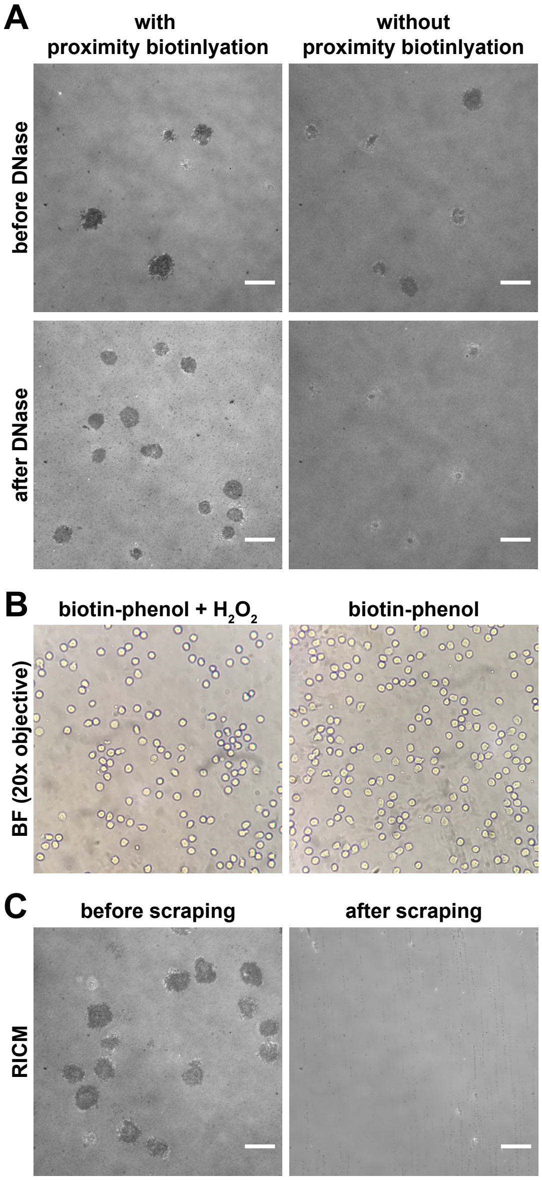

Figure A4.6. Heterogeneity among T cells. (A) Representative images showing the spreading of the OT-1 naïve CD8+ T cells on DNA tension probe substrate presenting pMHC N4, and producing tension, which was locked by 250 nM lock-HRP for 5 min. Cells with more frequent mechanical sampling of the pMHC N4 showed higher tension signal and vice versa. Scale bar = 10 µm. (B) Histogram of the distribution of OT-1 contact area on pMHC N4 DNA tension probes. (C) Histogram of the distribution of the OT-1 TCR tension integrated intensity after 5 min incubation with lock-HRP. Note that the quantitative analysis is from the same set of data as the representative images. The quantitative analysis was repeated, and we observe the same trend with the biological replicates (data not shown).

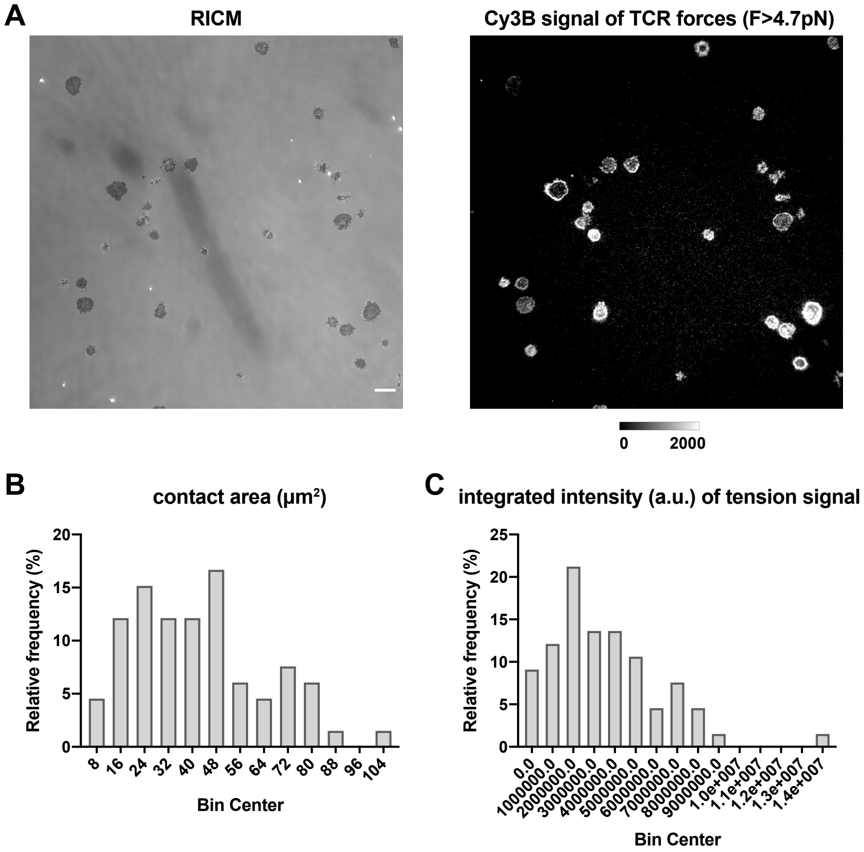

Figure A4.7. Representative gating of live singlet T cells with forward scatter and side scatter plots. Cell debris and aggregations were gated out, and only live singlet cells were analyzed in the flow cytometry data.

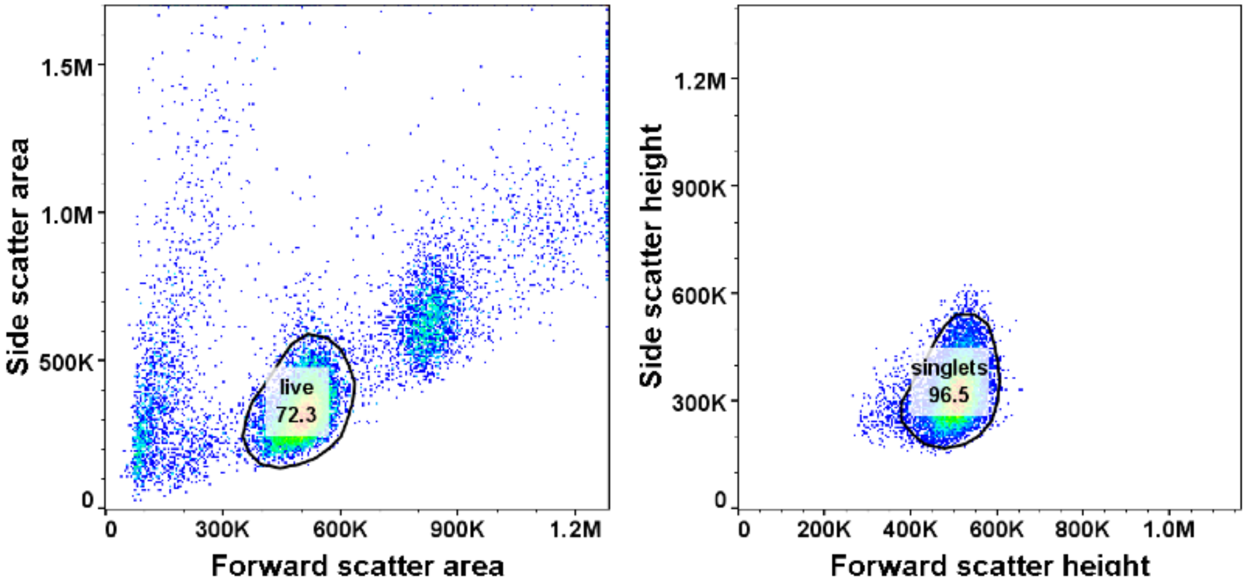

4.6. References

1. A. H. Courtney; W. L. Lo; A. Weiss, TCR Signaling: Mechanisms of Initiation and Propagation. *Trends Biochem Sci* **2018,** *43* (2), 108.

2. P. A. van der Merwe; O. Dushek, Mechanisms for T cell receptor triggering. *Nat Rev Immunol* **2011,** *11* (1), 47.

3. W. A. Comrie; J. K. Burkhardt, Action and Traction: Cytoskeletal Control of Receptor Triggering at the Immunological Synapse. *Front Immunol* **2016,** *7*, 68.

4. Y. Feng; E. L. Reinherz; M. J. Lang, alphabeta T Cell Receptor Mechanosensing Forces out Serial Engagement. *Trends Immunol* **2018,** *39* (8), 596.

5. C. Zhu; W. Chen; J. Lou; W. Rittase; K. Li, Mechanosensing through immunoreceptors. *Nat Immunol* **2019,** *20* (10), 1269.

6. Y. Liu; L. Blanchfield; V. P.-Y. Ma; R. Andargachew; K. Galior; Z. Liu; B. Evavold; K. Salaita, DNA-based nanoparticle tension sensors reveal that T-cell receptors transmit defined pN forces to their antigens for enhanced fidelity. *Proceedings of the National Academy of Sciences* **2016,** *113* (20), 5610.

7. V. P. Ma; Y. Liu; L. Blanchfield; H. Su; B. D. Evavold; K. Salaita, Ratiometric Tension Probes for Mapping Receptor Forces and Clustering at Intermembrane Junctions. *Nano Lett* **2016,** *16* (7), 4552.

8. J. Huang; V. I. Zarnitsyna; B. Liu; L. J. Edwards; N. Jiang; B. D. Evavold; C. Zhu, The kinetics of two-dimensional TCR and pMHC interactions determine T-cell responsiveness. *Nature* **2010,** *464* (7290), 932.

9. L. V. Sibener; R. A. Fernandes; E. M. Kolawole; C. B. Carbone; F. Liu; D. McAffee; M. E. Birnbaum; X. Yang; L. F. Su; W. Yu; S. Dong; M. H. Gee; K. M. Jude; M. M. Davis; J. T.

Groves; W. A. Goddard, 3rd; J. R. Heath; B. D. Evavold; R. D. Vale; K. C. Garcia, Isolation of a Structural Mechanism for Uncoupling T Cell Receptor Signaling from Peptide-MHC Binding. *Cell* **2018,** *174* (3), 672.

10. R. Ma; A. V. Kellner; V. P.-Y. Ma; H. Su; B. R. Deal; J. M. Brockman; K. Salaita, DNA probes that store mechanical information reveal transient piconewton forces applied by T cells. *Proceedings of the National Academy of Sciences* **2019,** *116* (34), 16949.

11. K. H. Hu; M. J. Butte, T cell activation requires force generation. *J Cell Biol* **2016,** *213* (5), 535.

12. D. L. Harrison; Y. Fang; J. Huang, T-Cell Mechanobiology: Force Sensation, Potentiation, and Translation. *Front Phys* **2019,** *7*.

13. R. Li; C. Ma; H. Cai; W. Chen, The CAR T-Cell Mechanoimmunology at a Glance. *Adv Sci (Weinh)* **2020,** *7* (24), 2002628.

14. J. S. Rees; X. W. Li; S. Perrett; K. S. Lilley; A. P. Jackson, Protein Neighbors and Proximity Proteomics. *Molecular & cellular proteomics : MCP* **2015,** *14* (11), 2848.

15. E. Choi-Rhee; H. Schulman; J. E. Cronan, Promiscuous protein biotinylation by Escherichia coli biotin protein ligase. *Protein Science : A Publication of the Protein Society* **2004,** *13* (11), 3043.

16. J. M. Dong; F. P. Tay; H. L. Swa; J. Gunaratne; T. Leung; B. Burke; E. Manser, Proximity biotinylation provides insight into the molecular composition of focal adhesions at the nanometer scale. *Science signaling* **2016,** *9* (432), rs4.

17. H. W. Rhee; P. Zou; N. D. Udeshi; J. D. Martell; V. K. Mootha; S. A. Carr; A. Y. Ting, Proteomic Mapping of Mitochondria in Living Cells via Spatially-Restricted Enzymatic Tagging. *Science* **2013,** *339* (6125), 1328.

18. K. Minamihata; M. Goto; N. Kamiya, Protein heteroconjugation by the peroxidase-catalyzed tyrosine coupling reaction. *Bioconjugate chemistry* **2011,** *22* (11), 2332.

19. J. Dai; A. L. Sloat; M. W. Wright; R. A. Manderville, Role of Phenoxyl Radicals in DNA Adduction by Chlorophenol Xenobiotics Following Peroxidase Activation. *Chemical Research in Toxicology* **2005,** *18* (4), 771.

20. R. Basu; M. Huse, Mechanical Communication at the Immunological Synapse. *Trends Cell Biol* **2017,** *27* (4), 241.

21. M. L. Dustin; L. C. Kam, Tapping out a mechanical code for T cell triggering. *J Cell Biol* **2016,** *213* (5), 501.

22. M. Huse, Mechanical forces in the immune system. *Nat Rev Immunol* **2017,** *17* (11), 679.

Chapter 5. Molecular tension probe based on force-induced DNA peeling mechanism maps integrin forces with microscopy and enables force-based cell high throughput identification

5.1. Introduction

Cells frequently transduce mechanical cues such as substrate rigidity, external forces, and endogenous forces into biochemical signals [1]. With these biochemical signals originating from mechanical information, cells are able to adapt to their microenvironment, as well as make decisions to migrate, proliferate, and differentiate [2-3]. Adhesion proteins, such as the integrin family, participate extensively in this process. Upon binding to extracellular ligands, integrins become activated and recruit multiple proteins such as talin, vinculin, and paxillin to form focal adhesions (FA), which transduce mechanical forces into biochemical signals through the mechanotransduction network [2, 4-5]. To further study how mechanical cues are processed into biochemical signals, tools to detect the molecular mechanical forces are required. Traction force microscopy and micropillars are two of the most commonly used methods to map the cellular traction forces, however the spatial resolution and the force sensitivity of these methods is not sufficient to study forces from individual receptors [6-8].

Our lab took advantage of the mechanical properties of polymer-based materials in order to pioneer the development of molecular tension probes, with spring elements ranging from polyethylene glycol (PEG) to DNA. PEG-based force probes are entropic springs that generate an "analog" response as they experience force. This analog response makes signal interpretation difficult, as a substantial extension of a single PEG spring will look similar to a subtle extension of several proximal PEG springs[9]. Alternatively, the DNA-based tension probes are "digital" probes, generating a consistent signal only when they experience a force greater than the threshold needed to induce a structural change. For example, the DNA hairpin tension probes only report forces greater than the $F_{1/2}$ of the stem-loop, which is the equilibrium force with a 50% probability of driving hairpin unfolding. Though the interpretation of the force signal is simplified with DNA hairpin probes, one drawback is that the detection range is between a few pN and 20 pN, far weaker than the forces that integrins can exert [10]. Ha et al developed DNA-based tension gauge tethers (TGTs), which are DNA duplexes that can rupture under force. Originally, TGTs were developed to control the peak magnitude of force that a single receptor can experience [11]. Since the force that these DNA duplexes can tolerate before rupturing is tunable from 12 pN to 56 pN, Wang et al were able to utilize TGTs to map the integrin forces generated by different cell types, including platelets [12]. However, using TGTs as molecular force sensors instead of molecular force controllers is problematic, as the mechanical signaling is terminated throughout the receptor force detection, thus altering cellular responses [11]. Hence, to accurately map receptor tension and study mechanotransduction, a molecular tension probe that exhibits a high force detection range but does not interfere with the mechanical signaling of the cell is needed.

To tackle this problem, we take advantage of the DNA "peeling" mechanism under force (**Figure 5.1A**). When a DNA duplex is stretched from both ends of the same strand, the complementary DNA will mechanically "peel" from the strand that bears the load [13-15]. For short DNA duplexes, due to the narrow range of forces at which this strand separation happens, the force-induced peeling process can be characterized as a simple two-state system. Specifically, the probe exists in the dsDNA form if the force that is applied is below the tension tolerance (T_{tol}, defined as force at which there is a 50% probability of separation), or in the completely separated ssDNA form if the force is above the tension tolerance (**Figure 5.1A**). For a 24mer (sequence in **Table A5.1**), the T_{tol} was measured to be ~41 pN using magnetic tweezer characterization [16]. Therefore, we designed a DNA tension probe based on this peeling mechanism. The peeling probe is comprised of a Cy3B labeled load-bearing strand, anchored on a glass slide on one end and presenting a ligand (cRGDfk) for cell attachment on the other end, and a complementary Atto647N labeled strand that peels off once a force greater than the T_{tol} is applied to the ligand on the load-bearing strand (**Figure 5.1B**). The Cy3B and Atto647N forms a Förster resonance energy transfer (FRET) pair. When force is absent and the probe is in the dsDNA form, the fluorescence of Cy3B is quenched by Atto647N on the peeling strand, and when force is present, the Atto647N strand peels off, thus unquenching the Cy3B. This DNA peeling probe would enable us to observe receptor forces > T_{tol} with turn-on fluorescence signals of Cy3B and turn-off fluorescence signals of Atto647N. The inclusion of a turn-on fluorescence response is important for confirming that depletion in the Atto647N signal is due to peeling and not nuclease-mediated destruction of the DNA probe or detachment of the load-bearing strand from the surface. Furthermore, in this probe design, duplex denaturation of the probe, which allows for observation of the force, does not result in termination of the mechanical force, as is the case with TGTs. Instead, termination of the interaction between the cell and the surface only occurs when the receptor dissociates from the ligand or the force exceeds the much higher tension tolerance of the biotin-streptavidin bond (~160 pN) [17]. This decoupling of the force observation and force transmission is essential to characterize the physical properties and biological functions of forces generated by integrins, as it is in a biology-mimicking setting where integrin forces do not terminate the mechanotransduction.

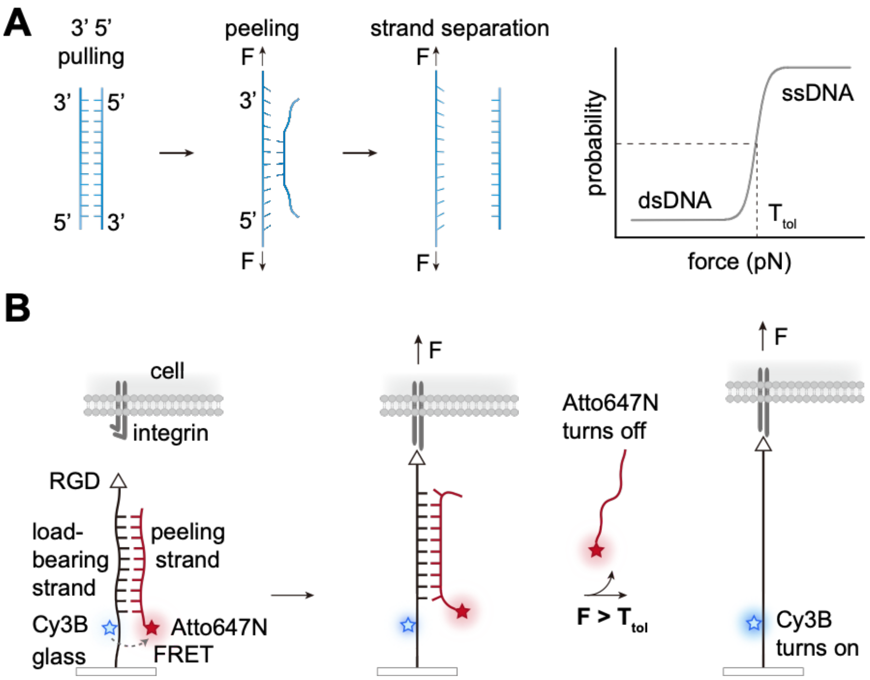

Figure 5.1. Schematic of the DNA tension probe design based on the DNA peeling mechanism. (A) DNA peeling occurs when 3'5' pulling is applied to a DNA duplex, which is a two-state system with the transition happening at a narrow range. The T_{tol} is defined as the force at which there is a 50% probability of strand peeling. (B) The peeling probe consists of a Cy3B labeled load-bearing strand and a Atto647N labeled peeling strand. The constructs are immobilized on a glass slide and present RGD ligand for integrins. Without force the Cy3B fluorescence is quenched by FRET. Once a cell binds and pulls on the RGD molecule, the force drives the peeling of the Atto647N strand, and thus generates a turn-on Cy3B signal and a turn-off Atto647N signal.

We employed this peeling probe to map the tension produced by NIH3T3 cells and found that the cells had significantly higher contact area and tension area compared to when cells spread on a 56 pN TGT surface, and were able to produce tension signals with a high signal-to-noise ratio. Moreover, the cells plated on the peeling probes also showed different phenotypes of actin distribution compared to TGTs, with a significantly higher percentage of cells forming actin stress fibers, specifically perinuclear actin caps. We further took advantage of the diffusion of the peeling strand after the force-induced strand separation, by functionalizing the peeling strand with a cholesterol moiety, which can insert into the proximal cell membrane and enable tagging of the cells that induced peeling due to integrin forces.

5.2. Results and discussion

5.2.1. Design and preparation of the DNA tension probes based on peeling mechanism

As the load-bearing strand in the DNA peeling probe needs to be anchored on a substrate, present the ligand, and generate a turn-on fluorescence signal, two terminal modifications and an internal modification were incorporated. Specifically, the load-bearing strand has a biotin on its 3’ end that allowed it to be anchored on biotin surfaces, a thiol on its 5’ that was conjugated with a ligand, and an internal amine that was conjugated with a Cy3B fluorophore (**Figure A5.1**). The complementary peeling strand was conjugated with Atto647N on its 5’ end to enable reporting of peeling events with depletion signals (**Figure A5.1**). We adopted the sequence from literature with a reported critical force T_{tol} of ~41 pN for the design of the DNA peeling probe [16]. The DNA construct was annealed and immobilized on streptavidin-coated biotin functionalized glass slides. The FRET efficiency was calculated to be 96.5% using probes bearing or lacking the acceptor Atto647N (**Figure A5.2**). And the probe density was estimated to be ~4000 molecules/μm^2 using a method reported in literature [10].

5.2.2. Visualizing the integrin forces in fibroblasts

With the DNA tension probe substrates prepared and characterized, first a proof-of-concept was performed with NIH3T3 cells. A 24mer DNA duplex (24 peeling probe) that has an estimated T_{tol} of ~ 41 pN was used to probe the integrin mechanical activities. NIH3T3 cells were plated on the tension probe functionalized substrate and allowed to attach at 37 °C for 15 minutes. Then, the cells were kept at room temperature, and the integrin tension signal was imaged with a fluorescence microscope from t = 40 min to t = 60 min after plating. As the Cy3B-labeled load-bearing strand was stretched due to the binding between the RGD and integrin, Atto647N-labeled peeling strands detached and generated a fluorescence turn-on signal in Cy3B channel and turn-off signal in Atto647N channel (**Figure 5.2A**). A linescan of an ROI shows that the turn-on Cy3B signal is anti-colocalized with the Atto647N intensity, further confirming the peeling of the Atto647N strand under force led to the dequenching of the Cy3B (**Figure 5.2B**). A control group of cells treated with Latrunculin B (Lat B), which inhibits actin polymerization and disrupts force generation, was included to confirm peeling is cell mediated. With Lat B early treatment (added at t = 20 min), cells showed significantly less spreading and fluorescence signal, suggesting that the force generated by the cellular machinery caused the DNA peeling and generated tension signal (**Figure A5.3A**). Cells treated with Lat B at a later stage after visualizing the tension signal (added at t = 50 min) showed no signal change though force transmission was terminated, suggesting that the peeling probe is an irreversible molecular force sensor (**Figure A5.3B**).

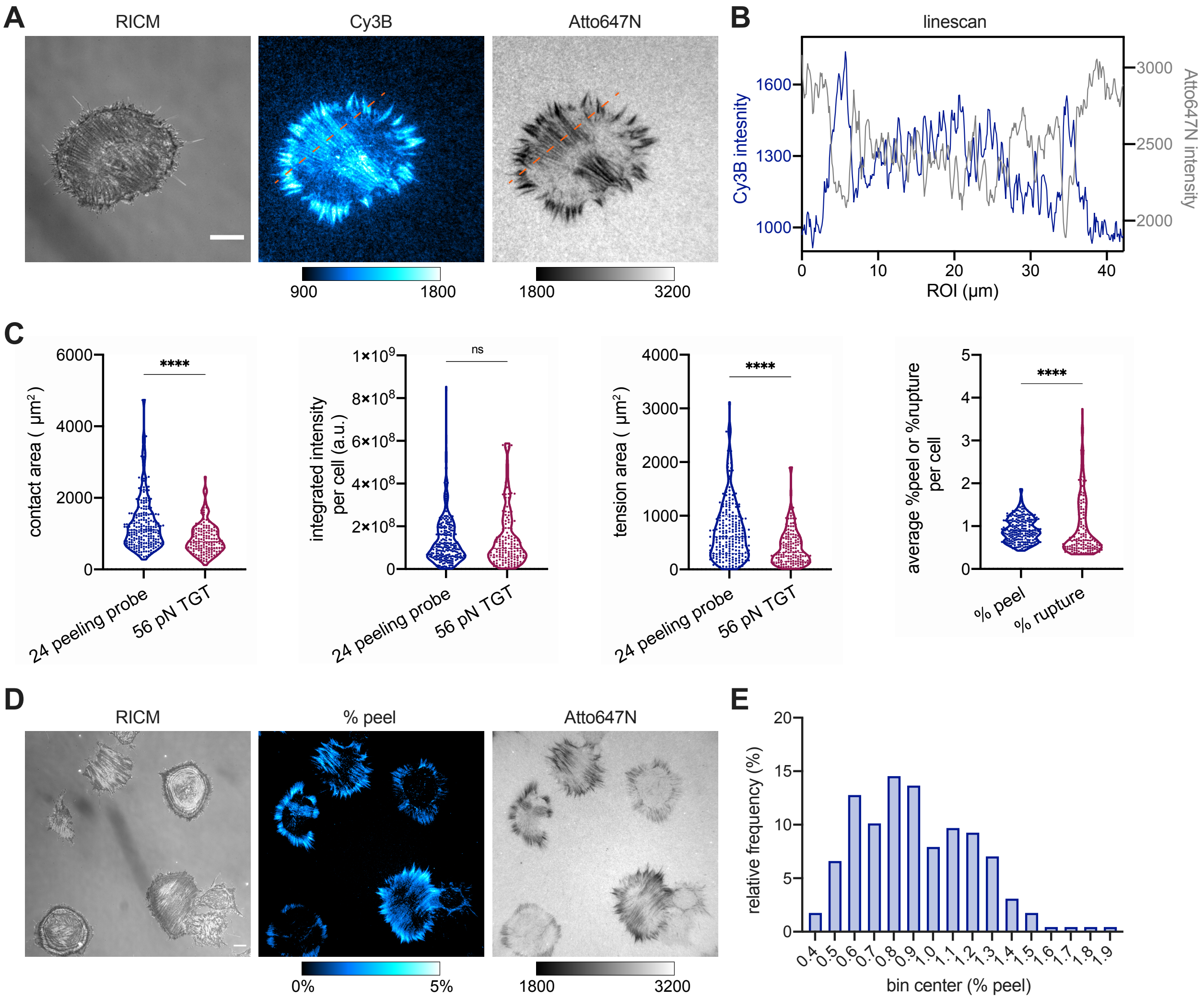

Figure 5.2. Mapping integrin tension generated by NIH3T3 cells with 24 peeling probes. (A) Representative microscopy images of NIH3T3 cells producing integrin forces greater than 41 pN towards RGD ligands on a 24 peeling probe substrate. The RICM image shows the cell spreading, the Cy3B image shows the turn-on fluorescence signal of the tension, and the Atto647N image shows the turn-off fluorescence signal after the peeling strand was released due to force application. Scale bar = 10 μm. (B) Linescan of the ROI in (A) shows the anti-colocalization of the fluorescence intensity in Cy3B and Atto647N channels. (C) Quantitative analysis of the contact area, integrated tension signal, tension area, %peel / %rupture of NIH3T3 cells on peeling probe substrates in comparison with 56 pN TGT substrates. Data was acquired with 3 biological replicates (total n = 227 and 149 for cells on 24 peeling probe substrate and 56 pN TGT substrate, respectively). Plots show lines at the median and interquartile values. Unpaired Welch t test was used for statistical analysis in contact area, integrated intensity, and tension area. Kolmogorov-Smirnov test was used to compare the distribution of %peel and %rupture. ns, $P > 0.05$. ****, $P < 0.0001$. (D) Representative microscopy images of 7 cells show the heterogeneous level and distribution of the integrin force. Three of the cells showed clear polarized tension at the center of the cells that are related to actin stress fibers. Two showed clear tension signal only at the periphery focal adhesions. One cell showed tension signal only at the cell cortex and filopodia. One cell did not show any

obvious tension signal. The image in Cy3B channel was processed and presented as %peel. Scale bar = 10 μm. (E) Histogram of 227 cells from 3 biological replicates show the distribution of average %peel per cell for cells plated on peeling probe after 1 h incubation. Bin width = 0.1%.

5.2.3. Quantitative analysis of integrin tension on peeling probe in comparison with 56 pN TGT

As previously mentioned, the TGTs terminate receptor mechanical signaling after the top strand is unzipped or sheared (**Figure A5.4A**). Though this feature is ideal for manipulating the forces allowed for mechanical signaling of a single receptor, we speculated that TGTs are less advantageous as tension probes due to this perturbation of cell mechanotransduction. Therefore, we compared the cell spreading area, tension signal intensity, and tension area of the cells on the peeling probes to those of the cells on a TGT substrate (**Figure 5.2C**). We chose to use 56 pN TGT to compare with 24 peeling probe, as the cells do not spread well on 12 pN TGTs for the same reasons. To ensure this is a fair comparison, the TGT substrates were prepared in the same way and had a similar density of ~4000 molecules/μm^2. Also, NIH3T3 cells were plated on the TGT substrates and imaged in parallel with the peeling probe substrates (**Figure A5.4B**). The contact area of the cells that were incubated on the peeling probe surfaces was significantly larger than that of cells on 56 pN TGT substrates, further implying that the cells were losing their integrin-RGD "anchors" on the surfaces as the TGTs rupture even though it is the highest possible tension tolerance (~56 pN) for a TGT. The tension area (area under the cell that produced tension signal) for cells on the peeling probe surface was also significantly higher compared to that of cells on 56 pN TGTs, though no statistical difference was found in the integrated tension intensity. The turn-on fluorescence intensity is transformed to %peel or %rupture according to literature [10]. Given that the surface probe density is ~4000 probes/μm^2, and the cells on the peeling probe had 0.9 ± 0.02% probe peeling (mean ± SEM), there were effectively ~40 integrins per μm^2 that could generate force greater 41 pN (**Figure 5.2C**). The number of integrins per μm^2 that generated forces agreed well with the previously reported %unfold using the DNA hairpin tension probes by integrins (~ 9% at ~400 probes/μm^2, effectively 36 integrins per μm^2 generated forces) [10]. Moreover, 56 pN TGT also showed a lower level of probe rupture (%rupture = 0.67 ± 0.06, median ± SEM) compared to 24 peeling probe, and a wider distribution of %rupture, likely an artifact due to cells losing their anchor on the substrate, trying to spread, and lacking sustained mechanical signaling.

5.2.4. Peeling probe revealed that the formation of perinuclear actin requires sustained force transmission, and the associated focal adhesions exert force > 41 pN

Based on qualitative observation of differences in the cell morphology and tension pattern between cells plated on peeling probe (**Figure 5.2D)** compared to that of the 56 pN TGT surfaces (**Figure A5.4B**), we sought to further analyze cell morphology and cytoskeletal organization. As the polarized/symmetric stress fiber pattern was commonly observed in the tension map of cells plated on the peeling probe surface, and it aligned closely with the actin stress fibers that were be observed in the RICM images, we stained the NIH3T3 cells with SiRActin, a small molecule that becomes fluourescent upon binding to actin. After 1 h of incubation on peeling probe, 56 pN TGT, or 12 pN TGT substrates (**Figure A5.5A**), the cells were stained, and actin was imaged on the fluorescence microscope (**Figure A5.5B**). Different phenotypes of actin distribution were observed from cells on the three types of substrates and categorized into 8 distinct sub-types (**Figure A5.5C**) [18-22]. Interestingly, cells with polarized perinuclear actin stress fibers (category 6, 7, 8) were the most frequently observed phenotype on the peeling probe, whereas these phenotypes were less observed in of cells on the 56 pN TGT substrate, and not observed in any cells on the 12 pN TGT substrate (**Figure A5.5D**). Studies have shown that the perinuclear actin cap is required in Yes-associated protein (YAP) nuclear signaling, and is critical in regulating cell morphology, protecting the nucleus from deformation, and contributing to cellular mechanical homeostasis [23]. Since the DNA constructs all have a 21-24 bp duplex region and present the same ligand at a density of ~4000 molecules/μm^2, we hypothesize that the differences in frequency of each phenotype that we observed are a result of the different magnitude of force required to rupture each of the three probes and terminate mechanical signaling (**Figure A5.5A**) [24]. By positioning the ligand and anchor at different locations on the duplex, the TGTs are mechanically denatured, terminating force transmission, at 12 or 56 pN as they undergo the unzipping or shearing mechanism, respectively. However, for the peeling probe, the load-bearing strand continues as the anchorage for the cell, unless the force exceeds 160 pN, which causes biotin-streptavidin dissociation (**Figure A5.5A**) [17]. The relatively abundant perinuclear actin cap phenotype on peeling probe implies that the assembly of this cellular structure likely requires persistent integrin-RGD bindings at higher forces.

Conversely, the peeling probe tension maps revealed that the perinuclear actin cap associated focal adhesions around the nucleus was capable of transmitting > 41 pN force. This finding agrees with a recent report using nanopillars, which showed that the actin cap is capable of transducing high forces compared to focal adhesions at the periphery of the cell [25], though both the force sensitivity and spatial resolution of nanopillars are not comparable to the peeling probe. Additionally, the tension produced at the actin cap-associated focal adhesions is intriguing because a previous report showed that the organization of perinuclear actin cap is different between healthy and diseased cells, potentially leading to differences in the cells ability to generate tension. Moreover, cells from animal models lacking a gene called LMNA showed no actin cap and significantly reduced stiffness, suggesting that the actin cap tension is related to specific genes. Moreover, if this is true, it raises the question of what is involved in the mechano-regulatory network that controls the expression of those genes [26]. As more detailed investigations are needed in the speculation of the actin cap's regulatory role in cell motility, polarization, and differentiation [23, 26-28], we envision that the peeling probe will help reveal how actin cap mediates mechanosensing and mechanotransduction, which is likely to be distinct from that of conventional focal adhesions [25].

5.2.5. High throughput detection of cells with higher integrin mechanical activity.

In addition to the high degree of heterogeneity observed in the actin structures that cells were able to form, even when plated on the same substrate, the tension signal and %peel of each cell was also highly heterogeneous among cells plated on the same substrate (**Figure 5.2E**). To better investigate this heterogeneity in integrin forces, we aimed to further develop the peeling probe so that it can quantify the forces each cell exerts in a high throughput manner. To achieve this goal, we needed a marker that would specifically tag each cell based on its integrin mechanical activity, reflected in the %peel value. To take advantage of the Atto647N-labeled peeling strand that is released into the solution following mechanical denaturation, a cholesterol group was added to the 3' end to mediate insertion into the proximal cell membrane following peeling. This approach will be referred to as Load-Induced Proximal Insertion of DNA (LIPID) (**Figure 5.3A**).

Briefly, NIH3T3 cells were incubated on the LIPID substrate as before, rinsed, and collected by gentle scraping. The tension-related peeling strand insertion was then detected with flow cytometry in a high-throughput manner. Cells incubated on the surfaces in the presence of EDTA, which prevents the integrin-RGD binding, and latrunculin B, which inhibits the actin polymerization and force generation, were included as controls (**Figure 5.3B, C)**. Cells incubated in the presence of EDTA showed minimal background fluorescence increase, which can serve as the baseline of this mechanically selective tagging technique. Cells treated with latrunculin B (added 15 min after plating) showed minimal increase in strand incorporation, which was consistent with observations from microscopy (**Figure A5.3**). Since the difference in spreading area could be a factor that contributed to the high level of tagging with 24LIPID, we included negative control substrates prepared with either a mixture of biotin-RGD and 24LIPID (no RGD) constructs or a mixture of 24mer load-bearing RGD strands and 18LIPID (no RGD) constructs. Cells spread well on both surfaces, yet only had a minimal increase in signal above the baseline, confirming that the tagging was specific to integrin mechanics (**Figure A5.6**). The Cy3B signal was also measured with flow cytometry, which showed only a subtle increase when cells were incubated on the LIPID substrates (**Figure 5.3C**). Furthermore, with a control group of cells incubated on the 24 peeling probe (lacking cholesterol), we confirmed the tagging mechanism was cholesterol-mediated (**Figure A5.6**).

Similar to the heterogeneous distribution of forces generated by each cell observed with microscopy, the flow cytometry results revealed a wide range of tension signals in the 24LIPID group. To further investigate this heterogeneity in tension-mediated tagging, the LIPID platform should allow the cells to be sorted based on their degree of tagging using fluorescence-activated cell sorting (FACS) allowing for further biological studies of each population. For applications such as these, it is particularly important that there is minimal loss/dissociation of the inserted cholesterol strands occurs over time. Thus, the stability of cholesterol-mediated strand insertion into the cell membrane was examined. Briefly, NIH3T3 cells were incubated with 100 nM cholesterol Atto647N peeling strand for 30 min and the fluorescence of the cells were measured over time (**Figure A5.7**). The cholesterol strand slowly dissociated from the cells over time, however ~ 90% remained after 60 min. Since the loss was only around 10% during the duration of the experiment, it is negligible for this assay. To further simplify this assay and reduce the costs of future applications, we also tested a version of the LIPID substrate that only has the Atto647N fluorophore (**Figure A5.8**). We anticipate that the mechano-phenotyping potential of this method would aid in establishing mechanical biomarkers such as integrin force to connect mechanobiology with tissue plasticity studies. For example, the cancer collective migration packet has leader and follower cells, which was demonstrated to have heterogeneous functions and mechanosensing abilities [29]. Thus, the LIPID approach might provide an effective approach to benchmark and predict metastasis potential in cancer.

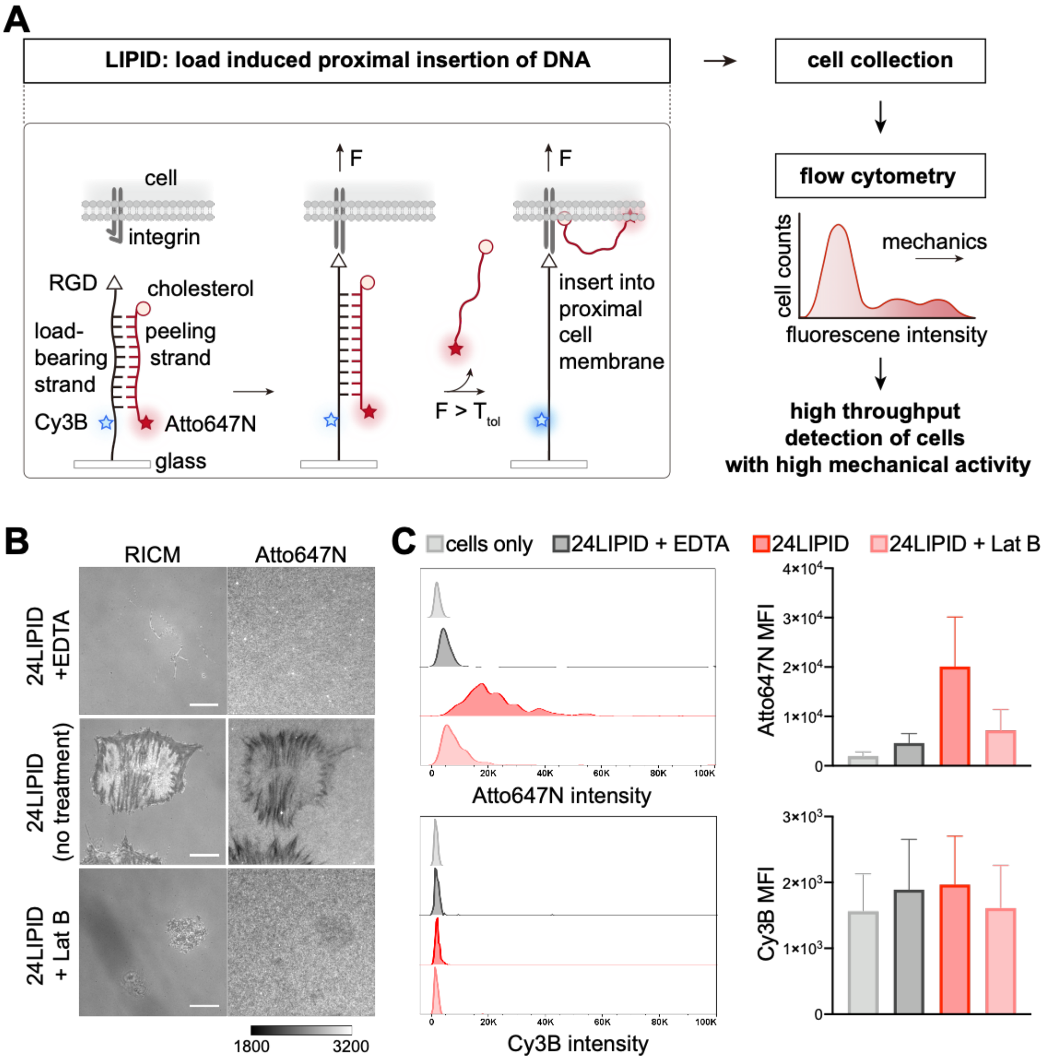

Figure 5.3. High throughput detection of NIH3T3 cells with integrin mechanical activity with LIPID. (A) Schematic showing the design and workflow of the LIPID method. (B) Microscopy images showing the effect of EDTA and Lat B on cell spreading and force generation. Scale bar = 10 µm. (C) Flow cytometry data showing that NIH3T3 cells incubated on LIPID substrate were tagged with the peeled Atto647N strand, and the tagging was specific to integrin-RGD force. Error bars represent SD.

5.3. Conclusion

We took advantage of the DNA peeling mechanism under force and developed a new class of irreversible DNA molecular tension probes. We applied the 24 bp peeling probes in fibroblasts and visualized integrin tension > 41 pN, including tension generated at the actin-cap associated focal adhesions. Unlike TGTs, peeling probes do not terminate mechanical signaling at the force threshold they detect, which makes them superior in detecting molecular forces at the cell-extracellular matrix (ECM) interface. We further introduced a cholesterol group on the peeling strand, which enabled tagging of cells with high integrin forces and subsequent high-throughput detection using flow cytometry. Therefore, we anticipate this platform will be a powerful tool to investigate the role of mechanics as a biomarker and to integrate mechanobiology perspectives with cell biology studies.

5.4. Materials and methods

5.4.1. Oligonucleotides

The oligonucleotides used in this study are listed in **Table A5.1.**

Table A5.1. List of oligonucleotides used in Chapter 5.

oligo name	5'	sequence (5' to 3')	3'
24 load-bearing strand	/5ThioMC6-D/	TTT TTT TTT TAG TGA GCT CTG AAG TCT TAG AAC T/iAmMC6T/T TT	/3Bio/
24peel_5NH2	/5AmMC6/	AG TTC TAA GAC TTC AGA GCT CAC T	
24peel647chol	/5ATTO647NN/	AG TTC TAA GAC TTC AGA GCT CAC T	/3cholTEG/
18 load-bearing strand	/5ThioMC6-D/	TTT TTT TTT TCA TAC GGT TAT AGA GTA G/iAmMC6T/T TT	/3Bio/
18peel_5NH2	/5AmMC6/	CTA CTC TAT AAC CGT ATG	
18peel647chol	/5ATTO647NN/	CTA CTC TAT AAC CGT ATG	/3cholTEG/
TGT 12 pN bottom	/5AmMC6/	CGC ATC TGT GCG GTA TTT CAC TTT	/3Bio/
TGT 56 pN bottom	/5Biosg/	TT T/iUniAmM/C GCA TCT GTG CGG TAT TTC AC	
TGT top quencher strand	/5Hexynyl/	GTG AAA TAC CGC ACA GAT GCG	/3BHQ-2/

5.4.2. Reagents

The reagents used in this study are listed in **Table A5.2.**

Table A5.2. List of reagents used in Chapter 5.

Material	Company	Catalog Number
Dulbecco’s Modified Eagle’s Medium (DMEM)	Corning	10-013-cm
Trypsin	Corning	25-053-CI
Bovine Calf Serum (CCS)	Corning	35-054-CM
Penicillin-Streptomycin Solution, 100x	Corning	30-002-CI
Atto647N NHS ester	Sigma	18373-1MG-F
Cy3B NHS ester	GE Healthcare	PA63101
3-Hydroxypicolinic acid (3-HPA)	Sigma	56197
Nanosep MF centrifugal devices	Pall laboratory	ODM02C35
P2 gel	Bio-rad	1504118
Triethylammonium acetate buffer	Sigma	90358
(3-Aminopropyl)triethoxysilane	Acros	AC430941000
Ethanol	Sigma	459836
Hydrogen peroxide	Sigma	H1009
EZ-Link™ NHS-Biotin	Thermo Fisher	20217
Sufuric acid	EMD Millipore Corporation	SX1244-6
Sulfo-NHS acetate	Thermo Fisher Scientific	26777
Wash-N-Dry™ Slide Rack	Sigma	Z758108
Glass Coverslips for sticky-Slides 25 / 75 mm	Ibidi	10812
Sticky-slide 18 Well	Ibidi	81818
Bovine serum albumin	Sigma	735078001
Dimethyl Sulfoxide (DMSO)	EMD-Millipore	M1096780100
UltraPure™ 0.5M EDTA, pH 8.0	Thermo Fisher	15575020
Formaldehyde solution	Sigma	252549
Triton™ X-100	Sigma	X100
streptavidin	Thermo Fisher	434302
Amicon® Ultra 0.5 mL Centrifugal Filters	Sigma	UFC503024
Bond-Breaker™ TCEP Solution, Neutral pH	Thermo Fisher	77720
c(RGDfK(Biotin-PEG-PEG))	VIVITIDE	PCI-3697-PI
Cyclo[Arg-Gly-Asp-D-Phe-Lys(Mal)]	VIVITIDE	50-168-6952
Cyclo[Arg-Gly-Asp-D-Phe-Lys(PEG-PEG)]	VIVITIDE	PCI-3696-PI
azide NHS	Thermo Fisher	88902
SiR-Actin Kit	Cytoskeleton	CY-SC001

5.4.3. Equipment

The equipment used in this study are listed in **Table A5.3.**

Table A5.3. List of equipment used in Chapter 5.

Equipment	Company
Barnstead Nanopure water purifying system	Thermo Fisher
AdvanceBio Oligonucleotide C18 column, 4.6 x 150 mm, 2.7 µm	Agilent
High-performance liquid chromatography	Agilent 1100
Matrix-assisted laser desorption/ionization time-of-flight mass spectrometer (MALDI-TOF-MS)	Voyager STR
Nanodrop 2000 UV-Vis Spectrophotometer	Thermo Fisher
CFI60 Apochromat TIRF 100X Oil Immersion Objective Lens, N.A. 1.49	Nikon
Prime 95B-25MM Back-illuminated sCMOS Camera. 1608x1608,30fps	Photometrics
Nikon Ti2-E Motorized Research Microscope	Nikon
Ti2-ND-P Perfect Focus System 4	Nikon
SOLA SE II 365 Light Engine	Nikon
NIS Elements software	Nikon
C-FL Surface Reflection Interference Contrast (SRIC) Cube	CHROMA
CF-L AT CY5/Alexa Fluor 647/Draq 5 Filter Set	CHROMA
C-FL DS Red Hard Coat, High Signal-to-Noise, Zero Shift Filter Set	CHROMA
CytoFLEX V0-B3-R1 Flow Cytometer	BECKMAN COULTER

5.4.4. Oligonucleotide preparation

Conjugation with dye. An excess amount of dye-NHS (50 μg) was dissolved in DMSO immediately before use and then reacted with 10 nmol amine oligonucleotide at room temperature for 1 h in 1×PBS containing 0.1 M $NaHCO_3$. The mixture after reaction was desalted with P2 gel and purified with a HPLC coupled to an Advanced oligonucleotide C18 column. The product was eluted with 0.1 M TEAA as mobile phase A and acetonitrile as mobile phase B (gradient linear elution: 10%-100% over 50 min), and dried in a Vacufuge. The dried product was reconstituted in water and the concentration was determined by its absorbance at 260 nm with Nanodrop.

Conjugation with cRGD. For thiol oligonucleotide strands (load-bearing strands), maleimide-cRGDfk was used for the conjugation. Briefly, 5 nmol of thiol oligonucleotide was reduced in 200× molar excess TCEP at room temperature for 15 min, and the mixture was added to 0.5 mg (excess) of maleimide-cRGDfk in 1× PBS (pH = 6.8) to react at room temperature for 1 h. The reaction mixture was then desalted with P2 gel and purified with HPLC as described above.

For alkyne oligonucleotide TGT top quencher strand, azide-RGD was first prepared and then conjugated to the oligo. Briefly, excess amount of azide-NHS (around 0.5 mg) was used to react with 100 μg cyclic(RGD)fk-PEG2-amine overnight at 4 °C. The product was purified with HPLC coupled to a Grace C18 column for peptide purification. The mobile phase was A: 0.5% TFA in water, and B 0.5% TFA in ACN. The purified product was dried and characterized with Maldi-TOF-MS (data not shown). Stock solutions of $CuSO_4$ (20 mM in water), THPTA [Tris(3-hybroxypropyltriazolyl methyl)amine] (50 mM in water), sodium ascorbate (100 mM in water) were prepared. A final mixture of 100 μM azide-RGD, 50 μM of alkyne-DNA, 0.1 mM $CuSO_4$, 0.5 mM THPTA, and 5 mM sodium ascorbate in 1X PBS was allowed to react at room temperature for 2 h. The product was purified by P2 gel, followed by HPLC with advance oligo column (mobile phase A: 0.1 M TEAA, B: ACN). The final product is characterized with UV-Vis and Maldi-TOF-MS (data not shown).

5.4.5 DNA tension probe substrate preparation

Amine glass slides. Glass slides (25 × 75 mm) were placed on a Wash-N-Dry rack, rinsed by water (18.2 MΩ), and sonicated in ethanol and water for 15 min each, followed by 6 rinses with water. Fresh piranha solution was made by mixing concentrated sulfuric acid and hydrogen peroxide (30%) at 3:1 ratio (v/v) in a total volume of 200 mL and added to the slides for etching. CAUTION: PIRANHA SOLUTION IS HIGHLY REACTIVE AND MAY EXPLODE IF MIXED WITH ORGANIC SOLVENTS. Next, the slides were rinsed again with copious amount of water to remove the acid, and then rinsed in ethanol to remove water. 3% APTES in ethanol was prepared and added to the glass slides at room temperature to react for 1 h for amine modification. After reaction, the glass slides were washed with copious ethanol, and bake dried in an oven (80 °C) for 20 min. The amine modified glass slides were stored at -20 °C until use.

Biotin substrate preparation. An amine modified glass slide was carefully placed on a parafilm-lined petri dish. Then, 1 mL of 2 mg/mL Biotin-NHS in DMSO was added to the slide and incubated overnight. On the second day, after washing with copious amounts of ethanol and then water several times, the glass slide was air-dried, and attached to an ibidi sticky-slide imaging chamber. The wells were passivated in 0.5% BSA in PBS for 10 min at room temperature and then washed with PBS. Streptavidin at 50 µg/mL in PBS was added to each well and incubated for 30 min at room temperature, and the excess was washed away with PBS. Meanwhile, peeling probe (load-bearing strand:peeling strand = 1:1.5) was annealed at 50 nM by heating to 95 °C for 5 min and then gradually cooling down to 20 °C in 20 min. Next, the probes were added to each streptavidin-coated well and incubated for 30 min. The excess was rinsed away with PBS before imaging.

5.4.6. Cell culture

NIH3T3 cells were cultured in DMEM (10% CCS, 1% P/S) at 37 °C with 5% CO_2. Cells were passaged at 80% confluency every two days by detaching using trypsin and replating at lower density.

5.4.7. Fluorescence microscopy

Imaging was conducted with a Nikon Ti2-E microscope. Briefly, the cells were plated onto the DNA probe substrates and allowed to attach for 15 min in the incubator at 37 °C in medium. Then the cells were taken out from the incubator and allowed to further spread at room temperature for another 15-25 min. The cells were then imaged within 40 min to 60 min after plating in RICM, Cy3B, and Atto647N channels with accommodating filter settings and a sCMOS detector.

5.4.8. Flow cytometry

After cells were plated on the substrate for 45-60 min and generated integrin tension against RGD ligands, the cells were gently rinsed with PBS twice and collected by scraping in PBS containing 5 mM EDTA. The collected cells were immediately run through a flow cytometer for analysis.

5.4.9. General experiments

All the experiments were carried out with biological replicates.

Cell treatment. Aliquoted latrunculin B stock was reconstituted with ethanol at 25 mg/mL and stored at -20 °C. For cells treated with lat B, 20 µM lat B was added to NIH3T3 cells at t = 15 min after plating and incubated with cells for 30 min. For cells treated with EDTA, 10 mM EDTA was added to the cells when plating to prevent the binding between integrins and RGD.

Actin staining. Cells incubated on peeling probe, 56 pN TGT, or 12 pN TGT substrates were fixed in 4% formaldehyde for 15 min, followed by 2 gentle PBS washes and permeabilization with 0.1% triton X-100 in PBS for 10 min. The cells were then blocked in 1% BSA for 1 h and then stained with 1 μM SiR-actin at 4 °C overnight. The cells were rinsed gently with PBS and then imaged.

5.4.10. Data analysis

All microscopy data was analyzed with Image J software. For quantification of FRET efficiency, Cy3B load-bearing strand and Atto647N peeling strand were annealed and immobilized on a biotin substrate and imaged to obtain the fluorescence intensity with both donor and acceptor present (I_{DA}). Similarly, Cy3B load-bearing strand and amine peeling strand were annealed and immobilized on a biotin substrate and imaged to obtain fluorescence intensity when only the donor was present (I_D). After sCMOS background subtraction of the images, the fluorescence intensity in Cy3B was averaged from 5 different positions of the substrates. The FRET efficiency was calculated with by $1 - I_{DA}/I_D$.

The probe density was estimated as described previously in literature [10]. Briefly, peeling probe and TGT substrates with unquenched Cy3B fluorescence strand was prepared. A calibration curve was made with fluorescent supported lipid bilayers (SLB) to provide a count for molecules/μm^2, and the F-factor was calculated by a standard curve with a series of Cy3B concentrations (data not shown). The average intensity of three substrates was used to calculate the probe density using the calibration curve.

For quantitative analysis of microscopy data with cells, the sCMOS background was subtracted, and the fluorescence intensity (mean±SD) of the substrate background was used as a threshold. Raw integrated intensity, contact area, and tension area of the ROIs of the cells were measured and plotted. The tension signal in Cy3B for each image was used to calculate the %peel or %rupture according to literature (**Figure A5.9**) [10].

Flow cytometry data was analyzed with the Flowjo software. Briefly, the debris and aggregated cells were gated out by first identifying the live cells using the forward scatter and side scatter area and then the singlet cells using the forward and side scatter height (**Figure A5.10**). Following gating, the fluorescence signal of each viable singlet cell in the Atto647N channel and Cy3B channel was measured and analyzed. The signal intensity was presented in histograms, and the median fluorescence intensity (MFI) was used for comparison between groups. The number of %positive cells was determined by creating a vertical gate in the histogram of the negative control group so that ~99.5% of cells in the negative control had a lower fluorescence than the gate.

5.5. Appendix

Figure A5.1. Oligonucleotide preparation. (A) Chemical structures of the modifications on the oligonucleotides. (B) HPLC traces showing the purification of the synthesized oligos.

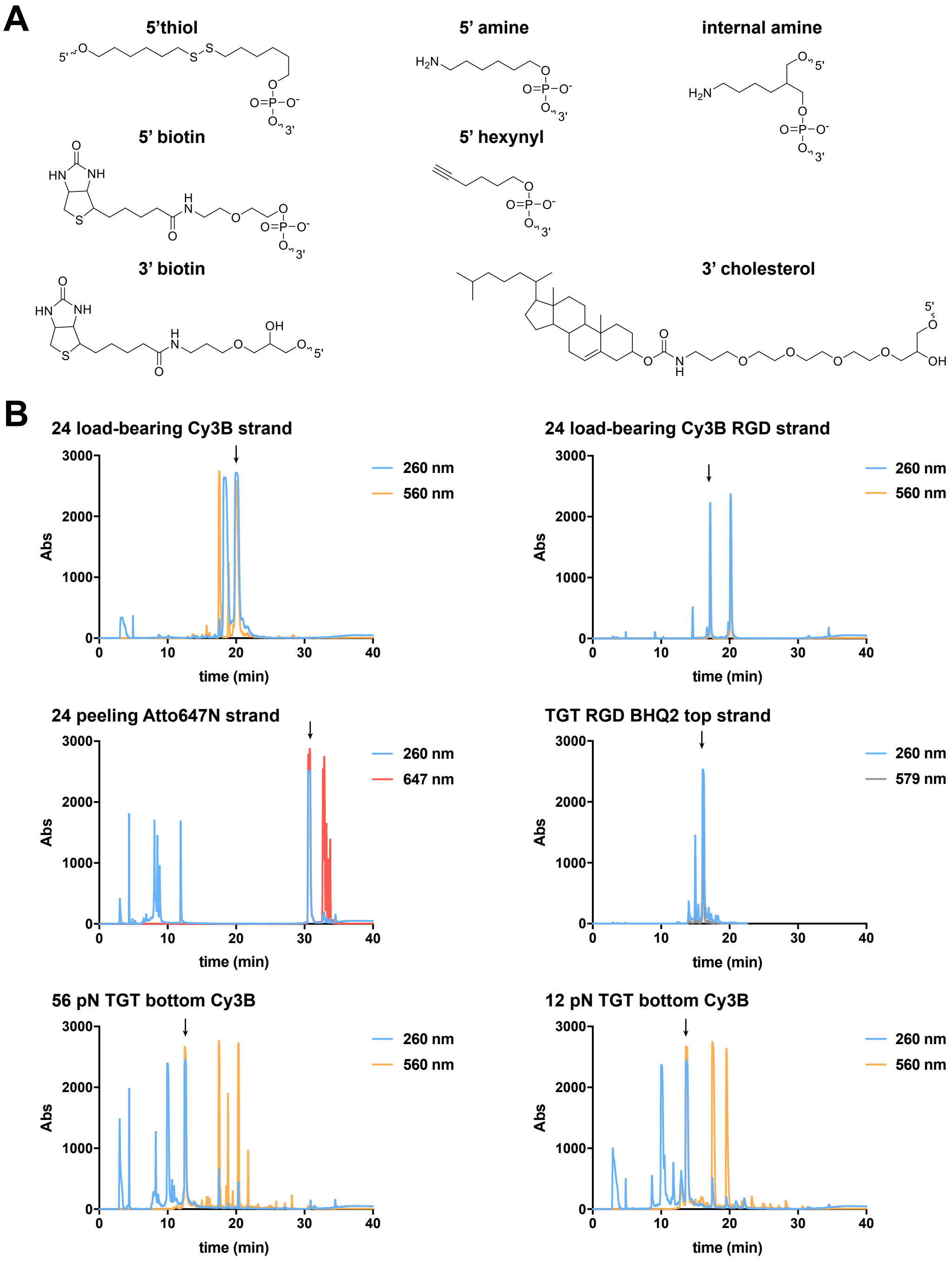

Figure A5.2. FRET efficiency calculation. (A) Scheme and representative microscopy images of the DNA peeling probe substrate with or without the acceptor Atto647N. The FRET efficiency was calculated to be 96.5% using the equation 1 – I_{DA}/I_D. Scale bar = 10 µm. (B) Conversion between I_{DA}/I_D and %peel.

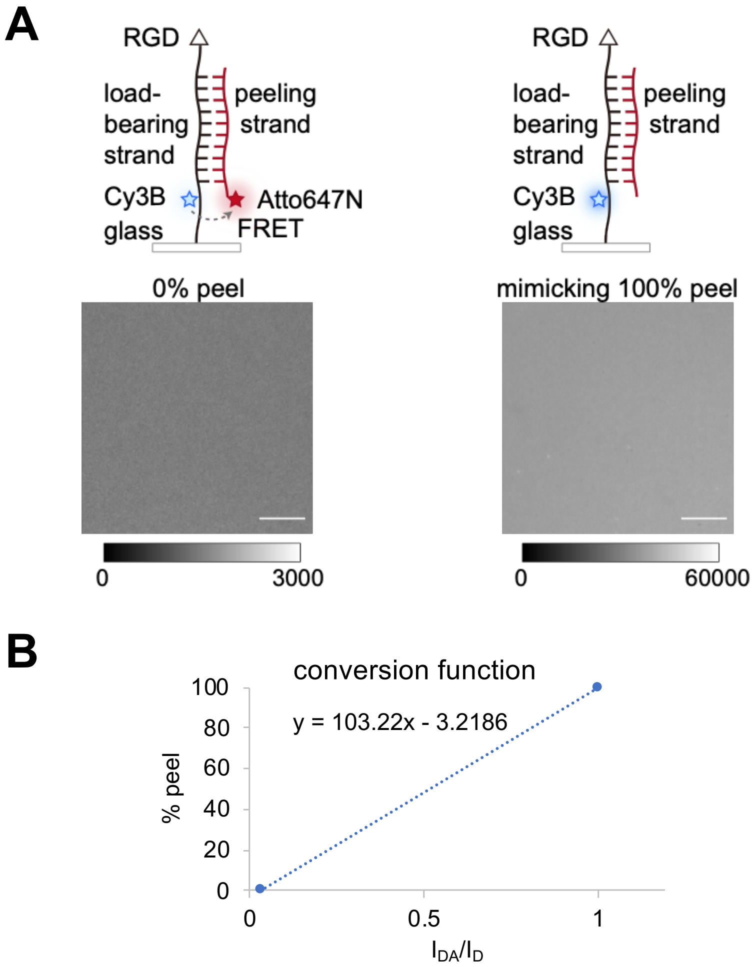

Figure A5.3. Representative microscopy images showing integrin tension of cells treated with Latrunculin B. (A) Representative microscopy images of NIH3T3 cells in RICM, Cy3B, and Atto647N channels after early Lat B treatment. Cells were treated with 20 µM Lat B after 20 min of plating on the substrate, and imaged following 30 min of incubation. The cells did not spread well, and only minimal tension signals were observed, demonstrating that the tension probe signal was due to force generated by cell machinery and transmitted through integrin to RGD. (B) Representative microscopy images of NIH3T3 cells in RICM, Cy3B, and Atto647N channels after late Lat B treatment. The cells were imaged in both the Cy3B and Atto647N channel 50 min after plating and observed to be generating forces > 41 pN. Then, Lat B was added to the cells and incubated for 10 min. Linescan analysis was performed before and after Lat B incubation and showed that the tension signal in both channels remained though the force was aborted by disrupting the actin network, proving that the peeling probe is an irreversible tension sensor. Scale bar = 10 µm.

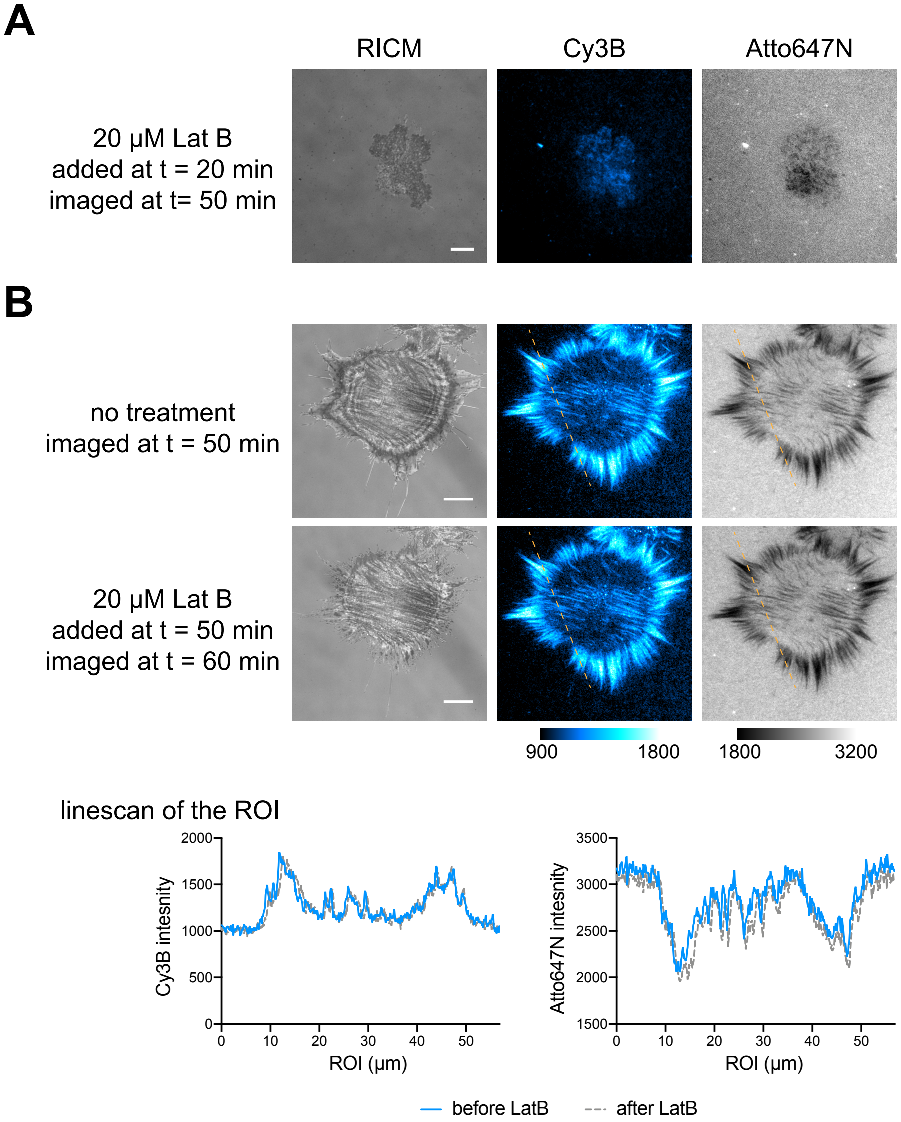

Figure A5.4. NIH3T3 cells plated on TGT tension probes. (A) Schematic shows the shearing and unzipping TGT tension probe designs which rupture at 56 pN and 12 pN, respectively, and de-quench the Cy3B. (B) NIH3T3 cells incubated on a 56 pN TGT substrate produced tension > 56 pN. Scale bar = 10 µm.

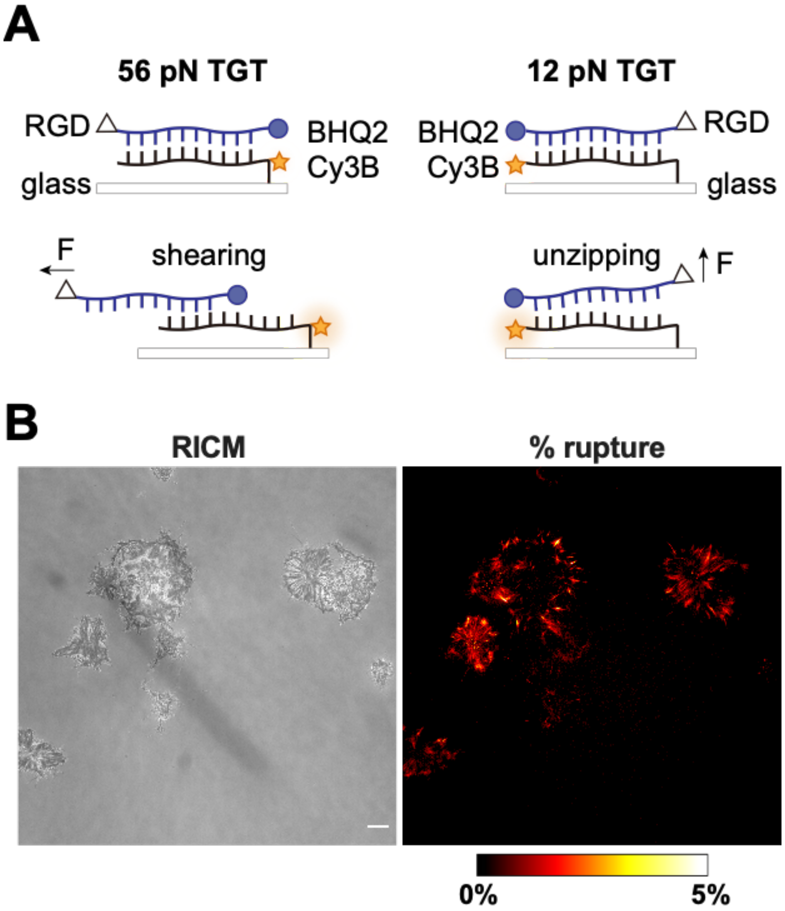

Figure A5.5. Different phenotypes of actin distribution observed in NIH3T3s incubated on three substrates. NIH3T3 cells were incubated on the surface for 1 h and then fixed and permeabilized. The actin was then stained with SiRActin reagent and imaged. (A) The DNA force-induced dehybridization mechanisms that could contribute to the formation of the distinct phenotype distributions. (B) Representative microscopy images showing the distribution of actin stress fibers inside cells. The stress fibers were likely located on top of the nucleus forming perinuclear actin cap (as the focal plane elevated, the fibers at the center were more in focus, see side view and top-down view illustration). Scale bar = 5 µm. (C) Representative microscopy images showing the distribution of actin inside the cells which showed distinct phenotypes. Based on these phenotypes, cells were categorized into 8 different types[19-20, 24, 30-33]. The non-spreading (type 1) and minimal spreading with clear cortex actin and filopodia (type 2) were the phenotypes observed with cells plated on 12 pN TGT substrates. The cells that only showed actin mesh and did not form actin stress fibers (type 3) were commonly observed on 56 pN TGT, as well as the cells with cortical and less organized actin stress fibers (type 5) and (type 2). Actin stress fibers were observed among cells on the peeling probe substrate most frequently (Type 4, 5, 6, 7, 8), and in the center of the cells, polarized actin stress fibers that are likely to be the perinuclear actin cap were often observed (Type 6, 7, 8). N = 41 cells for 12 pN TGT, 50 cells for 56 pN, and 170 cells for peeling probe. Scale bar = 10 µm. (D) A semi-quantitative analysis of the relative frequency of each phenotype on the 3 different substrates.

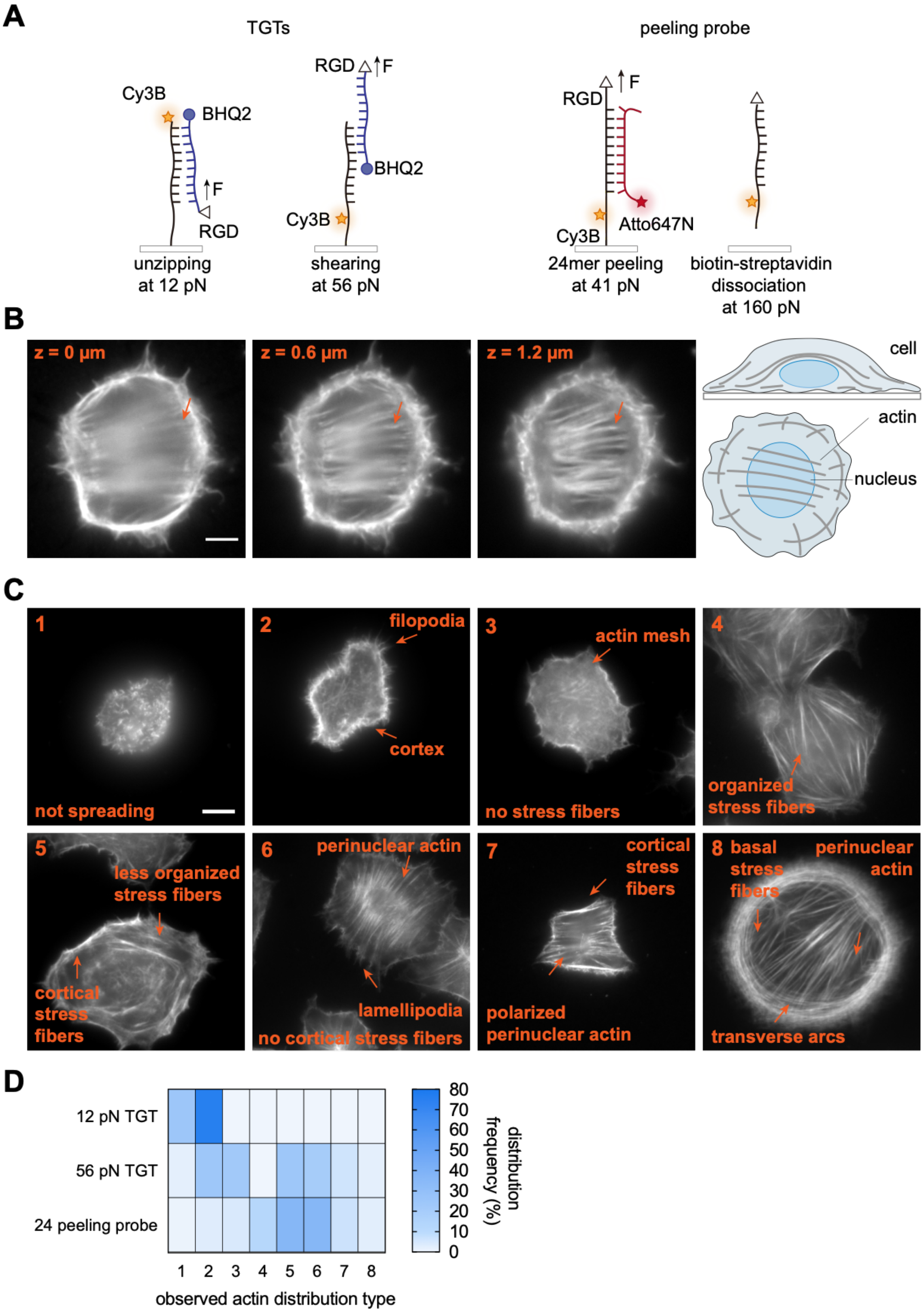
A
TGTs
Cy3B
BHQ2
F
RGD
unzipping
at 12 pN
RGD
F
BHQ2
Cy3B
shearing
at 56 pN
peeling probe
RGD
F
Cy3B
Atto647N
24mer peeling
at 41 pN
biotin-streptavidin
dissociation
at 160 pN
B
z = 0 μm
z = 0.6 μm
z = 1.2 μm
cell
actin
nucleus
C
1
not spreading
2
filopodia
cortex
3
actin mesh
no stress fibers
4
organized
stress fibers
5
less organized
stress fibers
cortical
stress
fibers
6
perinuclear actin
lamellipodia
no cortical stress fibers
7
cortical
stress
fibers
polarized
perinuclear actin
8 basal
stress
fibers
perinuclear
actin
transverse arcs
D
12 pN TGT
56 pN TGT
24 peeling probe
1
2
3
4
5
6
7
8
observed actin distribution type
80
70
60
50
40
30
20
10
0
distribution
frequency (%)

Figure A5.6. Control groups show that the tagging was specific to integrin-RGD forces and was cholesterol-mediated. (A) Representative microscopy images of NIH3T3 cells incubated on the control substrates, on which the RGD ligands were not presented on the LIPID probe. No tension signal was observed and no significant loss of peeling strand from the LIPID probe was observed. (B) Representative flow cytometry histograms show that the fluorescence tagging with the cholesterol peeling strand was specific to integrin tension and was cholesterol mediated. The median fluorescence intensity and %positive was plotted to show the selectivity of force. For %positive, the gate was drawn using the negative controls. Histogram and MFI of Cy3B fluorescence is also included to show that rupture and insertion of only the peeling strand is leading to tagging. The 24 peeling probe (no cholesterol) group was included to show that the cholesterol moiety led to the tagging result.

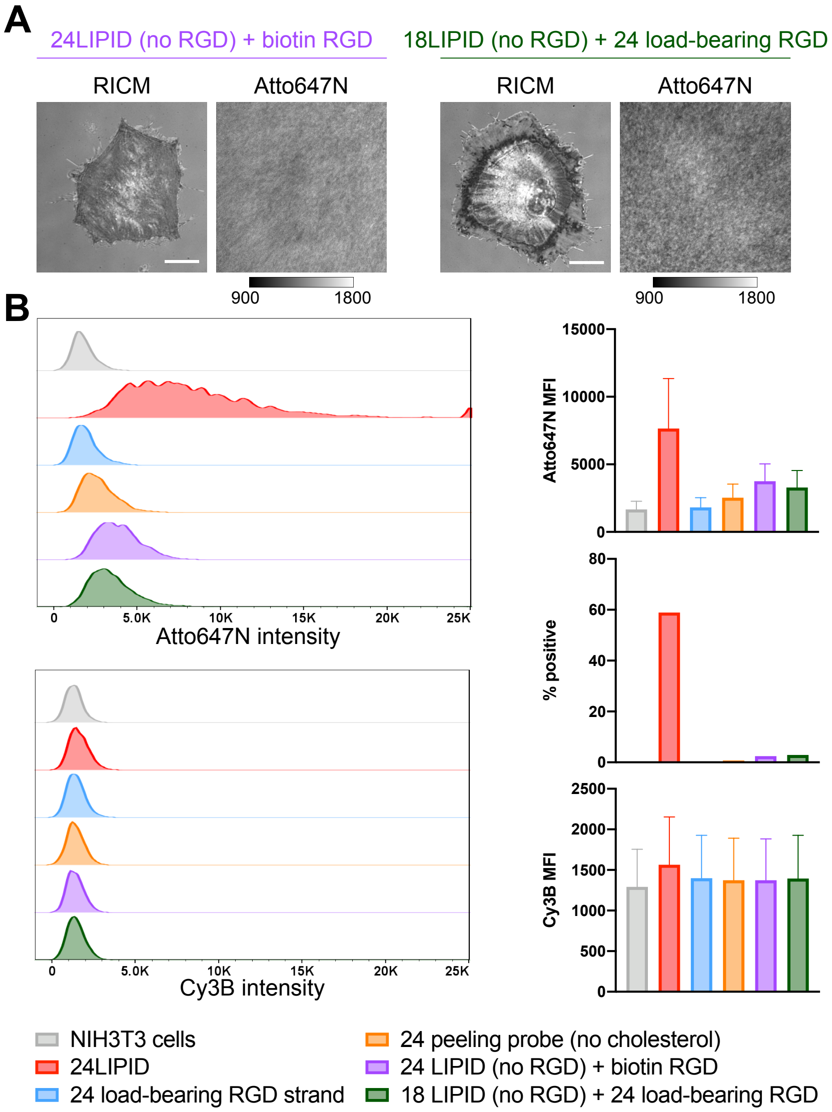

Figure A5.7. The stability of cholesterol tagging. NIH3T3 cells were incubated with 100 nM 24mer cholesterol 647N strand for 30 min and rinsed with PBS 3 times. Then, the cells were resuspended in medium containing 2 mM EDTA to prevent clumping and divided into 6 aliquots. Cells were run in a flow cytometer to detect the strand incorporation level every 30 min for 150 min using the 6 aliquots. During the incubation, samples were kept on ice in the dark. (A) Representative histogram shows the decay of fluorescence over time. (B) The normalized median fluorescence intensity (MFI) was plotted to show the dissociation of cholesterol strand over time in NIH3T3 cells. Experiments were conducted in biological replicates.

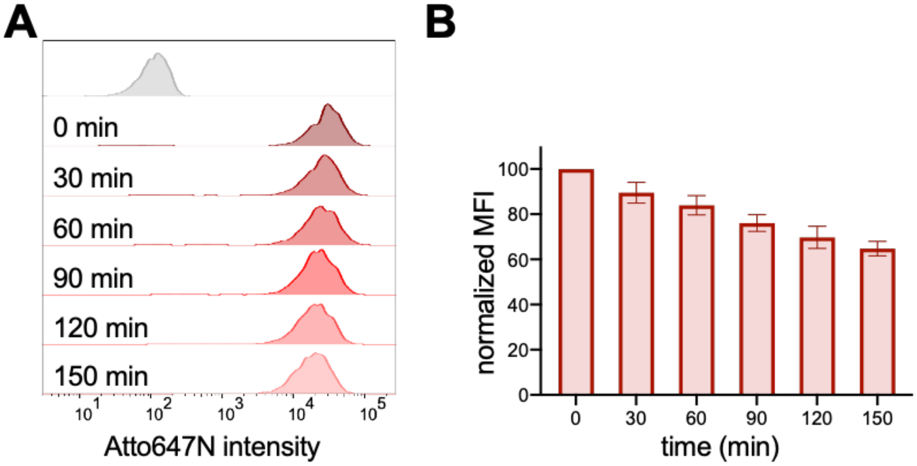

Figure A5.8. LIPID approach using a non-fluorescent load-bearing strand. Flow cytometry histograms showing that the LIPID approach is reproducible with a non-fluorescent load-bearing strand. This could reduce the cost of making the LIPID substrate, as the fluorescent load-bearing strand has 3 modifications, which is expensive and unnecessary if the LIPID approach is only being used for flow cytometry. The negative controls showed minimal background strand incorporation while the 24LIPID showed strong tagging with good reproducibility.

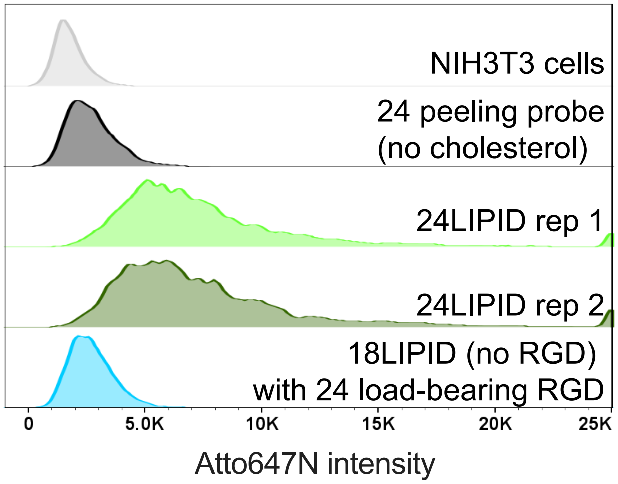

Figure A5.9. Microscopy data analysis. Raw fluorescence imaging data was collected and the sCMOS background was subtracted. Three local ROIs were drawn, and the duplex probe background $I_{DA\ resting}$ was measured and averaged. Then, the fluorescence of the fully peeled background I_D was calculated using FRET efficiency calculated from Figure A.5.2. The image was then divided by I_D to obtain an I_{DA}/I_D tension image. The I_{DA}/I_D image was then converted to %peel by applying a predefined conversion function in Figure A.5.2.

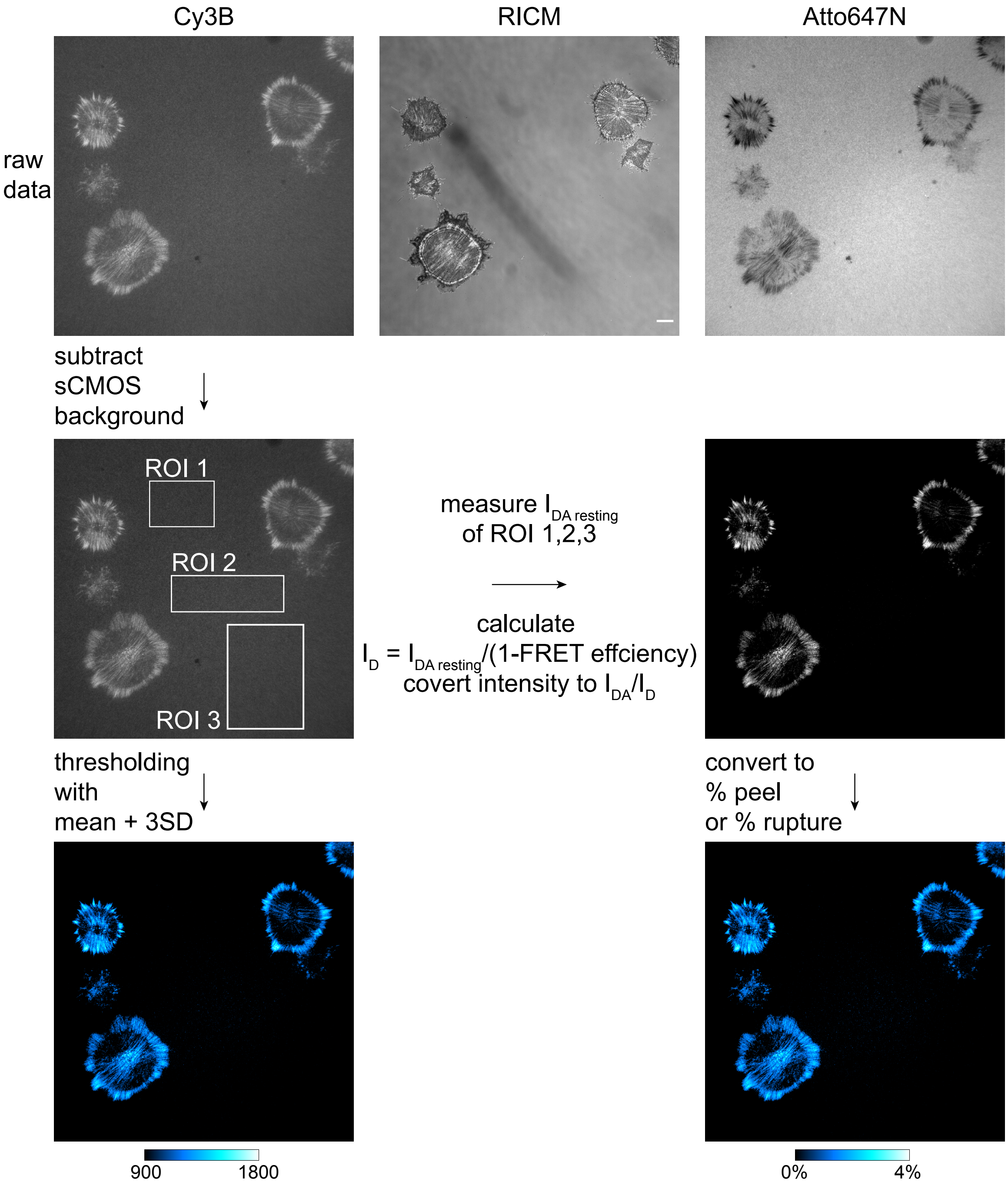

Figure A5.10. Representative flow cytometry gating. For the flow cytometry analysis of the LIPID tagging, live cells and singlets cells were identified sequentially using the forward scatter/side scatter area and height, respectively.

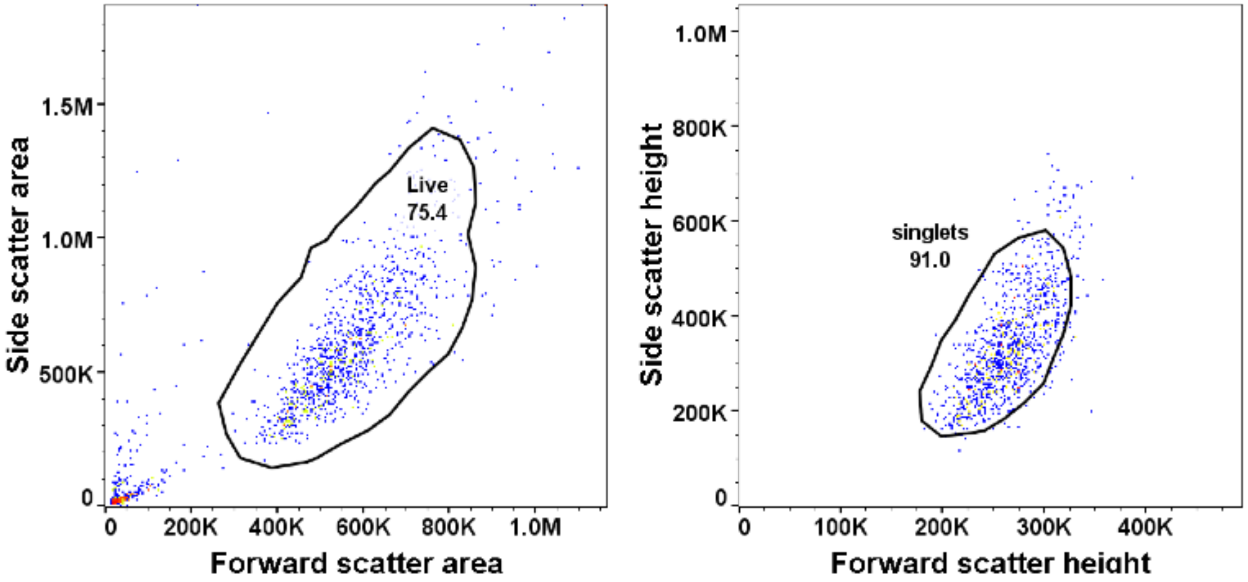

5.6. References

1. C. S. Chen, Mechanotransduction - a field pulling together? *J Cell Sci* **2008,** *121* (Pt 20), 3285.

2. T. Iskratsch; H. Wolfenson; M. P. Sheetz, Appreciating force and shape-the rise of mechanotransduction in cell biology. *Nat Rev Mol Cell Biol* **2014,** *15* (12), 825.

3. D. Mohammed; M. Versaevel; C. Bruyere; L. Alaimo; M. Luciano; E. Vercruysse; A. Proces; S. Gabriele, Innovative Tools for Mechanobiology: Unraveling Outside-In and Inside-Out Mechanotransduction. *Front Bioeng Biotechnol* **2019,** *7*, 162.

4. D. S. Harburger; D. A. Calderwood, Integrin signalling at a glance. *Journal of cell science* **2009,** *122* (2), 159.

5. S. K. Mitra; D. A. Hanson; D. D. Schlaepfer, Focal adhesion kinase: in command and control of cell motility. *Nat Rev Mol Cell Biol* **2005,** *6* (1), 56.

6. A. Stubb; R. F. Laine; M. Miihkinen; H. Hamidi; C. Guzman; R. Henriques; G. Jacquemet; J. Ivaska, Fluctuation-Based Super-Resolution Traction Force Microscopy. *Nano Lett* **2020,** *20* (4), 2230.

7. W. J. Polacheck; C. S. Chen, Measuring cell-generated forces: a guide to the available tools. *Nat Methods* **2016,** *13* (5), 415.

8. B. L. Blakely; C. E. Dumelin; B. Trappmann; L. M. McGregor; C. K. Choi; P. C. Anthony; V. K. Duesterberg; B. M. Baker; S. M. Block; D. R. Liu; C. S. Chen, A DNA-based molecular probe for optically reporting cellular traction forces. *Nat Methods* **2014,** *11* (12), 1229.

9. Y. Liu; K. Yehl; Y. Narui; K. Salaita, Tension sensing nanoparticles for mechano-imaging at the living/nonliving interface. *Journal of the American Chemical Society* **2013,** *135* (14), 5320.

10. Y. Zhang; C. Ge; C. Zhu; K. Salaita, DNA-based digital tension probes reveal integrin forces during early cell adhesion. *Nature communications* **2014,** *5*, 5167.

11. X. Wang; T. Ha, Defining single molecular forces required to activate integrin and notch signaling. *Science* **2013,** *340* (6135), 991.

12. Y. Wang; D. N. LeVine; M. Gannon; Y. Zhao; A. Sarkar; B. Hoch; X. Wang, Force-activatable biosensor enables single platelet force mapping directly by fluorescence imaging. *Biosens Bioelectron* **2018,** *100*, 192.

13. Z. J. Yang; G. H. Yuan; W. L. Zhai; J. Yan; H. Chen, The kinetics of force-dependent hybridization and strand-peeling of short DNA fragments. *Science China Physics, Mechanics & Astronomy* **2016,** *59* (8).

14. S. Cocco; J. Yan; J. F. Leger; D. Chatenay; J. F. Marko, Overstretching and force-driven strand separation of double-helix DNA. *Phys Rev E Stat Nonlin Soft Matter Phys* **2004,** *70* (1 Pt 1), 011910.

15. X. Zhang; H. Chen; H. Fu; P. S. Doyle; J. Yan, Two distinct overstretched DNA structures revealed by single-molecule thermodynamics measurements. *Proc Natl Acad Sci U S A* **2012,** *109* (21), 8103.

16. Z. Yang; G. Yuan; W. Zhai; J. Yan; H. Chen, The kinetics of force-dependent hybridization and strand-peeling of short DNA fragments. *Science China Physics, Mechanics & Astronomy* **2016,** *59* (8).

17. C. Jurchenko; Y. Chang; Y. Narui; Y. Zhang; K. S. Salaita, Integrin-generated forces lead to streptavidin-biotin unbinding in cellular adhesions. *Biophys J* **2014,** *106* (7), 1436.

18. K. Burridge; E. S. Wittchen, The tension mounts: stress fibers as force-generating mechanotransducers. *J Cell Biol* **2013,** *200* (1), 9.

19. M. Maninova; T. Vomastek, Dorsal stress fibers, transverse actin arcs, and perinuclear actin fibers form an interconnected network that induces nuclear movement in polarizing fibroblasts. *FEBS J* **2016,** *283* (20), 3676.

20. T. M. Svitkina, Actin Cell Cortex: Structure and Molecular Organization. *Trends Cell Biol* **2020,** *30* (7), 556.

21. J. I. Lehtimaki; E. K. Rajakyla; S. Tojkander; P. Lappalainen, Generation of stress fibers through myosin-driven reorganization of the actin cortex. *Elife* **2021,** *10*.

22. D. H. Kim; S. B. Khatau; Y. Feng; S. Walcott; S. X. Sun; G. D. Longmore; D. Wirtz, Actin cap associated focal adhesions and their distinct role in cellular mechanosensing. *Sci Rep* **2012,** *2*, 555.

23. S. B. Khatau; C. M. Hale; P. J. Stewart-Hutchinson; M. S. Patel; C. L. Stewart; P. C. Searson; D. Hodzic; D. Wirtz, A perinuclear actin cap regulates nuclear shape. *Proc Natl Acad Sci U S A* **2009,** *106* (45), 19017.

24. X. Shao; Q. Li; A. Mogilner; A. D. Bershadsky; G. V. Shivashankar, Mechanical stimulation induces formin-dependent assembly of a perinuclear actin rim. *Proc Natl Acad Sci U S A* **2015,** *112* (20), E2595.

25. J. Y. Shiu; L. Aires; Z. Lin; V. Vogel, Nanopillar force measurements reveal actin-cap-mediated YAP mechanotransduction. *Nat Cell Biol* **2018,** *20* (3), 262.

26. S. B. Khatau; D. H. Kim; C. M. Hale; R. J. Bloom; D. Wirtz, The perinuclear actin cap in health and disease. *Nucleus* **2010,** *1* (4), 337.

27. D. H. Kim; A. B. Chambliss; D. Wirtz, The multi-faceted role of the actin cap in cellular mechanosensation and mechanotransduction. *Soft Matter* **2013,** *9* (23), 5516.

28. Y. M. Efremov; M. Velay-Lizancos; C. J. Weaver; A. I. Athamneh; P. D. Zavattieri; D. M. Suter; A. Raman, Anisotropy vs isotropy in living cell indentation with AFM. *Sci Rep* **2019,** *9* (1), 5757.

29. J. Konen; E. Summerbell; B. Dwivedi; K. Galior; Y. Hou; L. Rusnak; A. Chen; J. Saltz; W. Zhou; L. H. Boise; P. Vertino; L. Cooper; K. Salaita; J. Kowalski; A. I. Marcus, Image-guided genomics of phenotypically heterogeneous populations reveals vascular signalling during symbiotic collective cancer invasion. *Nat Commun* **2017,** *8*, 15078.

30. L. Blanchoin; R. Boujemaa-Paterski; C. Sykes; J. Plastino, Actin dynamics, architecture, and mechanics in cell motility. *Physiol Rev* **2014,** *94* (1), 235.

31. E. Kassianidou; S. Kumar, A biomechanical perspective on stress fiber structure and function. *Biochim Biophys Acta* **2015,** *1853* (11 Pt B), 3065.

32. G. Letort; H. Ennomani; L. Gressin; M. Thery; L. Blanchoin, Dynamic reorganization of the actin cytoskeleton. *F1000Res* **2015,** *4*.

33. T. Vignaud; C. Copos; C. Leterrier; M. Toro-Nahuelpan; Q. Tseng; J. Mahamid; L. Blanchoin; A. Mogilner; M. Thery; L. Kurzawa, Stress fibres are embedded in a contractile cortical network. *Nat Mater* **2021,** *20* (3), 410.

Chapter 6. Summary and future outlook

6.1. Summary

This dissertation began with a discussion of the current molecular tension probe techniques that are used to investigate receptor mechanics. To further advance the field and build better tools to study receptor mechanics, the research described herein all started with a simple question: can we design a complementary strand that would selectively hybridize to an oligonucleotide when it is under force? To address this question, a small library of oligonucleotides was designed and screened for their ability to initiate mechanically selective hybridization. When this concept was tested with different cells transmitting pN forces to unfold the DNA hairpin, a fundamental phenomenon was observed: only weaker forces (<19 pN) allow the mechanically selective hybridization to occur. This phenomenon is a result of stronger forces' ability to significantly stretch the oligonucleotide and hinder hybridization.

Starting with this observation, **Chapter 2** discussed the development of a mechanical information storing DNA tension probe with mechanically selective hybridization, which was designed to be applied to immune cells with the goal of visualizing difficult-to-detect receptor forces. The ability of the probe to toggle between measuring real-time tension and accumulative tension made it versatile, allowing for applications in both static and migratory cells. The application in T cells revealed that T cells transmit > 4.7 pN TCR forces to altered peptide ligands (APL) and that the mechanical sampling of APLs is correlated with their potency. In addition, we also used it in activated T cells and discovered that PD1 transmits > 4.7 pN forces to PDL2. This tension probe is among the most sensitive molecular force detection methods, ideal for visualizing weak and transient forces, as well as forces that are transmitted through low-density receptors. Note however that the forces accumulated and amplified with this method are limited to 4.7 – 19 pN.

Building on the mechanical information storing probes, **Chapter 3** discussed a method to measure ensemble TCR force lifetimes. We manipulated the DNA hybridization kinetics and used it to benchmark the TCR force lifetimes against antiCD3ε, cognate peptide antigen, and an APL. Additionally, we studied the effect of CD28 and LFA-1 engagement on TCR force and force lifetimes, as well as the cytoskeleton network. This method measures force lifetimes when T cells actively exert forces to challenge the TCR-pMHC binding, as opposed to single molecule force spectroscopy methods which apply external force to cells with less relevant force loading rates. Currently this method is limited to measuring force lifetimes for $4.7 \text{ pN} < F < 19 \text{ pN}$, with a lifetime detection range of approximately hundreds of milliseconds to tens of seconds.

Furthermore, we expanded the utilities of the mechanically selective hybridization strategy by coupling it with a proximity labeling technique. In **Chapter 4**, we designed an enzymatic tagging reaction with which we were able to covalently tag specifically the mechanically active cells for high throughput identification and sorting. Despite the significant potential of mechano-tagging in identifying mechanically active T cells and TCRs against antigens in a potency dependent manner, the limitation of this method is once again that it only works for receptor forces <19 pN.

In addition to utilizing mechanically selective hybridization with forces < 19 pN to develop new tools for mechanobiology studies, the failed hybridization under higher magnitude forces was also taken advantage of and used to develop a new type of DNA tension probe featuring a unique peeling mechanism. **Chapter 5** discussed the design and application of the peeling probe in fibroblast cells to irreversibly map the integrin tension without perturbation of cell mechanical signaling. This approach was also found to be effective in platelets and stem cells, but the data was not included in this dissertation. The peeling probe was further functionalized with a cell-targeting moiety, which enabled high throughput detection of individual cells with a more active mechanical status. This method simplified the mechano-tagging procedure and expanded the detection range to forces between 41 and 160 pN.

Taken together, this dissertation started from a simple observation regarding the effectiveness of DNA hybridization under different levels of force and made the most of both successful and failed hybridization. Four new methods that are suitable to address a wide range of questions in mechanobiology were developed. We envision that this toolbox based on DNA nanotechnology will greatly aid the field as it continues to investigate cell mechanics from many different angles.

6.2. Future outlook for cell receptor mechanics studies with current techniques

6.2.1. Direct observation of catch-bond in TCR

For most non-covalent bonds, the bond lifetime decreases when the bond is under mechanical strain (slip-bond); however, for catch-bonds, the lifetime increases while under strain, as certain levels of force stabilize the interaction [1]. A growing number of single-molecule studies show that the TCR-pMHC complex displays catch-bond behavior [2]. However, this model was recently put into question when a cell-free flow system did not find catch bond characteristics for the TCR-pMHC complex [3]. Since current observations of catch-bond behavior were made with experiments where the force is applied externally [2], it is vital to observe a living cell exhibiting the catch-bond behavior as it applies force itself during TCR triggering. The DNA probe-based technique to measure the ensemble force lifetimes described in Chapter 3 offers a promising approach to address this question. For example, if we can measure the lifetimes for TCR F > 12 pN, and F > 4.7 pN and demonstrate that the lifetime of > 12 pN forces is longer than that of > 4.7 pN forces, this would be a critical piece of direct evidence that catch-bonds exist and are actively applied by cells to challenge antigens.

6.2.2. Neoantigen and neoantigen-specific T cell identification

Neoantigens have received tremendous attention because of their huge potential in triggering T cell responses. They are exquisite, tumor-specific peptides containing mutations that are derived from genetic alterations in the tumor. Therefore, with better identification of neoantigens and neoantigen-specific T cells, personalized immunotherapy used to elicit antitumor responses can be developed [4]. Current techniques for neoantigen identification rely on whole exome and RNA sequencing to predict epitopes, followed by peptide HLA binding assay and MS-based immunopeptidomics to validate the epitope binding, and then finally evaluation of immunogenicity by pMHC tetramer staining [5]. Despite some successes, a significant limitation of this prediction-validation-evaluation method is that it lacks a faithful marker for immunogenicity. Alternatively, since T cells harness mechanical forces during antigen recognition and T cell activation, mechanical proximity biotinylation during TCR-pMHC binding would label the pMHCs and the TCRs that have mechanical activity, which is hypothesized to be an improved marker for immunogenicity. These antigen-specific T cells and the recognized antigens can then be isolated and identified with proteomics as it carries the biotin tag. This approach has the potential to aid the development of personalized cancer immunotherapy.

6.2.3 Elucidating the TCR “mechanome” to better understand the T cell triggering mechanism

Given that the TCR forms signaling clusters during triggering, it is highly likely that T cells strategically organize co-receptors to apply defined forces for antigen discrimination. Elucidating this TCR “mechanome” will be critical in better understanding the T cell triggering mechanism. The mechanical proximity tagging technique can be applied, which selectively labels proteins within a restricted radius of the enzyme (~20 nm). If the labeled proteins on the T cells' membranes can be isolated using a pull-down technique, the key players during TCR mechano-triggering can be identified with proteomics.

6.2.4. Elucidating the mechanical regulation network and predicting mechanical plasticity with transcriptomics

As mechanical heterogeneity is often observed among various types of cells with different methods, identifying the genes that regulate the cell mechanics will be a major advance in mechanobiology. The mechano-tagging techniques for cells coupled with RNA sequencing and expression analysis could be an effective method to find out the gene expression differences in cells with high and low mechanical activities and map the mechano-regulation network. If successful, this method could begin to offer fundamental mechanisms to explain the many observations that have been made, and further develop mechanics as a biomarker to predict cell fate, such as stem cell differentiation or cancer metastasis potential.

6.2.5. Applying mechanically selective hybridization-based methods to integrins

As one of the limitations of the current mechanically selective hybridization is that only forces below 19 pN are compatible, forces exerted by focal adhesions are largely excluded from the applications based on the mechanically selective hybridization. One alternative approach that could expand the utility of this hybridization is to have an unstrained binding site that is specific to mechanical forces. An unstrained real-time DNA tension probe that was developed recently to accommodate super-resolution tension imaging can be repurposed and used for both integrin force lifetime measurements and proximity tagging [6].

6.2.6. Other directions

Mapping the cell mechanics inside and outside cells simultaneously can be powerful in elucidating how force is transmitted throughout different components within the cellular machinery. Coupling the DNA tension probes with protein-based FRET probes or measurement of actin retrograde flow are good starting points for such investigations. Other interesting topics to explore further include the mechanical forces of virus particle entry, mechanics of engineered CAR-T cells, the cell nuclear mechanosensing of the ECM, differences in mechanics in healthy versus diseased cells, etc. To summarize, elucidating the relationship between tension and function needs extensive work and there are many uncharted territories in the field of mechanobiology.

6.3. Future outlook for DNA mechano-technology

DNA tension probes are exceptional when used outside cells at the interface between cells and surfaces. However, their use inside cells is limited because of nuclease-mediated degradation. Nuclease-resistant DNA tension probes will allow force mapping for cells in culture in order to, for example, track the mechanical footprint of stem cell differentiation. Moreover, integrating tension probes into 3D matrices or cell-cell junctions is critical, as it better mimics the biological environment than a 2D planar surface. The next generation of tools based on DNA nanotechnology that are used to study cell mechanics should also try to deconvolute the effects of force and work when evaluating the cell mechanics. As the length of DNA can be easily tuned and its extension obeys the WLC model, new types of probes can be designed to achieve this goal. Likewise, another domain that is forgotten is time. Specifically, there are interesting questions that can be asked to further characterize the receptor mechanics in regard to the loading rate of the force, as well as the output power of a single receptor. Furthermore, tools that can detect molecular pushing or protrusive forces are equally important, as the cells not only mechanically sense the environment, but also respond to it, especially at the cell-cell junction.

6.4. Concluding remarks

The nature of DNA has made it stand out among all the polymers that can act like a molecular spring for the purpose of tool development in mechanobiology. Beyond that, the power of DNA nanotechnology reaches far beyond the field of mechanobiology for a few reasons. First, DNA is a highly tunable material. The length and GC% can be easily tuned and delicately designed to accommodate any needs. Second, DNA is highly customizable. It is exceedingly easily to chemically functionalize DNA, allowing for applications requiring fluorescence and chemical attachment. The purification and quantification of DNA is facile and standardized, assuring the reproducibility of its applications. Third, DNA obeys the simple rules of base-pairing, giving it a unique ability to form many highly specific interactions with its complementary strand, as well as other molecules, including small molecule drugs, fluorophores, or proteins (e.g., aptamers). Desired reaction/interaction/response with DNA can be achieved easily on both molecular and cellular levels. For example, a wide range of enzymes are available to specifically react with DNA, many with sequence-specificity. Desired binding and unbinding can be designed by incorporating recognition sequences or tuned by the thermodynamics and kinetics. Furthermore, if a biological response is desired, the DNA sequence is easily controlled in order to give cells specific orders. Fourth, DNA structures are highly modular. With the simple rule of base-pairing and a variety of modifications, DNA can be assembled easily into constructs with functions that can be tuned conveniently, from precisely controlling the spacing between molecules (DNA origami) to sensing and controlling forces (DNA tension probes and TGTs). These features highlight the versality and power of DNA nanotechnology. It is truly a field full of possibilities.

6.5. References

1. C. Zhu; W. Chen; J. Lou; W. Rittase; K. Li, Mechanosensing through immunoreceptors. *Nat Immunol* **2019,** *20* (10), 1269.

2. J. Huang; V. I. Zarnitsyna; B. Liu; L. J. Edwards; N. Jiang; B. D. Evavold; C. Zhu, The kinetics of two-dimensional TCR and pMHC interactions determine T-cell responsiveness. *Nature* **2010,** *464* (7290), 932.

3. L. Limozin; M. Bridge; P. Bongrand; O. Dushek; P. A. van der Merwe; P. Robert, TCR-pMHC kinetics under force in a cell-free system show no intrinsic catch bond, but a minimal encounter duration before binding. *Proc Natl Acad Sci U S A* **2019,** *116* (34), 16943.

4. T. P. Riley; G. L. J. Keller; A. R. Smith; L. M. Davancaze; A. G. Arbuiso; J. R. Devlin; B. M. Baker, Structure Based Prediction of Neoantigen Immunogenicity. *Front Immunol* **2019,** *10*, 2047.

5. J. Galvez; J. J. Galvez; P. Garcia-Penarrubia, Is TCR/pMHC Affinity a Good Estimate of the T-cell Response? An Answer Based on Predictions From 12 Phenotypic Models. *Front Immunol* **2019,** *10*, 349.

6. J. M. Brockman; H. Su; A. T. Blanchard; Y. Duan; T. Meyer; M. E. Quach; R. Glazier; A. Bazrafshan; R. L. Bender; A. V. Kellner, Live-cell super-resolved PAINT imaging of piconewton cellular traction forces. *Nature Methods* **2020,** *17* (10), 1018.